

Carboxylic derivatives of spin-crossover complexes in switchable materials and surfaces



Universidad de Valencia

Instituto de Ciencia Molecular (ICMol)

Memoria presentada por **Víctor García López** para aspirar al título de
Doctor en Nanociencia y nanotecnología.

Dirigida por:

Prof. Miguel Clemente León

Prof. Eugenio Coronado Miralles

Noviembre 2022

Los profesores Eugenio Coronado Miralles y Miguel Clemente León, investigadores del Instituto de Ciencia Molecular (ICMol) de la Universidad de Valencia

CERTIFICAN

Que Víctor García López ha realizado la presente Tesis Doctoral, titulada “Carboxylic derivatives of spin-crossover complexes in switchable materials and surfaces”, corresponde al trabajo realizado bajo su dirección en el ICMol, autorizando mediante este escrito la presentación de la misma para optar al grado de Doctor en Nanociencia y Nanotecnología por la Universidad de Valencia.

Y para que conste firman el presente certificado en Paterna, a 21/07/2022.

Fdo. Prof. Miguel Clemente León

Prof. Eugenio Coronado

1. Index

1. Index.....	i
2. Summary and organization	v
3. List of publications	xi
4. Abbreviations.....	xiii
5. Figures.....	xv
5.1. Main text figures	xv
5.2. Supporting information figures	xix
6. Tables.....	xxix
6.1. Main text tables	xxix
6.2. Supporting information tables	xxix
1. Introduction to Fe(II) and Co(II) spin-crossover complexes and switchable self-assembled monolayers	1
1.1. Crystal Field Theory	3
1.2. Ligand Field Theory.....	4
1.3. Spin-Crossover phenomenon	6
1.4. Light-Induced Excited Spin-State Trapping.....	7
1.5. Iron(II) SCO complexes of 2,6-bis(pyrazol-1-yl)pyridine (1bpp) and derivatives	9
1.6. Co(II) SCO complexes of 2,2':6',2''-terpyridine (terpy) and derivatives	11
1.7. Self-Assembled Monolayers	14
1.8. Switchable SAMs.....	15
1.9. Characterization techniques	18
1.10. References	23
2. Spin-crossover compounds based on Fe(II) complexes of 2,6-bis(pyrazol-1-yl)pyridine (1bpp) functionalized with carboxylic acid (1bppCOOH) and ethyl carboxylate (1bppCOOEt)...	29

2.1. Motivation.....	31
2.2. Results and discussion.....	32
Synthesis of the compounds.....	32
Structure of [Fe(1bppCOOH) ₂](ClO ₄) ₂ (1(ClO₄)₂) and [Fe(1bppCOOH) ₂](BF ₄) ₂ (1(BF₄)₂)	32
Structure of [Fe(1bppCOOH) ₂](CF ₃ SO ₃) ₂ ·yMe ₂ CO (1(CF₃SO₃)₂·yMe₂CO).....	34
Structure of [Fe(1bppCOOH) ₂](AsF ₆) ₂ ·yMe ₂ CO (1(AsF₆)₂·yMe₂CO) and [Fe(1bppCOOH) ₂](SbF ₆) ₂ ·yMe ₂ CO (1(SbF₆)₂·yMe₂CO).....	36
Structure of [Fe(1bppCOOEt) ₂](ClO ₄) ₂ ·yMe ₂ CO (2(ClO₄)₂·yMe₂CO).....	38
Magnetic and photomagnetic properties.....	40
Deposition of 1	47
2.3. Conclusions.....	52
2.4. Supporting Information.....	54
2.5. References.....	75
3. Fe(II) SCO complexes of 1bpp derivatives functionalized with carboxylic acid groups in the 3-pyridyl (1bpp3COOH) and 4-pyrazolyl (1bpCOOH ₂ p) positions.....	79
3.1. Motivation.....	81
3.2. Results and discussion.....	82
Synthesis of [Fe(1bpp3COOH) ₂](ClO ₄) ₂ ·0.5EtOH·0.5H ₂ O (1).....	82
Structure of [Fe(1bpp3COOH) ₂](ClO ₄) ₂ ·0.5EtOH·0.5H ₂ O (1).....	83
Magnetic and photomagnetic properties.....	84
Deposition.....	85
Synthesis of Fe(1bpCOOH ₂ p) ₂](ClO ₄) ₂ ·3.5Me ₂ CO (2) and [Fe(1bpCOOCOOPh)(1bpCOOH ₂ p)Fe(1bpCOOH ₂ p)(ClO ₄)](ClO ₄) ₂ ·H ₂ O·1.5Me ₂ CO (3)....	86
Magnetic properties.....	86
Structure of Fe(1bpCOOH ₂ p) ₂](ClO ₄) ₂ ·3.5Me ₂ CO (2).....	87
Photomagnetic properties.....	89

Low temperature X-ray diffraction studies with light	91
Deposition.....	93
3.3. Conclusions.....	95
3.4. Supporting Information	98
Deposition.....	101
Structure and magnetic properties of 3	106
Supporting information of $\text{Fe}(\text{1bpCOOH}_2\text{p})_2(\text{ClO}_4)_2 \cdot 3.5\text{Me}_2\text{CO}$ (2).....	108
3.5. References	131
4. Heteroleptic Fe(II) SCO complexes based on 1bppCOOH.....	135
4.1. Motivation.....	137
4.2. Results and discussion	138
Structure of $[\text{Fe}(\text{1bppCOOH})(\text{3bpp-bph})](\text{ClO}_4)_2 \cdot 2\text{Me}_2\text{CO} \cdot 0.5\text{Et}_2\text{O}$ (1-2Me₂CO-0.5Et₂O) and $[\text{Fe}(\text{1bppCOOH})(\text{3bpp-bph})](\text{ClO}_4)_2 \cdot \text{Me}_2\text{CO}$ (1-Me₂CO)	139
Structure of $[\text{Fe}(\text{1bppCOOH})(\text{1bppCOOEt})](\text{ClO}_4)_2 \cdot 0.5\text{Me}_2\text{CO}$ (2-0.5Me₂CO)	141
Magnetic and photomagnetic properties of $[\text{Fe}(\text{1bppCOOH})(\text{3bpp-bph})](\text{ClO}_4)_2 \cdot 2\text{Me}_2\text{CO} \cdot 0.5\text{Et}_2\text{O}$ (1-2Me₂CO-0.5Et₂O) and $[\text{Fe}(\text{1bppCOOH})(\text{3bpp-bph})](\text{ClO}_4)_2 \cdot \text{Me}_2\text{CO}$ (1-Me₂CO)	142
Deposition of the heteroleptic complexes.....	145
4.3. Conclusions.....	145
4.4. Supporting information	147
Synthesis of (2,6-bis(5-([1,1'-biphenyl]-4-yl)-1H-pyrazol-3-yl)pyridine) (3bpp-bph) ..	147
Synthesis of $[\text{Fe}(\text{1bppCOOH})(\text{3bpp-bph})](\text{ClO}_4)_2 \cdot 2\text{Me}_2\text{CO} \cdot 0.5\text{Et}_2\text{O}$ (1-2Me₂CO-0.5Et₂O), $[\text{Fe}(\text{1bppCOOH})(\text{3bpp-bph})](\text{ClO}_4)_2 \cdot \text{Me}_2\text{CO}$ (1-Me₂CO) and $[\text{Fe}(\text{1bppCOOH})(\text{1bppCOOEt})](\text{ClO}_4)_2 \cdot 0.5\text{Me}_2\text{CO}$ (2-0.5Me₂CO).....	147
4.5. References	159
5. Self-assembled monolayer of active SCO molecules based on a Co(II) terpyridine derivative bearing carboxylic acid groups.....	161

5.1. Motivation.....	163
5.2. Results and discussion.....	164
Synthesis of $[\text{Co}(4'-(4\text{-carboxyphenyl})-2,2':6',2''\text{-terpyridine})_2](\text{ClO}_4)_2 \cdot 4\text{DMA}$, (1)....	164
Structure of $[\text{Co}(4'-(4\text{-carboxyphenyl})-2,2':6',2''\text{-terpyridine})_2](\text{ClO}_4)_2 \cdot 4\text{DMA}$, (1).....	164
Magnetic properties	165
Deposition.....	166
5.3. Conclusions.....	177
5.4. Supporting Information	178
Synthesis of of $[\text{Co}(\text{L})(4'-(4\text{-carboxyphenyl})-2,2':6',2''\text{-terpyridine})_2](\text{ClO}_4)_2 \cdot 4\text{DMA}$, (1)	178
Magnetic properties of $[\text{Co}(\text{L})_2] \cdot 5\text{H}_2\text{O}$	179
Deposition of $[\text{Co}(\text{L})_2] \cdot 5\text{H}_2\text{O}$	180
5.5. References	191
6. General conclusions	193
6.1. Conclusions.....	195
6.2. References.....	197
7. Appendix.....	199
7.1. Characterization techniques.	199
7.2. Materials.....	204
7.3. References.....	204

2. Summary and organization

During the past ten years, after the discovery of the first spin-crossover (SCO) molecule thermally evaporated on top of a surface, there has been a rapid increase in the research of ultra-high vacuum thermally evaporable SCO complexes. So far, a few families of SCO complexes are suitable for this high-cost technique. Separately, self-assembly of molecules through wet-chemistry protocols also offers the opportunity to form nanostructures with low-cost methodologies. However, most of the attempts regarding SCO molecules have failed, leaving a void of scientific background on this topic. Therefore, this thesis is an input into that lack of knowledge by aiming to the preparation of SCO molecules suitable for surface deposition from solution. Hopefully it will be useful for the next generation of experiments and will be used as a guide towards the right direction.

In order to pursue this aim, rational design of new SCO complexes functionalized with anchoring groups able to specifically interact with the surface have been carried out. The SCO complexes investigated in this work are mainly Fe(II) and Co(II). Derivatives of two ligands well-known to give rise to SCO family of complexes have been employed, 2,6-bis(pyrazol-1-yl)pyridine and 2,2':6'',2'''-terpyridine, for Fe(II) and Co(II), respectively. Regarding the anchoring point, functionalization with a carboxylic acid group has been chosen due to its versatility to form self-assembled monolayers (SAMs) in different surfaces.

To a better understanding of the different strategies and approaches, the manuscript is divided in six main chapters:

The first chapter has been written with the intention to give the reader the basic knowledge to set the necessary background on the topic ahead of us. A concise introduction to the SCO phenomenon together with the most known SCO complexes, the concept of SAM, and its current situation on switchable molecules are presented to understand the difficulty of the challenge faced. Then, the most commonly used techniques to characterized magnetic properties in the monolayer regime, also employed by us, are briefly introduced.

Chapters 2 to 4 are based on Fe(II) 1bpp SCO complexes, while Chapter 5 is focused on a Co(II) terpy-based one. In all chapters, synthesis and characterization of the solid state is first presented and then SAM formation is studied and discussed.

In Chapter 2, a thorough study of our starting point-SCO molecule, $[\text{Fe}(\text{1bppCOOH})_2]^{2+}$, in the solid state is shown in order to get a better understanding of its magnetic properties. For that,

different counteranions (ClO_4^- , BF_4^- , CF_3SO_3^- , AsF_6^- , SbF_6^-), degrees of solvation and a slightly different ligand (bppCOOEt) are employed. Then, deposition of the molecules is studied and some problems that we will have to overcome are revealed.

In Chapter 3, two different variations of the ligand by changing the position of the carboxylic acid group are investigated. Characterization of the SCO complexes $[\text{Fe}(\text{1bpp3COOH})_2]^{2+}$ and $[\text{Fe}(\text{1bpCOOHp}_2)_2]^{2+}$ are presented in parts A and B, respectively. While the first one displays a gradual and incomplete thermal spin crossover, the second one shows a hysteretic thermal spin transition close to room temperature and an unusually high $T(\text{LIESST})$. This is related to thermal- and photoinduced SCO with symmetry breaking, which has been studied in detail with photocrystallographic measurements at low temperatures. Deposition of the two complexes has been unsuccessful due to oxidation of the $[\text{Fe}(\text{1bpp3COOH})_2]^{2+}$ complexes and the low processability of $[\text{Fe}(\text{1bpCOOHp}_2)_2]^{2+}$.

In Chapter 4, we approach the formation of heteroleptic complexes in an attempt to understand the role played by the ligand non-interacting with the surface. For that, a similar ligand, 1bppCOOEt also used in Chapter 2, and a bulkier one, 3bpp-bph, are employed. After the characterization of the bulk material, the similar structure of the $[\text{Fe}(\text{1bppCOOH})(\text{1bppCOOEt})]^{2+}$ heteroleptic complex with respect to our starting point-SCO molecule $[\text{Fe}(\text{bppCOOH})_2]^{2+}$, does not change the outcome upon deposition. On the other hand, the bulky ligand of $[\text{Fe}(\text{1bppCOOH})(\text{3bpp-bph})]^{2+}$ improves the SCO behavior of the bulk and the stability of the deposited monolayer.

In Chapter 5, a Co(II) complex based on the expanded ligand of the terpy functionalized with a carboxylic acid group, 4'-(4-carboxyphenyl)-2,2':6',2''-terpyridine, has been prepared. It gives rise to a SCO complex suitable for surface deposition. The formation of a SAM on top of silver surfaces has been investigated confirming the presence of an intact monolayer of SCO molecules bonded to the surface. Several spectroscopic techniques have evidenced a thermal spin transition of such molecules. To the best of our knowledge, this represents the first example of an active SCO SAM from solution in direct contact with the surface.

Finally, in the last chapter, 6, general conclusions extracted from the results of each chapter in both, the solid state and surface deposition, have been summarized along with some questions that we expect to tackle in the future

Resumen en castellano

En los últimos diez años, tras el descubrimiento de la primera molécula de transición de spin (SCO, de las siglas en inglés spin-crossover) depositada mediante la técnica de evaporación térmica en ultra alto vacío en una superficie, ha habido un gran aumento en la búsqueda de compuestos de SCO adecuados para dicha técnica. Hasta el momento, tan sólo una pequeña familia de compuestos de SCO son capaces de soportar las condiciones extremas que supone la evaporación térmica en ultra alto vacío además del alto coste económico que supone. Por otro lado, el autoensamblaje de moléculas desde una disolución también ofrece la oportunidad de formar nanoestructuras con metodologías mucho más económicas. Sin embargo, la mayoría de los intentos relacionados con la deposición de moléculas de SCO han fracasado, dejando un vacío de conocimiento científico en este tema. Por lo tanto, esta tesis es una pequeña aportación para empezar a llenar la falta de conocimientos dirigido a la preparación de dispositivos conmutables basados en moléculas de SCO mediante protocolos en disolución. Esperamos que este trabajo sea útil para la siguiente generación de experimentos y sea utilizado como guía hacia la dirección correcta.

Con el fin de perseguir nuestro objetivo, el diseño racional de nuevos compuestos de SCO funcionalizados con un punto de anclaje capaz de interactuar específicamente con la superficie ha sido llevado a cabo. Los compuestos de SCO investigados en este trabajo son principalmente de Fe(II) y Co(II). Se han utilizado derivados de dos ligandos ampliamente conocidos por dar lugar a familias de SCO, 2,6-bis(pirazol-1-il)piridina (1bpp) y 2,2':6'',2'''-terpiridina (terpy), para Fe(II) y Co(II), respectivamente. Respecto al punto de anclaje, la funcionalización con un grupo ácido carboxílico ha sido elegida gracias a su versatilidad para formar monocapas autoensambladas (SAMs, de las siglas en inglés selfs-assembled monolayers) en diferentes superficies.

Para facilitar la lectura de las diferentes estrategias utilizadas, el manuscrito se divide en seis capítulos principales:

El primer capítulo se ha escrito con la intención de proporcionar al lector el conocimiento necesario para establecer las bases sobre el tema a tratar. Se compone de una concisa introducción al fenómeno de SCO junto con los compuestos de SCO más utilizados, el concepto de SAM y su situación actual respecto a moléculas conmutables con el fin de dar a conocer la dificultad del reto abordado. Finalmente, se explican las técnicas de caracterización de monocapas más comúnmente empleadas, también utilizadas a lo largo de este trabajo.

En los capítulos 2 a 4 se utilizan compuestos de SCO de Fe(II) con ligandos derivados del 1bpp, mientras que el Capítulo 5 está enfocado en un compuesto de Co(II) basado en un ligando tipo terpy. En todos los capítulos primero se presentará la síntesis y caracterización del compuesto en estado sólido y después se estudiará y discutirá la formación de SAMs.

En el Capítulo 2, un estudio exhaustivo en estado sólido sobre la molécula utilizada como punto de partida, $[\text{Fe}(\text{1bppCOOH})_2]^{2+}$ se ha realizado con la intención de tener un mejor conocimiento sobre las propiedades magnéticas. Para ello se han utilizado diferentes contraiones (ClO_4^- , BF_4^- , CF_3SO_3^- , AsF_6^- , SbF_6^-), grados de solvatación y un ligando ligeramente diferente (bppCOOEt). Después se ha estudiado la deposición de las moléculas y, con ello, se han revelado algunos de los problemas que se van a tener que superar.

En el Capítulo 3, se han investigado dos variaciones diferentes del ligando cambiando la posición del grupo carboxílico. Para ello, se han cristalizado y caracterizado los compuestos $[\text{Fe}(\text{bpp3COOH})_2]^{2+}$ y $[\text{Fe}(\text{bpCOOHp}_2)_2]^{2+}$ en estado sólido. Mientras que el primero presenta una transición gradual e incompleta con la temperatura, el segundo, cuenta con una transición térmica abrupta cerca de temperatura ambiente y una T(LIESST) inusualmente alta. Esto está relacionado con una SCO inducida tanto con temperatura como con luz que involucra un cambio de simetría. Dichas propiedades se han estudiado en detalle. La deposición de ambos compuestos ha sido insatisfactoria debido a la oxidación de los compuestos de $[\text{Fe}(\text{1bpp3COOH})_2]^{2+}$ y la baja procesabilidad del $[\text{Fe}(\text{1bpCOOHp}_2)_2]^{2+}$.

En el Capítulo 4, hemos cambiado el enfoque hacia la formación de compuestos heterolépticos con el fin de entender el papel jugado por el ligando que no está interaccionando con la superficie. Para ello, un ligando similar, 1bppCOOEt empleado en el Capítulo 2, y uno más voluminoso, 3bpp-bph, se han utilizado. Tras la caracterización del material en estado sólido, el compuesto heteroléptico $[\text{Fe}(\text{1bppCOOH})(\text{1bppCOOEt})]^{2+}$ que presenta una estructura molecular muy similar respecto a $[\text{Fe}(\text{1bppCOOH})_2]^{2+}$, da lugar a un resultado análogo tras su deposición. Por otro lado, el ligando más voluminoso en $[\text{Fe}(\text{bppCOOH})(\text{3bpp-bph})]^{2+}$ mejora el comportamiento magnético en estado sólido y la estabilidad de la monocapa depositada.

En el Capítulo 5, se ha preparado un compuesto de SCO basado en el ligando expandido de la terpiridina funcionalizada con un ácido carboxílico, 4'-(4-carboxifenilo)-2,2':6',2''-terpiridina. Esto ha dado lugar a un compuesto de SCO adecuado para la deposición. La formación de SAM en diferentes superficies se ha investigado confirmando la presencia de una monocapa de moléculas intactas enlazadas a la superficie. Varias técnicas espectroscópicas han evidenciado las propiedades de transición de espín térmica en dichas moléculas. Este trabajo representa,

hasta donde alcanza nuestro conocimiento, el primer ejemplo de una SAM de moléculas de SCO activas desde disolución en contacto directo con la superficie.

Finalmente, en el último capítulo, el 6, se han resumido las conclusiones generales de cada capítulo tanto en el estado sólido como en la deposición en superficie, junto con algunas preguntas que esperamos abordar en un futuro.

3. List of publications

During the development of this thesis, I have contributed to the following publications. Those related to the thesis are marked with an asterisk:

S. Mañas-Valero, V. García-López, A. Cantarero, and M. Galbiati, "Raman spectra of ZrS_2 and $ZrSe_2$ from bulk to atomically thin layers" *Applied Sciences (Switzerland)*, vol. 6, no. 9, **2016**, doi: 10.3390/app6090264.

V. García-López, J. C. Waerenborgh, B. J. C. Vieira, M. Clemente-León, and E. Coronado, "Iron(II) complexes of tris(2-pyridylmethyl)amine (TPMA) and neutral bidentate ligands showing thermal- and photo-induced spin crossover" *Dalton Transactions*, vol. 47, no. 27, **2018**, doi: 10.1039/c8dt01425f.

V. García-López, M. Palacios-Corella, M. Clemente-León, and E. Coronado, "Spin-crossover compounds based on iron(II) complexes of 2,6-bis(pyrazol-1-yl)pyridine (bpp) functionalized with carboxylic acid and ethyl carboxylic acid" *Dalton Transactions*, vol. 47, no. 47, **2018**, doi: 10.1039/c8dt03511c.*

V. García-López, M. Palacios-Corella, M. Clemente-León, and E. Coronado, "Iron(II) complex of 2-(1H-pyrazol-1-yl)pyridine-4-carboxylic acid (ppCOOH) suitable for surface deposition" *Journal of Coordination Chemistry*, vol. 71, no. 6, **2018**, doi: 10.1080/00958972.2018.1430790.

V. García-López, F. J. Orts-Mula, M. Palacios-Corella, J. M. Clemente-Juan, M. Clemente-León, and E. Coronado, "Field-induced slow relaxation of magnetization in a mononuclear Co(II) complex of 2,6-bis(pyrazol-1-yl)pyridine functionalized with a carboxylic acid" *Polyhedron*, vol. 150, **2018**, doi: 10.1016/j.poly.2018.05.006.

V. García-López, M. Palacios-Corella, S. Cardona-Serra, M. Clemente-León, and E. Coronado, "Spin-crossover iron(II) complex showing thermal hysteresis around room temperature with symmetry breaking and an unusually high: T (LIESST) of 120 K" *Chemical Communications*, vol. 55, no. 81, **2019**, doi: 10.1039/c9cc05988a.*

V. García-López, M. Palacios-Corella, M. Clemente-León, and E. Coronado, "Fe(II) spin crossover complexes of a derivative of 2,6-bis(pyrazol-1-yl)pyridine (1-bpp) functionalized with a carboxylic acid in the 3-pyridyl position" *Polyhedron*, vol. 170, **2019**, doi: 10.1016/j.poly.2019.05.029.

V. García-López, M. Palacios-Corella, V. Gironés-Pérez, C. Bartual-Murgui, J. A. Real, E. Pellegrin, J. Herrero-Martín, G. Aromí, M. Clemente-León, E. Coronado, "Heteroleptic Iron(II) Spin-Crossover Complexes Based on a 2,6-Bis(pyrazol-1-yl)pyridine-type Ligand Functionalized with a Carboxylic Acid" *Inorganic Chemistry*, vol. 58, no. 18, **2019**, doi: 10.1021/acs.inorgchem.9b01526.*

V. García-López, M. Clemente-León, and E. Coronado, "Thermal- and photo-induced spin crossover in the 1D coordination polymer [Fe(4-t-Bupy)₃][Au(CN)₂]₂ (4-t-Bupy = 4-tert-butylpyridine)" *Journal of Applied Physics*, vol. 129, no. 12, **2021**, doi: 10.1063/5.0046998.

I. Capel Berdiell, V. García-López, M. J. Howard, M. Clemente-León, and M. A. Halcrow, "The effect of tether groups on the spin states of iron(ii)/bis[2,6-di(pyrazol-1-yl)pyridine] complexes" *Dalton Transactions*, vol. 50, no. 21, **2021**, doi: 10.1039/d1dt01076j.

M. Palacios-Corella, V. García-López, C. Sánchez-Sánchez, J. M. Clemente-Juan, M. Clemente-León, and E. Coronado, "Insertion of single-ion magnets based on mononuclear Co(II) complexes into ferromagnetic oxalate-based networks" *Dalton Transactions*, vol. 50, no. 17, **2021**, doi: 10.1039/d1dt00595b.

N. Monni, E. Andres-Garcia, K. Caamaño, V. García-López, J. M. Clemente-Juan, M. Giménez-Marqués, M. Oggianu, E. Cadoni, G. Mínguez Espallargas, M. Clemente-León, M. L. Mercuri, E. Coronado, "A thermally/chemically robust and easily regenerable anilato-based ultramicroporous 3D MOF for CO₂ uptake and separation" *Journal of Materials Chemistry A*, vol. 9, no. 44, **2021**, doi: 10.1039/d1ta07436a.

C. Boix-Constant, V. García-López, E. Navarro-Moratalla, M. Clemente-León, J. L. Zafra, J. Casado, F. Guinea, S. Mañas-Valero, E. Coronado, "Strain Switching in van der Waals Heterostructures Triggered by a Spin-Crossover Metal–Organic Framework" *Advanced Materials*, vol. 34, no. 11, **2022**, doi: 10.1002/adma.202110027.

N. Monni, J. J. Baldoví, V. García-López, M. Oggianu, E. Cadoni, F. Quochi, M. Clemente-León, M. L. Mercuri, E. Coronado, "Reversible tuning of luminescence and magnetism in a structurally flexible erbium–anilato MOF" *Chemical Science*, vol. 13, no. 25, **2022**, doi: 10.1039/d2sc00769j.

V. García López, N. Giaconi, M. Mannini, L. Poggini, M. Clemente Leon and E. Coronado. Manuscript in preparation

4. Abbreviations

CFT	Crystal Field Theory
O_h	Octahedral
Δ_o	Crystal field splitting
LFT	Ligand field theory
MO	Molecular orbitals
P	Spin pair energy
LS	Low spin
HS	High spin
SCO	Spin crossover
CISCO	Coordination induced spin crossover
CISSS	Coordination induced spin state switching
ELIESST	Electron-induced excited spin state trapping
H	Enthalpy
S	Entropy
γ_{HS}	HS relative concentration
s	Multiplicity number
SQUID	Superconducting quantum interference devices
χ_M	Molar magnetic susceptibility
T	Temperature
LIESST	Light induced excited spin state trapping
r-LIESST	Reverse light induced excited spin state trapping
T(LIESST)	Relaxation temperature above which the metastable photoinduced state is erased
T_{1/2}	Temperature of 50% HS to LS conversion

T₀	Initial value of the linear function related to denticity and rigidity of the ligand
ISC	Intersystem crossing
K_BT	Thermal energy
ΔE⁰_{HL}	Potential surfaces
1bpp	2,6-bis(pyrazol-1-yl)pyridine
3bpp	2,6-bis(pyrazol-3-yl)pyridine
1bppCOOH	2,6-bis(pyrazol-1-yl)pyridine-4-carboxylic acid
1bppCOOEt	ethyl 2,6-bis(pyrazol-1-yl)pyridine-4-carboxylate
terpy	2,2':6'',2'''-terpyridine
terpyCOOH	4'-carboxyl-2,2':6',2''-terpyridine
HL	4'-(4-carboxyphenyl)-2,2':6',2''-terpyridine
SAM	Self-assembled monolayer
MALDI-TOF	Matrix assisted laser desorption/ionization time of flight
AFM	Atomic force microscopy
SERS	Surface enhanced Raman scattering
XPS	X-ray photoelectron spectroscopy
XAS	X-ray absorption spectroscopy
XMCD	X-ray magnetic circular dichroism
ε	Molar extinction coefficient
TG	Thermogravimetric
DSC	Differential scanning calorimetry
MLCT	Metal to ligand charge transfer
HS*	Metastable photoinduced high spin
LS-HS*	Metastable photoinduced intermediate low spin high spin state

5. Figures

5.1. Main text figures

- Figure 1.1.1.** Different geometries of 3d orbitals of an octahedral coordination sphere. 3
- Figure 1.2.1.** Molecular orbital diagram for an octahedral molecule. t_{2g} corresponds to the non-bonding d_{xy} , d_{xz} and d_{yz} orbitals, while e_g^* are the anti-bonding orbitals coming from the hybridization of the $d_{x^2-y^2}$ and d_{z^2} orbitals. Figure adapted from literature.^[1] 4
- Figure 1.2.2.** Possible configurations for octahedral transition metal complexes of the 3d row depending on the magnitude of Δ_o . Figure adapted from literature.^[2] 5
- Figure 1.2.3.** Simplified Tanabe-Sugano diagram and the electronic configurations of the two possible spin states of a d^6 ion in an octahedral environment. 5
- Figure 1.3.1.** Different types of SCO curves: left-to-right, abrupt, gradual, step-like, hysteretic, and gradual and incomplete. Figure extracted from the literature.^[19] 7
- Figure 1.4.1.** Schematic illustration of LIESST and r-LIESST of a d^6 complex in the SCO range. Spin allowed d–d transitions are denoted by arrows and the radiation-less relaxation processes by wavy lines. Figure extracted from the literature.^[24] 8
- Figure 1.5.1.** Electronic arrangement for HS and LS Fe(II) complex for SCO behavior. Extracted from the literature.^[30] 9
- Figure 1.6.1.** Electronic arrangement for HS and LS Co(II) complex for SCO behavior. Extracted from the literature.^[30] 12
- Figure 1.6.2. Left**, schematic structure of $\text{Co}(\text{FPh-terpy})_2(\text{BPh}_4)_2$ (top) and its magnetic and ferroelectric curves (bot). **Right**, structure of $\text{Co}(\text{terpyCOO})_2$ (top) and its magnetization curves at different CO_2 pressure, the maxima of the first derivative at the bottom show the $T_{1/2}$ value. Figures adapted from the references ^[46] and ^[47], respectively 13
- Figure 1.7.1.** 3D representation of the structure of a SAM highlighting its different parts. 14
- Figure 1.8.1.** Schematic representation of the molecular structures of sublimable SCO complexes. Figure extracted from the literature.^[57] 15
- Figure 1.8.2. Top left**, schematic representation of the complexes $[\text{Co}(\text{Me}_n\text{tpa})\text{DBCatSH}]$ ($n = 0, 2, 3$). **Top right**, a) Temperature evolution of the normalized Co L_3 -edge XAS spectra of a monolayer of $[\text{Co}(\text{Me}_2\text{tpa})\text{DBCatSH}]$ along with reference signals used for the spectral deconvolution. HS-Co(II)

thermal distribution profile (empty circles) obtained from XAS spectra taken before (b) and after (c) laser light irradiation. **Bottom**, cartoon of the micro-printed gold nanoparticle array. Enclosed in red rectangle, schematic representation of [Fe(AcS-bpp)₂] in a junction-like environment. Enclosed in red circle, Raman spectra of the molecule at low (blue) and high (red) temperature in the nanoparticle array from 900 - 1200 cm⁻¹ range. Figures extracted from the literature.^[68,69]..... 17

Figure 1.9.1. Schematical representation of a typical AFM cantilever deflection measurement setup. The deflection of the AFM cantilever is measured by reflecting a laser off the backside of the cantilever, while the tip on the opposite site is scanning the surface of the sample..... 19

Figure 1.9.2. Simplify diagram of the Rayleigh and Raman scattering processes for one vibration. Figure extracted from the literature.^[73].....20

Figure 1.9.3. Processes that result from X-ray bombardment of a surface: (left) emission of a photoelectron, (middle) X-ray fluorescence and (right) emission of an Auger electron. Figure adapted from literature.^[75].....21

Figure 1.9.4. Diagram of the TEY mode. **Left**, energy-level diagram of the X-ray absorption process. **Right**, inelastic scattering of Auger electrons and reabsorption of fluorescence photons emitted during decay of the photoexcited atom result in an electron cascade. This cascade is detected as the current into the sample and the variation in the current as a function of energy provides the TEY XAS spectrum. Figure extracted from literature.^[76].....22

Figure 2.2.1. Chain of hydrogen-bonded [Fe(1bppCOOH)₂]²⁺ complexes in the structure of **1(ClO₄)₂** (top) and **1(BF₄)₂** (bot) at 120 K. Hydrogen atoms have been omitted for clarity.....33

Figure 2.2.2. Hydrogen-bonded [Fe(1bppCOOH)₂]²⁺ complexes and triflate anions in the structure of **1(CF₃SO₃)₂·yMe₂CO** at 120 K. Hydrogen atoms have been omitted for clarity.36

Figure 2.2.3. Hydrogen bonds (blue-dashed lines) between [Fe(1bppCOOH)₂]²⁺ complexes and acetone molecules in the structure of, **1(AsF₆)₂·yMe₂CO** (left) and **1(SbF₆)₂·yMe₂CO** (right) at 120 K. Hydrogen atoms have been omitted for clarity.....38

Figure 2.2.4. Projection in the *bc* plane of the structure of **2(ClO₄)₂·yMe₂CO** at 120 K.39

Figure 2.2.5. Thermal dependence of magnetic susceptibility times temperature (χ_{MT}) of **1(ClO₄)₂** (red circles), **1(BF₄)₂** (blue circles), **1(CF₃SO₃)₂·yMe₂CO** (turquoise circles), **1(AsF₆)₂·yMe₂CO** (green circles) and **1(SbF₆)₂·yMe₂CO** (pink circles).41

Figure 2.2.6. Thermal variation of χ_{MT} of **1(ClO₄)₂** (red) and **1(BF₄)₂** (blue). Full dots: data recorded without irradiation; empty dots: data recorded after irradiation at 10 K. The inset graph shows the temperature dependence of the first derivative of χ_{MT} with respect to the temperature.....42

- Figure 2.2.7.** Thermal variation of χ_{MT} for **1(CF₃SO₃)₂·yMe₂CO** (turquoise). Full dots: data recorded without irradiation; empty dots: data recorded after irradiation at 10 K. The inset graph shows the temperature dependence of the first derivative of χ_{MT} with respect to the temperature..... 43
- Figure 2.2.8.** Thermal variation of χ_{MT} of **1(AsF₆)₂·yMe₂CO** (green) and **1(SbF₆)₂·yMe₂CO** (pink). Full dots: data recorded without irradiation; empty dots: data recorded after irradiation at 10 K. The inset graph shows the temperature dependence of the first derivative of χ_{MT} with respect to the temperature..... 44
- Figure 2.2.9.** χ_{MT} in front of temperature for **2(ClO₄)₂·yMe₂CO** (yellow). Full dots: data recorded without irradiation; empty dots: data recorded after irradiation at 10 K. The inset graph shows the temperature dependence of the first derivative of χ_{MT} with respect to the temperature..... 46
- Figure 2.2.10.** UV/Vis spectra of a freshly prepared 0.1 mM solution of **1(ClO₄)₂** in MeCN (black line) and after one day in inert atmosphere (red line)..... 47
- Figure 2.2.11.** AFM images of a thermally grown SiO₂ substrate before (left) and after (right) deposition..... 48
- Figure 2.2.12.** MALDI-TOF region of the ligand ([1bppCOOH+H]⁺, 256.06 Da) of **1·SAM** (red) and bare SiO₂ substrate (violet)..... 49
- Figure 2.2.13.** XPS C 1s, N 1s, Cl 2p and Fe 2p regions of **1·SAM**..... 50
- Figure 2.2.14.** Normalized XAS Fe L_{2,3}-edge spectra of crystals of, **left, 1(BF₄)₂** at 350 K (HS) and 200 K (LS) and, **right, 1·SAM** and a Fe(III) L_{2,3}-edge extracted from the literature.^[42] 51
- Figure 3.2.1.** Structural view of [Fe(1bpp3COOH)₂]²⁺ complex in **1**; hydrogen atoms have been omitted for clarity; only one of the two possible configurations of disordered carboxylic acid groups is shown for clarity. 83
- Figure 3.2.2.** Temperature dependence of χ_{MT} for solvated (dark yellow) and desolvated (orange) **1** before (full circles) and after (empty circles) light irradiation. 85
- Figure 3.2.3.** Thermal variation of χ_{MT} of **2** before (black circles) and after (red circles) 660 nm light irradiation. The inset graph shows the temperature dependence of the first derivative of χ_{MT} with respect to the temperature..... 87
- Figure 3.2.4.** Asymmetric unit cell of **2** measured at, **left, 120 K (P2₁/c)** and, **right, 300 K (P-1)**. 88
- Figure 3.2.5. Left,** Thermal variation of χ_{MT} after 660 nm light irradiation for 18 hours (red empty circles) and 8 hours (orange empty circles). **Right,** temperature-dependence of χ_{MT} before (full circles) and after (empty circles) 808 nm light irradiation for 18 hours. 90

Figure 3.2.6. Simulated PXRD pattern from the structure solved in the dark (grey) and under continuous irradiation with 660 nm for ca. 360 seconds (light red) and experimental PXRD pattern of a powder sample measured in the dark (black) and (red) under continuous light irradiation with 660nm for ca. 1200 seconds at 20 K. 92

Figure 3.2.7. Experimental PXRD patterns of a powder sample of **2** measured after irradiation with 1064 nm (violet) for ca. 1200 seconds, during a short period of time with 660 nm (210 s, red) and 782 nm (540 s, green) at low temperature and the average of three spectra collected at 48K from the temperature scan experiment (go to SI for more information). 92

Figure 3.2.8. Schematic representation of the behavior of the different structural phases with light and temperature. 93

Figure 4.2.1. Representation of the molecular units of **1·2Me₂CO·0.5Et₂O** (left) and **1·Me₂CO** (right) at 120 K. Hydrogen bonds shown with blue dashed lines. Half of the disordered acetone molecules were omitted for clarity. 140

Figure 4.2.2. Dimers of [Fe(1bppCOOH)(3bpp-bph)]²⁺ complexes in the structure of **1·2Me₂CO·0.5Et₂O** (left) and **1·Me₂CO** (right) at 120 K. Hydrogen atoms have been omitted for clarity. 140

Figure 4.2.3. Representation of [Fe(1bppCOOH)(1bppCOOEt)]²⁺ and acetone molecule in **2·0.5Me₂CO** at 120 K. Hydrogen bonds are shown with blue dashed lines. Hydrogen atoms and half of the disordered acetone molecules have been omitted for clarity. 141

Figure 4.2.4. Temperature dependence of the product of the molar magnetic susceptibility times temperature ($\chi_M T$) for solvated (dark green) and desolvated (green) **1** before (full circles) and after (empty circles) light irradiation. 143

Figure 4.2.5. Temperature dependence $\chi_M T$ for solvated **2·0.5Me₂CO** before (full circles) and after (empty circles) light irradiation. 144

Figure 5.2.1. X-ray structure of the complex **1**. Hydrogen atoms are omitted for clarity. Hydrogen bonds are represented with dashed blue lines. 165

Figure 5.2.2. $\chi_M T$ vs temperature for **1** in contact with mother liquor (grey circles), filtered (blue empty circles) and after desolvation (blue circles). 166

Figure 5.2.3. UV/Vis spectra of a 0.1mM solution of **1** in DMA freshly prepared (black) and after one day stored in air (red). 167

Figure 5.2.4. AFM topographic images of silver substrates of **1·SAM** (left) and **L·SAM** (right). The scale bar represents 2 μ m. 167

Figure 5.2.5. MALDI-TOF spectra of **1** (blue), **1-SAM** (green) and bare Ag (grey). Magnification of the $[L+H+Ag]^+$, $[Co(LH_2)]^+$ and $[Co(LH+H+Na)(L+Ag)]^+$ (enclosed in red rectangles). The expected isotopic distribution pattern for each fragment is reported as black lines. Peaks coming from the matrix used for calibration are marked with an asterisk and are also present in bare Ag. 168

Figure 5.2.6. Raman fingerprints of **1** (blue), **1-SAM** (green) and $[Co(L)_2] \cdot 5H_2O$ (purple) in the 200-1800 cm^{-1} at 100K. Inset of the 700-900 cm^{-1} region. 169

Figure 5.2.7. Temperature dependent Raman spectra of **1-SAM** in the 200-1800 cm^{-1} range. 170

Figure 5.2.8. Temperature-dependence of the normalized intensity of the 1020 cm^{-1} features for **1** (blue squares), **1-SAM** (green circles) and **L-SAM** (orange circles) together with the χ_{MT} product (black). The lines are a guide to the eye. Error bars have been calculated from the median absolute deviation. 171

Figure 5.2.9. **Left**, temperature dependent Raman spectra of the same sample after being stored in air for one week in the 900-1800 cm^{-1} range. **Right**, subsequent normalized intensity of the 1020 cm^{-1} features at the given temperatures. The lines are a guide to the eye. Error bars have been calculated from the median absolute deviation. 172

Figure 5.2.10. C1s, N1s and Cl2p XPS regions of **1**, **1-SAM** and **L-SAM** along with the best fitting model. 173

Figure 5.2.11. Comparison of XPS Co2p spectra of **1** (top) and **1-SAM** (bot) along with deconvolution of the peaks and corresponding best fitting lines. 175

Figure 5.2.12. a) XAS CoL₃-edge of **1-SAM** at each temperature (empty circles) together with experimental LS Co(II) (blue curves) and theoretical HS Co(II) (red curves) and LS Co(III) (green curve) components. Black line is the best fitting curve with the sum of the three components. **b)** Co(II) HS molar fraction thermal distribution obtained from magnetic measurements of the bulk and from the one extracted from the XAS fitting of the monolayer in the first and second warming cycles. 176

5.2. Supporting information figures

Figure SI. 2.4.1. View of a layer of $[Fe(1bppCOOH)_2]^{2+}$ complexes with the intermolecular interactions between complexes belonging to different hydrogen-bonded chains as dashed lines in the structure of **1(CIO₄)₂** (top) and **1(BF₄)₂** (bot) at 120 K. Hydrogen atoms have been omitted for clarity. 55

Figure SI. 2.4.2. Projection of the structure of 1(ClO₄)₂ (top) and 1(BF₄)₂ (bot) at 120 K in the <i>ac</i> plane. Hydrogen atoms have been omitted for clarity.	56
Figure SI. 2.4.3. View of two layers of [Fe(1bppCOOH) ₂] ²⁺ complexes with the intermolecular interactions between complexes belonging to different layers as dashed lines in the structure of 1(ClO₄)₂ (left) and 1(BF₄)₂ (right) at 120 K. Hydrogen atoms have been omitted for clarity.....	57
Figure SI. 2.4.4. Thermal dependence of the parameter <i>b</i> of 1(ClO₄)₂ (left) and 1(BF₄)₂ (right).	57
Figure SI. 2.4.5. Experimental powder X-ray diffraction patterns (top) at 298 K (blue line) and 400 K (red line) and simulated one (bottom) at 120 K (blue line) and 400 K (red line) of [Fe(bppCOOH) ₂](ClO ₄) ₂ (1(ClO₄)₂).....	58
Figure SI. 2.4.6. Thermal dependence of the experimental powder X-ray diffraction pattern of [Fe(bppCOOH) ₂](ClO ₄) ₂ (1(ClO₄)₂).....	58
Figure SI. 2.4.7. Simulated PXRD pattern from the structure solved at 120 K (blue) and experimental one at 300 K (red) of 1(BF₄)₂	59
Figure SI. 2.4.8. View of the asymmetric unit of 1(CF₃S₃)₂·yMe₂CO at 120 K. Hydrogen atoms have been omitted for clarity.....	59
Figure SI. 2.4.9. Projection in the <i>bc</i> plane of the structure of 1(CF₃SO₃)₂·Me₂CO at 120 K. Hydrogen atoms have been omitted for clarity.....	60
Figure SI. 2.4.10. Simulated PXRD pattern from the structure solve at 300 K (blue), experimental one at 300 K (red), experimental PXRD pattern of the desolvated sample (yellow) and experimental PXRD pattern of the resolvated sample (orange) of 1(CF₃SO₃)₂·yMe₂CO	61
Figure SI. 2.4.11. Thermogravimetric profile of 1(CF₃SO₃)₂·yMe₂CO (1.169 mg, black line) and its derivative (red line) in heating mode from 350 K to 450 K (at 10 °C/min). The mass lost after this ramp corresponds to 2.18 % of the total weigh, which is lower than the expected weight loss of half molecule of Me ₂ CO (<i>ca.</i> 2.8 %).	61
Figure SI. 2.4.12. CH···π contacts between [Fe(1bppCOOH) ₂] ²⁺ complexes in the structures of 1(AsF₆)₂·yMe₂CO (top) and 1(SbF₆)₂·yMe₂CO at 120 K (bottom). Hydrogen atoms have been omitted for clarity.....	62
Figure SI. 2.4.13. Projection in the <i>ab</i> plane of the structures of 1(AsF₆)₂·yMe₂CO (top) and 1(SbF₆)₂·yMe₂CO (bottom) at 120 K. Hydrogen atoms have been omitted for clarity.....	63

Figure SI. 2.4.14. Simulated PXRD pattern from the structure solve at 300 K (blue), experimental one at 300 K (red), experimental PXRD pattern of the desolvated sample (yellow) and experimental PXRD pattern of the resolvated sample (orange) of **1(AsF₆)₂·yMe₂CO**. 64

Figure SI. 2.4.15. Simulated PXRD pattern from the structure solve at 300 K (blue), experimental one at 300 K (red), experimental PXRD pattern of the desolvated sample (yellow) and experimental PXRD pattern of the resolvated sample (orange) of **1(SbF₆)₂·yMe₂CO**. 64

Figure SI. 2.4.16. Thermogravimetric profile of **1(AsF₆)₂·yMe₂CO** (7.15 mg, black line) and its derivative (red line) in heating mode from 300 K to 450 K (at 10 °C/min). The mass lost after this ramp corresponds to 5.70 % of the total weigh, which is in agreement with the loss of one molecule of Me₂CO (ca. 5.7 %). 65

Figure SI. 2.4.17. Thermogravimetric profile of **1(SbF₆)₂·yMe₂CO** (12.28 mg, black line) and its derivative (red line) in heating mode from 312 K to 450 K (at 10 °C/min). The mass lost after this ramp corresponds to 5.01 % of the total weigh, which is in agreement with the loss of one molecule of Me₂CO (ca. 5.3 %). 65

Figure SI. 2.4.18. Projection in the *bc* plane of the structure of **2(ClO₄)₂·yMe₂CO** at 300K. Hydrogen atoms have been omitted for clarity. 66

Figure SI. 2.4.19. Simulated PXRD pattern from the structure solved at 300 K (blue), experimental one at 300 K (red) and experimental PXRD pattern of the desolvated sample (yellow) of **2(ClO₄)₂·yMe₂CO**. 66

Figure SI. 2.4.20. Kinetics for **1(ClO₄)₂**. 67

Figure SI. 2.4.21. LITH and static points for **1(ClO₄)₂**. 69

Figure SI. 2.4.22. Kinetics of the static points for **1(ClO₄)₂**. 70

Figure SI. 2.4.23. Thermal dependence of χ_{MT} product in the heating mode from 2 – 400 K (light) and subsequent cooling mode from 400 – 2 K (dark) of **1(AsF₆)₂·yMe₂CO** (left, green) and **1(SbF₆)₂·yMe₂CO** (right, pink). 70

Figure SI. 3.4.1. Thermogravimetric profile of **1** (1.1643 mg, black line) and its derivative (red line) in heating mode from 315 K to 385 K (at 10 °C/min). The mass lost after this ramp corresponds to 2.04 % of the total weight, which is in agreement with the loss of one water molecule (ca. 2 %). .. 99

Figure SI. 3.4.2. Simulated PXRD pattern from the structure at 120 K (blue) and experimental ones at 300 K (red) and after heating the sample at 400 K (yellow) of **1**. 99

Figure SI. 3.4.3. Projection on the ab plane of the structure of **1**. Hydrogen atoms have been omitted for clarity. Only one of the two possible configurations of disordered carboxylic acid groups is shown for clarity. 100

Figure SI. 3.4.4. View of the hydrogen-bonds in the structure of **1** as blue dashed-lines. Hydrogen atoms have been omitted for clarity. Only one of the two possible configurations of disordered carboxylic acid groups is shown for clarity. 101

Figure SI. 3.4.5. UV/Vis spectra of a 0.1 mM solution of **1** in MeCN freshly prepared (black line) and after one day in inert atmosphere (red line)..... 101

Figure SI. 3.4.6. AFM images of SiO₂ substrates after deposition of **1**. 102

Figure SI. 3.4.7. MALDI-ToF region of the ligand [1bpp3COOH+H]⁺ (256.08 Da) of **1-SAM** in red and bare SiO₂ substrate as reference in violet..... 103

Figure SI. 3.4.8. XPS region of, from top to bottom, C 1s, N 1s, Cl 2p and Fe 2p of **1-SAM**. ... 104

Figure SI. 3.4.9. Left, XAS Fe L_{2,3}-edge spectra of **1-SAM** (red) and an Fe(III) (black) extracted from the literature.^[45] 105

Figure SI. 3.4.10. Simulated PXRD pattern from the structure solved at 120 K (blue), experimental PXRD pattern of a freshly filtered sample (red) and the sample in contact with the mother liquors (green) both at 300K of **3**. 105

Figure SI. 3.4.11. Structure of the [Fe^{II}(1bpCOOH₂p)(1bpCOO⁻COOHp)Fe^{II}(1bpCOOH₂p)(ClO₄)²⁺]_n chains in the structure of **3** at 120 K. Fe (orange) C (black), N (blue), O (red), Cl (yellow). Hydrogen atoms are omitted for clarity..... 107

Figure SI. 3.4.12. Thermal dependence of χ_{MT} of **3**. Camouflage yellow: Compound measured in contact with the mother liquor. Dark green: data recorded without irradiation after desolvation at 400 K. Yellow: data recorded after irradiation at 10 K for the same desolvated sample. The inset graph shows the temperature dependence of the first derivative of χ_{MT} with respect to the temperature. 108

Figure SI. 3.4.13. Differential scanning calorimetry of **2** from 310K to 270K; first cooling (dark blue) and heating mode (red) and second cooling (light blue) and heating (orange) mode after keeping the sample at 310K for 2 hours..... 108

Figure SI. 3.4.14. Thermal variation of χ_{MT} of filtered crystals of **2**. 109

Figure SI. 3.4.15. Simulated PXRD pattern from the structure solved at 300 K (blue), experimental PXRD pattern of a freshly filtered sample (red), desolvated sample (yellow) and the sample in contact with the mother liquors (green) at 300K of **2**. 110

- Figure SI. 3.4.16.** Bragg peaks from the $h0l$ plane of the structure of **2** solved at 120K (left) and 300K (right). Doubling of the number of peaks take place. 111
- Figure SI. 3.4.17.** Left, systematic absences from the $h0l$ plane that fulfill the $h=2n+1$, $l=m$ condition. Right, equivalent reflections from the $0k0$ plane that fulfill the $k=2n+1$ condition. Values of the intensity extracted from the hkl file at the different temperatures. 111
- Figure SI. 3.4.18.** Temperature dependence of the unit cell parameters of a crystal of **2** extracted directly from the mother liquors before (empty dots) and after heating the crystal at 300K for 2 hours (full dots) under the nitrogen stream..... 112
- Figure SI. 3.4.19.** Hydrogen bond interactions of $[\text{Fe}(\text{1bpCOOH}_2\text{p})_2]^{2+}$ complexes (blue-dashed lines) in the structure of **2** at 120 K (left) and 300 K (mid and right). Hydrogen atoms have been omitted for clarity..... 113
- Figure SI. 3.4.20.** Projection of the structure of **2** in the ab plane at 120 K (top) and in the bc plane at 300 K (bottom). Hydrogen atoms have been omitted for clarity..... 114
- Figure SI. 3.4.21.** Chains of $[\text{Fe}(\text{1bpCOOH}_2\text{p})_2]^{2+}$ complexes linked through intermolecular interactions (red-dashed lines) in the structure of **2** at 120 K (top) and 300 K (mid and bot). Hydrogen atoms and perchlorate counteranions have been omitted for clarity..... 115
- Figure SI. 3.4.22.** Interchain interactions between $[\text{Fe}(\text{1bpCOOH}_2\text{p})_2]^{2+}$ complexes (red-dashed lines) in the structure of **2** at 300 K. Hydrogen atoms and perchlorate counteranions have been omitted for clarity..... 116
- Figure SI. 3.4.23.** PXRD patterns of **2**; **left**, simulated at 300 K (blue) and 250 K (red) and experimental at 300 K (light blue) and 250 K (light red); **right**, experimental at 300 K (light blue) and 250 K (light red) and 300 K after cooling to 250 K (dark red) to confirm reversibility of the crystallographic symmetry breaking. 117
- Figure SI. 3.4.24.** Time dependence of χ_{MT} of **2** under light irradiation with a 660 nm wavelength laser for ca. 16 h (top-left), 6 h (top-right) and under light irradiation with a 1064 nm wavelength laser for ca. 18 h (bottom) at 10 K..... 117
- Figure SI. 3.4.25.** Left, time dependence at various temperatures of the photoinduced HS molar fraction. The relaxation curves are fitted according to sigmoidal behavior (see text for more details). Right, Arrhenius fitting of the activate process (the measurement at 105K has been removed from the fitting, see text)..... 118

Figure SI. 3.4.26. Thermal dependence of $\chi_M T$ of **1**. Full squares: data recorded without irradiation; Black empty circles: data recorded after the first irradiation at 10 K and; Red empty circles: data recorder after second irradiation at 10 K. 119

Figure SI. 3.4.27. Bragg peaks from the $h0l$ plane of the structure of **2** before (left) and after (right) irradiation with 660 nm for ca. 360 s. The systematic absences $h0l$ ($h = 2n + 1, l = m$) are fulfilled. 121

Figure SI. 3.4.28. Bragg peaks from the $h0l$ plane of the structure of **2** before (left) and after (right) irradiation with 660 nm ca. 60 s. Doubling of the number of peaks take place. 121

Figure SI. 3.4.29. Simulated PXRD pattern of **3** (yellow), **2** (grey) and experimental PXRD pattern of a powder sample of **2** (black) before irradiation in the 2 - 5 2θ range at low temperature. Areas highlighted in blue are guides to the eye. 122

Figure SI. 3.4.30. Experimental PXRD patterns of a powder sample of **2** measured before (black) and after (green) irradiation with 782 nm at 20 K for ca. 4800 seconds. In red, the PXRD pattern of a powder sample measured with 660 nm for comparison purposes. 122

Figure SI. 3.4.31. Experimental PXRD patterns of a powder sample of **2** measured before (black) and after (blue) irradiation with 472 nm at low temperature. In red, experimental PXRD of the HS* is shown for comparison purposes. Dashed lines are a guide to eye. 123

Figure SI. 3.4.32. Time dependent 3D surface maps of a spin and symmetry dependent peaks in the 3.6 – 4 2θ range of a powder sample of **2** under light irradiation with 660 nm (left) and 782 nm (right). The first spectra are collected in the dark as a reference. 123

Figure SI. 3.4.33. Simulated PXRD pattern of a single crystal (violet) after irradiation for 60 seconds and a powder sample in the HS* state (pink) of **2** under continuous irradiation for ca. 4500 seconds with 1064 nm at 20 K. 124

Figure SI. 3.4.34. Time dependent 3D surface maps of a spin and symmetry dependent peaks in the 3.6 – 4 2θ range of a powder sample of **2** under light irradiation with 1064 nm from the HS* state (left) and LS state (right). The first spectra are collected in the dark as a reference. 124

Figure SI. 3.4.35. Top, experimental PXRD of the first (wine), 48 K averaged spectrum (yellow) and last scan (yellow) of the temperature variation experiment of a powder sample of **2**. Experimental PXRD of the LS and HS* phases are also included for comparison purposes. **Bottom**, Temperature dependent 3D surface maps of a spin and symmetry dependent peaks in the 3.6 – 4 2θ range of the powder sample. Each scan represents a step of $\Delta T = 1$ K. 125

Figure SI. 3.4.36. Top, experimental PXRD patterns of a powder sample of **2** measured before (black), after irradiation with 472 (blue) and 660 nm (red) at low temperature. **Bottom-left**, Time dependent 3D surface maps of a spin and symmetry dependent peaks in the 3.6 – 4 2θ range of the powder sample under light irradiation with 472 nm. **Bottom-right**, time distribution of the HS photoinduced molar fraction obtained from the linear regression fit of the single spectra with the experimental LS and HS* used as references..... 126

Figure SI. 3.4.37. UV/Vis spectra of a 0.1 mM solution of **2** in MeCN freshly prepared (black line) and after one day in inert atmosphere (red line)..... 127

Figure SI. 4.4.1. Simulated PXRD pattern from single crystal measured at 120 K (blue), a mixture of **1·2Me₂CO·0.5Et₂O** and **1·Me₂CO** after filtering (red) and after desolvation at 400 K in the squid (yellow). 148

Figure SI. 4.4.2. Intermolecular contacts between $[\text{Fe}(\text{1bppCOOH})(\text{3bpp-bph})]^{2+}$ complexes shown with blue dashed lines. 148

Figure SI. 4.4.3. Chains of $[\text{Fe}(\text{1bppCOOH})(\text{3bpp-bph})]^{2+}$ dimers running along the *b* axis in the structure of **1·2Me₂CO·0.5Et₂O** at 120 K. Hydrogen atoms have been omitted for clarity..... 149

Figure SI. 4.4.4. Chains of $[\text{Fe}(\text{1bppCOOH})(\text{3bpp-bph})]^{2+}$ dimers running along the *b* axis in the structure of **1·Me₂CO** at 120 K displaying a more compact crystal packing. Hydrogen atoms have been omitted for clarity..... 150

Figure SI. 4.4.5. Simulated PXRD pattern at 120 K (blue) and experimental at room temperature (red) of **2·0.5Me₂CO**..... 151

Figure SI. 4.4.6. View of chains of $[\text{Fe}(\text{1bppCOOH})(\text{1bppCOOEt})]^{2+}$ complexes running in the *a* axis in the structure of **2·0.5Me₂CO** at 120 K. Intermolecular contacts shown with blue dashed lines. Hydrogen atoms, perchlorate counteranions and disordered acetone molecules have been omitted for clarity. 151

Figure SI. 4.4.7. View of chains of $[\text{Fe}(\text{1bppCOOH})(\text{1bppCOOEt})]^{2+}$ complexes in the *bc* plane of the structure of **2·0.5Me₂CO** at 120 K. Intermolecular contacts shown with blue dashed lines. Hydrogen atoms and disordered acetone molecules have been omitted for clarity. 152

Figure SI. 4.4.8. Thermal variation of $\chi_{\text{M}}T$ for **2·0.5Me₂CO**. Orange circles: first heating cycle; brown circles: first cooling after heating to 400 K..... 153

Figure SI. 4.4.9. UV/Vis spectra of a 0.1 mM solution of, left, **1** and, right, **2** in MeCN freshly prepared and after one day in inert atmosphere. 153

Figure SI. 4.4.10. AFM images of SiO₂ substrates after deposition of **1** (left) and **2** (right). ... 154

Figure SI. 4.4.11. MALDI-TOF region of 1bppCOOH (left) and 3bpp-bph (right) of 1 (green), 2-SAM (orange) and bare SiO ₂ (light purple).	154
Figure SI. 4.4.12. XPS C 1s, N 1s, Cl 2p and Fe 2p regions of 1-SAM (left) and 2-SAM (right).	156
Figure SI. 4.4.13. Left, XAS Fe L _{2,3} -edge spectra of 1-SAM (green), Fe(III) ^[21] (black) and Fe(II) HS (red) and LS (blue) obtained from the bulk of [Fe(1bppCOOH) ₂](BF ₄) ₂ from Chapter 2 used as a reference. Right, XAS Fe L _{2,3} -edge spectra of 2-SAM and an Fe(III) L _{2,3} -edge extracted from the literature. ^[21]	157
Figure SI. 5.4.1. Simulated PXRD pattern from single crystal of 1 measured at 300 K (blue) and experimental (red).	178
Figure SI. 5.4.2. View of the supramolecular π···π and CH···π interactions between pairs of molecules of 1 (C (black), N (blue), O (red), Co (dark blue)). π···π interactions are represented with dashed red lines. Counter ions, solvent molecules, and hydrogen atoms are omitted for clarity.	179
Figure SI. 5.4.3. Temperature dependence of the product of the molar magnetic susceptibility and the temperature (χ_{MT}) of Co(L ₂) (green, first heating, red, first cooling and blue, second heating). Scan rates 2 Kmin ⁻¹ for the first heating and cooling and 1 Kmin ⁻¹ for the second heating.	180
Figure SI. 5.4.4. Temperature-dependent Raman spectra of 1	181
Figure SI. 5.4.5. χ_{MT} vs temperature (black) and normalized intensity value of the pyridine ring breathing mode at 1020 cm ⁻¹ (blue squares) for desolvated 1	181
Figure SI. 5.4.6. Temperature dependent Raman spectra of L-SAM	182
Figure SI. 5.4.7. Raman spectra of 1-SAM before and after heating the sample at 400 K. Irreversible changes in the spectra at 1567 cm ⁻¹ and 1020cm ⁻¹ (highlighted in cyan) take place.	182
Figure SI. 5.4.8. Raman spectra of L-SAM before and after heating the sample at 390 K. Irreversible changes in the spectra at ca. 1550 cm ⁻¹ (highlighted in cyan) take place.	183
Figure SI. 5.4.9. Time evolution of CoL ₃ -edge XAS spectra of 1-SAM at 100 K and 300 K. .	185
Figure SI. 5.4.10.a) Time-dependence XAS spectra of the CoL _{2,3} -edges acquired on the same spot in the bulk sample with a high photon flux at 300K. b) Difference between the XAS spectra of the CoL _{2,3} -edges acquired at high and low photon flux conditions for the bulk.	185
Figure SI. 5.4.11. XAS CoL ₃ -edge of the desolvated bulk at 100 K in the LS state (left), at the highest available temperature (370 K) after subtracting a 0.4 fraction of the LS spectra (middle) and	

the calculated difference of the altered molecules together with the theoretical calculated spectra. The references used for the fitting procedure are highlighted in colours. 186

Figure SI. 5.4.12. XAS $\text{CoL}_{2,3}$ -edge of **1-SAM** (empty circles) together with the reference HS Co(II) (red curves), LS Co(II) (blue curves) and LS Co(III) (green curve) at each temperature for the first cycle. Black line is the best fitting curve with the sum of the three components..... 187

Figure SI. 5.4.13. XAS $\text{CoL}_{2,3}$ -edge of **1-SAM** (empty circles) together with the reference HS Co(II) (red curves), LS Co(II) (blue curves) and LS Co(III) (green curve) at each temperature for the second cycle. Black line is the best fitting curve with the sum of the three components..... 188

Figure SI. 5.4.14. $\text{CoL}_{2,3}$ -edge XAS comparison of the spectra of **a) 1-SAM** and calculated HS state of the bulk and **b) 1-SAM** at 370K and its subsequent cooling down to 100K..... 188

6. Tables

6.1. Main text tables

Table 2.2.1. Theoretical and XPS estimated atomic semiquantitative analysis (top) and ratios (bottom) for **1**. Theoretical values have been calculated guessing one ligand and one acetonitrile molecule per iron, **Fe(1bppCOOH)(MeCN)**.50

Table 7.1.1. CCDC numbers of each structure.200

6.2. Supporting information tables

Table S.I. 2.4.1. Theoretical and experimental values of elemental analysis.54

Table S.I. 2.4.2. $k_{HL}(T)$ and $\alpha(T)$ for compound **1(ClO₄)₂**.....68

Table S.I. 2.4.3. Crystallographic data72

Table S.I. 3.4.1. Theoretical and XPS estimated atomic semiquantitative analysis (top) and ratios (bot) for **1-SAM**. The higher value marked with an asterisk comes from spurious contamination of the adventitious carbon. 104

Table S.I. 3.4.2. Unit cell parameters of single crystals of **2** measured before and after irradiation with 660 for different periods of time..... 120

Table S.I. 3.4.3. Fe-N bond distances of the single crystals of **2** measured before and after irradiation with 660 for different periods of time..... 120

Table S.I. 3.4.4. Distortion parameters of the single crystals of **2** measured before and after irradiation with 660 for different periods of time at low temperature. 121

Table S.I. 3.4.5. Crystallographic tables..... 128

Table S.I. 4.4.1. Theoretical and XPS estimated atomic semiquantitative analysis (top) and ratios (bot) for **1-SAM** and **2-SAM**. 155

Table S.I. 4.4.2. Crystallographic tables..... 158

Table S.I. 5.4.1. MALDI-TOF peaks expected and experimentally found for **1** and **1-SAM**...180

Table S.I. 5.4.2. XPS peak position and estimated and theoretical percentages (relative error about 5%) of C 1s and N 1s elements for compound **1**, **1-SAM** and **L-SAM**..... 183

Table S.I. 5.4.3. Theoretical and XPS estimated atomic semiquantitative analysis and ratios for bulk and monolayer of **1**..... 184

Table S.I. 5.4.4. Peak position of the spectral components employed for least squares fitting of the Co2*p* XPS binding energies (B.E.) for **1** and **1•SAM** at 170 K and 300 K. Integrated areas are reported in percentages for each component in brackets. Spin–orbit splitting (ΔSO) and intensity ratios of the satellites ($\Sigma I_{\text{sat}}/I_{\text{Co}2p_{3/2}}$) are also gathered..... 184

Table S.I. 5.4.5. Crystallographic tables..... 190

Chapter 1

1. Introduction to Fe(II) and Co(II) spin-crossover complexes and switchable self-assembled monolayers

1.1. Crystal Field Theory

Metal complexes are chemical substances composed of a metal ion center surrounded by molecules called ligands. They have been known for a very long time and present unique and interesting properties. However, some properties had not been explained until crystal field theory (CFT) was developed. CFT is a simple bonding model that considers metal-ligand interactions to be purely electrostatic, nonetheless enables chemists to explain many properties such as color, magnetism, structures, stability, and reactivity.

This model treats ligands as point charges; therefore, a complex can be described as a positively charged metal ion surrounded by negative point charges. Despite the noticeable attraction, electrons of the outer layer of the metal cation (d or f orbitals) and electrons of the ligand repel each other due to repulsion between like charges. Such electrostatic repulsion leads the electrons to stay in particular orbitals of the metal ion, and therefore give rise to a splitting of the degeneracy.

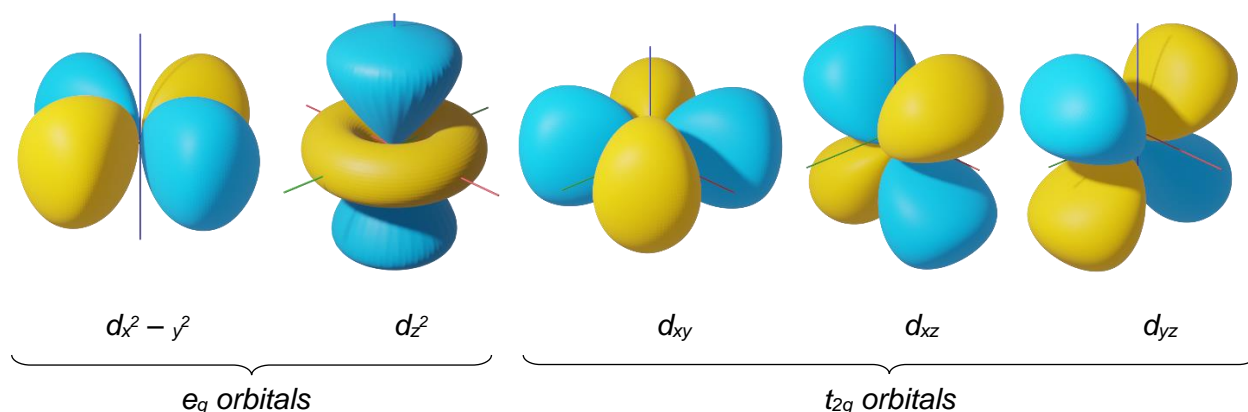


Figure 1.1.1. Different geometries of 3d orbitals of an octahedral coordination sphere.

According to CFT, six ligands (or negatively point charges) form the vertices of an octahedron in order to minimize electrostatic interactions between them. The octahedral (O_h) configuration is by far the most common arrangement and, other configurations such as tetrahedral or square planar can be explained as a distortion of the O_h model. Thus, if each ligand is positioned along x , y , and z Cartesian axes, in transition metal ions, an overlapping of d -orbitals takes place. $d_{x^2-y^2}$ interacts with four ligands positioned on the x and y axes, and d_{z^2} with two ligands placed on the z axis. On the other hand, the orbitals d_{xy} , d_{xz} and d_{yz} are located between the ligands (see **Figure 1.1.1**). Hence, the energy of an electron in the two first orbitals

(named e_g) will be higher than in the other three (named t_{2g} , **Figure 1.1.1**). The energy gap between these two energy levels is known as crystal field splitting (Δ_o or $10Dq$).

1.2. Ligand Field Theory

Ligand Field Theory (LFT) can be considered as an extension of the CFT. It is more accurate but also more complex. In LFT each point charged is replaced by molecular orbitals (MOs), where each ligand gives two electrons per bond. This explains the bonding of neutral ligands and provides a more accurate explanation of the properties.

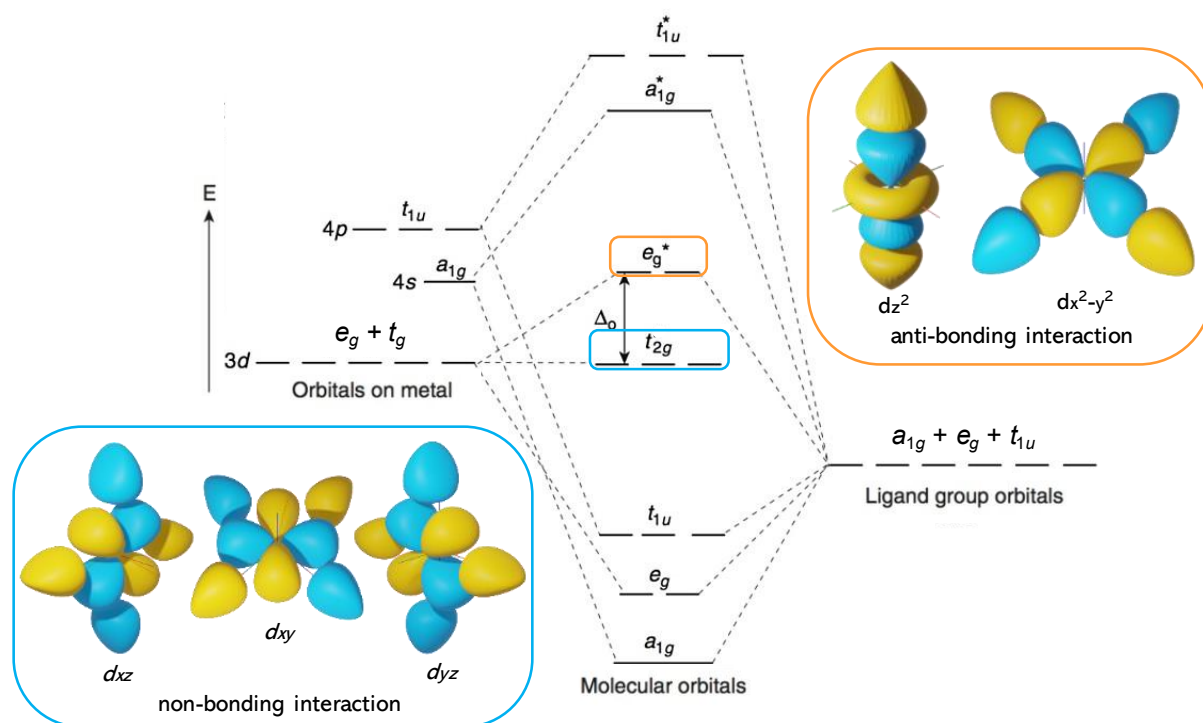


Figure 1.2.1. Molecular orbital diagram for an octahedral molecule. t_{2g} corresponds to the non-bonding d_{xy} , d_{xz} and d_{yz} orbitals, while e_g^* are the anti-bonding orbitals coming from the hybridization of the $d_{x^2-y^2}$ and d_{z^2} orbitals. Figure adapted from literature.^[1]

In an O_h symmetry, the 6 orbitals of the ligand and the 6 orbitals of the metal ion hybridize to give rise to 12 MOs (6 bonding and 6 anti-bonding orbitals). From the d orbitals, $d_{x^2-y^2}$ and d_{z^2} orbitals constitute molecular bonding orbitals due to overlapping with ligand orbitals of wave functions of the same sign (bonding e_g and anti-bonding e_g^* , see **Error! No se encuentra el origen de la referencia.**). However, the overlapping of d_{xy} , d_{xz} and d_{yz} with ligand orbitals is performed alternatively with positive and negative sign leading to a zero integral of the wave functions resulting in molecular non-bonding orbitals (t_{2g}^n , **Figure 1.2.1**).

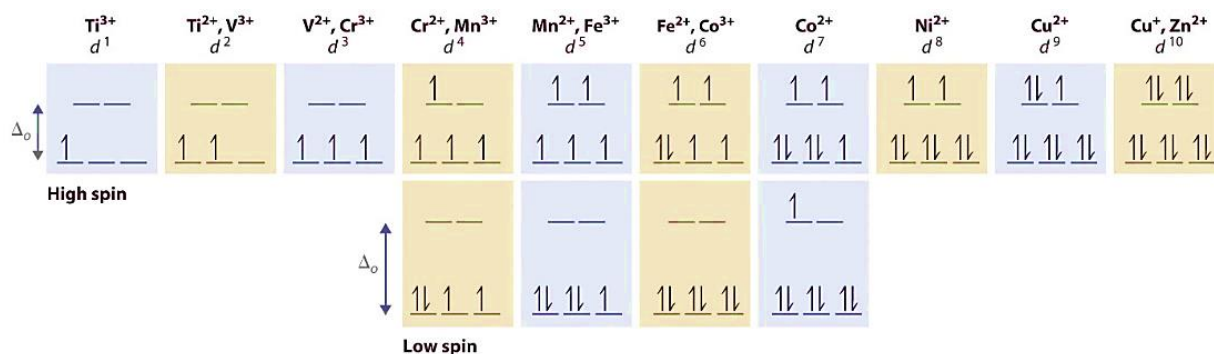


Figure 1.2.2. Possible configurations for octahedral transition metal complexes of the 3d row depending on the magnitude of Δ_o . Figure adapted from literature.^[2]

In the Oh configuration, d^{4-7} transition metal ions present two possible electronic configurations (see **Figure 1.2.2**). These different configurations depend on the energy splitting Δ_o , and thus on the ligand-field strength. But in order to determine which electronic configuration is preferred we have to introduce the spin pairing energy (P). This energy cost arises by placing an electron in an already occupied orbital due to Coulomb repulsion. Therefore, large values of Δ_o (i.e., $\Delta_o > P$) yield the lower multiplicity $t_{2g}^6 e_g^0$ configuration ($^1A_{1g}$) or low-spin (LS) state, while small values of Δ_o (i.e., $\Delta_o < P$) yield the higher multiplicity $t_{2g}^4 e_g^2$ configuration ($^5T_{2g}$) or high spin (HS) state (see **Figure 1.2.3**).

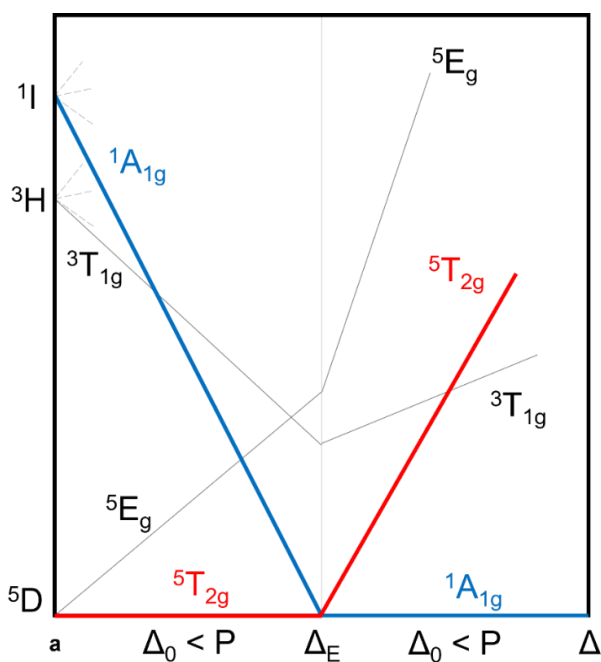


Figure 1.2.3. Simplified Tanabe-Sugano diagram and the electronic configurations of the two possible spin states of a d^6 ion in an octahedral environment.

However, for intermediate values of Δ_o , the energy difference between the two states may be sufficiently small in such a way that the application of an external perturbation induces a spin transition between the HS state to the LS state or the other way around.

1.3. Spin-Crossover phenomenon

In 1932, Linus Pauling suggested that the transition between two different electronic states in the same system was feasible.^[3] In fact, in the 1930s, Cambi *et. al.* had already discovered the phenomenon of thermal spin transition on an Fe(III) dithiocarbamate complex.^[4] By that time, the wide word acceptance of the LFT (see above) gave rise to a rapidly increase in the search of systems capable of undergoing spin transition. While mostly all the efforts where focused on Fe(III) as the metal ion,^[5] almost 30 years later, Busch and co-workers reported the first Co(II) spin crossover (SCO) complex,^[6] followed by König and Madeja with the first SCO system based on Fe(II).^[7] Thanks to the pioneering work of Fisher and Drickamer, where they determined the role of pressure in influencing the spin state,^[8] a large number of external stimuli have been investigated and demonstrated to influence the SCO behavior of the systems (*i.e.*, light,^[9] pressure,^[10] magnetic field,^[11] electric field,^[12] pH,^[13] solvent,^[14] etcetera). Over the years, transition metal ions such us Mn(II), Mn(III), Cr(II) and Co(III) were also found to display thermal SCO.^[15] Else, different types of spin transition have been discovered, such as tautomerism of mixed-valence metals,^[16] coordination induced spin crossover (CISCO, or Coordination-Induced Spin State Switching (CISSS))^[17] and, very recently, electron-induced excited spin state trapping (ELIESST) effect.^[18]

In general terms, the SCO phenomena can be described as the property of certain transition metal complexes (d^{4-7}) to undergo spin transition between two different electronic states. Such transition occurs due to the rearrangement of the 3d electrons from the higher enthalpy (H) LS state to the greater electronic and vibrational entropy (S) of the HS state or *vice versa*. As mentioned above, this transition can be triggered through a large variety of external stimuli, nonetheless, most commonly, it is triggered by a change in temperature. In this way, by measuring the temperature-dependence of the properties of a SCO system, it is possible to follow the relative concentrations of HS and LS states as a function of temperature (γ_{HS} vs. T , **Figure 1.3.1**). Among all the temperature-dependence properties in which thermally induced spin transition may be manifested, perhaps molecular structure, color and magnetism are the most important.

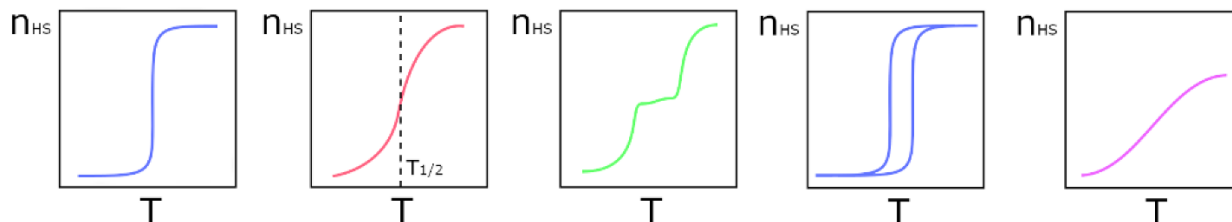


Figure 1.3.1. Different types of SCO curves: left-to-right, abrupt, gradual, step-like, hysteretic, and gradual and incomplete. Figure extracted from the literature.^[19]

Molecular structure. Since the HS and LS states present different occupancies of the anti-bonding e_g^* orbitals in particular, the metal–donor atom distance is remarkably sensitive to spin-state. Such distance becomes larger in the HS state (with higher occupancy of the e_g^* orbitals) and shorter in the LS state (with lower occupancy of the e_g^* orbitals).

Color. The color of a complex depends on the magnitude of Δ_o . Thus, the LS state (with larger Δ_o) will absorb higher energy-photons compared to the HS state (with lower Δ_o) that will absorb lower energy-photons. Thus, a thermally induced transition will usually result in strong and visible thermochromism. This change of color between the two different electronic states frequently provides a simple and rapid mean for the detection of the likely occurrence of spin transition.

Magnetism. The magnetic response is directly proportional to the number of the multiplicity (s). Therefore, a strong temperature-dependence of the magnetic moment is expected between the HS state with maximum multiplicity and the LS state with lower multiplicity. Magnetic properties of SCO systems are typically recorded with a superconducting quantum interference device (SQUID) magnetometer and is expressed as the $\chi_M T$ product vs T (χ_M is the molecular magnetic susceptibility and T the temperature).

1.4. Light-Induced Excited Spin-State Trapping

Among the different perturbations used in SCO systems, temperature and light are probably the most studied in comparison with other external stimuli such as pressure.^[20] The first light-induced spin transition experiment was observed by McGarvey *et al.* in 1982 in solution,^[21] and then, two years later by Decurtins *et al.* in the solid state.^[22] After irradiation at 514 nm, the photoinduced population of the metastable HS state at low temperatures (below 50 K) observed by spectroscopic techniques was named Light-Induced Excited Spin-State Trapping (LIESST). In 1986, the work of Hauser and co-workers proved that irradiation of the photo-excited metastable

HS state with higher wavelengths (820 nm) gave rise to re-population of the LS state, demonstrating the reversibility of the LIESST process, referred as reverse-LIESST (r-LIESST).^[23]

A schematic representation of the LIESST mechanism is shown in **Figure 1.4.1**. Thus, irradiation of the LS state of a SCO system at low temperatures induces a spin allowed $^1A_1 \rightarrow ^1T_1$ transition with 1T_1 lifetimes typically of nanoseconds. A fast relaxation cascading occurs via two consecutive intersystem crossing (ISC) to the intermediate states 3T_1 or 3T_2 . Then, these spin states can in turn decay via two possible ISC, one leads back to the 1A_1 (LS) ground state, the other implies the 5T_2 (HS*) metastable state. Radiative relaxation from 5T_2 to 1A_1 is forbidden and decay by thermal tunnelling to the 1A_1 ground state is slow at low temperatures. This gives rise to a virtually infinite lifetime as long as the thermal energy ($K_B T$) is lower than the energy barrier between HS and LS potential surfaces (ΔE_{HL}^0). The mechanism of r-LIESST is also illustrated in **Figure 1.4.1**. It is explained by application of the appropriate radiative source whereby the 5T_2 state is excited to the 5E state with two subsequent ISC processes via $^5E \rightarrow ^3T_1 \rightarrow ^1A_1$, leading back to the LS ground state.^[24]

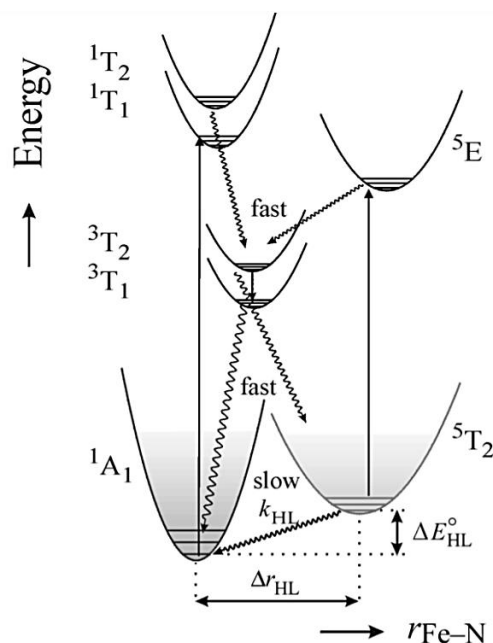


Figure 1.4.1. Schematic illustration of LIESST and r-LIESST of a d^6 complex in the SCO range. Spin allowed d–d transitions are denoted by arrows and the radiation-less relaxation processes by wavy lines. Figure extracted from the literature.^[24]

Based on magnetic characterization, an arbitrarily protocol was initially fixed to ensure that results are comparable from one compound to the other. The magnetic response is followed in a SQUID magnetometer while light irradiation is applied to the material at 10 K. It results in the

population of the higher multiplicity state through the LIESST phenomenon. This can be observed by a sharp increase of the magnetic signal. Once the photosaturation of the signal is observed *i.e.*, a plateau is reached, means that the equilibrium is operating between the population and relaxation of the excited state and the irradiation is stopped. Then, the temperature is increased at a rate of $0.3 \text{ K}\cdot\text{min}^{-1}$, while the magnetic behavior is recorded continuously. The magnetic response of the light-induced HS state remains almost constant until the energy barrier between HS and LS can be thermally overcome. Then, $\chi_M T$ drastically decreases and rapidly recovers its initial value. The T(LIESST) temperature was defined as the inflexion point of this relaxation in the thermally activated region and determined by the minimum of the $\partial\chi_M T/\partial T$ curve.^[25]

From a theoretical point of view, mean-field theory predicts an inverse relationship between the thermodynamic thermal SCO temperature $T_{1/2}$ ($T_{1/2}$ = temperature of 50% HS to LS conversion) and the lifetime of the photoinduced metastable state. Thus, in Fe(II) complexes, an empirical linear dependence between T(LIESST), which is the relaxation temperature above which the metastable photoinduced state is erased, and $T_{1/2}$ has been proposed by Létard et al.,^[26] in which $T(\text{LIESST}) = T_0 + 0.3T_{1/2}$. T_0 is the initial value of the linear function, which could be related to the denticity and rigidity of the ligand.^[27-29]

1.5. Iron(II) SCO complexes of 2,6-bis(pyrazol-1-yl)pyridine (1bpp) and derivatives

Fe(II) SCO complexes display a spin transition from $S = 0$ ($t_{2g}^6 e_g^0$) LS state to $S = 2$ ($t_{2g}^4 e_g^2$) HS state. Such transition involves two-electron transfer from the t_{2g} to the e_g orbital (**Figure 1.5.1**).

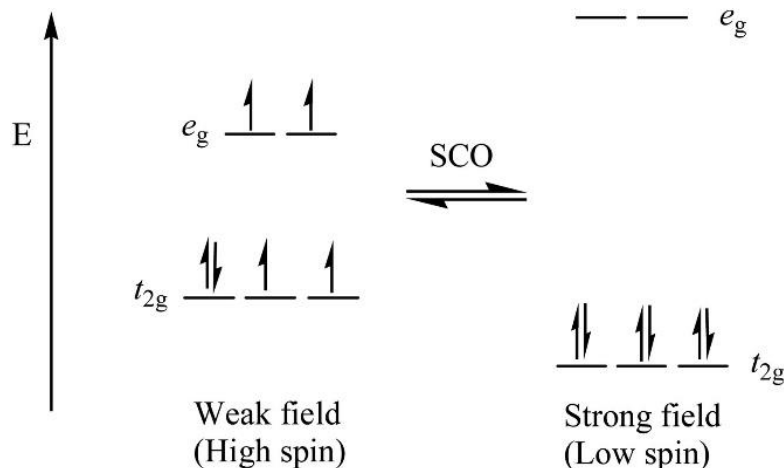
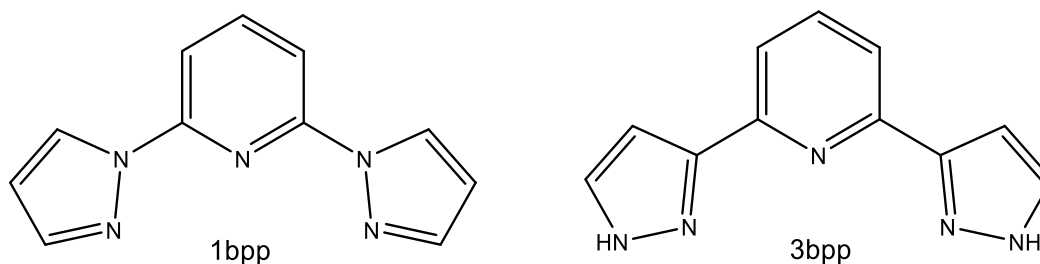


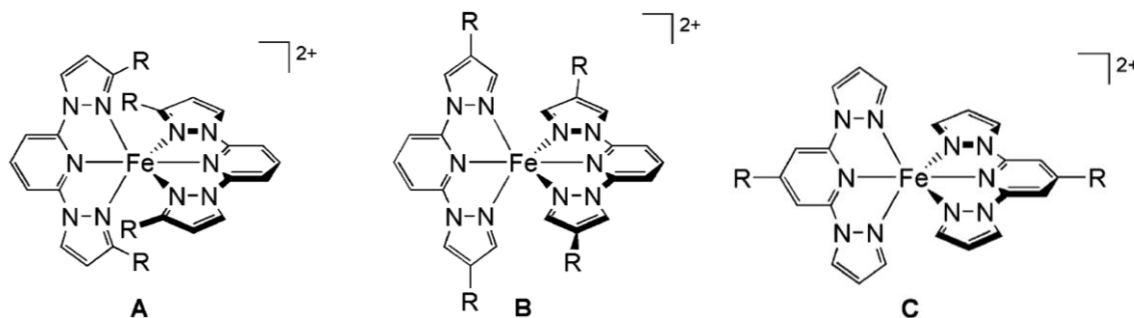
Figure 1.5.1. Electronic arrangement for HS and LS Fe(II) complex for SCO behavior. Extracted from the literature.^[30]

Iron(II) complexes of 2,6-bis(pyrazol-1-yl)pyridine (1bpp), its regioisomer 2,6-bis(pyrazol-3-yl)pyridine (3bpp) (**Scheme 1.5.1**. Schematic representation of 1bpp (left) and 3bpp), and their derivatives (**Scheme 1.5.2**) have proven to be very versatile compounds for the study of SCO systems. They often undergo thermal spin transition at accessible temperatures^[31] and LIESST effect with complete or high photoconversions at relatively high temperatures.^[28]



Scheme 1.5.1. Schematic representation of 1bpp (left) and 3bpp (right) ligands.

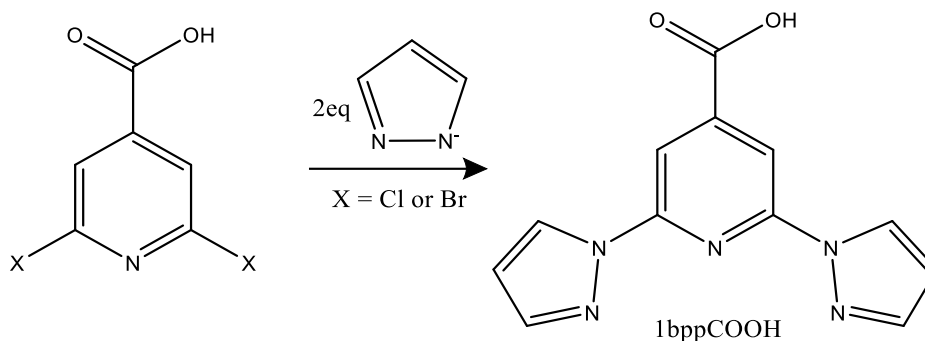
Addition of different functional groups in almost every site of the 1bpp skeleton is feasible and synthetically facile. Functionalization at the 3-pyrazolyl positions provides some control over the spin state^[32] (**Scheme 1.5.2, A**), while functionalization at the 4-pyrazolyl or 4-pyridyl positions allows modification of the periphery of the complex, without disturbing the iron center in great measure (**Scheme 1.5.2, B and C**). Therefore, we can conclude that is one of the most synthetically flexible ligands used in SCO research.^[33]



Scheme 1.5.2. Different orientation of ligand substituents at the pyrazole 3-position (**A**), the pyrazole 4-position (**B**) and the pyridine 4-position (**C**) in $[\text{Fe}(\text{1bpp})_2]^{2+}$. Figure extracted from literature.^[33]

The most common route to attach additional functionality to the 1bpp pyridine 4-position ring begins with commercially available 2,6-dihydroxyisonicotinic acid. After a halogenation step, nucleophilic coupling of pyrazolide anions with 2,6-dihalopyridines yields 2,6-bis(pyrazol-1-yl)pyridine-4-carboxylic acid (1bppCOOH, see **Scheme 1.5.3**).^[34] From there, it can be converted

into a wider range of 4-substituted-1bpp products by subsequent functional group transformations.^[33]

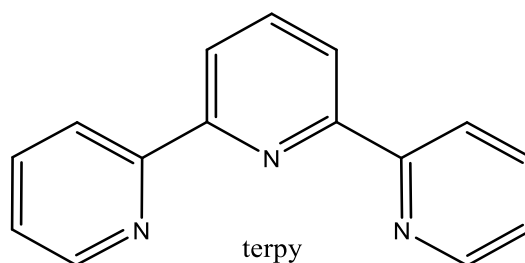


Scheme 1.5.3. Schematic representation of the synthesis of 1bppCOOH.

In a previous work, our group reported the solvent-free perchlorate salt of the homoleptic Fe(II) complex of the ligand 1bppCOOH named $[\text{Fe}(\text{1bppCOOH})_2](\text{ClO}_4)_2$.^[35] It shows an abrupt and hysteretic temperature- and light-induced spin transition. Characterization will be completed and presented in this work. The ethyl ester derivative of 1bppCOOH (ethyl 2,6-bis(pyrazol-1-yl)pyridine-4-carboxylate, 1bppCOOEt) has also been prepared and characterized for comparison purposes.

1.6. Co(II) SCO complexes of 2,2':6',2''-terpyridine (terpy) and derivatives

2,2':6',2''-terpyridine (terpy, **Scheme 1.6.1**) and its derivatives also constitute one of the most widely studied types of ligands in coordination chemistry.^[36] The popularity of terpy as a ligand is easy to understand. It is commercially available and straightforward to synthesize. It has been reacted with a large variety of metals to prepare complexes for different fields and different applications.^[37,38] Among them, Co(II) complexes of terpy and derivatives have been shown to present interesting SCO properties.



Scheme 1.6.1. Schematic representation of the 2,2':6',2''-terpyridine ligand, terpy.

SCO phenomenon for Co(II) complexes shows a transition from $S = 1/2$ ($t_{2g}^6 e_g^1$) LS state to $S = 3/2$ ($t_{2g}^5 e_g^2$) HS state. Such spin transition involves one-electron transfer from the t_{2g} to the e_g orbitals (see **Figure 1.6.1**), in contrast to the two-electron transfer process of Fe(II) or Fe(III) SCO complexes (see above). This is the origin of important differences in the feature of SCO between Co(II) and Fe(II) complexes. Thus, the small change of distance between the metal and the coordinated donor atom accompanying SCO of ~ 0.10 Å in Co(II), which is shorter than that of ~ 0.20 Å in Fe(II), as well as the smaller change for Co(II) of both ΔH and ΔS thermodynamic parameters of the SCO.^[39] This may also be the origin of the fact that LIESST effect has been observable for a large variety of Fe(II) SCO systems, but so far it has not been reported for Co(II).

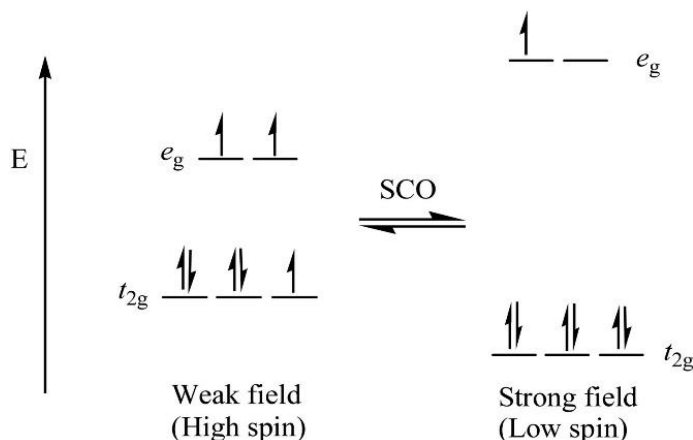


Figure 1.6.1. Electronic arrangement for HS and LS Co(II) complex for SCO behavior. Extracted from the literature.^[30]

Co(II) SCO complexes with a large diversity of terpy derivative ligands have been widely studied, especially those containing substituents at the C(4') position.^[40] Depending on the substituent, the complex can show different features combined with SCO properties such as: (i) Porosity. Adding a pyridine to the terpy moiety gives rise to a very well-packed 1D chain of $[\text{Co}(\text{pyterpy})\text{Cl}_2] \cdot \text{Solv}$ (pyterpy, 4'-(4'''-pyridyl)-2,2':6',2''-terpyridine) complexes in which the insertion of different guests in the microporous strongly modifies the magnetic behavior;^[41] (ii) Liquid crystal properties. Functionalization with long alkyl chains in the C(4') position adds flexibility in a way that structural phase transitions, and unique SCO properties such as reverse-SCO, take place;^[42–45] (iii) Ferroelectricity. Employing polar ligands like FPh-terpy (FPh-terpy=4'-((3-fluorophenyl)ethynyl)-2,2':6',2''-terpyridine) produces ferroelectric SCO complexes that depend on the degree of 180° flip–flop motion of the ligand's polar fluoro-phenyl ring (see **Figure 1.6.2, left**);^[46] (iv) Gas sensing. Adding a carboxylic acid group allows the formation of neutral complexes such as $\text{Co}(\text{terpyCOO})_2$ (terpyCOO, 4'-carboxy-2,2':6',2''-terpyridine) where the

absence of counteranions give rise to a compact pseudo-3D structure with small pores that selectively tune the $T_{1/2}$ by varying the CO_2 pressure (see **Figure 1.6.2, right**).^[47]

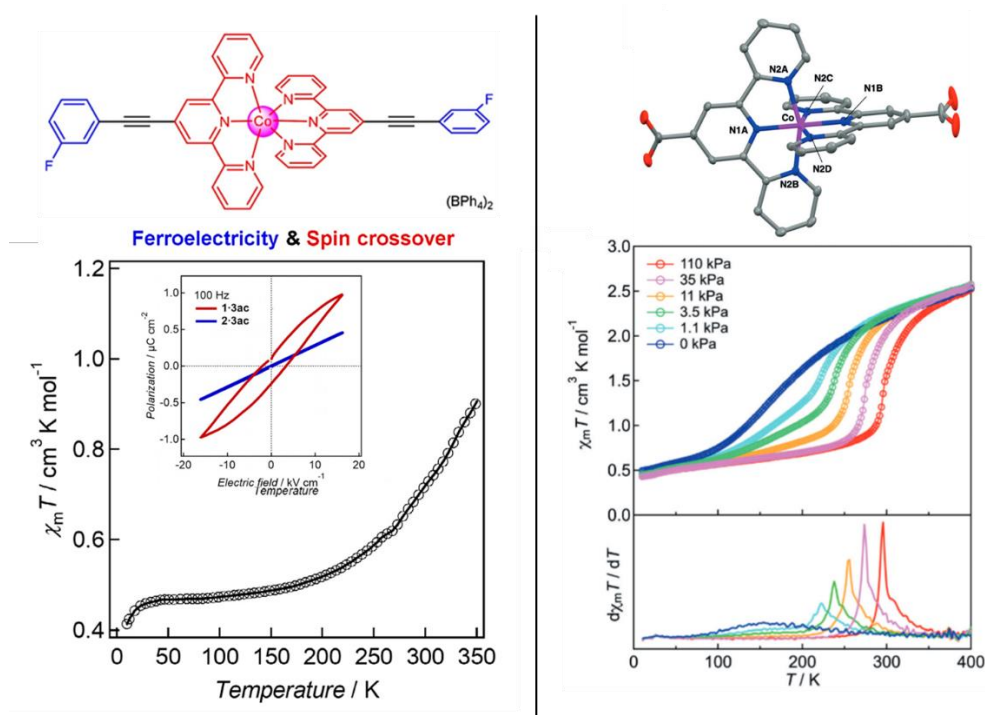
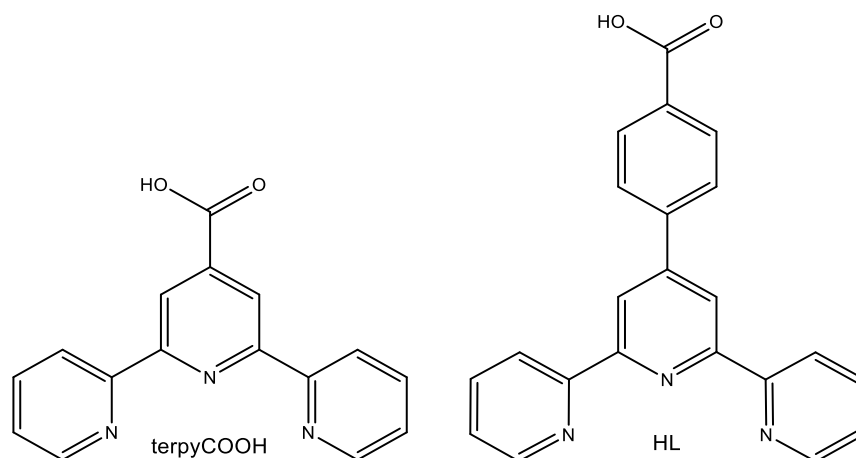


Figure 1.6.2. Left, schematic structure of $\text{Co}(\text{FPh-terpy})_2(\text{BPh}_4)_2$ (top) and its magnetic and ferroelectric curves (bot). Right, structure of $\text{Co}(\text{terpyCOO})_2$ (top) and its magnetization curves at different CO_2 pressure, the maxima of the first derivative at the bottom show the $T_{1/2}$ value. Figures adapted from the references ^[46] and ^[47], respectively.



Scheme 1.6.2. Schematic representation of the ligands 4'-carboxyl-2,2':6',2''-terpyridine, terpyCOOH (left); 4'-(4-carboxyphenyl)-2,2':6',2''-terpyridine, HL (right).

The functionalization with a carboxyphenyl group gives rise to the expanded ligand of the 4'-carboxyl-2,2':6',2''-terpyridine ligand (terpyCOOH), 4'-(4-carboxyphenyl)-2,2':6',2''-terpyridine (HL, see **Scheme 1.6.2**). Co(II) neutral complex of such terpy derivative has also been reported by deprotonation of the ligand in aqueous base media, as for the case of $[\text{Co}(\text{terpyCOO})_2]\cdot 4\text{H}_2\text{O}$ [47] (see above), resulting in $[\text{Co}(\text{L})_2]\cdot 5\text{H}_2\text{O}$. [48] However, only the crystallographic structure was reported. This complex is also synthesized and magnetically characterized by us during this work to be used as a reference.

1.7. Self-Assembled Monolayers

Self-assembled monolayers (SAMs) are nanostructured assemblies spontaneously formed by the adsorption of an active surfactant on a solid surface. [49] A schematic representation of the three main parts in which a surfactant is usually divided is shown in **Figure 1.7.1**; *anchoring group*, *body*, and *head*. Each one of them owns a particular function in the assembly.

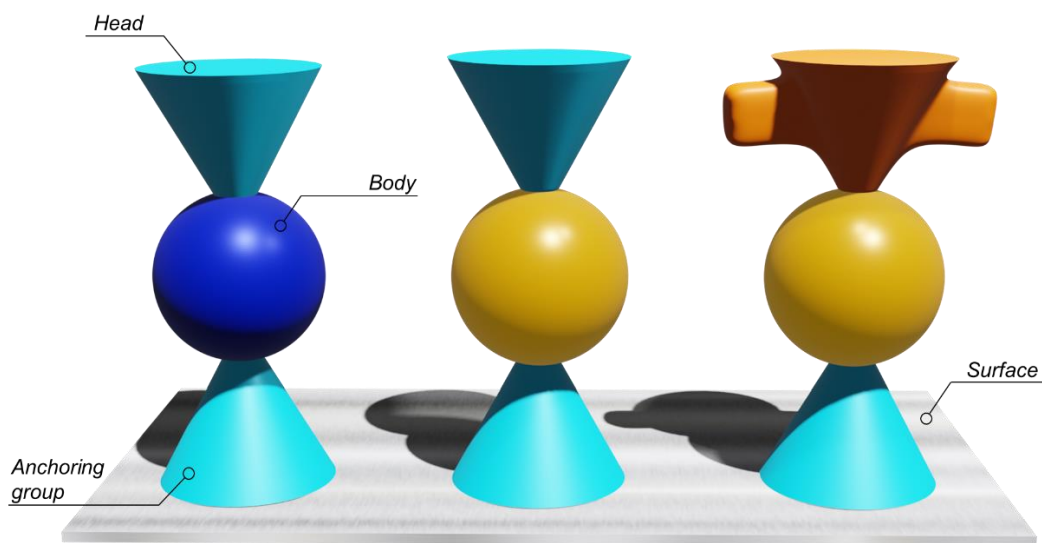


Figure 1.7.1. 3D representation of the structure of a SAM highlighting its different parts.

Anchoring group. The anchoring group is responsible to link the molecule to the surface through chemical interactions. It is capable of specifically interact with the surface. For example, silane groups, [50] carboxylic [51] and phosphonic [52] acids and chalcogenide elements, such as sulphur and selenium, [53] are the most employed anchoring groups. In this work, the anchoring group will be carboxylic acid group.

Body. The body usually contains aromatic rings or hydrocarbonated chains. In the nanostructure assembly, intermolecular forces between neighboring molecules tend to contribute

to stabilize and favor the assembly process, lead to an efficient molecular packing, and even modify or add some properties. A core made of different metal ions will be employed in this work in order to add switchability to the SAM. Such core will be surrounded by aromatic rings. Thus, $\pi \cdots \pi$ stacking or $\text{CH} \cdots \pi$ interactions are the only ones expected that could play a significant role.

Head. At last, the head group mainly defines the new air-substrate interface and, for that, usually determines some of the different uses of the functionalized surface such as wettability^[54] or as an anchoring point to other nanostructures.^[55]

As one can imagine, this wide range of possibilities to synthetically modify the surfactant together with its spontaneous formation of highly packed, ordered, and oriented monolayers, has drawn the attention of the scientific community. SAMs have proven to be able to control surface properties such as wettability, adhesion, electron transfer or sensing, which are just a few of many different uses that have been published.^[56]

1.8. Switchable SAMs

Bistable magnetic molecules such as valence tautomers, single molecule magnets and SCO complexes are perfect candidates for a large variety of molecular switches. The feasibility of these complexes as components of molecular spintronic devices are directly related to the successful assembly of nanostructures and control of the switching properties.

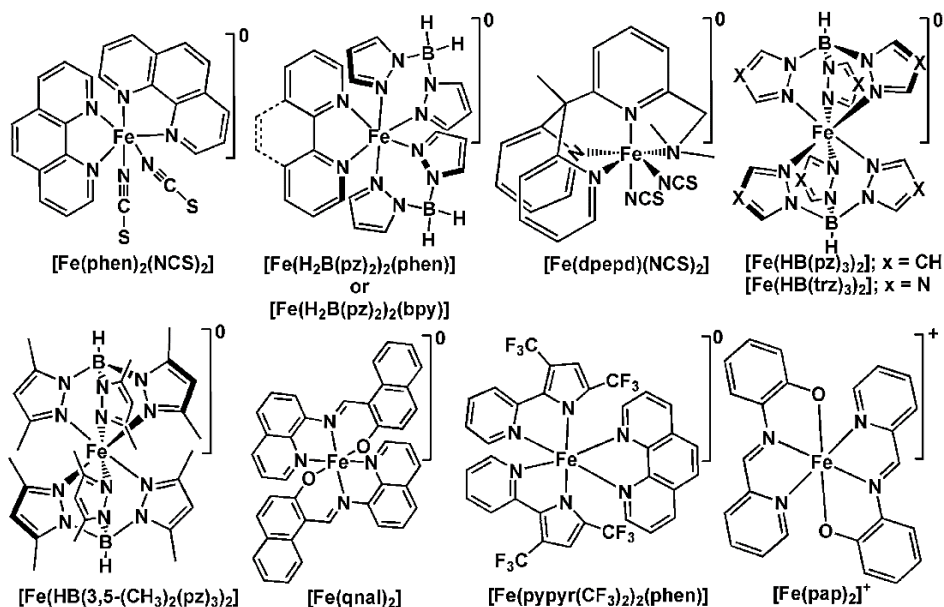


Figure 1.8.1. Schematic representation of the molecular structures of sublimable SCO complexes. Figure extracted from the literature.^[57]

Over the past ten years, amazing results with different SCO nanostructured assemblies have been reported. Most of the research has been focused on Fe(II) SCO complexes since they presents the most drastic change in the magnetic properties between the diamagnetic ($S = 0$) LS state and the paramagnetic ($S = 2$) HS state (see above). They have been proven to be able to maintain switchability even down to the (sub)monolayer regime.^[58] Although, very recently, one example of Co(II) SCO system has been proposed with a new switching mechanism (ELIESST) aswell.^[18] The preferred method for depositing this type of systems has been sublimation at ultrahigh vacuum of neutral complexes.^[59–65] However, this high-cost technique has restricted this deposition method to a few families of vacuum evaporable molecules (see **Figure 1.8.1**).^[57]

Separately, solution-based approaches, as self-assembly methodologies, have remained almost unexplored. Self-assembly from solution is a general simple grafting method that only requires molecules (neutral or not) functionalized with suitable anchoring groups capable of specifically interact with the surface (see above). In the case of SCO complexes, maintaining the ligand field of the deposited complex on the surface has been less straightforward. The difficulty of the challenge can be corroborated by the lack of works reporting the occurrence of this effect at the nanoscale level. The high lability of the coordinative bonds in these systems and the non-innocent role of the environment, causes a change in the structure that alters the fragile energetic balance keeping away the crossover point and pinning the spin state of the system. Most of the attempts on assembling SAMs of SCO complexes through wet-chemistry protocols have failed due to modifications in the coordination sphere or deformations of the ligand's structure.^[66,67] Only two successful examples of thermal-switchable magnetic molecules assembled from solution have been reported so far. On one hand, Poneti *et. al.* reported a SAM of cobalt-dioxolene complexes ($[\text{Co}(\text{Me}_n\text{tpa})\text{DBCatSH}](\text{PF}_6)\text{CH}_3\text{OH}$, $n = 0, 2, 3$, see **Figure 1.8.2**, top) by incubating a Au(111) substrate in a solution of the complexes. They were able to qualitatively control the magnetic state of the complex with varying the number of methyl substituents. With $n = 0$ or 3 the molecules stabilized the LS or HS state, respectively, while $n = 2$ featured a partially thermal- and light-induced valence tautomerism. Such behavior was also observed on the monolayer with X-ray photoelectron spectroscopy (XPS) and X-ray absorption spectroscopy (XAS).^[68] On the other hand, Devid E. J. *et. al.* was able to detect the spin transition of SCO $[\text{Fe}(\text{AcS-bpp})_2](\text{ClO}_4)_2$ (AcS-bpp, (S)-(4-([2,6-(dipyrazol-1-yl)pyrid-4-yl]ethynyl)phenyl)ethanethioate) molecules chemisorbed onto a micro-contact printed array of gold nanoparticles (see **Figure 1.8.2**, bottom). After 4 days of incubation in a diluted solution of the above-mentioned molecules, temperature-dependent Raman, SQUID and charge transport measurements demonstrated the presence of intact SCO molecules in the system.^[69]

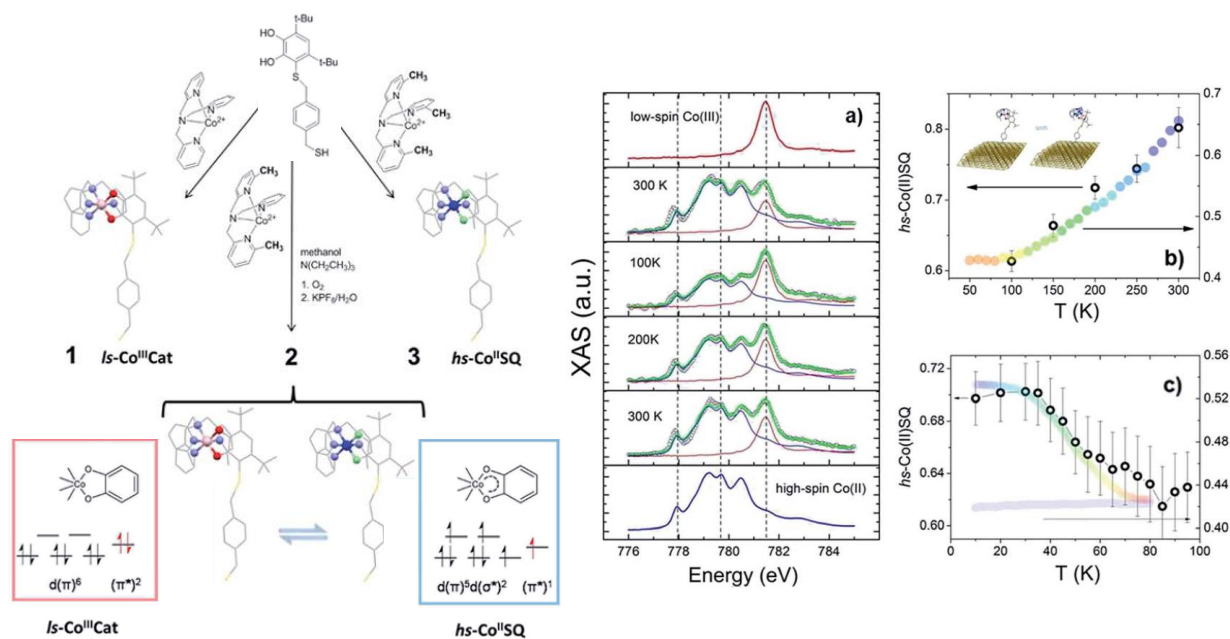


Figure 1.8.2. Top left, schematic representation of the complexes [Co(Me_ntpa)DBCatSH] ($n = 0, 2, 3$). Top right, a) Temperature evolution of the normalized Co L₃-edge XAS spectra of a monolayer of [Co(Me₂tpa)DBCatSH] along with reference signals used for the spectral deconvolution. HS-Co(II) thermal distribution profile (empty circles) obtained from XAS spectra taken before (b) and after (c) laser light irradiation. Bottom, cartoon of the micro-printed gold nanoparticle array. Enclosed in red rectangle, schematic representation of [Fe(AcS-bpp)₂] in a junction-like environment. Enclosed in red circle, Raman spectra of the molecule at low (blue) and high (red) temperature in the nanoparticle array from 900 - 1200 cm⁻¹ range. Figures extracted from the literature.^[68,69]

1.9. Characterization techniques

Matrix assisted laser desorption/ionization time of flight Mass Spectroscopy. MALDI-TOF MS is commonly used in the field of the proteomics to characterize proteins and peptides rapidly.^[70] This is a soft ionization technique that uses a polymer matrix, deposited on the surface, which is irradiated with a laser. Then, the analyte molecules are usually ionized by being protonated or deprotonated with the nearby matrix (being the most common MALDI ionization format for the analyte molecules to carry a single positive charge). Thus, ions of different m/z are dispersed in time during their flight along a drift path of known length allowing the detection of their charged mass (the lighter ones will arrive earlier at the detector than the heavier ones). Last developments in instrumentation have permitted to extend this technique to characterize thin films and SAMs.^[71]

Atomic Force Microscopy.^[72] AFM is a technique to get topographic information of a surface. A sharp tip, placed at the end of a cantilever, is brought into close proximity to the surface of the sample. Piezoelectric tube scanners ensure micrometric positioning of the tip and allows the scanning of the surface topography. A laser which illuminates the back of the cantilever is reflected into a four-quadrant photodetector that monitors the x and y axis (**Figure 1.9.1**). This registers the attractive or repulsive interactions of the tip transforming the signal into a topographic image. There are two modes of operation. The first and most used working mode is the dynamic mode, so-call **tapping mode**, also referred as noncontact imaging mode. During the surface scan, the tip (or sample) moves back and forth to maintain a constant distance of a few nanometres between tip and sample. It minimizes the effects of friction as well as other lateral forces and avoids the “snap-in” of the tip to the sample due to adhesive attractions. The second is a static mode called **contact mode**, where the tip is brought into contact with the surface. The variations of the later causes the cantilever to deflect and are measured and recorded by optical detectors. In this thesis, the tapping mode has been employed.

In cases where the formed monolayer replicates the topography of the underlying surface, such as the ones reported in this work, topographic AFM measurements will provide us information about the homogeneity of the surface and the lack of aggregates, but they do not provide information about the formation of the SAM.

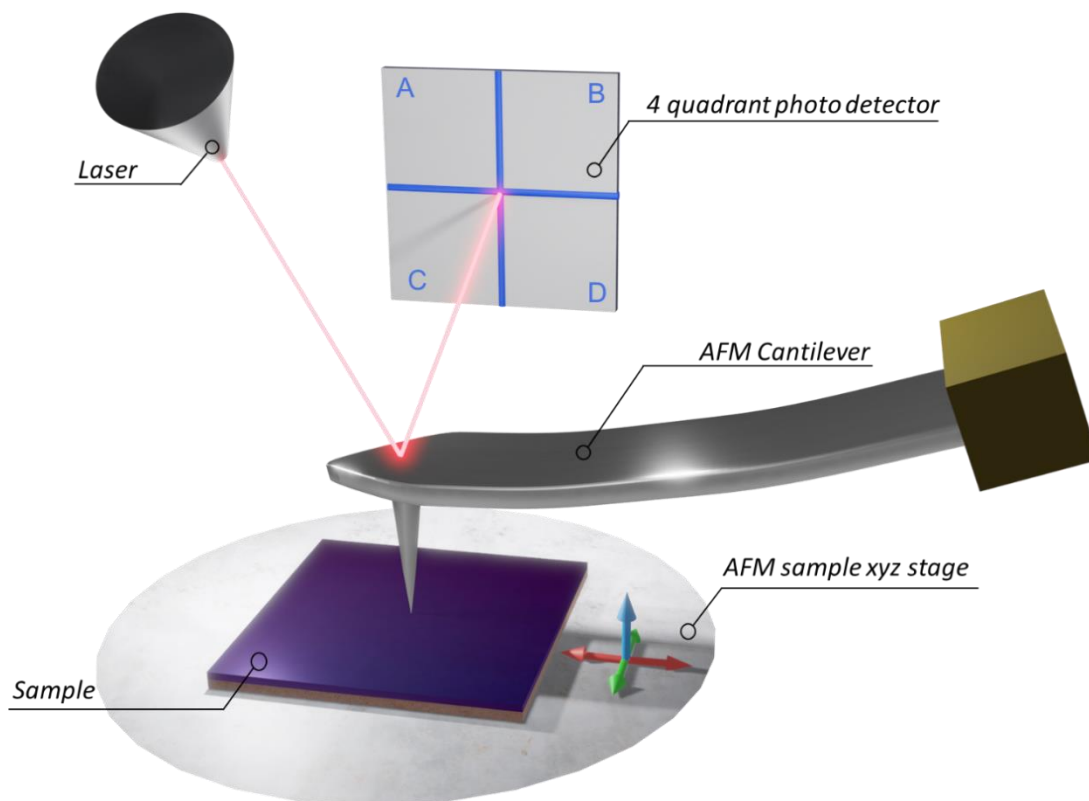


Figure 1.9.1. Schematical representation of a typical AFM cantilever deflection measurement setup. The deflection of the AFM cantilever is measured by reflecting a laser off the backside of the cantilever, while the tip on the opposite site is scanning the surface of the sample.

Raman Spectroscopy^[73] and **Surface-Enhance Raman Spectroscopy**.^[74] This technique is based on the scattering of the light affected by a change in the rotational and vibrational energy of the molecule and gives information on its energy levels and chemical structure. Thus, the light interacts with the molecule and energy is exchanged between the photon and the molecule. The energy changes detected are those involved in nuclear motion. Therefore, if only electron cloud distortions are involved in scattering, the photons will be scattered with very small frequency changes, as electrons are comparatively light, and an elastic scattering will take place. In other words, the energy of the scattered photon is equal to that of the incident photon. It is the dominant process and is known as Rayleigh scattering (see **Figure 1.9.2**). In a much rarer event (one in every 10^6 - 10^8 photons), nuclear motion is involved, and the incident photon suffers an inelastic process. The energy of the scattered photon will be different from that of the incident one giving rise to the so-called Raman scattering. If the Raman scattering process leads to absorption of energy by the molecule or the photon, a Stokes or Anti-Stokes scattering process takes place.

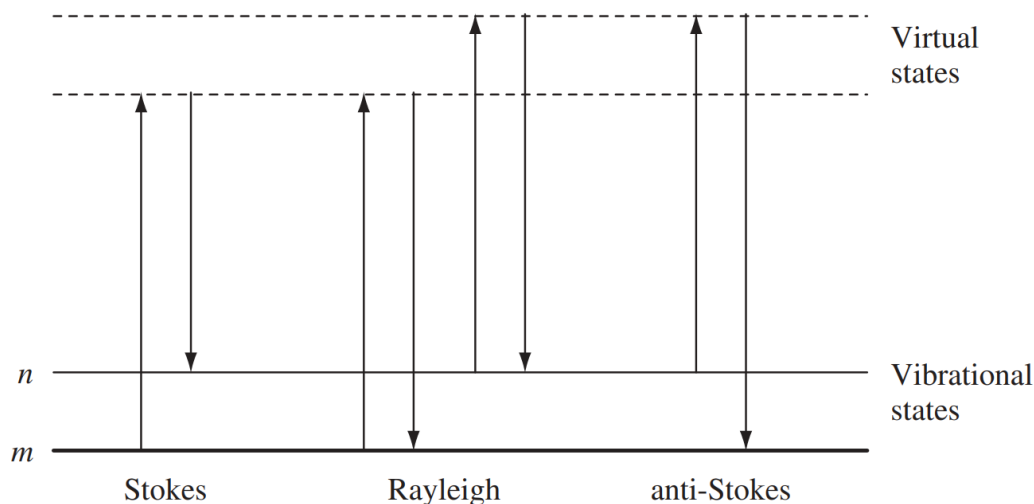


Figure 1.9.2. Simplify diagram of the Rayleigh and Raman scattering processes for one vibration. Figure extracted from the literature.^[73]

As stated before, about one in every 10^6 - 10^8 photons is scattered, which means that is a very weak phenomenon. Surface-enhanced Raman spectroscopy (SERS) amplifies Raman signals from molecules by several orders of magnitude. SERS is a technique where molecules undergo much higher scattering efficiencies when adsorbed on metal colloidal nanoparticles or rough metal surfaces such as Ag, Au, Cu, Pt or Pd. Two mechanisms are now broadly accepted: (i) Electromagnetic theory treats the molecule as a point dipole which responds to the enhanced local fields at or near the metal surface. These enhanced fields arise from roughness features that couple the incident field to surface plasmons. (ii) Chemical enhancement theory attributes SERS intensity to modification of the molecular polarizability by interaction of the metal with ensuing molecular resonances, giving rise to enhancements such as those associated with resonance Raman scattering.^[74]

Thanks to the molecular fingerprint provided by Raman and the structural information that can be extracted, this spectroscopic technique is a very powerful and versatile tool to study the different spin states of the samples in different environments ranging from the solid state to nanostructured assemblies.

X-ray Photoelectron Spectroscopy.^[75] XPS is a surface sensitive analytical technique that can be used to get information about the elemental composition of SAMs.^[75] Surface analysis by XPS is based on the interaction of the atoms in the surface with monoenergetic soft X-rays. Such interaction causes electrons to be emitted by the photoelectric effect (**Figure 1.9.3**) and, because each element has a specific set of binding energies (BE), analyzing the energy of the detected

electron can be used to identify and qualitatively determine the concentration of the elements on the surface. The BE may be referred as the energy difference between the Fermi level (by definition, zero BE) and the relative energy of the ion remaining after electron emission. Variations in the elemental BE (chemical shifts) arise from differences in the chemical potential and polarizability of compounds. These chemical shifts can be used to identify the oxidation and chemical state of the materials being analyzed. The electrons leaving the sample are detected by an electron spectrometer according to their kinetic energy. The analyzer is usually operated as an energy window, referred to as the pass energy, accepting only those electrons having an energy within the range of this window. To maintain a constant energy resolution, the pass energy is fixed. Incoming electrons are adjusted to the pass energy before entering the energy analyzer.

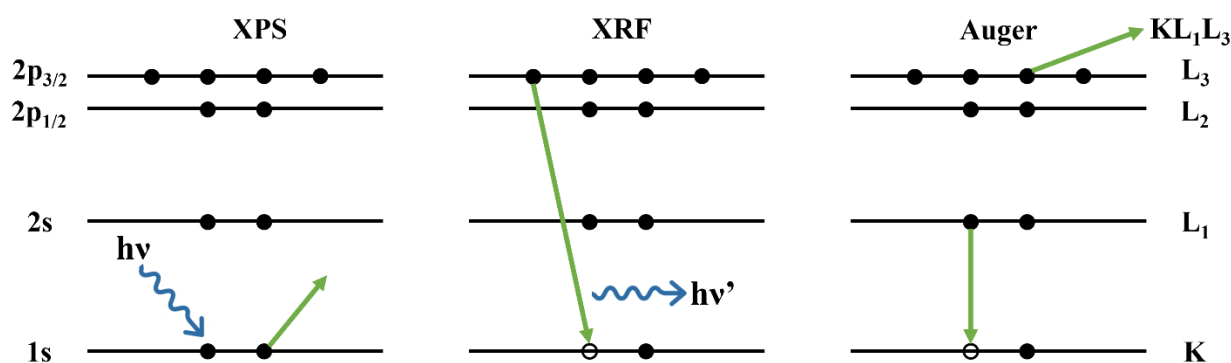


Figure 1.9.3. Processes that result from X-ray bombardment of a surface: (left) emission of a photoelectron, (middle) X-ray fluorescence and (right) emission of an Auger electron. Figure adapted from literature.^[75]

In addition to photoelectrons emitted in the photoelectric process, fluorescence emission (XRF) or Auger electrons may occur, although the latter is less favored in the working energy range. In the Auger process (

Figure 1.9.3.), an outer electron falls into the inner orbital vacancy, and a second electron is simultaneously emitted, carrying off the excess energy. Such electrons are also detected and known to be specific for each element as well.

X-ray Absorption Spectroscopy. XAS is a synchrotron-based absorption technique that gives information about the elemental composition of the sample but, most importantly, provides the requested sensitivity to monitor different oxidation and electronic states of SAMs. This technique is based on the electronic detection of an atomic empty inner-shell orbital promoted by the synchrotron radiation (**Figure 1.9.4, left**).^[76] In XAS measurement, the X-ray photon energy is tuned through the electronic core-level binding energy of a specific element while the

absorption of such photons is recorded. When the energy of the incident photon corresponds to the core-level electronic photoexcitation of the lowest-energy unoccupied electronic state, an absorption onset will be observed. Different modes of detection can be employed for the XAS study of SAMs. They are mainly separated into two categories: the electron yield (EY) and fluorescence yield (FY) modes. The total electron yield (TEY, **Figure 1.9.4, right**) mode is the one conducted on almost all soft X-ray beamlines due to its set-up simplicity and is the one employed in this work. The relaxation of an absorbed X-ray photon results in an inelastic scattering of either an Auger electron or a fluorescence photon. Such process creates a cascade of excited electrons leaving the sample. The concomitant drain current is large enough to be measured and, since the current into the sample is proportional to the absorption, its evolution as a function of the photon energy yields the XAS spectrum.

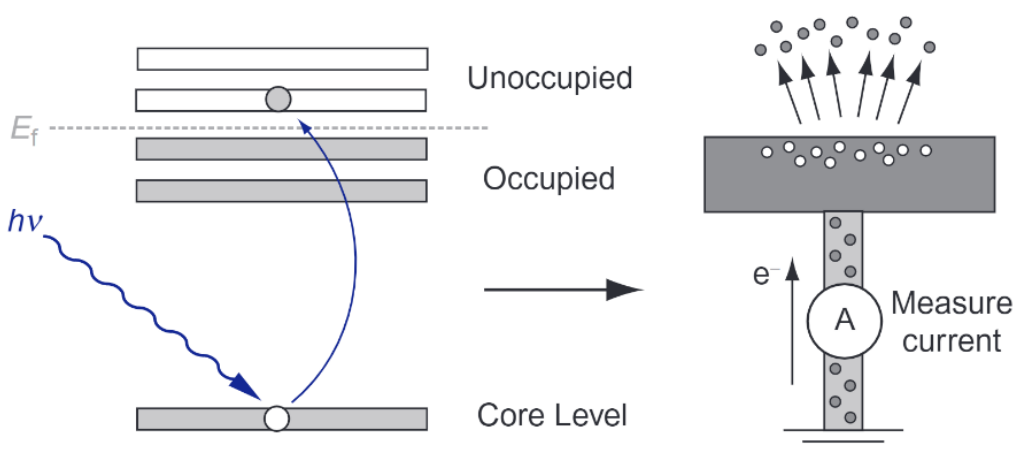


Figure 1.9.4. Diagram of the TEY mode. **Left**, energy-level diagram of the X-ray absorption process. **Right**, inelastic scattering of Auger electrons and reabsorption of fluorescence photons emitted during decay of the photoexcited atom result in an electron cascade. This cascade is detected as the current into the sample and the variation in the current as a function of energy provides the TEY XAS spectrum. Figure extracted from literature.^[76]

Else, by changing the polarization of the X-ray beam, from linear to circular, magnetic materials can also be characterized. The difference between two XAS spectra, recorded with opposite polarizations and under an applied magnetic field, is known as X-ray magnetic circular dichroism (XMCD). Information such as the spin state and orbital magnetic moment could be extracted.

1.10. References

- [1] J. E. House, *Inorganic Chemistry*, Elsevier, **2013**.
- [2] A. Schmitz, "General Chemistry: Principles, Patterns, and Applications," **2012**.
- [3] L. Pauling, *Journal of the American Chemical Society* **1932**, *54*, 988.
- [4] S. Cambi, *Berichte der Deutschen Chemischen Gesellschaft* **1931**, *10*, 2591.
- [5] P. J. Koningsbruggen, Y. Maeda, H. Oshio, in *Spin Crossover in Transition Metal Compounds* (Eds.: P. Gütllich, H. A. Goodwin), Springer, Berlin, Heidelberg, **2012**, pp. 259–324.
- [6] E. J. Wheelwright, F. H. Spedding, G. Schwarzenbach, *Journal of American Chemical Society* **1960**, *82*, 820.
- [7] E. König, K. Madeja, *Inorganic Chemistry* **1966**, *6*, 48.
- [8] D. C. Fisher, H. G. Drickamer, *The Journal of Chemical Physics* **1971**, *54*, 4819.
- [9] G. Chastanet, M. Lorenc, R. Bertoni, C. Desplanches, *Comptes Rendus Chimie* **2018**, *21*, 1075.
- [10] V. Ksenofontov, A. B. Gaspar, P. Gütllich, in *Spin Crossover in Transition Metal Compounds III*, Springer, Berlin, Heidelberg, **2006**, pp. 23–64.
- [11] A. Bousseksou, F. Varret, M. Goiran, K. Boukheddaden, J. P. Tuchagues, in *Spin Crossover in Transition Metal Compounds III*, **2006**, pp. 65–84.
- [12] X. Zhang, T. Palamarciuc, J. François Létard, P. Rosa, E. V. Lozada, F. Torres, L. G. Rosa, B. Doudin, P. A. Dowben, *Chemical Communications* **2014**, *50*, 2255.
- [13] M. Enamullah, W. Linert, V. Gutmann, R. F. Jameson, *Monatshefte für Chemie* **1994**, *125*, 1301.
- [14] P. D. Southon, L. Liu, E. A. Fellows, D. J. Price, G. J. Halder, K. W. Chapman, B. Mobaraki, K. S. Murray, J. F. Létard, C. J. Kepert, *Journal of American Chemical Society* **2009**, *131*, 10998.
- [15] Y. Garcia, P. Gütllich, in *Spin Crossover in Transition Metal Compounds II*, **2012**, pp. 49–62.

- [16] J. M. Herrera, A. Bachschmidt, F. Villain, A. Bleuzen, V. Marvaud, W. Wernsdorfer, M. Verdaguer, *Philosophical Transactions of the Royal Society A: Mathematical, Physical and Engineering Sciences* **2008**, 366, 127.
- [17] A. Köbke, F. Gutzeit, F. Röhricht, A. Schlimm, J. Grunwald, F. Tuczek, M. Studniarek, D. Longo, F. Choueikani, E. Otero, P. Ohresser, S. Rohlf, S. Johannsen, F. Diekmann, K. Rossnagel, A. Weismann, T. Jasper-Toennies, C. Näther, R. Herges, R. Berndt, M. Gruber, *Nature Nanotechnology* **2020**, 15, 18.
- [18] S. Johannsen, S. Ossinger, J. Grunwald, A. Herman, H. Wende, F. Tuczek, M. Gruber, R. Berndt, *Angewandte Chemie International Edition* **2022**, 61, 1.
- [19] P. N. Martinho, F. F. Martins, N. A. G. Bandeira, M. J. Calhorda, *Sustainability (Switzerland)* **2020**, 12.
- [20] M. A. Halcrow, *Spin-Crossover Materials: Properties and Applications*, John Wiley & Sons, Ltd., **2013**.
- [21] J. J. McGarvey, I. Lawthers, *Chemical Communication* **1982**, 906.
- [22] S. Decurtins, P. Gütlich, C. P. Köhler, H. Spiering, A. Hauser, *Chemical Physics Letters* **1984**, 105, 1.
- [23] A. Hauser, *Chemical Physics Letters* **1986**, 124, 543.
- [24] P. Gütlich, Y. Garcia, H. A. Goodwin, *Chemical Society Reviews* **2000**, 29, 419.
- [25] G. Chastanet, C. Desplanches, C. Baldé, P. Rosa, M. Marchivie, P. Guionneau, C. Baldé, *Chemistry Squared - Chem2* **2018**, 2, 1.
- [26] J. F. Letard, L. Capes, G. Chastanet, N. Moliner, S. Letard, J.-A. Real, O. Kahn, *Chemical Physics Letters* **1999**, 313, 115.
- [27] S. Marcén, L. Lecren, L. Capes, H. A. Goodwin, J. F. Létard, *Chemical Physics Letters* **2002**, 358, 87.
- [28] V. A. Money, J. S. Costa, S. Marcén, G. Chastanet, J. Elhaïk, M. A. Halcrow, J. A. K. Howard, J. F. Létard, *Chemical Physics Letters* **2004**, 391, 273.
- [29] J. F. Létard, P. Guionneau, O. Nguyen, J. S. Costa, S. Marcén, G. Chastanet, M. Marchivie, L. Goux-Capes, *Chemistry - A European Journal* **2005**, 11, 4582.

- [30] N. M. J. Nik Ibrahim, S. M. Said, A. Mainal, M. F. Mohd Sabri, N. Abdullah, M. M. I. Megat Hasnan, H. Che Hassan, M. F. Mohd Salleh, W. A. Wan Mohd Mahiyiddin, *Materials Research Bulletin* **2020**, *126*, 110828.
- [31] M. A. Halcrow, *Coordination Chemistry Reviews* **2005**, *249*, 2880.
- [32] J. M. Holland, S. A. Barrett, C. A. Kilner, M. A. Halcrow, *Inorganic Chemistry communications* **2002**, *5*, 328.
- [33] M. A. Halcrow, *Coordination Chemistry Reviews* **2009**, *253*, 2493.
- [34] C. Klein, E. Baranoff, M. Grätzel, M. K. Nazeeruddin, *Tetrahedron Letters* **2011**, *52*, 584.
- [35] A. Abhervé, M. Clemente-León, E. Coronado, C. J. Gómez-García, M. López-Jordà, *Dalton Transactions* **2014**, *43*, 9406.
- [36] E. C. Constable, *Advances in inorganic chemistry and radiochemistry* **1986**, *30*, 69.
- [37] S. Wang, W. Chu, Y. Wang, S. Liu, J. Zhang, S. Li, H. Wei, G. Zhou, X. Qin, *Applied Organometallic Chemistry* **2013**, *27*, 373.
- [38] Y. H. Lee, J. Y. Kim, S. Kusumoto, H. Ohmagari, M. Hasegawa, P. Thuéry, J. Harrowfield, S. Hayami, Y. Kim, *Chemistry (Easton)* **2021**, *3*, 199.
- [39] H. A. Goodwin, in *Spin Crossover in Transition Metal Compounds II*, Springer, Berlin, Heidelberg, **2004**, pp. 23–47.
- [40] S. Hayami, Y. Komatsu, T. Shimizu, H. Kamihata, Y. H. Lee, *Coordination Chemistry Reviews* **2011**, *255*, 1981.
- [41] S. Hayami, K. Hashiguchi, G. Juhász, M. Ohba, H. Okawa, Y. Maeda, K. Kato, K. Osaka, M. Takata, K. Inoue, *Inorganic Chemistry* **2004**, *43*, 4124.
- [42] S. Hayami, Y. Shigeyoshi, M. Akita, K. Inoue, K. Kato, K. Osaka, M. Takata, R. Kawajiri, T. Mitani, Y. Maeda, *Angewandte Chemie - International Edition* **2005**, *44*, 4899.
- [43] S. Hayami, N. Motokawa, A. Shuto, N. Masuhara, T. Someya, Y. Ogawa, K. Inoue, Y. Maeda, *Inorganic Chemistry* **2007**, *46*, 1789.
- [44] S. Hayami, K. Murata, D. Urakami, Y. Kojima, M. Akita, K. Inoue, *Chemical Communications* **2008**, 6510.
- [45] S. Hayami, K. Kato, Y. Komatsu, A. Fuyuhiko, M. Ohba, *Dalton Transactions* **2011**, *40*, 2167.

- [46] R. Akiyoshi, Y. Komatsumaru, M. Donoshita, S. Dekura, Y. Yoshida, H. Kitagawa, Y. Kitagawa, L. F. Lindoy, S. Hayami, *Angewandte Chemie - International Edition* **2021**, *60*, 12717.
- [47] M. Nakaya, W. Kosaka, H. Miyasaka, Y. Komatsumaru, S. Kawaguchi, K. Sugimoto, Y. Zhang, M. Nakamura, L. F. Lindoy, S. Hayami, *Angewandte Chemie - International Edition* **2020**, *59*, 10658.
- [48] J. Yang, R. X. Hu, M. B. Zhang, *Journal of Solid State Chemistry* **2012**, *196*, 398.
- [49] A. Ulman, *Chemical Reviews* **1996**, *96*, 1533.
- [50] L. Wang, U. S. Schubert, S. Hoepfner, *Chemical Society Reviews* **2021**, *50*, 6507.
- [51] S. A. Jadhav, *Central European Journal of Chemistry* **2011**, *9*, 369.
- [52] C. Queffelec, M. Petit, P. Janvier, D. A. Knight, B. Bujoli, *Chemical Reviews* **2012**, *112*, 3777.
- [53] C. Vericat, M. E. Vela, G. Corthey, E. Pensa, E. Cortés, M. H. Fonticelli, F. Ibañez, G. E. Benitez, P. Carro, R. C. Salvarezza, *RSC Advances* **2014**, *4*, 27730.
- [54] P. E. Laibinis, G. M. Whitesides, D. L. Allara, Y.-T. Tao, A. N. Parikh, R. G. Nuzzo, *Journal of the American Chemical Society* **1991**, *113*, 7152.
- [55] J. P. Collman, N. K. Devaraj, C. E. D. Chidsey, *Langmuir* **2004**, *20*, 1051.
- [56] F. Schreiber, *Journal of Physics Condensed Matter* **2004**, *16*.
- [57] K. S. Kumar, M. Ruben, *Angewandte Chemie - International Edition* **2021**, *60*, 7502.
- [58] M. Bernien, D. Wiedemann, C. F. Hermanns, A. Krüger, D. Rolf, W. Kroener, P. Müller, A. Grohmann, W. Kuch, *Journal of Physical Chemistry Letters* **2012**, *3*, 3431.
- [59] B. Warner, J. C. Oberg, T. G. Gill, F. el Hallak, C. F. Hirjibehedin, M. Serri, S. Heutz, M. A. Arrio, P. Sainctavit, M. Mannini, G. Poneti, R. Sessoli, P. Rosa, *Journal of Physical Chemistry Letters* **2013**, *4*, 1546.
- [60] T. G. Gopakumar, M. Bernien, H. Naggert, F. Matino, C. F. Hermanns, A. Bannwarth, S. Mühlenberend, A. Krüger, D. Krüger, F. Nickel, W. Walter, R. Berndt, W. Kuch, F. Tucek, *Chemistry - A European Journal* **2013**, *19*, 15702.
- [61] M. Bernien, H. Naggert, L. M. Arruda, L. Kipgen, F. Nickel, J. Miguel, C. F. Hermanns, A. Krüger, D. Krüger, E. Schierle, E. Weschke, F. Tucek, W. Kuch, *ACS Nano* **2015**, *9*, 8960.

- [62] S. Beniwal, X. Zhang, S. Mu, A. Naim, P. Rosa, G. Chastanet, J. F. Létard, J. Liu, G. E. Sterbinsky, D. A. Arena, P. A. Dowben, A. Enders, *Journal of Physics Condensed Matter* **2016**, *28*.
- [63] S. Ossinger, H. Naggert, L. Kipgen, T. Jasper-Toennies, A. Rai, J. Rudnik, F. Nickel, L. M. Arruda, M. Bernien, W. Kuch, R. Berndt, F. Tucek, *Journal of Physical Chemistry C* **2017**, *121*, 1210.
- [64] L. Kipgen, M. Bernien, S. Ossinger, F. Nickel, A. J. Britton, L. M. Arruda, H. Naggert, C. Luo, C. Lotze, H. Ryll, F. Radu, E. Schierle, E. Weschke, F. Tucek, W. Kuch, *Nature Communications* **2018**, *9*, 1.
- [65] K. Bairagi, A. Bellec, C. Fourmental, O. Iasco, J. Lagoute, C. Chacon, Y. Girard, S. Rousset, F. Choueikani, E. Otero, P. Ohresser, P. Saintavit, M. L. Boillot, T. Mallah, V. Repain, *Journal of Physical Chemistry C* **2018**, *122*, 727.
- [66] L. Pukenas, F. Benn, E. Lovell, A. Santoro, L. J. Kershaw Cook, M. A. Halcrow, S. D. Evans, *Journal of Materials Chemistry C* **2015**, *3*, 7890.
- [67] N. Giaconi, A. L. Sorrentino, L. Poggini, G. Serrano, G. Cucinotta, E. Otero, D. Longo, H. Douib, F. Pointillart, A. Caneschi, R. Sessoli, M. Mannini, *Magnetochemistry* **2022**, *8*, 1.
- [68] G. Poneti, L. Poggini, M. Mannini, B. Cortigiani, L. Sorace, E. Otero, P. Saintavit, A. Magnani, R. Sessoli, A. Dei, *Chemical Science* **2015**, *6*, 2268.
- [69] E. J. Devid, P. N. Martinho, M. V. Kamalakar, I. Šalitroš, Ú. Prendergast, J. F. Dayen, V. Meded, T. Lemma, R. González-Prieto, F. Evers, T. E. Keyes, M. Ruben, B. Doudin, S. J. van der Molen, *ACS Nano* **2015**, *9*, 4496.
- [70] J. O. Lay, *Mass Spectrometry Reviews* **2001**, *20*, 172.
- [71] J. Su, M. Mrksich, *Langmuir* **2003**, *19*, 4867.
- [72] D. Hussain, K. Ahmad, *Europhysics Letters* **1987**, *3*, 1281.
- [73] E. Smith, G. Dent, *Modern Raman Spectroscopy-A Practical Approach*, John Wiley & Sons, Ltd, **2005**.
- [74] S. Kumar, P. Kumar, A. Das, C. Shakher Pathak, in *Recent Advances in Nanophotonics - Fundamentals and Applications*, IntechOpen, **2020**, pp. 1–24.
- [75] F. A. Stevie, C. L. Donley, *Journal of Vacuum Science & Technology A* **2020**, *38*, 063204.

[76] J. R. I. Lee, M. Bagge-Hansen, T. M. Willey, R. W. Meulenberg, M. H. Nielsen, I. C. Tran, T. van Buuren, in *Methods in Enzymology*, Academic Press Inc., **2013**, pp. 165–187.

Chapter 2

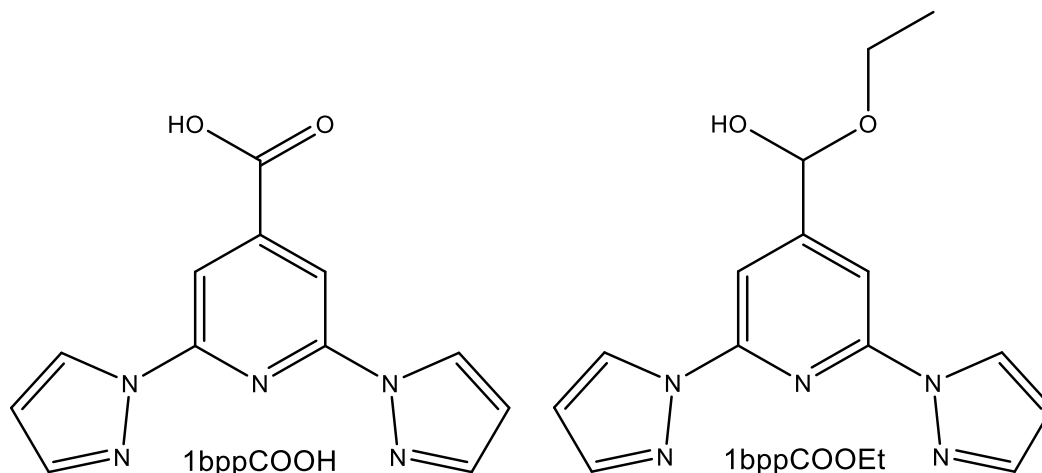
2. Spin-crossover compounds based on Fe(II) complexes of 2,6-bis(pyrazol-1-yl)pyridine (1bpp) functionalized with carboxylic acid (1bppCOOH) and ethyl carboxylate (1bppCOOEt)

V. García-López, M. Palacios-Corella, M. Clemente-León, and E. Coronado, "Spin-crossover compounds based on iron(II) complexes of 2,6-bis(pyrazol-1-yl)pyridine (bpp) functionalized with carboxylic acid and ethyl carboxylic acid" *Dalton Transactions*, vol. 47, no. 47, **2018**, doi: 10.1039/c8dt03511c.

2.1. Motivation

Being able to control bistable nanostructures at the molecular level assures a breakthrough in applications such as memory and data storage devices. For that, SCO complexes have been in the spotlight since their two distinct states are reachable through application of external forces. Prior to integration into devices, deposition on solid surfaces is a mandatory step.

As mentioned in Chapter 1, over the past decade, ultra-high vacuum deposition of SCO neutral molecules has been the main route to get deposits of nanostructured assemblies of Fe(II), while wet chemistry protocols have been less explored. Apart from the work of Devid *et. al.* (see Chapter 1),^[1] other authors (L. Pukenas^[2] and I. Capell^[3]) tried to construct SAMs of Fe(II) 1bpp derivatives from solution onto surfaces, unfortunately the results were unsuccessful. Led by this lack of scientific background, we look for improvement in the SAM formation by the synthesis of new SCO molecules. In a previous work, our group prepared the Fe(II) complex of 1bpp ligand functionalized with a carboxylic acid (1bppCOOH, see **Scheme 2.1.1**).^[4] This resulted in the SCO compound $[\text{Fe}(\text{1bppCOOH})_2](\text{ClO}_4)_2$, which formed an extended 1D network built via hydrogen-bond intermolecular interactions. This led to an abrupt spin transition with $T_{1/2}$ of ca. 380 K and a $T(\text{LIESST})$ of 60 K.



Scheme 2.1.1. Schematic representation of 2,6-bis(pyrazol-1-yl)pyridine-4-carboxylic acid (1bppCOOH) and ethyl 2,6-bis(pyrazol-1-yl)pyridine-4-carboxylate (1bppCOOEt) ligands.

In this chapter, we have completed the structural and photomagnetic characterization of $[\text{Fe}(\text{1bppCOOH})_2](\text{ClO}_4)_2$ (**1(ClO₄)₂**) and prepared and characterized new salts of the $[\text{Fe}(\text{1bppCOOH})_2]^{2+}$ complex with BF_4^- , CF_3SO_3^- , SbF_6^- and AsF_6^- counteranions. Moreover, we have prepared the Fe(II) complex of the ethyl ester derivative of 1bppCOOH (1bppCOOEt, see

Scheme 2.1.1) in compound $[\text{Fe}(\text{1bppCOOEt})_2](\text{ClO}_4)_2 \cdot y\text{Me}_2\text{CO}$ (**2(ClO₄)₂·yMe₂CO**). This has led to a variety of SCO behaviors, which could help to understand the role played by the carboxylic acid group and that of the intermolecular interactions, solvent molecules, and counteranions in the SCO properties of this family of compounds. Then, we have taken advantage of the well-known affinity of the carboxylic acid group^[5] to metal oxide surfaces to try to form SAMs on SiO₂. Characterization of these SAMs will be discussed.

2.2. Results and discussion

Herein, we describe the synthesis and characterization of **1(X)₂·yMe₂CO** {1 = $[\text{Fe}(\text{1bppCOOH})_2]^{2+}$, X = ClO₄⁻, BF₄⁻, CF₃SO₃⁻, AsF₆⁻, SbF₆⁻} and **2(ClO₄)₂·yMe₂CO** {2 = $[\text{Fe}(\text{1bppCOOEt})_2]^{2+}$ }.

Synthesis of the compounds

Both ligands were synthesized following previously reported procedures.^[6,7] Compounds **1(ClO₄)₂**, **1(BF₄)₂**, **1(CF₃SO₃)₂·yMe₂CO**, and **2(ClO₄)₂·yMe₂CO** were synthesized by slow diffusion of diethyl ether into solutions of Fe(II) salts and the corresponding ligand in a 1:2 molar ratio in acetone. **1(AsF₆)₂·yMe₂CO** and **1(SbF₆)₂·yMe₂CO** were obtained in the same manner, but the Fe(II) salt was prepared *in situ* by metathesis of the FeCl₂ salt with AgAsF₆ or AgSbF₆ in a 1:2 molar ratio (for more details see SI).

*Structure of $[\text{Fe}(\text{1bppCOOH})_2](\text{ClO}_4)_2$ (**1(ClO₄)₂**) and $[\text{Fe}(\text{1bppCOOH})_2](\text{BF}_4)_2$ (**1(BF₄)₂**)*

1(ClO₄)₂ and **1(BF₄)₂** crystallize in a monoclinic crystal system with a centrosymmetric C2/c space group. The asymmetric unit is formed by half $[\text{Fe}(\text{1bppCOOH})_2]^{2+}$ cation and one perchlorate or tetrafluoroborate anion. The central Fe(II) of the complex is coordinated by six nitrogen atoms from two tridentate 1bppCOOH ligands with a distorted octahedral coordination geometry. The Fe-N bond lengths at 120 K are indicative that the complexes are in the LS state (1.888(4) - 1.981(2) Å for **1(ClO₄)₂** and 1.889(3) - 1.974(6) Å for **1(BF₄)₂**), whereas the longer Fe-N bond lengths at higher temperatures indicate that they are in the HS state (2.113(6) - 2.159(5) Å for **1(ClO₄)₂** at 400K and 2.111(6) - 2.171(3) Å for **1(BF₄)₂** at 350 K). This suggests that the HS state of **1(BF₄)₂** is reached at lower temperatures, in agreement with the magnetic properties (see below). The coordination geometry is close to the ideal D_{2d} symmetry associated with a $[\text{Fe}(\text{1bpp})_2]^{2+}$ center at both temperatures. Thus, a trans-N(pyridyl)-Fe-N(pyridyl) angle (ϕ) of 180° and a dihedral angle between the least squares planes of the two ligands (θ) of 87° at 120 K and

89° at 400 K for **1(ClO₄)₂** and 88° at 120 K and 89° at 350 K for **1(BF₄)₂** are consistent with those of the other 1bpp complexes exhibiting spin crossover.^[8–10]

The crystal packing of the complexes is very similar at the two temperatures. In both cases, neighboring [Fe(1bppCOOH)₂]²⁺ cations are linked through hydrogen bonds between the carboxylic acid groups (dO1...O2 = 2.671 Å at 120 K and dO1...O2 = 2.732 Å at 400 K for **1(ClO₄)₂** and dO1...O2 = 2.676 Å at 120 K and dO1...O2 = 2.724 Å at 350 K for **1(BF₄)₂**, **Figure 2.2.1**), forming chains that run along the *b* axis. These chains present numerous short contacts involving CH groups from pyrazole and pyridine groups with ClO₄[−] or BF₄[−] counteranions. These chains are linked through intermolecular interactions that involve oxygen atoms from a carboxylic acid group and C atoms from a pyrazole group (see **Figure SI. 2.4.1**, **Figure SI. 2.4.2** and **Figure SI. 2.4.3** and associated text in the SI). O and F atoms from ClO₄[−] (**1(ClO₄)₂**) and BF₄[−] (**1(BF₄)₂**) are disordered at 400 and 350 K, respectively. These disorders have been solved considering eight O or F atoms with a 50% occupancy. Then, we can conclude that the presence of the carboxylic acid groups may cause a different packing to the “terpyridine embrace” crystal packing motif found in many salts of [Fe(bpp)₂]²⁺ and derivatives, which is a four-fold layer formed by π...π and edge to face CH...π interactions between pyrazole groups of neighboring molecules.^[8–10]

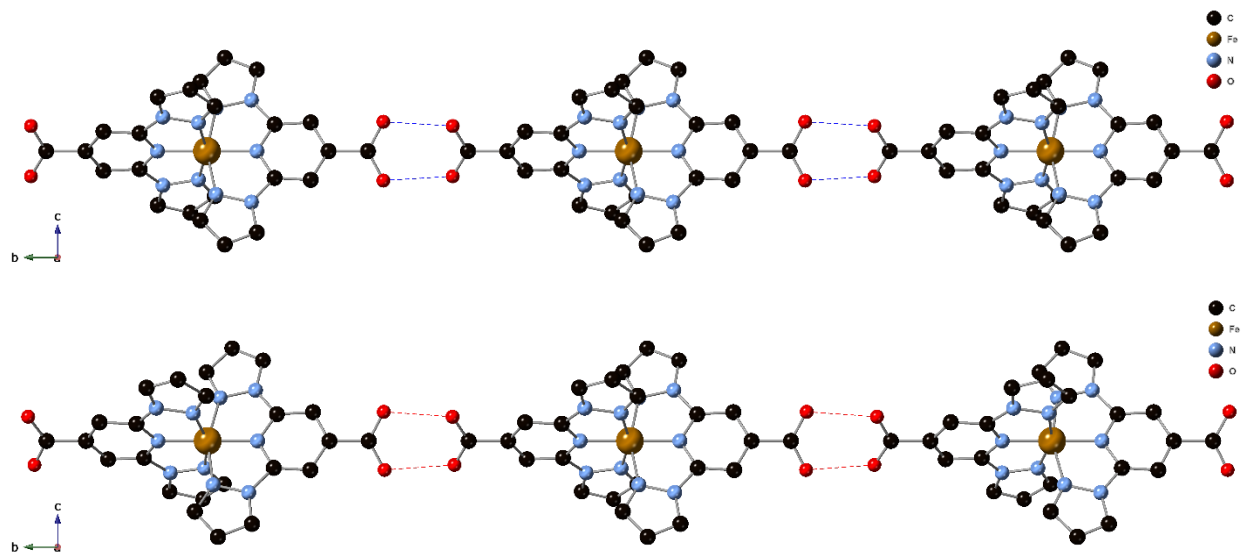


Figure 2.2.1. Chain of hydrogen-bonded [Fe(1bppCOOH)₂]²⁺ complexes in the structure of **1(ClO₄)₂** (top) and **1(BF₄)₂** (bot) at 120 K. Hydrogen atoms have been omitted for clarity.

Changes in the parameters of the unit cell with the temperature measured by single-crystal X-ray diffraction of the two salts are consistent with an abrupt spin transition. The most relevant change is an abrupt increase of the *b* parameter above 380 K for **1(ClO₄)₂** and 340 K for **1(BF₄)₂**

(see **Figure SI. 2.4.4**) which correspond to the direction of the hydrogen-bonded chains (see above). On the other hand, a and c parameters and the unit cell volume of $\mathbf{1}(\text{ClO}_4)_2$ are higher than those of $\mathbf{1}(\text{BF}_4)_2$, in agreement with the smaller size of BF_4^- counteranion (see crystallographic tables in the SI). In contrast to this, the b parameters of the two compounds in the LS and HS states are very close. This indicates that the hydrogen-bonded chains of the complexes, which run in this direction, are very similar in the two compounds.

Variable-temperature powder X-ray diffraction (PXRD) measurements of $\mathbf{1}(\text{ClO}_4)_2$ were performed between 400 and 298 K. The most notable change is the shift to lower 2θ values of the intense diffraction peaks near 15 and 18.5° at increasing temperature (see **Figure SI. 2.4.5** and

Figure SI. 2.4.6 in the SI). As the position of these peaks changes just below and above the temperature of the spin transition ($T_{1/2}\uparrow = 384$ K) (see patterns at 380 and 390 K in **Figure SI. 2.4.6**), they correspond to the LS and HS phases. This is confirmed by the pattern measured at an intermediate temperature of 385 K (

Figure SI. 2.4.6), which shows that the LS and HS peaks coexist in agreement with the magnetic properties (see below). PXRD pattern of $\mathbf{1}(\text{BF}_4)_2$ at 298 K is consistent with the structure solved at 120 K (see **Figure SI. 2.4.7**).

Structure of $[\text{Fe}(\text{1bppCOOH})_2](\text{CF}_3\text{SO}_3)_2 \cdot y\text{Me}_2\text{CO}$ ($\mathbf{1}(\text{CF}_3\text{SO}_3)_2 \cdot y\text{Me}_2\text{CO}$)

The structure of $\mathbf{1}(\text{CF}_3\text{SO}_3)_2 \cdot y\text{Me}_2\text{CO}$ was solved by performing single-crystal X-ray diffraction at 120 K of a crystal transferred directly to the cold nitrogen stream of the diffractometer from the mother liquor and at 300 K of another crystal that was previously filtered and stored in air. In both cases, they crystallize in the orthorhombic system with the centrosymmetric $Pcab$ space group. The asymmetric unit is constructed by one $[\text{Fe}(\text{1bppCOOH})_2]^{2+}$ cation, two CF_3SO_3^- anions and one or half acetone solvent molecule at 120 K or 300 K, respectively (see **Figure SI. 2.4.8** in the SI). Therefore, the compound can be formulated as $[\text{Fe}(\text{1bppCOOH})_2](\text{CF}_3\text{SO}_3)_2 \cdot \text{Me}_2\text{CO}$ at 120 K and $[\text{Fe}(\text{1bppCOOH})_2](\text{CF}_3\text{SO}_3)_2 \cdot 0.5\text{Me}_2\text{CO}$ at 300 K. Fe-N bond distances lie in the range of 1.892(2) - 1.968(3) Å at 120 K and 1.897(2) - 1.970(3) at 300 K, typical distances for a LS configuration, which are in agreement with magnetic properties (see below). Neighboring $[\text{Fe}(\text{1bppCOOH})_2]^{2+}$ cations are linked through hydrogen bonds involving the oxygen atoms from the carboxylic acid groups ($d_{\text{O1}\cdots\text{O4}} = 2.673$ Å at 120 K and $d_{\text{O1}\cdots\text{O4}} = 2.694$ Å at 300 K), forming a zigzag chain that runs along the b axis (**Figure 2.2.2**). The free OH group forms a hydrogen bond with a triflate counteranion ($d_{\text{O2}\cdots\text{O8}} = 2.638$ Å at 120

K and $d_{O2 \cdots O9} = 2.654 \text{ \AA}$ at 300 K). These chains are connected through $CH \cdots \pi$ interactions, which involve CH groups from pyrazole and pyridine rings, and they present numerous short contacts with the surrounding $CF_3SO_3^-$ anions and Me_2CO solvent molecules (**Figure SI. 2.4.9**). Such molecules are not involved in any hydrogen bond. The crystallinity of a single crystal of this compound is maintained up to 380 K. Above this temperature, the crystal loses its crystallinity and a change in color from red-orange to yellow is observed, and with it, the spin state also changes from LS to HS, in agreement with the magnetic properties (see below). Interestingly, by placing the crystals under an atmosphere saturated in acetone, it is possible to recover the red-orange color and, therefore, the LS state. PXRD pattern at room temperature is consistent with that of the simulated one obtained from the single-crystal X-ray diffraction structure at 300 K. After desolvation, PXRD pattern of the yellow crystals changes completely with respect to the solvated ones, indicating that a new phase is obtained. PXRD pattern of the resolvated sample confirms the recovery of the initial solvated phase (see **Figure SI. 2.4.10** in the SI). Therefore, the loss of half of the acetone solvent molecules from 120 to 300 K does not induce important changes in the structure, while the complete removal of the acetone solvent molecules at higher temperatures leads to a drastic change in the structure, which is reversible. Thermogravimetric (TG) analysis shows a weight decrease of *ca.* 2% below 350 K (see **Figure SI. 2.4.11** in the SI). This weight loss is lower than the expected one for 0.5 acetone molecules found in the structure of the filtered sample (expected weight loss of *ca.* 3%), indicating a higher loss of solvent molecules after extracting the crystals from the mother liquor.

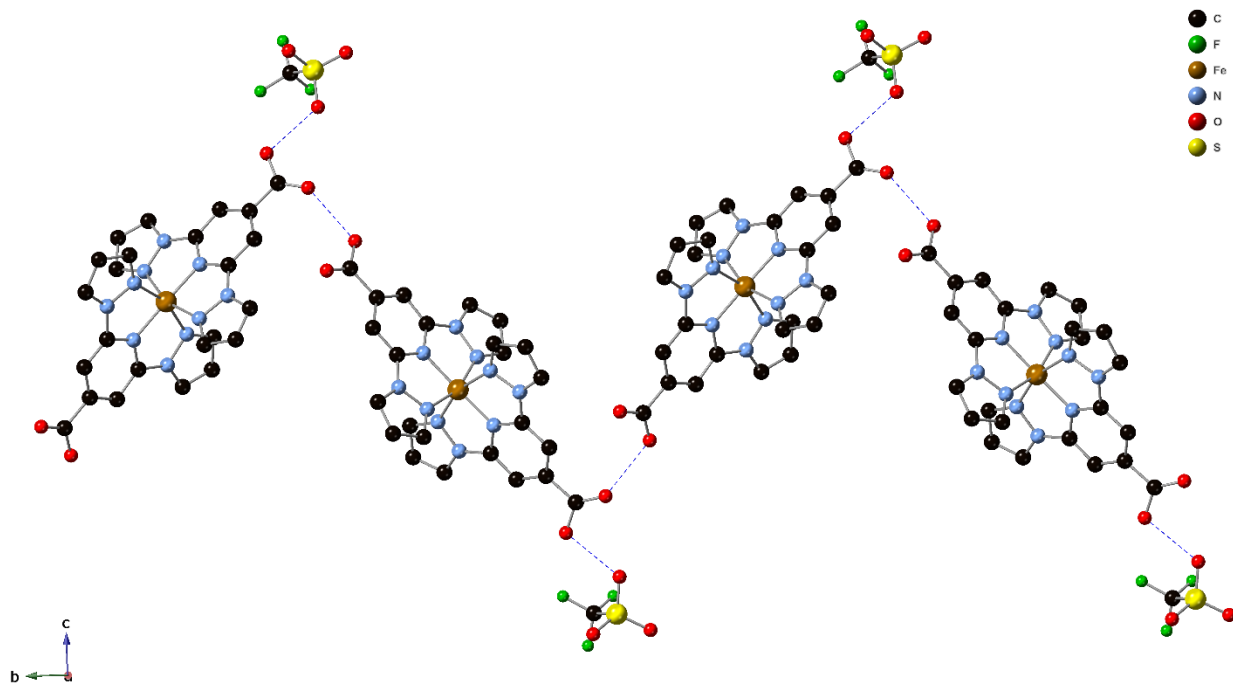


Figure 2.2.2. Hydrogen-bonded $[\text{Fe}(\text{1bppCOOH})_2]^{2+}$ complexes and triflate anions in the structure of $\mathbf{1}(\text{CF}_3\text{SO}_3)_2 \cdot y\text{Me}_2\text{CO}$ at 120 K. Hydrogen atoms have been omitted for clarity.

Structure of $[\text{Fe}(\text{1bppCOOH})_2](\text{AsF}_6)_2 \cdot y\text{Me}_2\text{CO}$ ($\mathbf{1}(\text{AsF}_6)_2 \cdot y\text{Me}_2\text{CO}$) and $[\text{Fe}(\text{1bppCOOH})_2](\text{SbF}_6)_2 \cdot y\text{Me}_2\text{CO}$ ($\mathbf{1}(\text{SbF}_6)_2 \cdot y\text{Me}_2\text{CO}$)

The crystal structure of these two compounds was solved by single-crystal X-ray diffraction of crystals transferred directly to the cold nitrogen stream of the diffractometer from the mother liquor at 120 K and then at 300 K. Both crystallize in the tetragonal system with the non-centrosymmetric $I4_1cd$ space group. The asymmetric unit cell is composed by half $[\text{Fe}(\text{1bppCOOH})_2]^{2+}$ cation, one AsF_6^- or SbF_6^- anion and one or half acetone solvent molecule at 120 K or 300 K, respectively (see **Figure 2.2.3**). Therefore, they can be formulated as $\text{Fe}(\text{1bppCOOH})_2(\text{AsF}_6)_2 \cdot 2\text{Me}_2\text{CO}$ or $[\text{Fe}(\text{1bppCOOH})_2](\text{SbF}_6)_2 \cdot 2\text{Me}_2\text{CO}$ at 120 K and $\text{Fe}(\text{1bppCOOH})_2(\text{AsF}_6)_2 \cdot \text{Me}_2\text{CO}$ or $[\text{Fe}(\text{1bppCOOH})_2](\text{SbF}_6)_2 \cdot \text{Me}_2\text{CO}$ at 300 K. Fe-N bond lengths lie in the range of 1.892(4) - 1.977(5) Å at 120 K and 1.917(8) - 1.997(10) Å at 300 K for $\mathbf{1}(\text{AsF}_6)_2 \cdot y\text{Me}_2\text{CO}$ and 1.898(4) - 1.979(5) Å at 120 K and 1.937(12) - 2.023(14) Å at 300 K for $\mathbf{1}(\text{SbF}_6)_2 \cdot y\text{Me}_2\text{CO}$. These are the typical distances of a LS configuration, but the increase in bond lengths with the temperature indicates that a fraction of HS molecules is increasing with temperature, being higher for $\mathbf{1}(\text{SbF}_6)_2 \cdot y\text{Me}_2\text{CO}$, in agreement with the magnetic properties (see below). Neighboring $[\text{Fe}(\text{1bppCOOH})_2]^{2+}$ cations are not linked through hydrogen bonds, as in the previous salts. Their OH groups are involved in hydrogen bonds with carbonyl groups from the

two neighboring acetone solvent molecules (**Figure 2.2.3**). Neighboring $[\text{Fe}(\text{1bppCOOH})_2]^{2+}$ cations present $\text{CH}\cdots\pi$ contacts involving the pyrazole rings giving rise to chains that run along the *c* axis (**Figure SI. 2.4.12** in the SI and the associated text) surrounded by AsF_6^- or SbF_6^- anions and acetone molecules (**Figure SI. 2.4.13**). F atoms from AsF_6^- are disordered at 300 K. This disorder has been solved by considering twelve F atoms with a 50% occupancy. PXRD patterns of the two compounds at room temperature are consistent with those of the simulated ones obtained from the single-crystal X-ray diffraction structure at 300 K (see **Figure SI. 2.4.14** and **Figure SI. 2.4.15** in the SI). Desolvation by heating at 400 K leads to a color change from red-orange to dark red and a completely different PXRD pattern with respect to the solvated ones, indicating that a new phase is obtained. As in $\mathbf{1}(\text{CF}_3\text{SO}_3)_2\cdot\mathbf{yMe}_2\text{CO}$, PXRD pattern confirms that the initial solvated phase is recovered after contact of the desolvated crystals with acetone vapors (see **Figure SI. 2.4.14** and **Figure SI. 2.4.15**). TG analysis of freshly prepared samples of $\mathbf{1}(\text{AsF}_6)_2\cdot\mathbf{yMe}_2\text{CO}$ and $\mathbf{1}(\text{SbF}_6)_2\cdot\mathbf{yMe}_2\text{CO}$ shows a weight decrease of around 6% and 5%, respectively, in two steps from 300 to 400 K. This decrease is consistent with the expected one for one acetone molecule found in the structure at 300 K (expected weight loss of 5.7% for $\mathbf{1}(\text{AsF}_6)_2\cdot\mathbf{yMe}_2\text{CO}$ and 5.3% for $\mathbf{1}(\text{SbF}_6)_2\cdot\mathbf{yMe}_2\text{CO}$, see **Figure SI. 2.4.16** and **Figure SI. 2.4.17** in the SI). The temperatures of these weight losses are lower than those of the compound $\mathbf{1}(\text{CF}_3\text{SO}_3)_2\cdot\mathbf{yMe}_2\text{CO}$, in agreement with the lack of hydrogen bonds of the acetone molecules of this last compound.

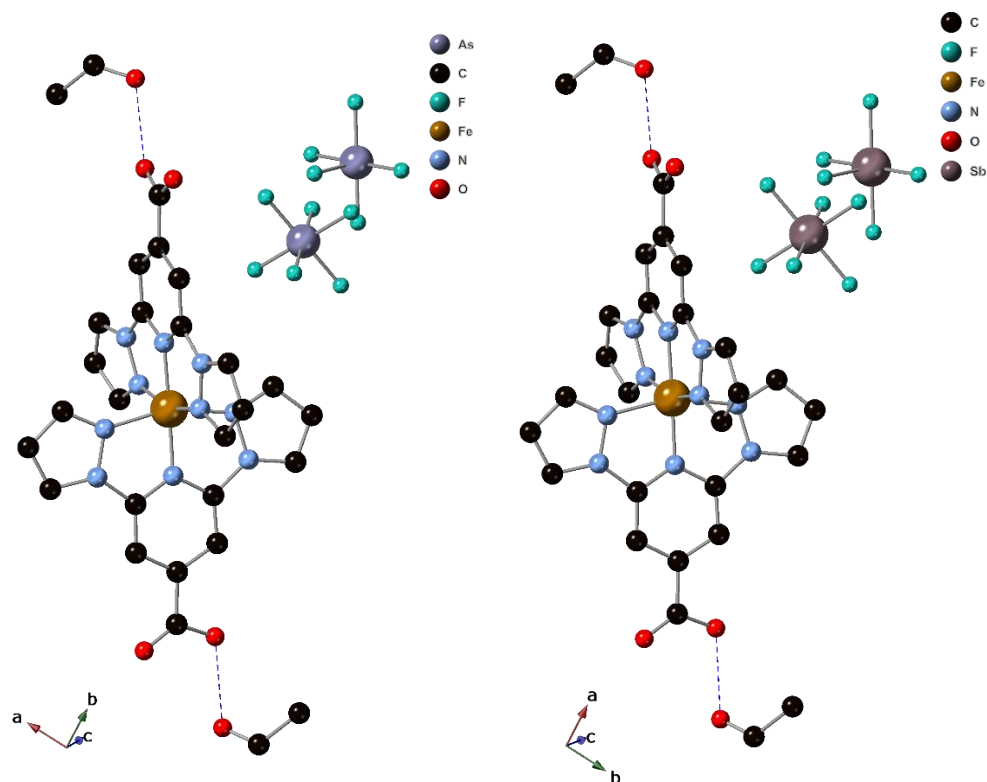


Figure 2.2.3. Hydrogen bonds (blue-dashed lines) between $[\text{Fe}(\text{1bppCOOH})_2]^{2+}$ complexes and acetone molecules in the structure of, **1(AsF₆)₂·yMe₂CO** (left) and **1(SbF₆)₂·yMe₂CO** (right) at 120 K. Hydrogen atoms have been omitted for clarity.

In contrast to this, elemental analyses of both compounds in older samples are more consistent with the presence of one acetone and one water molecule. This could suggest the absorption of water molecules after filtering the crystals. Elemental analysis of the desolvated samples after heating at 400 K confirms the complete loss of the solvent molecules (see SI).

*Structure of $[\text{Fe}(\text{1bppCOOEt})_2](\text{ClO}_4)_2 \cdot y\text{Me}_2\text{CO}$ (**2(ClO₄)₂·yMe₂CO**)*

Single-crystal X-ray diffraction was performed on **2(ClO₄)₂·yMe₂CO** at 120 and 300 K. At both temperatures, the compound crystallizes in a triclinic crystal system with a centrosymmetric *P*-1 space group. The asymmetric unit is composed by two $[\text{Fe}(\text{1bppCOOEt})_2]^{2+}$ cations, five perchlorate anions (two of them disordered with an occupancy of 0.5) and three acetone molecules (with an occupancy of 0.5 at 300 K) (see **Figure 2.2.4**). Therefore, this compound can be formulated as $[\text{Fe}(\text{1bppCOOEt})_2](\text{ClO}_4)_2 \cdot 1.5\text{Me}_2\text{CO}$ at 120 K and $[\text{Fe}(\text{1bppCOOEt})_2](\text{ClO}_4)_2 \cdot 0.75\text{Me}_2\text{CO}$ at 300 K. Elemental analysis at 300 K is more consistent with two water molecules, suggesting a complete loss of acetone solvent molecules after

extracting the crystals from the mother liquor and replacement with water molecules, or the coexistence of crystals with a different degree of desolvation (see the SI). Fe(II) ions present a distorted octahedral coordination geometry to 1bppCOOEt ligands similar to that of $[\text{Fe}(\text{1bppCOOH})_2]^{2+}$. Fe–N bond lengths at 120 K (1.889(3) - 1.975(4) and 1.893(3) - 1.974(4) Å) and at 300 K (1.889(5) - 1.977(6) and 1.880(5) - 1.987(6) Å) indicate that the complexes are in the LS state, in agreement with the magnetic measurements (see below). The coordination geometry is close to the ideal D_{2d} symmetry at the two temperatures. Thus, ϕ angles of 177.36(15) and 178.77(15)° at 120 K and 178.7(2) and 179.7(2)° at 300 K, and θ angles close to 85° at 120 K and 86° at 300 K are obtained. These values are in contrast with those reported for the Fe(II) complex of the methyl ester derivative of 1bppCOOH (1bppCOOMe) ($\phi = 158.77(5)^\circ$ and $\theta = 80.738(12)^\circ$),^[11] which is HS from 2 to 300 K. This confirms that a coordination geometry close to the ideal D_{2d} symmetry favors the LS state and SCO,^[9] also consistent with $1(\text{ClO}_4)_2$ and $1(\text{BF}_4)_2$.

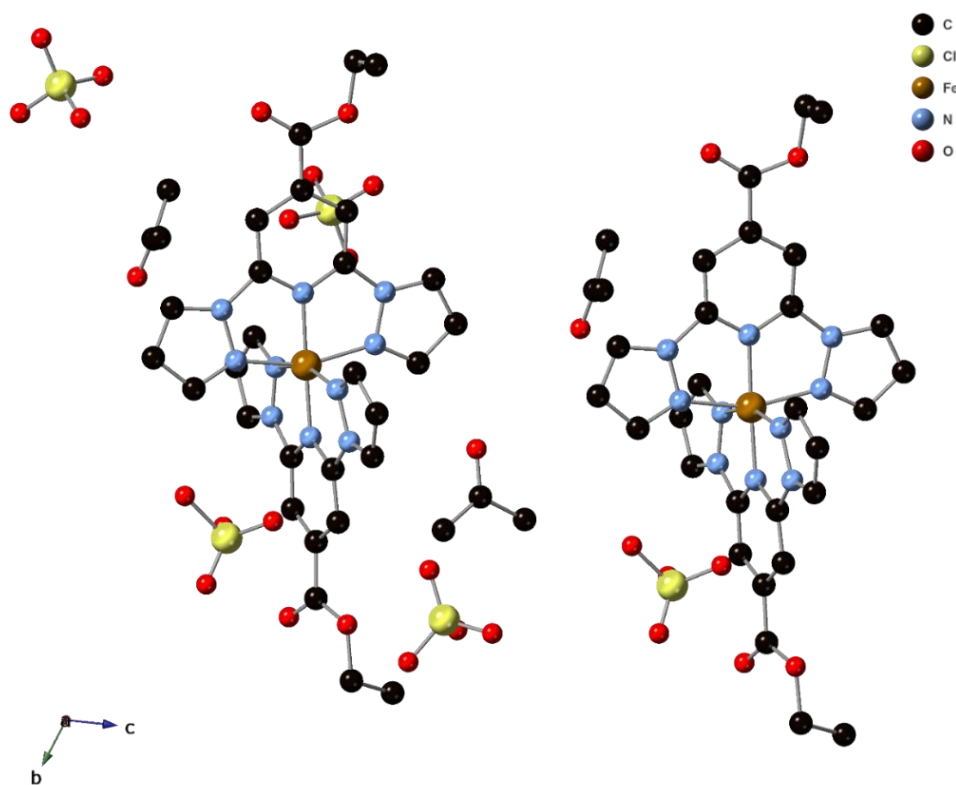


Figure 2.2.4. Projection in the bc plane of the structure of $2(\text{ClO}_4)_2 \cdot y\text{Me}_2\text{CO}$ at 120 K.

The crystal packing of $2(\text{ClO}_4)_2 \cdot y\text{Me}_2\text{CO}$ at the two temperatures is very different to that of $[\text{Fe}(\text{1bppCOOH})_2]^{2+}$ salts (**Figure SI. 2.4.18**). On one hand, oxygen atoms from the carboxyethyl ester group of $[\text{Fe}(\text{1bppCOOEt})_2]^{2+}$ complexes cannot form hydrogen bonds. On the other hand, the presence of the bulky ethyl group prevents the formation of the “terpyridine embrace” crystal

packing motif. Thus, neighboring $[\text{Fe}(\text{1bppCOOEt})_2]^{2+}$ complexes interact through numerous short contacts involving CH groups of pyrazole and pyridine rings, CO groups or CH_2 and CH_3 groups. This leads to a complicated network of weak intermolecular interactions that include many interactions with perchlorate counteranions and acetone solvent molecules. It was not possible to solve the structure at higher temperatures due to the loss of crystallinity after the evaporation of the solvent molecules. PXRD patterns from 300 to 340 K are consistent with that obtained from the single-crystal X-ray diffraction structure at 300 K but, at higher temperatures, a change of phase is observed (see **Figure SI. 2.4.19**). The initial solvated phase cannot be recovered after re-solvation in contrast to $[\text{Fe}(\text{1bppCOOH})_2]^{2+}$ salts. Elemental analysis of the desolvated sample is consistent with the presence of one water molecule. This could indicate the absorption of water from the desolvated sample (see SI).

Magnetic and photomagnetic properties

Temperature dependence of the product of the magnetic susceptibility times temperature ($\chi_{\text{M}}T$) of all the $[\text{Fe}(\text{1bppCOOH})_2]^{2+}$ salts together with that previously reported **1(ClO₄)₂**^[4] are shown in **Figure 2.2.5**.

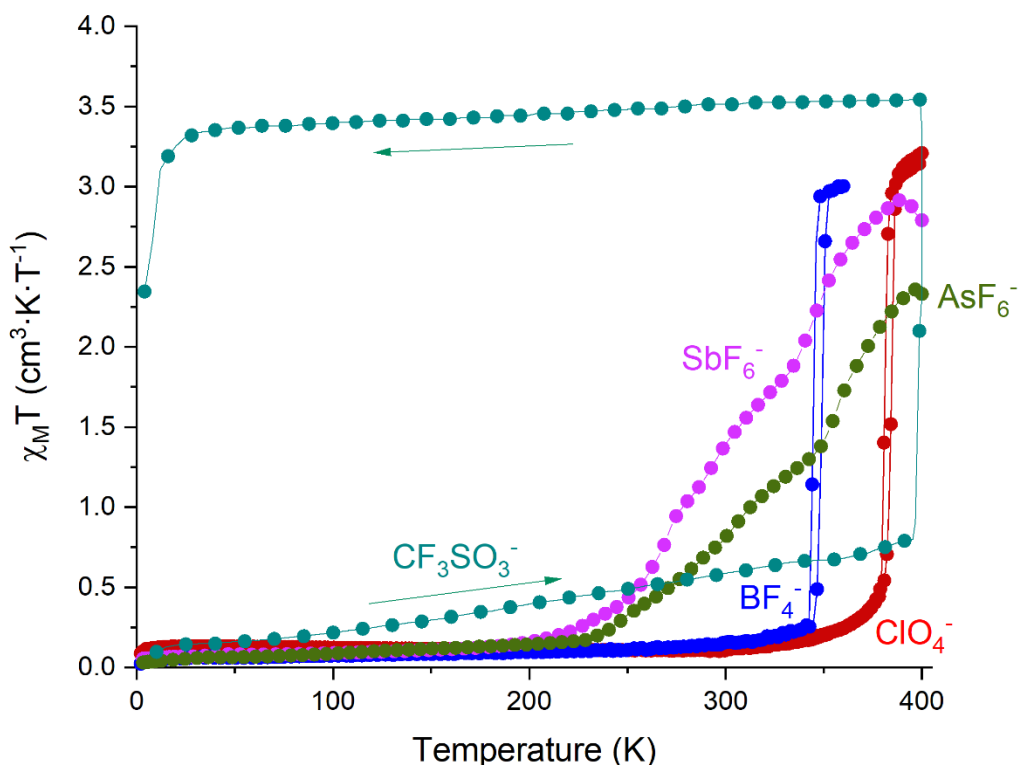


Figure 2.2.5. Thermal dependence of magnetic susceptibility times temperature ($\chi_{\text{M}}T$) of **1(ClO₄)₂** (red circles), **1(BF₄)₂** (blue circles), **1(CF₃SO₃)₂·yMe₂CO** (turquoise circles), **1(AsF₆)₂·yMe₂CO** (green circles) and **1(SbF₆)₂·yMe₂CO** (pink circles).

$\chi_{\text{M}}T$ product of **1(ClO₄)₂** and **1(BF₄)₂** show a constant value of *c.a.* 0 cm³·K·mol⁻¹ below 300K, consistent with the diamagnetic LS state ($S = 0$), in good agreement with the Fe-N bond distances from the crystallographic data at 120 K of both compounds. Above 340 K for **1(BF₄)₂** and 380 K for **1(ClO₄)₂**, $\chi_{\text{M}}T$ increases sharply reaching values of 3.0 and 3.2 cm³·K·mol⁻¹ at 350 K and 390 K, respectively, consistent with an almost complete LS to HS conversion. Both compounds present the same behavior in the heating and cooling modes with a small thermal hysteresis of 3 K ($T_{1/2\uparrow} = 349$ K and $T_{1/2\downarrow} = 345$ K for **1(BF₄)₂** and $T_{1/2\uparrow} = 384$ K and $T_{1/2\downarrow} = 381$ K for **1(ClO₄)₂**). The presence of this thermal hysteresis loop is indicative of the existence of a significant level of cooperativity between neighboring $[\text{Fe}(\text{1bppCOOH})_2]^{2+}$ complexes due to the presence of intermolecular interactions mediated by the hydrogen bonds. After irradiation with 532 nm at 10 K, a quantitative LS to HS photoconversion was observed in **1(ClO₄)₂** and **1(BF₄)₂** (see **Figure 2.2.6**). The drastic increase of the magnetic signal was observed until 60 K for **1(ClO₄)₂** and 67 K for **1(BF₄)₂** followed by an abrupt relaxation curve.

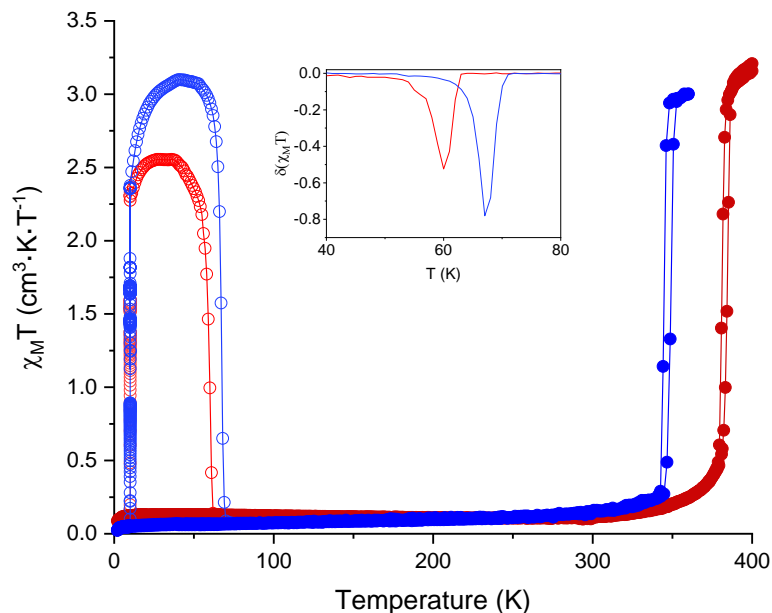


Figure 2.2.6. Thermal variation of $\chi_M T$ of **1(ClO₄)₂** (red) and **1(BF₄)₂** (blue). Full dots: data recorded without irradiation; empty dots: data recorded after irradiation at 10 K. The inset graph shows the temperature dependence of the first derivative of $\chi_M T$ with respect to the temperature.

In order to obtain some insights into the decay of the photoexcited state, the kinetics of relaxation of **1(ClO₄)₂** was recorded for different temperatures (see **Figure SI. 2.4.20** in the SI and the associated text). The decay of the photoinduced HS state of this compound is faster at high temperatures, consistent with a thermally activated process. It can also be observed that the decay is not exponential. The kinetics has been fitted using the so-called sigmoidal law. This law describes a self-accelerated process, often associated with cooperative systems. This cooperativity arises from the large difference in metal–ligand bond lengths, resulting in elastic interactions caused by the change in internal pressure as the spin transition proceeds.^[12,13] In a recent article, Paulsen and coworkers have been able to derive a cooperativity parameter using DFT *ab initio* calculations.^[14] As a result of these calculations, the degree of cooperativity in the two solvatomorphs, Fe(pic)₃Cl₂·EtOH (abrupt transition) and Fe(pic)₃Cl₂·MeOH (gradual transition), was recovered. Cooperativity and degree of octahedrity of Fe centers have been linked, emphasizing that the difference in metal–ligand bond lengths is not the only factor governing cooperativity. Magnetization under irradiation of **1(ClO₄)₂** as a function of the temperature has been recorded. More precisely, the temperature was decreased continuously from 100 K to 10 K under continuous irradiation (532 nm). The temperature was then re-increased up to 100 K, still under irradiation (see **Figure SI. 2.4.21** and **Figure SI. 2.4.22** in the SI and the

associated text). A clear light-induced thermal hysteresis (LITH)^[15] is observed below 70 K. Else, this compound then seems to be cooperative enough to present a static LITH.

$\chi_{\text{M}}T$ values of **1(CF₃SO₃)₂-yMe₂CO** are consistent with the LS state below 350K as suggested by Fe-N bond lengths at 120 K and 300 K (see above). In the warming mode, an increasing residual HS fraction appears probably due to desolvation of part of the crystals (**Figure SI. 2.4.10**). Above 350 K, $\chi_{\text{M}}T$ shows a sharp increase to reach the characteristic value of 3.5 cm³·K·mol⁻¹, consistent with 100% of complexes in the HS state. This increase is irreversible as $\chi_{\text{M}}T$ remains constant from 400 to 30 K, the decrease below 30 K is due to zero-field splitting as expected for a HS d⁶ Fe(II). This could indicate that the spin transition of this compound is related to the structural changes after losing the solvent molecules, in agreement with the change of color, PXRD measurements and TG measurements (see SI). Interestingly, the solvated form of this complex also shows LIESST effect. $\chi_{\text{M}}T$ showed an abrupt increase after photoirradiation at 10K and the signal is maintained until 41 K where the signal drops sharply (see **Figure 2.2.7**).

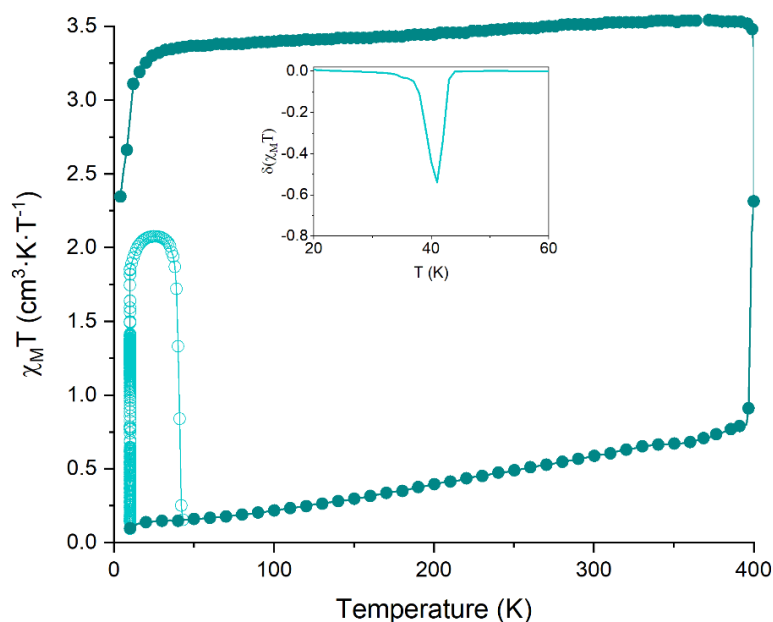


Figure 2.2.7. Thermal variation of $\chi_{\text{M}}T$ for **1(CF₃SO₃)₂-yMe₂CO** (turquoise). Full dots: data recorded without irradiation; empty dots: data recorded after irradiation at 10 K. The inset graph shows the temperature dependence of the first derivative of $\chi_{\text{M}}T$ with respect to the temperature.

Temperature dependence of $\chi_{\text{M}}T$ product of **1(AsF₆)₂-yMe₂CO** and **1(SbF₆)₂-yMe₂CO** shows a value close to 0 cm³·K·mol⁻¹ in the 2 - 200 K temperature range. At higher temperatures, a gradual increase of $\chi_{\text{M}}T$ takes place to reach c.a. 2.4 cm³·K·mol⁻¹ at 395 K for **1(AsF₆)₂-yMe₂CO** and 2.9 cm³·K·mol⁻¹ at 390 K for **1(SbF₆)₂-yMe₂CO**, indicating a gradual spin

transition (**Figure 2.2.8**). This is consistent with the Fe-N bond lengths at 120 and 300 K obtained from the structures (see above). The temperature of the steps observed in $\chi_M T$ overlaps with those of the weight loss seen in the TG analysis (see **Figure SI. 2.4.16** and **Figure SI. 2.4.17** in the SI). Therefore, it is not possible to determine whether they are related to a pure spin transition or desolvation. The presence of an intermediate phase by partial loss of acetone solvent molecules at the steps around 340 K for **1(AsF₆)₂·yMe₂CO** and 330 K for **1(SbF₆)₂·yMe₂CO** in this first heating is discarded. On one hand, single-crystal unit cell measurements from 300 to 400 K show a progressive decrease in unit cell volume and loss of crystallinity with time, but they do not show a drastic change in the unit cell. On the other hand, PXRD patterns of **1(AsF₆)₂·yMe₂CO** and **1(SbF₆)₂·yMe₂CO** only show a clear change of phase at temperatures close to 400 K (see **Figure SI. 2.4.14** and **Figure SI. 2.4.15** in the SI). In these two compounds, the complete loss of acetone molecules at higher temperatures leads to a decrease of $\chi_M T$ above 395 K for **1(AsF₆)₂·yMe₂CO** and 385 K for **1(SbF₆)₂·yMe₂CO**, to reach 2.0 cm³·K·mol⁻¹ and 2.5 cm³·K·mol⁻¹ at 400 K, respectively. $\chi_M T$ of the desolvated compounds, obtained in the cooling mode after heating to 400 K, decreases gradually to reach values below to 0.5 cm³·K·mol⁻¹ from 345 K for **1(AsF₆)₂·yMe₂CO** and 295 K for **1(SbF₆)₂·yMe₂CO** to 2 K (see **Figure SI. 2.4.23** in the SI) with a $T_{1/2}$ of 385 K for **1(AsF₆)₂·yMe₂CO** and 355 K for **1(SbF₆)₂·yMe₂CO**.

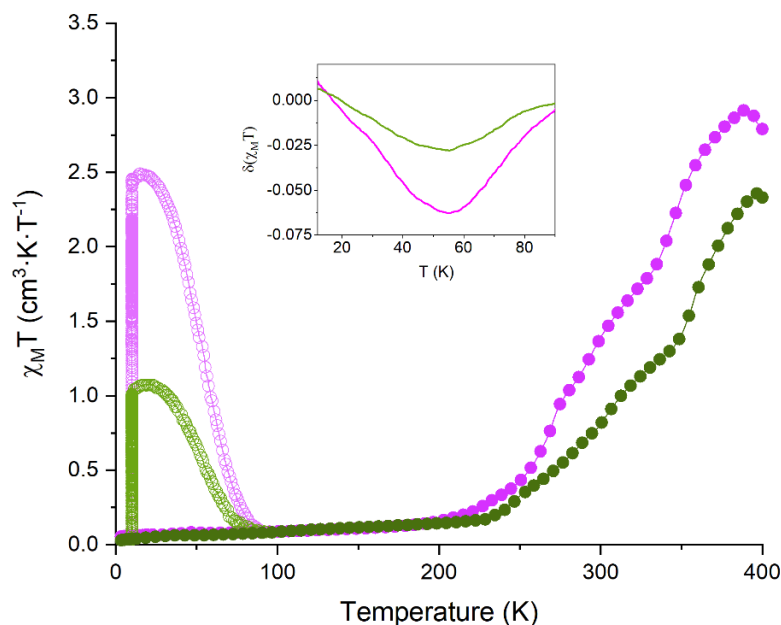


Figure 2.2.8. Thermal variation of $\chi_M T$ of **1(AsF₆)₂·yMe₂CO** (green) and **1(SbF₆)₂·yMe₂CO** (pink). Full dots: data recorded without irradiation; empty dots: data recorded after irradiation at 10 K. The inset graph shows the temperature dependence of the first derivative of $\chi_M T$ with respect to the temperature.

Desolvation in the two compounds decreases the HS fraction above 250 K but does not cause drastic changes in the magnetic behavior. Thus, gradual spin transitions are still observed in the desolvated phases with a higher HS fraction for **1(SbF₆)₂·yMe₂CO** than for **1(AsF₆)₂·yMe₂CO** (see **Figure SI. 2.4.23**). **Figure 2.2.8** shows that both complexes also present LIESST effect with a $T(\text{LIESST})$ of 54 K for **1(AsF₆)₂·yMe₂CO** and 57 K for **1(SbF₆)₂·yMe₂CO** with photoconversions close to 30% and 70% respectively.

The decrease in $T_{1/2}$ with decreasing the counteranion size of **1(BF₄)₂** with respect to that of **1(ClO₄)₂** contrasts with that observed for **1(AsF₆)₂·yMe₂CO** and **1(SbF₆)₂·yMe₂CO**. In these two compounds the opposite trend is observed, the bulkier counteranion stabilizes the HS state and gives rise to a lower $T_{1/2}$ in **1(SbF₆)₂·yMe₂CO**. These two trends have been observed for ClO₄⁻ and BF₄⁻ salts of Fe(II) complexes of similar ligands. Thus, although ClO₄⁻ stabilizes the HS state in isostructural salts of [Fe(bpp)₂]²⁺ with variable ClO₄⁻ and BF₄⁻ contents^[16] or other Fe(II) complexes of 4-pyridyl derivatives of bpp,^[17,18] there are examples of the opposite behavior.^[19,20] It was concluded that there is no predictable relationship between anion size and $T_{1/2}$, even between salts that are known to be crystallographically isostructural.^[21] A possible explanation of this opposite trend in our compounds is that in **1(ClO₄)₂** and **1(BF₄)₂**, the packing of the complexes is dominated by the hydrogen bonding, resulting in very similar unit cell parameters and chemical pressure in the two compounds. Due to this, the counteranion size does not affect the chemical pressure of the complexes and other factors such as the electronegativity of the counteranions become more important. Indeed, there are many short contacts among the [Fe(1bppCOOH)₂]²⁺ complexes and counteranions which could result in a different withdrawal of electron density and changes in the crystal field around Fe(II). In **1(AsF₆)₂·yMe₂CO** and **1(SbF₆)₂·yMe₂CO**, which do not present this type of packing and show smaller differences in the electronegativity, the changes in unit cell volume and chemical pressure induced by the size of the counteranion become the decisive parameter.

Interestingly, $T(\text{LIESST})$ curves of [Fe(1bppCOOH)₂]²⁺ salts with hydrogen bonds (**1(BF₄)₂**, **1(ClO₄)₂** and **1(CF₃SO₃)₂·yMe₂CO**) show abrupt LIESST relaxation curves. While, in contrast to this, **1(AsF₆)₂·2Me₂CO** and **1(SbF₆)₂·2Me₂CO**, which present weaker intermolecular interactions, show more gradual relaxation curves.

Finally, $\chi_{\text{M}}T$ values of **2(ClO₄)₂·yMe₂CO** are close to 0 from 2 to 300 K, in agreement with the Fe-N bond lengths at 120 and 300 K. At 330 K, $\chi_{\text{M}}T$ shows a sharp increase to values of 3.5 cm³·K·mol⁻¹ consistent with 100% of complexes in the HS state (**Figure 2.2.9**). This increase is irreversible as $\chi_{\text{M}}T$ measured from 400 to 2 K remains almost constant and close to this value

with a decrease below 30 K due to zero-field splitting as expected for the HS d^6 of Fe(II). This indicates again that the spin transition is related here with the structural changes after losing the solvent molecules. Indeed, PXRd measurements support this hypothesis as they show an irreversible change of phase due to desolvation (**Figure Si. 2.4.19**). A drastic increase of the magnetic signal was observed after irradiation at 532 nm. The fraction of Fe(II) photoconverted after irradiation is calculated to be close to 40% for **2(ClO₄)₂·yMe₂CO** with a $T(\text{LIESST})$ of 71 K.

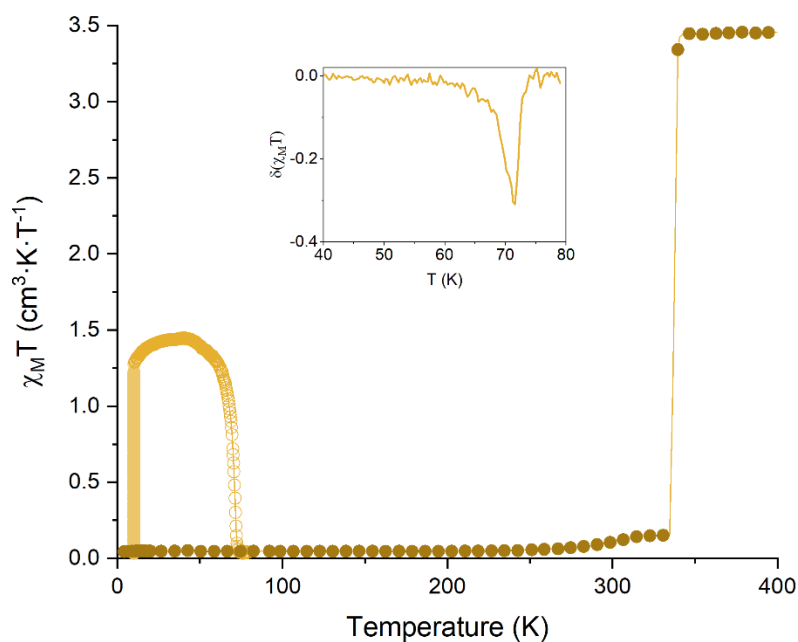


Figure 2.2.9. $\chi_M T$ in front of temperature for **2(ClO₄)₂·yMe₂CO** (yellow). Full dots: data recorded without irradiation; empty dots: data recorded after irradiation at 10 K. The inset graph shows the temperature dependence of the first derivative of $\chi_M T$ with respect to the temperature.

The $T(\text{LIESST})$ values for these compounds may be compared with those previously obtained for other bpp systems. For this family of compounds, a linear correlation has been proposed between the thermal spin crossover and the $T(\text{LIESST})$.^[22–27] These two physical quantities may be related by the formula $T(\text{LIESST}) = T_0 - 0.3 \cdot T_{1/2}$, with $T_0 = 150$ K (see Chapter 1). Taking 383 and 347 K as the mean values of $T_{1/2}$ of **1(ClO₄)₂** and **1(BF₄)₂**, respectively, $T(\text{LIESST})$ of 35.1 and 45.9 K are expected for these two compounds (ca. 20 K below the observed ones of 60 and 67 K). The same effect was observed for $[\text{Fe}(\text{bpp-triolH}_3)_2](\text{ClO}_4)_2$, where bpp-triolH₃ is an amide derived from bppCOOEt with triolH₃ = C(O)NHC(CH₂OH)₃.^[28] In the other compounds of this work, it is not possible to know the $T_{1/2}$ as the change of spin state with the temperature is related to desolvation. Thus, the “real $T_{1/2}$ ” is hidden by the desolvation of the compounds. From these results, it seems that the empirical formula used for 1bpp presents an

important deviation for bppCOOH and related ligands. This could indicate that they present a higher T_0 (close to 170 K) or that the $T(\text{LIESST})$ of compounds with high $T_{1/2}$ deviates significantly from that formula as observed for other Fe(II) complexes with tridentate ligands.^[29]

Deposition of **1**

Grafting of molecules functionalized with carboxylic acid groups onto metal-oxide surfaces is a well-known process.^[30] Si substrates covered with a layer of thermally grown SiO_2 were immersed overnight in a 1 mM MeCN solution of **1**(ClO_4)₂. Then, they were thoroughly rinsed with MeCN to remove any physisorbed material and then, dried under a N_2 stream. The stability of the solution was checked with UV/Vis and the deposits of **1** (**1-SAM**) were characterized by AFM, MALDI-TOF, XPS and XAS.

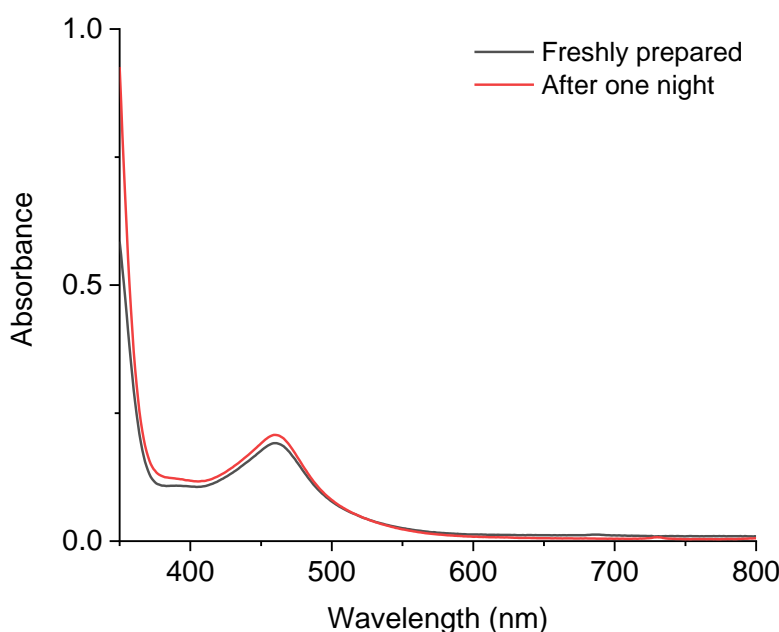


Figure 2.2.10. UV/Vis spectra of a freshly prepared 0.1 mM solution of **1**(ClO_4)₂ in MeCN (black line) and after one day in inert atmosphere (red line).

UV/Vis spectroscopy shows a band centered at around 460 nm ($\epsilon = 1.9 \times 10^3 \text{ L}^{-1} \text{ mol}^{-1} \text{ cm}^{-1}$), which could be assigned to a metal to ligand charge-transfer (MLCT) $t_2 \rightarrow \pi^*$ transition typical for Fe(II) 1bpp systems.^[31,32] The presence of this band suggests that there is *ca.* 50% of molecules in the LS state in solution, in agreement with published data that indicate that around half of Fe(II) 1bppCOOH complexes in solution are in the HS state at room temperature.^[33] Indeed, UV-vis spectra of pure LS bpp compounds present MLCT bands centered at around 420 nm ($\epsilon = 4\text{-}6 \times 10^3 \text{ L}^{-1} \text{ mol}^{-1} \text{ cm}^{-1}$), whereas MLCT bands attributed to HS complexes appear not well-resolved at lower

energies.^[34] The UV-Vis spectrum does not change after one night, confirming the stability of the solution (**Figure 2.2.10**). The small increase comes from concentration of the solution due to normal evaporation of the solvent.

AFM was used to determine the surface morphology and to verify the deposition without presence of complex aggregates on the metal oxide surface. The average of the R_{RMS} of the deposit obtained from 15 measurements in different points of the surface, show a small increase from 0.203 ± 0.010 nm to 0.243 ± 0.014 nm with respect to the naked substrate. This indicates the formation of a monolayer covering most of the surface with a small degree of disorder or the formation of a sub-monolayer. AFM images confirm the absence of aggregates or multilayers (see **Figure 2.2.11**). This result is expected if we consider that the carboxylic acid groups of $[\text{Fe}(\text{1bppCOOH})_2]^{2+}$ cause the grafting of the first layer of the complexes on the oxide surfaces, whereas additional layers are removed after rinsing with MeCN, since they are not chemically bonded to the substrate.

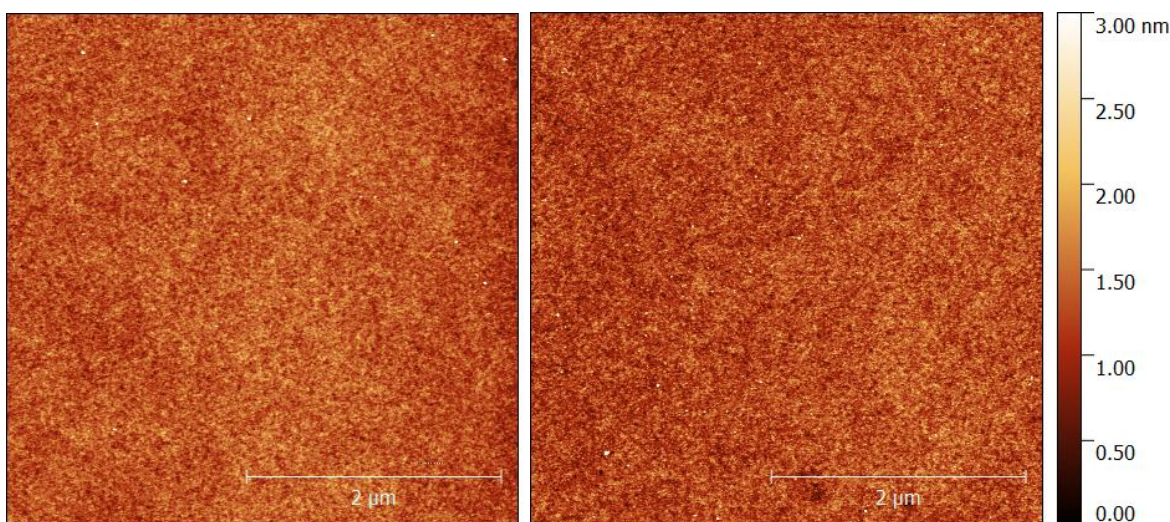


Figure 2.2.11. AFM images of a thermally grown SiO₂ substrate before (left) and after (right) deposition.

MALDI-TOF was used to identify fragments of the molecule on the surface. The peak corresponding to the protonated ligand $[\text{1bppCOOH}+\text{H}]^+$ (Calc. 256.08 Da, Found 256.08 Da, see **Figure 2.2.12**) was obtained confirming the anchoring of the ligand to the metal oxide surface.

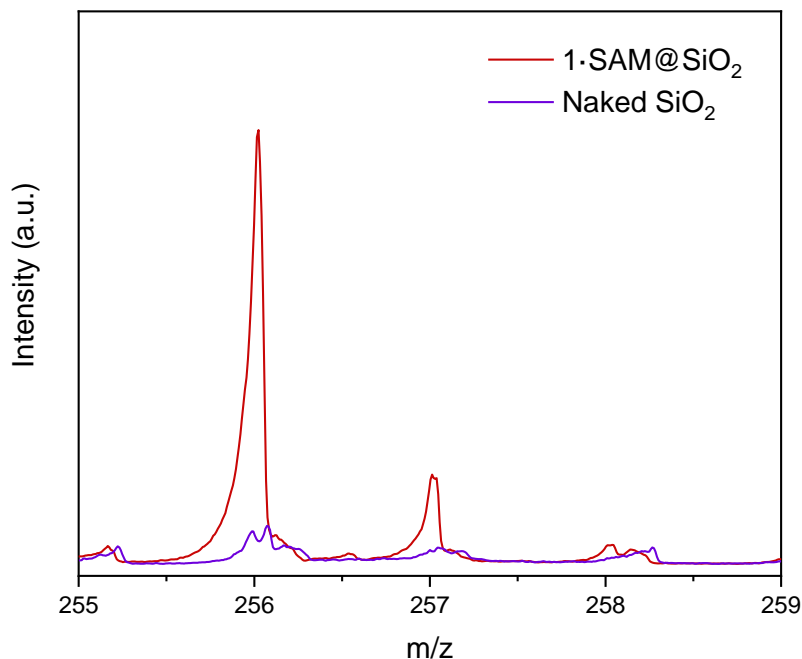


Figure 2.2.12. MALDI-TOF region of the ligand ($[1\text{bppCOOH}+\text{H}]^+$, 256.06 Da) of **1-SAM** (red) and bare SiO_2 substrate (violet).

In order to investigate structural and electronic properties of the SAM, XPS has been performed. $\text{C}1\text{s}$, $\text{N}1\text{s}$, $\text{Cl}2\text{p}$ and $\text{Fe}2\text{p}$ XPS regions were studied to analyze the atomic compositions of the deposit (**Figure 2.2.13**). $\text{C}1\text{s}$ region features three main components at 285.0, 286.0 and 288.2 eV assigned to the aliphatic carbon atoms and/or adventitious carbon (orange), heterobonds (green) and carbon atoms of the carboxylate group (blue), respectively.^[35,36] $\text{N}1\text{s}$ region features three components at 401.6 and 399.8 eV^[37] assigned to nitrogen atoms of the pyridine and pyrazolyl groups (coordinated and uncoordinated, green) and the third component at 397.0 eV is assigned to the CN of the MeCN (red).^[38] $\text{Fe}2\text{p}_{3/2}$ region has been reproduced with 5 components (A–E) along with the corresponding $\text{Fe}2\text{p}_{1/2}$ spin–orbit coupled contributions (A'–E') weighted by the expected 2:1 ratio.^[39] The disappearance of the perchlorate signal is experimental evidence of the absence of physisorbed molecules of $\mathbf{1}(\text{ClO}_4)_2$ on the surface. $\text{Fe}2\text{p}_{3/2}$ region has been reproduced with 5 components (A–E) along with the corresponding $\text{Fe}2\text{p}_{1/2}$ spin–orbit coupled contributions (A'–E') weighted by the expected 2:1 ratio.^[39] The disappearance of the perchlorate anion signal is experimental evidence of the absence of physisorbed molecules of $\mathbf{1}(\text{ClO}_4)_2$ on the surface. Semiquantitative analysis and stoichiometric ratios (see **Table 2.2.1**) do not match with the expected values for $[\text{Fe}(1\text{bppCOOH})_2]$ molecules. They suggest that $[\text{Fe}(1\text{bppCOOH})]$ species with only one ligand per iron is present on the surface together with solvent molecules such as MeCN probably completing the coordination sphere of the iron ion.

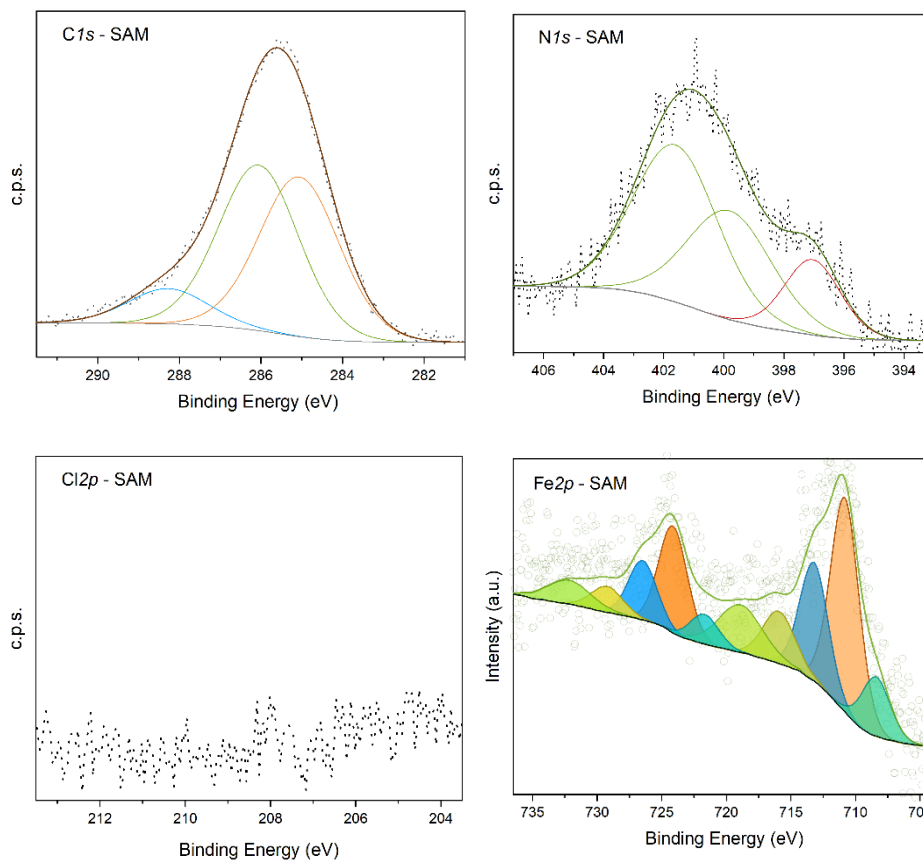


Figure 2.2.13. XPS C 1s, N 1s, Cl 2p and Fe 2p regions of **1-SAM**.

Table 2.2.1. Theoretical and XPS estimated atomic semiquantitative analysis (top) and ratios (bottom) for **1**. Theoretical values have been calculated guessing one ligand and one acetonitrile molecule per iron, **Fe(1bppCOOH)(MeCN)**.

	Semiquantitative analysis								
	Elements			Nitrogen components			Carbon components		
	Fe	N	C	N _{coordinated}	N _{uncoordinated}	CN	C-C	C-N	COO-
Theor.	5.0%	30.0%	65.0%	50.0%	33.3%	16.7%	45.5%	45.5%	9.1%
1-SAM@SiO₂	2.1%	12.2%	85.8%	49.8%	34.5%	15.8%	44.3%	45.9%	9.8%

	Iron Ratios			Nitrogen ratios			Carbon ratios		
	Fe/Fe	Fe/N	Fe/C	C-N _{coord} / C-N _{coord}	C-N _{coord} / C-N _{uncoord}	C-N/ CN	C-C/ C-N	C-N/ C-N	O-C=O/ C-N
Theor.	1.00	0.17	0.077	1.00	0.67	0.33	1.00	1.00	0.20
1-SAM@SiO₂	1.00	0.17	0.024	1.00	0.69	0.32	0.96	1.00	0.21

To further study the electronic state of our molecule, synchrotron-based absorption techniques are one of the best tools to analyze nanostructures. XAS measurements in the bulk of compound **1(BF₄)₂** that will be used as references are shown in **Figure 2.2.14**, left. At 350 K, the Fe L₃ edge is composed by a peak at 708.4 eV with a shoulder at 709.2 eV. This is an energy splitting typical for a HS state of Fe(II). The spectrum recorded at 200 K shows that the L₃ maximum is shifted to higher energies (710.1 eV), with a less structured and more intense L₂ edge also shifted to higher energies. The shift of the Fe L_{2,3} resonance intensity toward higher photon energies, the change in line shape, and the increase of the branching ratio are characteristic of a quantitative HS to LS transition as observed for similar SCO complexes^[40] in agreement with magnetic properties of the bulk compound (see above). XAS spectrum at Fe L_{2,3} edge of the monolayer was recorded at 100 K. It displays a characteristic Fe(III) shape (see **Figure 2.2.14**, right), as it has been seen previously in literature reports,^[41,42] and agrees with XPS measurements.

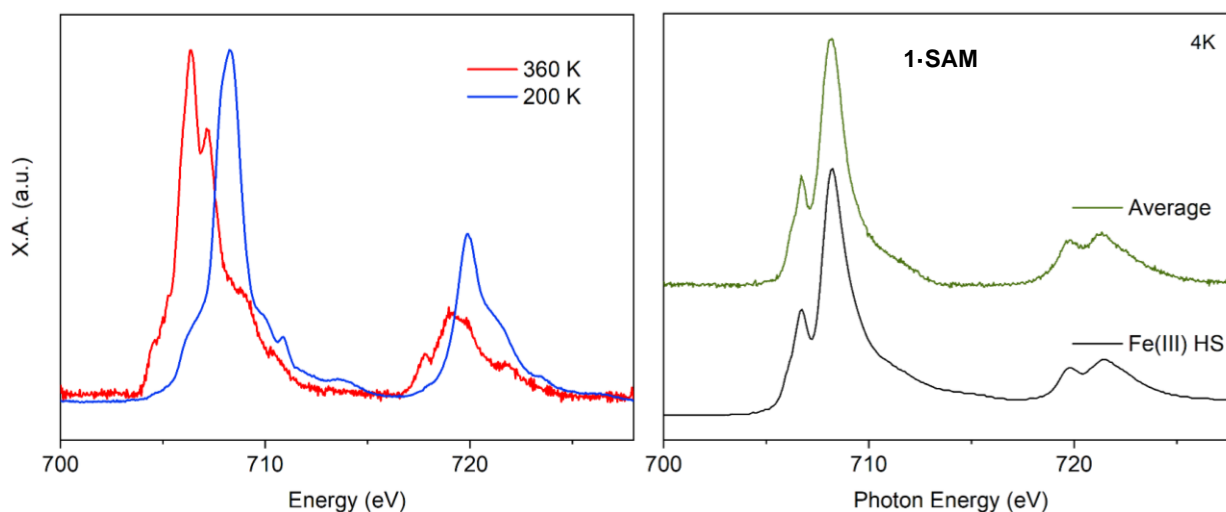


Figure 2.2.14. Normalized XAS Fe L_{2,3}-edge spectra of crystals of, **left**, **1(BF₄)₂** at 350 K (HS) and 200 K (LS) and, **right**, **1-SAM** and a Fe(III) L_{2,3}-edge extracted from the literature.^[42]

2.3. Conclusions

In this chapter, five salts of $\text{Fe}(\text{1bppCOOH})_2]^{2+}$ have been prepared and characterized. They show different magnetic properties such as reversible temperature-, light- and solvent-induced spin transitions. This is not unusual as it has been already seen in other 1bpp and 3bpp derivatives. [17–20,43] The fact that they present different magnetic behaviors makes it difficult to rationalize as they correspond to compounds with different structures and therefore, different crystal packings and intermolecular interactions, however some general conclusions can be extracted.

Counteranions with similar geometries such as ClO_4^- and BF_4^- , and AsF_6^- and SbF_6^- give rise to isostructural salts. The first ones, smaller tetrahedral counteranions, generate a denser crystal packing which avoids the insertion of solvent molecules in the structure and the presence of a hydrogen-bonded chain of complexes, that lead to abrupt and reversible SCO. The decrease in size of the counteranion favors the HS state, leading to a lower $T_{1/2}$ for **1(BF₄)₂** with respect to **1(ClO₄)₂**. This decrease of *c.a.* 40 K could be related to a greater withdrawal of electronic density from the BF_4^- .

Salts with larger counteranions present a less dense crystal packing which leads to the incorporation of solvent molecules in the structure. These molecules play an important role in their magnetic properties. The loss of solvent molecules in **1(CF₃SO₃)₂·yMe₂CO**, **1(AsF₆)₂·yMe₂CO** and **1(SbF₆)₂·yMe₂CO** is accompanied by spin transition of different sings. Whereas desolvation of **1(CF₃SO₃)₂·yMe₂CO** induces a change from the LS state to the HS state, desolvation of **1(AsF₆)₂·yMe₂CO** and **1(SbF₆)₂·yMe₂CO** slightly stabilizes the LS state. It is noteworthy that these changes are reversible as the samples recover the structure and color of the initial samples upon contact with a saturated atmosphere. Therefore, **1(CF₃SO₃)₂·yMe₂CO** presents a reversible solvent-induced spin transition. Interestingly, the bigger size of SbF_6^- in the isostructural **1(AsF₆)₂·yMe₂CO** and **1(SbF₆)₂·yMe₂CO** salts leads to a stabilization of the HS state and to a lower $T_{1/2}$ in contrast to **1(ClO₄)₂** and **1(BF₄)₂**. This trend could suggest that, in the absence of the hydrogen bonded chain of complexes found in **1(ClO₄)₂** and **1(BF₄)₂** that governs the crystal packing, the expansion of the unit cell volume by the larger SbF_6^- counteranion becomes the most important factor.

Finally, the use of the ethyl ester derivative 1bppCOOEt has a similar effect to that of the use of bulkier counteranions. Thus, an irreversible spin transition is obtained in **2(ClO₄)₂·yMe₂CO** as a result of the loss of solvent molecules after heating above 340 K. However, in contrast to the

[Fe(1bppCOOH)₂]²⁺ salts, the original structure is not recovered after re-solvation. This could indicate that the carboxylic acid group could play a role in the reversibility of the solvation or that the flexibility of the ethyl group favors the formation of different structures for the solvated and re-solvated compound.

All these results indicate that the spin state of [Fe(bppCOOH)₂]²⁺ complex is very sensitive to the counteranion and solvent molecules, and that the LS state is not as favored as the first results obtained with the ClO₄⁻ salt could suggest. All these compounds show a clear LIESST effect. As expected, the lower T_{1/2} of the BF₄⁻ salt, gives rise to an increase of the T(LIESST) with respect to that of **1(ClO₄)₂**. Finally, an interesting point of **1(AsF₆)₂·yMe₂CO** and **1(SbF₆)₂·yMe₂CO** is that they crystallize in a non-centrosymmetric space group. This could open the way to other phenomena in coexistence with the thermal-, photo- and solvent-induced SCO of these compounds such as ferroelectricity, which has been recently reported for a salt of [Fe(3-bpp)₂]²⁺.^[44] All these compounds show a clear LIESST effect. As expected, the lower T_{1/2} of the isostructural BF₄⁻ and SbF₆⁻ salts gives rise to an increase of the T(LIESST) with respect to that of **1(ClO₄)₂** and **1(AsF₆)₂·yMe₂CO**, respectively.

Regarding the surface deposition, a combination of techniques shows that a homogeneous assembly of molecules has been formed on the surface with absence of aggregates. The affinity of the 1bpp ligand functionalized with a carboxylic acid group for metal oxides is confirmed and coordination of an iron ion is feasible. X-ray techniques shows that decomposition of the molecules takes place during the deposition process giving rise to one ligand per iron and oxidation of the later. This result suggests that **1** decompose during the deposition procedure either by oxidation of the complex upon contact with the surface, considering that octahedral bis(tridentate) Fe(III) complexes based on 1bpp derivatives are not stable, either due to a weak binding of the ligand to the iron, as observed previously for other 1bpp complexes with sulphur substituents on Au, and its later oxidation.^[45] The use of other deposition conditions such as shorter deposition times, less polar solvents or increased concentrations of the complexes, and the preparation of more robust Fe(II) complexes based on other 1bpp derivatives could be possible strategies to improve these results. We have explored this last possibility in the chapters 3 and 4, with two different synthetic strategies: the change of position of the carboxylic acid substituent (Chapter 3) and the preparation of heteroleptic complexes (Chapter 4).

2.4. Supporting Information

Synthesis

Fe(X)₂ (X = ClO₄ (12.5 mg), BF₄ (17.5 mg) or CF₃SO₃ (17.7 mg), 0.05 mmol) in 1.5 mL of acetone or a filtered solution of FeCl₂ (6.40 mg, 0.05 mmol) reacted with AgAsF₆ (14.8 mg, 0.10 mmol) or AgSbF₆ (34.4 mg, 0.10 mmol) in 1.5 mL of acetone was added to a solution of the ligand (1bppCOOH (28.5 mg) or 1bppCOOEt (28.0 mg), 0.10 mmol) in acetone (1.5 mL) and the mixture was stirred for 15 minutes. An orange solution was formed. Red-orange prismatic crystals of all the complexes suitable for X-ray diffraction were obtained by slow diffusion of diethyl ether into this solution.

Table S.I. 2.4.1. Theoretical and experimental values of elemental analysis.

Compound	Mr (g/mol)	Calculated (%)				Found (%)			
		C	N	H	S	C	N	H	S
1(BF₄)₂	739.95	38.96	18.93	2.45	-	38.31	18.54	2.60	-
1(CF₃SO₃)·Me₂CO	1095.93	37.76	15.18	2.62	6.95	37.76	15.26	2.35	6.65
1(AsF₆)₂·Me₂CO·H₂O	1020.29	31.79	13.73	2.57	-	31.82	13.57	2.71	-
1(AsF₆)₂	944.13	30.53	14.84	1.92	-	30.39	14.76	1.91	-
1(SbF₆)₂·Me₂CO·H₂O	1113.91	29.11	12.57	2.35	-	29.80	12.29	2.46	-
1(SbF₆)₂	1037.81	27.78	13.50	1.75	-	27.46	13.43	1.72	-
2(ClO₄)₂·2H₂O	879.41	39.23	16.34	3.53	-	38.87	16.06	3.33	-

Intermolecular interactions in **1(ClO₄)₂** and **1(BF₄)₂**.

At 120 K the hydrogen-bonded chains are linked through intermolecular interactions that involve C atoms from a pyrazole group and oxygen atoms from a carboxylic acid group of neighboring molecules ($d_{O1...C8} = 3.055 \text{ \AA}$ and $d_{O2...C1} = 3.185 \text{ \AA}$ for **1(ClO₄)₂** and $d_{O1...C8} = 3.029 \text{ \AA}$ and $d_{O2...C1} = 3.151 \text{ \AA}$ for **1(BF₄)₂**) (**Figure SI. 2.4.1**) giving rise to layers of complexes on the *bc* plane separated by layers of perchlorate or tetrafluoroborates anions (**Figure SI. 2.4.2**). On the contrary, at 400 K the number of contacts decreases as a result of the significant enlarging of *a* and *b* axis on increasing the temperature. Thus, neighboring $[\text{Fe}(\text{1bppCOOH})_2]^{2+}$ complexes belonging to the *bc* planes present only one contact involving C atoms from a pyrazole group and oxygen atoms from a carboxylic acid group ($d_{O1...C8} = 3.192 \text{ \AA}$ for **1(ClO₄)₂** and $d_{O1...C8} = 3.162 \text{ \AA}$ for **1(BF₄)₂**). On the other hand, $[\text{Fe}(\text{1bppCOOH})_2]^{2+}$ complexes of neighboring layers present short contacts at 120 K, which involve CH groups of the pyrazole rings ($d_{C2...C2} = 3.709$

Å for $1(\text{ClO}_4)_2$ and $d\text{C}2\cdots\text{C}2 = 3.710$ Å for $1(\text{BF}_4)_2$ (Figure SI. 2.4.3). These short contacts do not appear in the structure at 400 K.

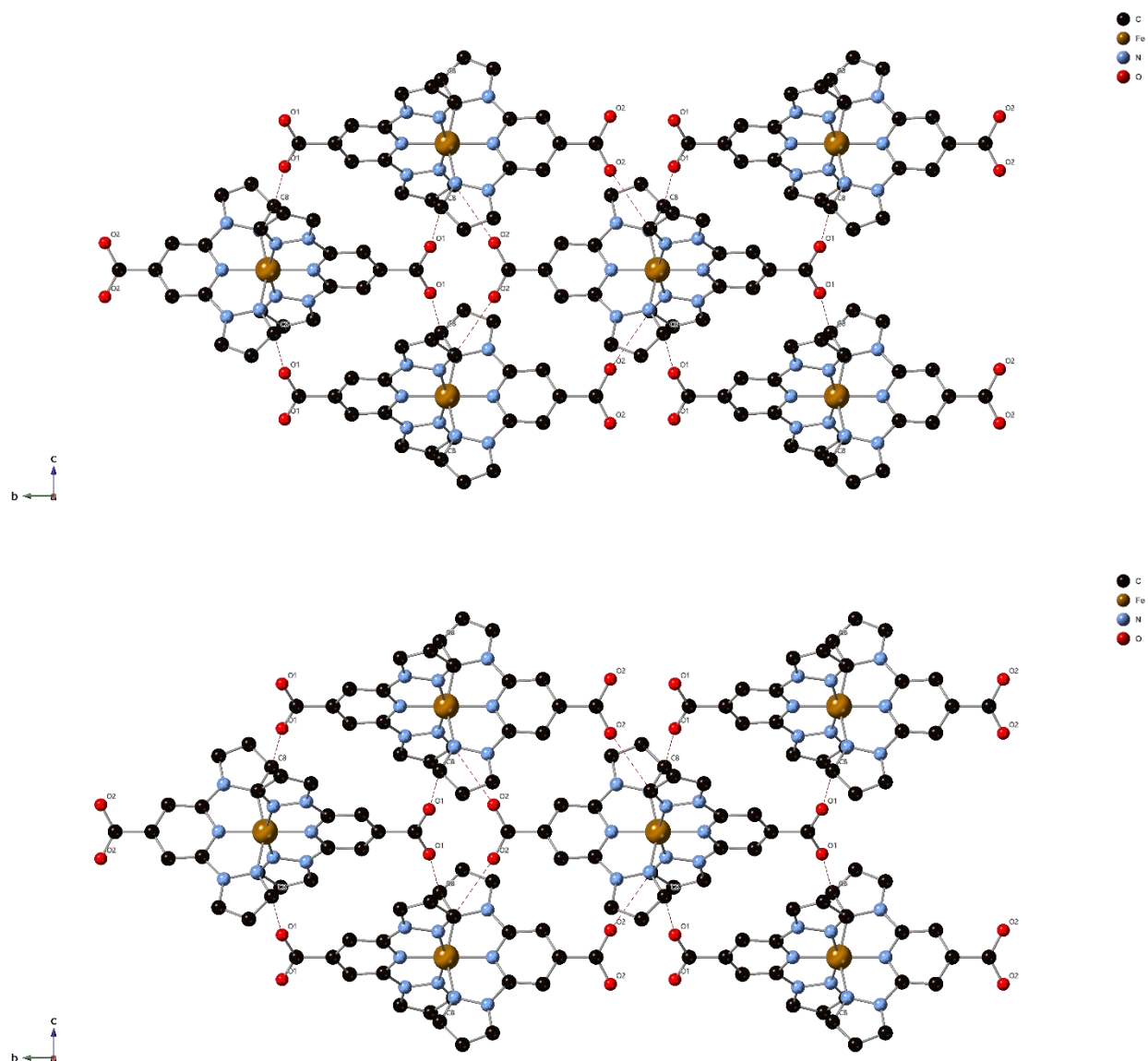


Figure SI. 2.4.1. View of a layer of $[\text{Fe}(1\text{bppCOOH})_2]^{2+}$ complexes with the intermolecular interactions between complexes belonging to different hydrogen-bonded chains as dashed lines in the structure of $1(\text{ClO}_4)_2$ (top) and $1(\text{BF}_4)_2$ (bot) at 120 K. Hydrogen atoms have been omitted for clarity.

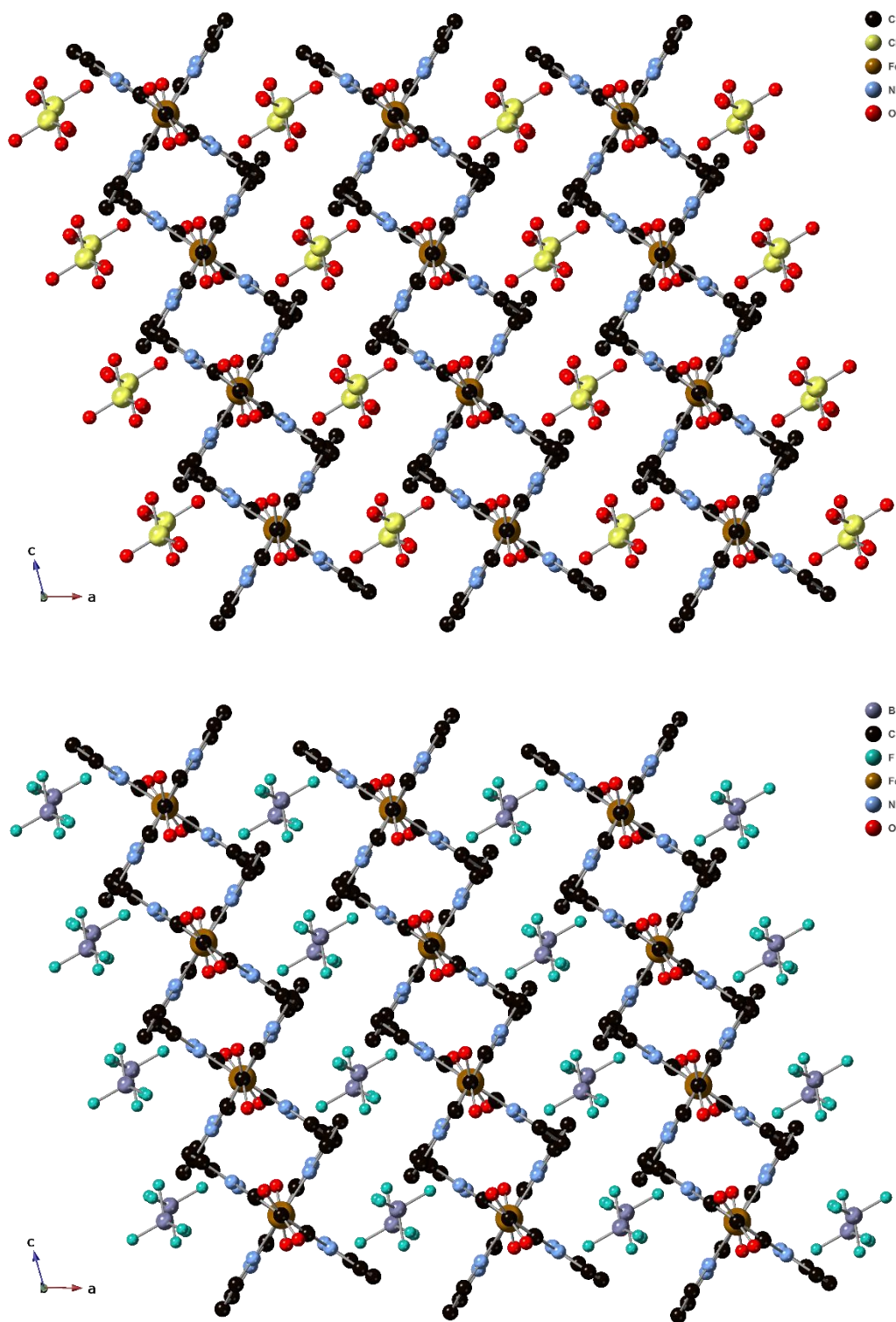


Figure SI. 2.4.2. Projection of the structure of $1(\text{ClO}_4)_2$ (top) and $1(\text{BF}_4)_2$ (bot) at 120 K in the *ac* plane. Hydrogen atoms have been omitted for clarity.

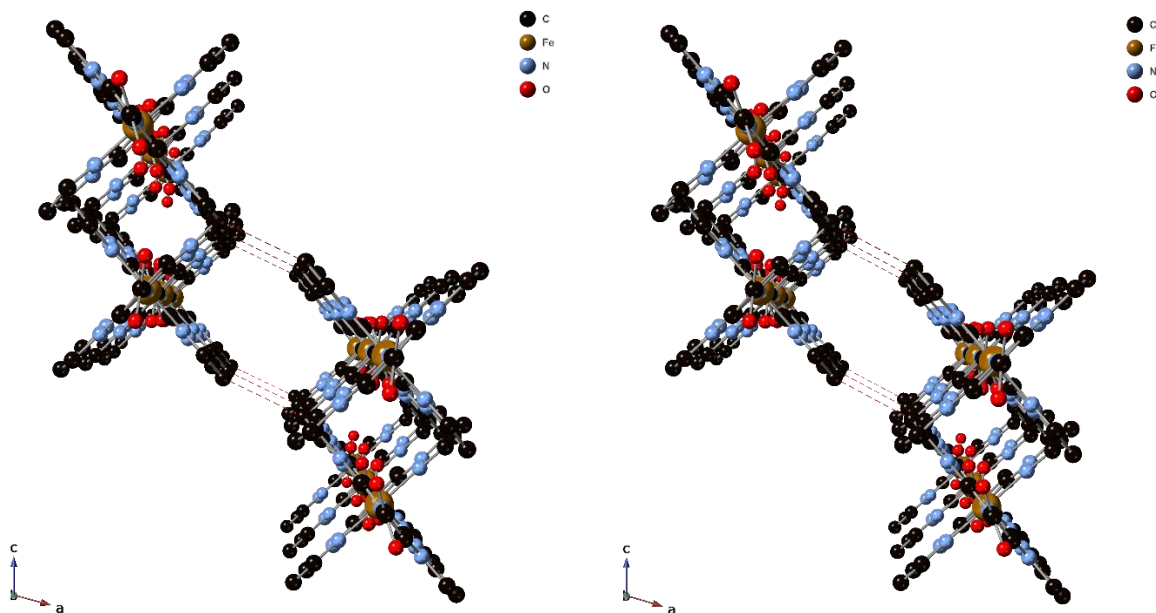


Figure SI. 2.4.3. View of two layers of $[\text{Fe}(\text{1bppCOOH})_2]^{2+}$ complexes with the intermolecular interactions between complexes belonging to different layers as dashed lines in the structure of $\mathbf{1}(\text{ClO}_4)_2$ (left) and $\mathbf{1}(\text{BF}_4)_2$ (right) at 120 K. Hydrogen atoms have been omitted for clarity.

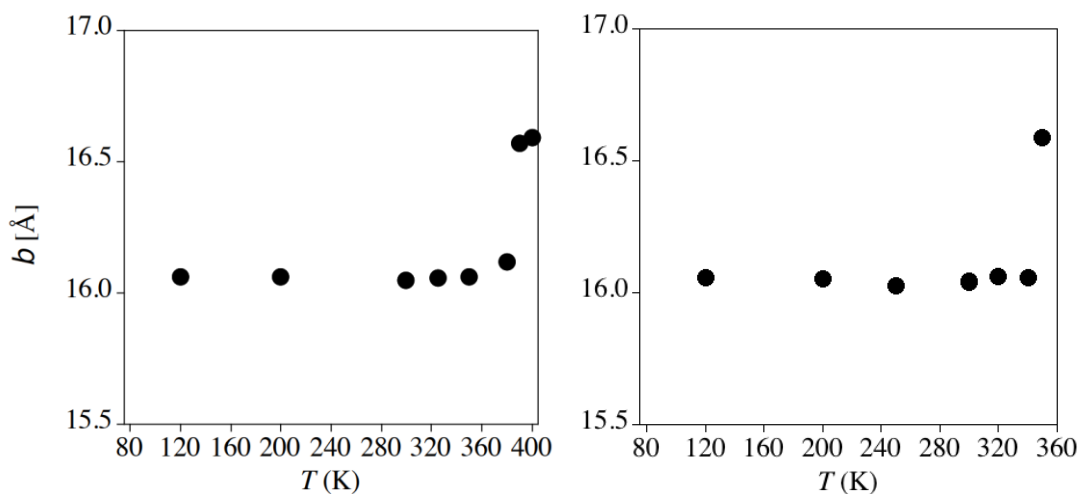


Figure SI. 2.4.4. Thermal dependence of the parameter b of $\mathbf{1}(\text{ClO}_4)_2$ (left) and $\mathbf{1}(\text{BF}_4)_2$ (right).

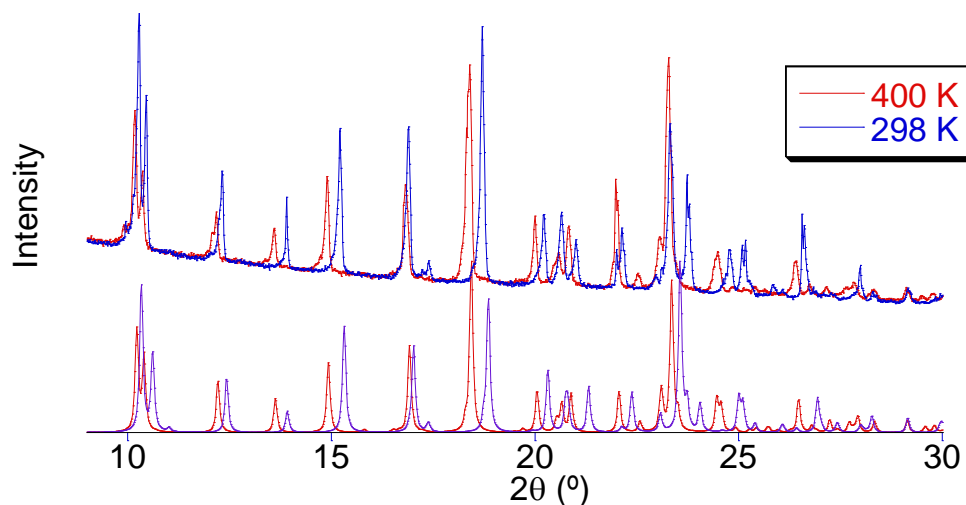


Figure SI. 2.4.5. Experimental powder X-ray diffraction patterns (top) at 298 K (blue line) and 400 K (red line) and simulated one (bottom) at 120 K (blue line) and 400 K (red line) of $1(\text{ClO}_4)_2$.

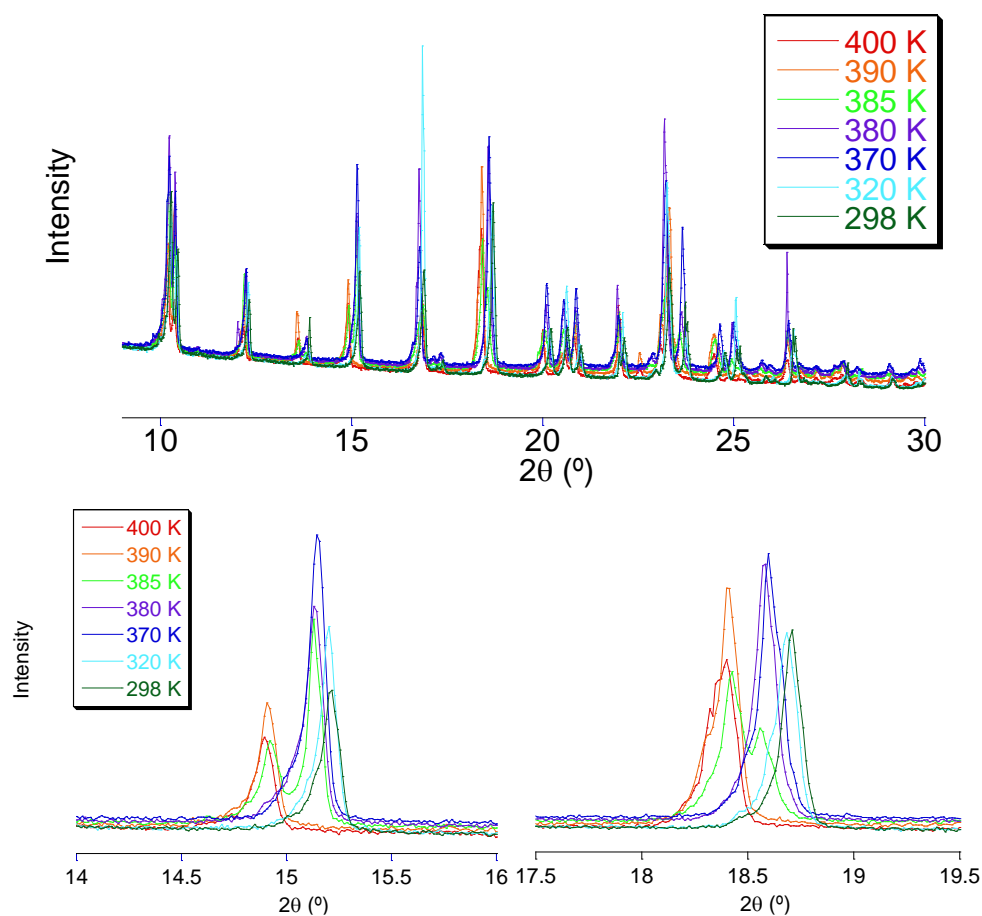


Figure SI. 2.4.6. Thermal dependence of the experimental powder X-ray diffraction pattern of $1(\text{ClO}_4)_2$.

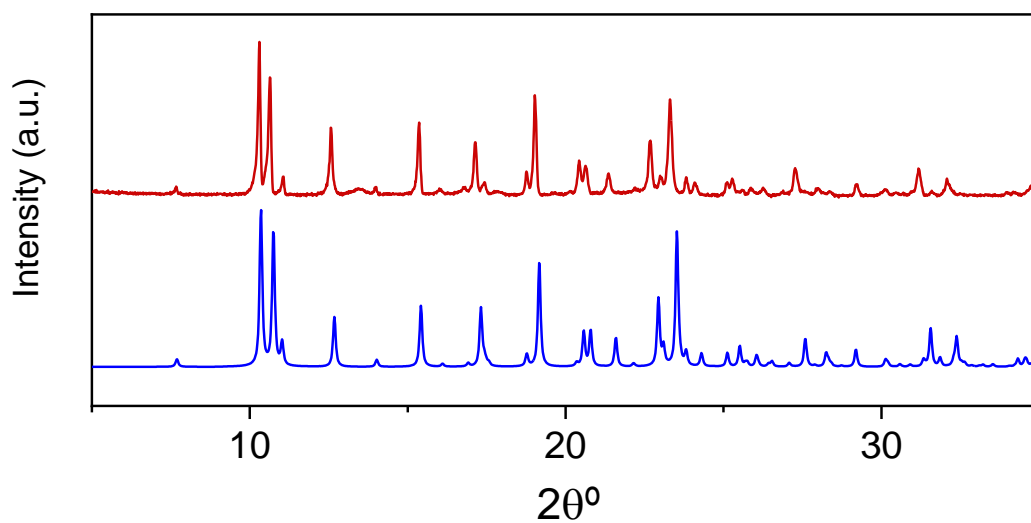


Figure SI. 2.4.7. Simulated PXRD pattern from the structure solved at 120 K (blue) and experimental one at 300 K (red) of **1(BF₄)₂**.

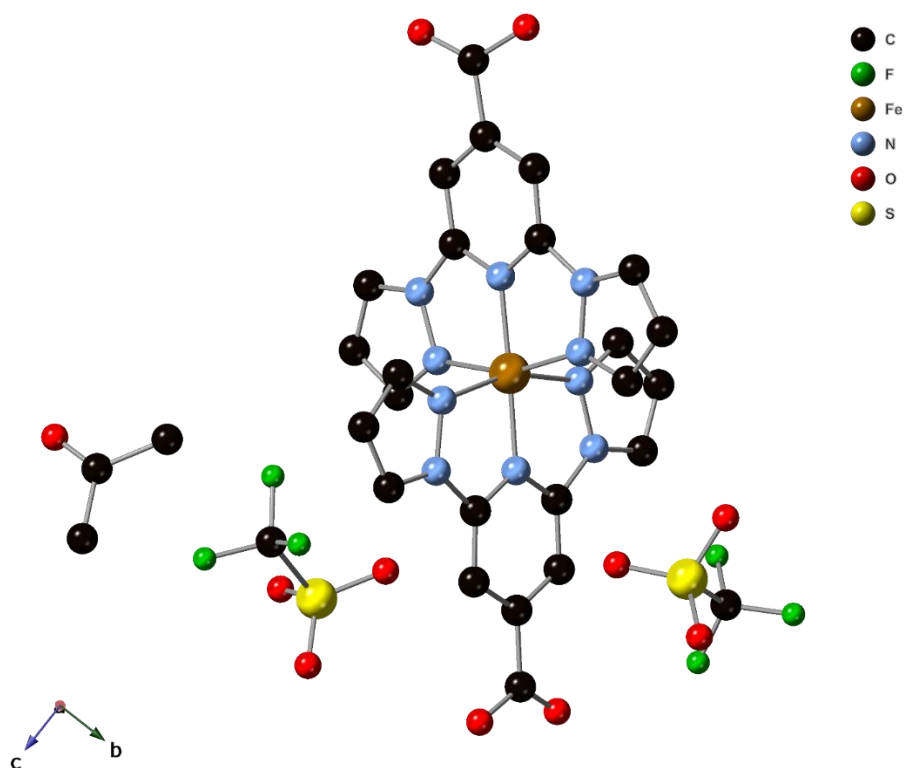


Figure SI. 2.4.8. View of the asymmetric unit of **1(CF₃S₃)-yMe₂CO** at 120 K. Hydrogen atoms have been omitted for clarity.

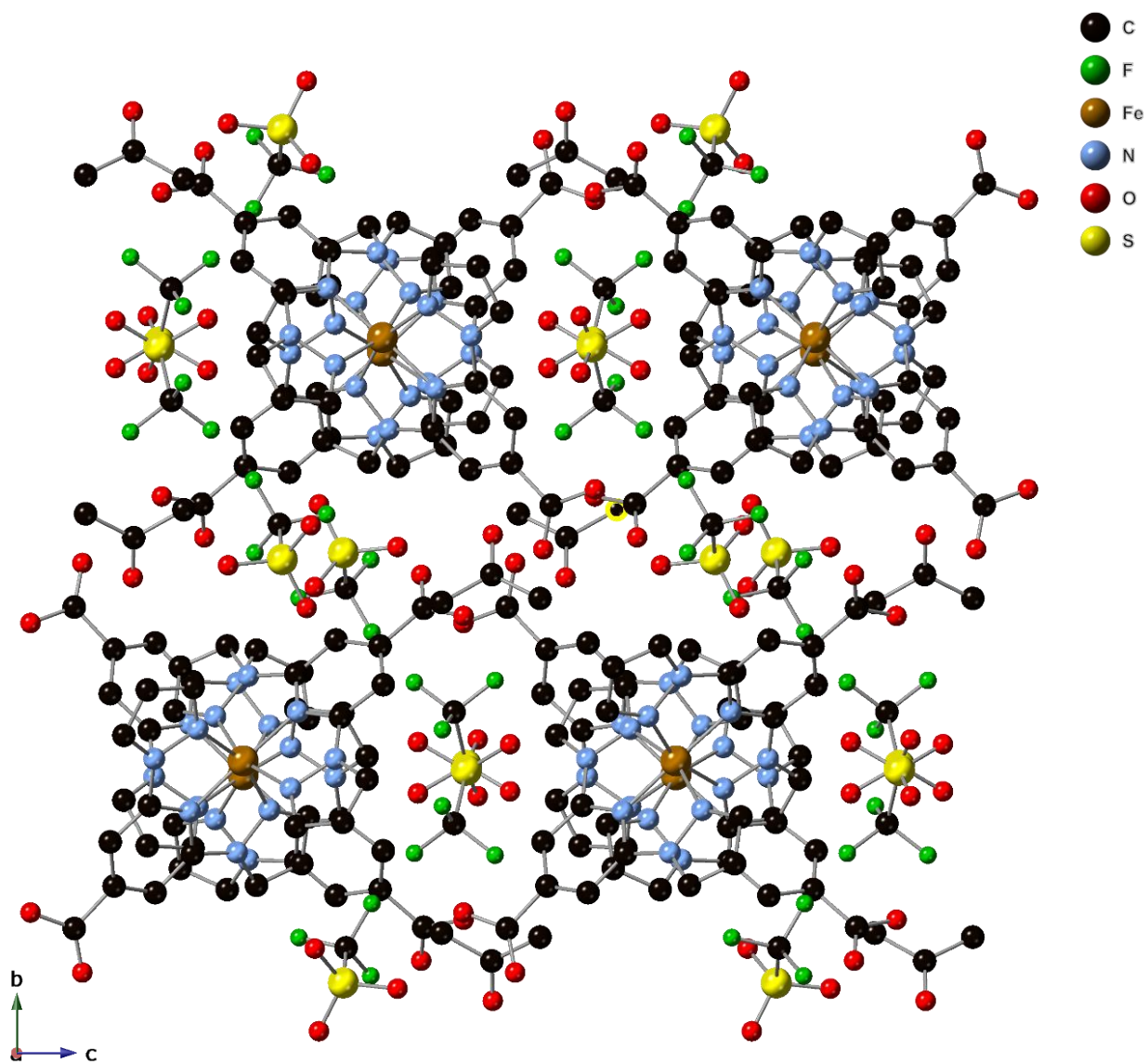


Figure SI. 2.4.9. Projection in the bc plane of the structure of $1(\text{CF}_3\text{SO}_3)_2 \cdot \text{Me}_2\text{CO}$ at 120 K. Hydrogen atoms have been omitted for clarity.

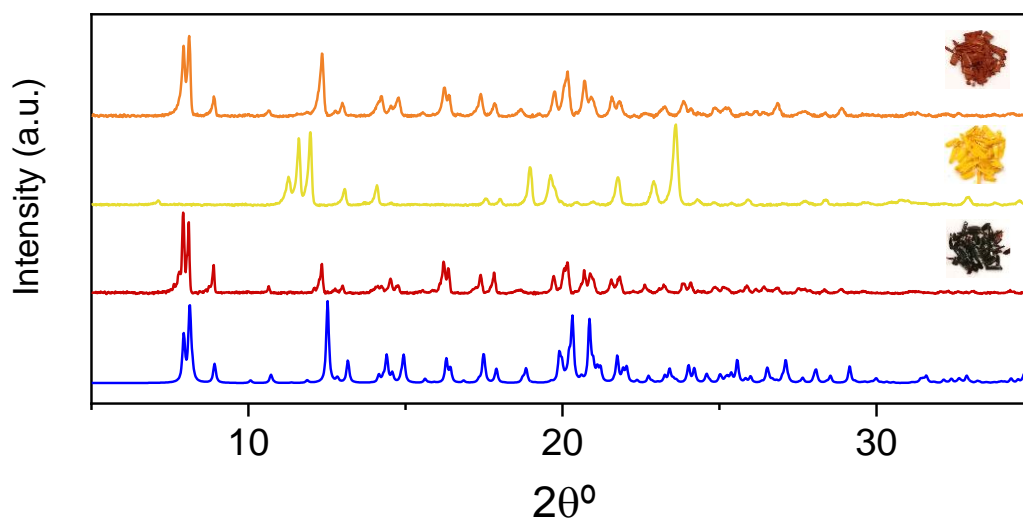


Figure SI. 2.4.10. Simulated PXRD pattern from the structure solve at 300 K (blue), experimental one at 300 K (red), experimental PXRD pattern of the desolvated sample (yellow) and experimental PXRD pattern of the resolvated sample (orange) of $1(\text{CF}_3\text{SO}_3)_2 \cdot y\text{Me}_2\text{CO}$.

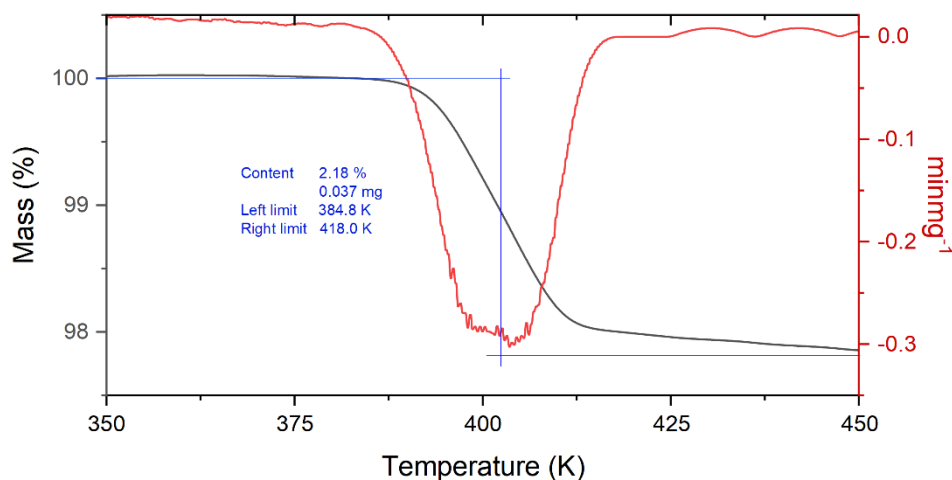


Figure SI. 2.4.11. Thermogravimetric profile of $1(\text{CF}_3\text{SO}_3)_2 \cdot y\text{Me}_2\text{CO}$ (1.169 mg, black line) and its derivative (red line) in heating mode from 350 K to 450 K (at 10 °C/min). The mass lost after this ramp corresponds to 2.18 % of the total weigh, which is lower than the expected weight loss of half molecule of Me_2CO (ca. 2.8 %).

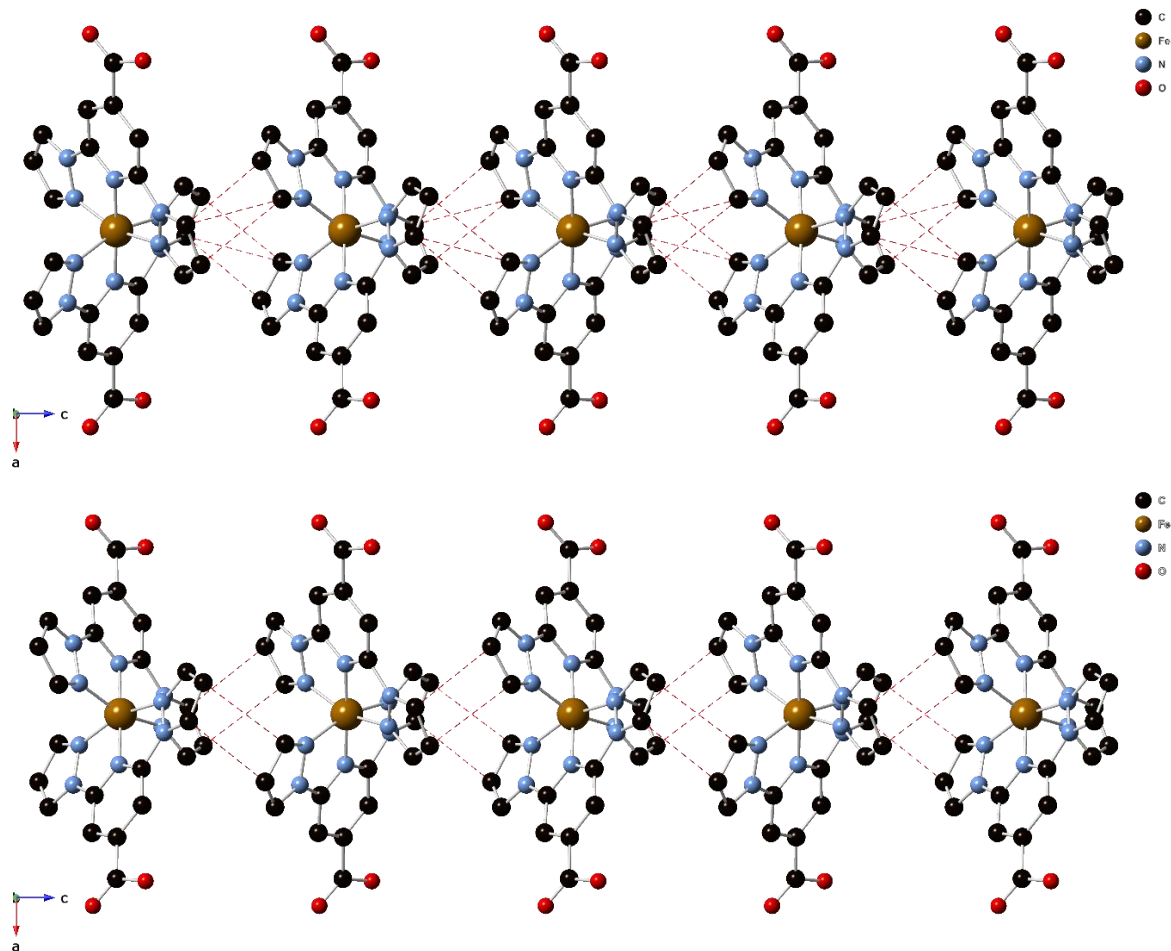


Figure SI. 2.4.12. CH $\cdots\pi$ contacts between $[\text{Fe}(\text{1bppCOOH})_2]^{2+}$ complexes in the structures of $\mathbf{1}(\text{AsF}_6)_2 \cdot y\text{Me}_2\text{CO}$ (top) and $\mathbf{1}(\text{SbF}_6)_2 \cdot y\text{Me}_2\text{CO}$ at 120 K (bottom). Hydrogen atoms have been omitted for clarity.

These chains are connected through short contacts involving C=O groups from carboxylic acid groups and two CH from pyrazole and pyridine rings from $[\text{Fe}(\text{1bppCOOH})_2]^{2+}$ complexes belonging to different chains with distances of 3.355 Å C1 \cdots C9, 3.265 Å C2 \cdots C9 and 2.871 Å C10 \cdots H1 for $\mathbf{1}(\text{AsF}_6)_2 \cdot y\text{Me}_2\text{CO}$ and 3.289 Å C3 \cdots C9 and 2.896 Å C2 \cdots H11 for $\mathbf{1}(\text{SbF}_6)_2 \cdot y\text{Me}_2\text{CO}$. In contrast to this, CH $\cdots\pi$ contacts are not observed in the structures solved at 300 K. Finally, AsF_6^- or SbF_6^- anions inserted between the chains present numerous short contacts with neighboring $[\text{Fe}(\text{1bppCOOH})_2]^{2+}$ complexes.

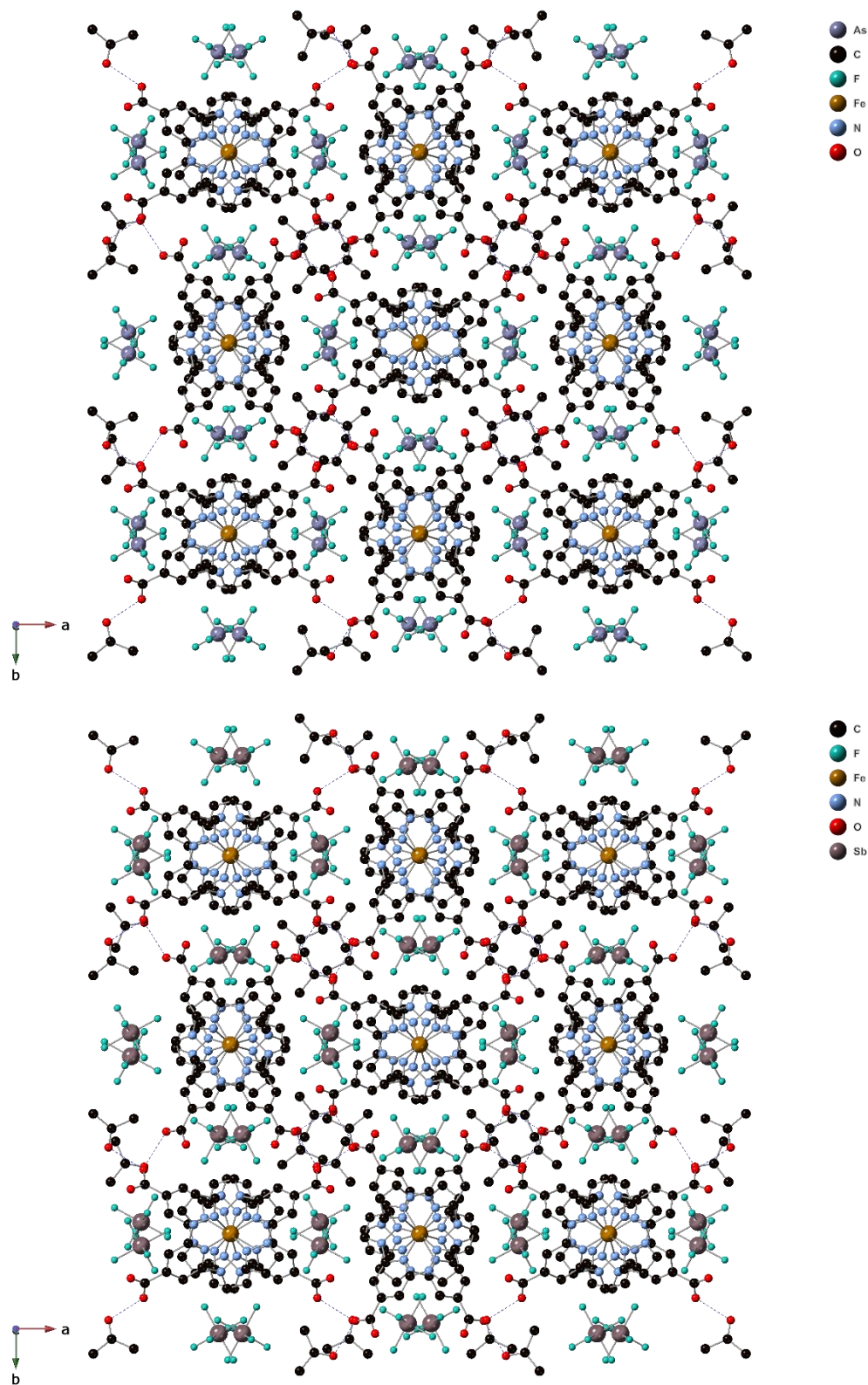


Figure SI. 2.4.13. Projection in the ab plane of the structures of $1(\text{AsF}_6)_2 \cdot y\text{Me}_2\text{CO}$ (top) and $1(\text{SbF}_6)_2 \cdot y\text{Me}_2\text{CO}$ (bottom) at 120 K. Hydrogen atoms have been omitted for clarity.

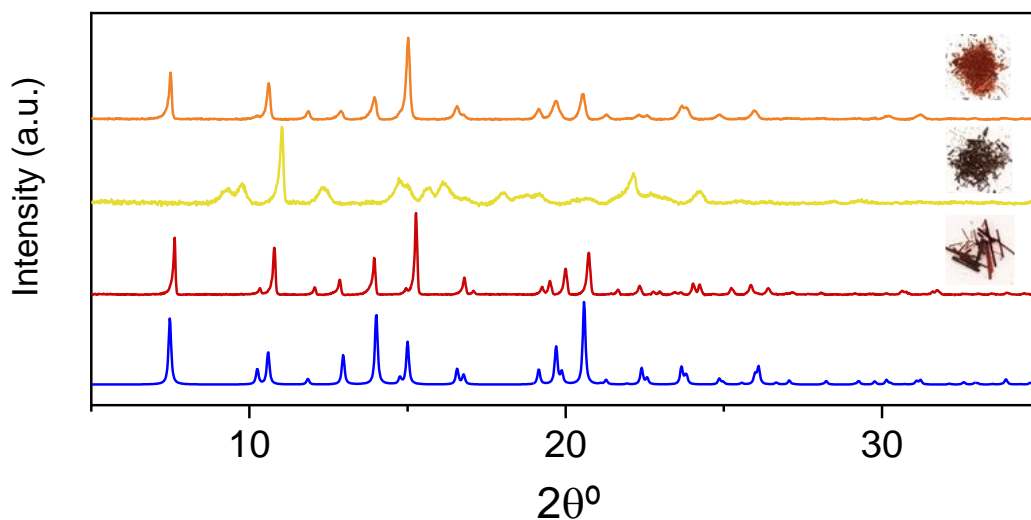


Figure SI. 2.4.14. Simulated PXRD pattern from the structure solve at 300 K (blue), experimental one at 300 K (red), experimental PXRD pattern of the desolvated sample (yellow) and experimental PXRD pattern of the resolvated sample (orange) of $1(\text{AsF}_6)_2 \cdot y\text{Me}_2\text{CO}$.

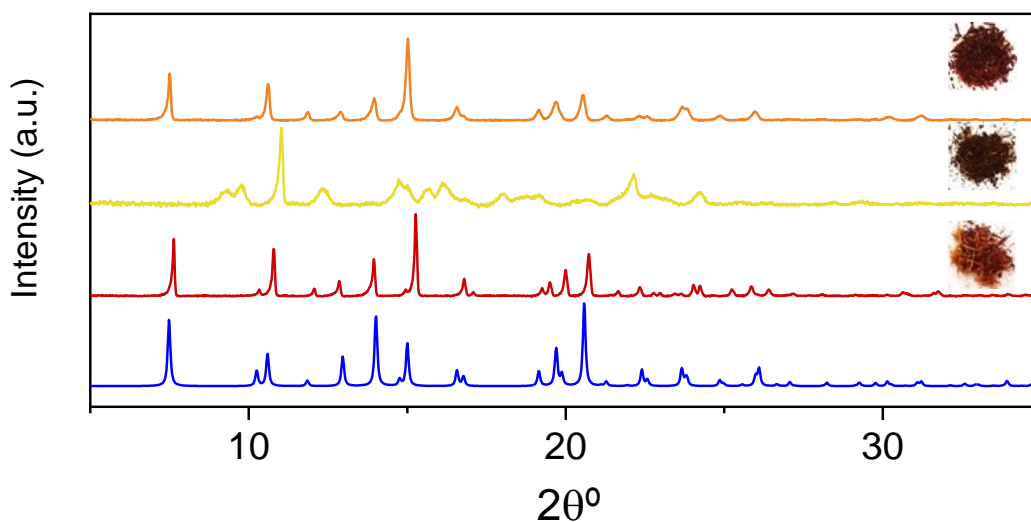


Figure SI. 2.4.15. Simulated PXRD pattern from the structure solve at 300 K (blue), experimental one at 300 K (red), experimental PXRD pattern of the desolvated sample (yellow) and experimental PXRD pattern of the resolvated sample (orange) of $1(\text{SbF}_6)_2 \cdot y\text{Me}_2\text{CO}$.

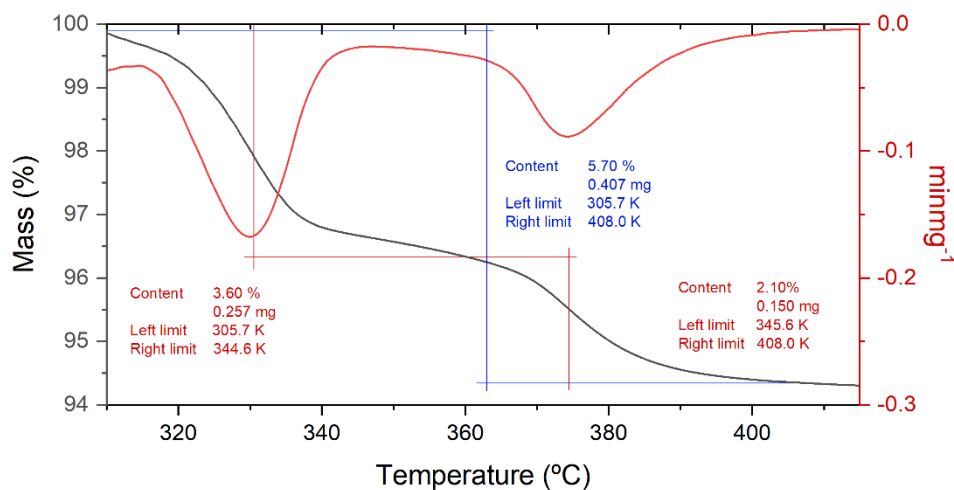


Figure SI. 2.4.16. Thermogravimetric profile of $1(\text{AsF}_6)_2 \cdot y\text{Me}_2\text{CO}$ (7.15 mg, black line) and its derivative (red line) in heating mode from 300 K to 450 K (at 10 °C/min). The mass lost after this ramp corresponds to 5.70 % of the total weigh, which is in agreement with the loss of one molecule of Me_2CO (ca. 5.7 %).

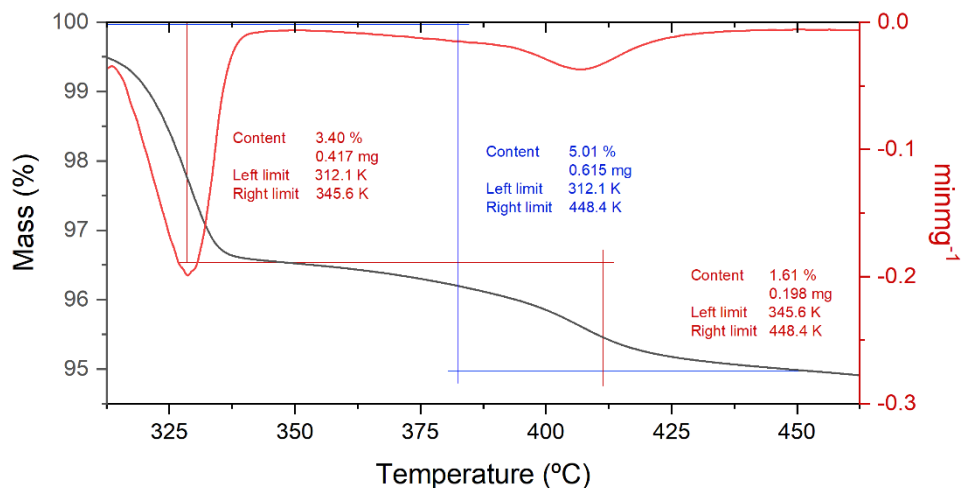


Figure SI. 2.4.17. Thermogravimetric profile of $1(\text{SbF}_6)_2 \cdot y\text{Me}_2\text{CO}$ (12.28 mg, black line) and its derivative (red line) in heating mode from 312 K to 450 K (at 10 °C/min). The mass lost after this ramp corresponds to 5.01 % of the total weigh, which is in agreement with the loss of one molecule of Me_2CO (ca. 5.3 %).

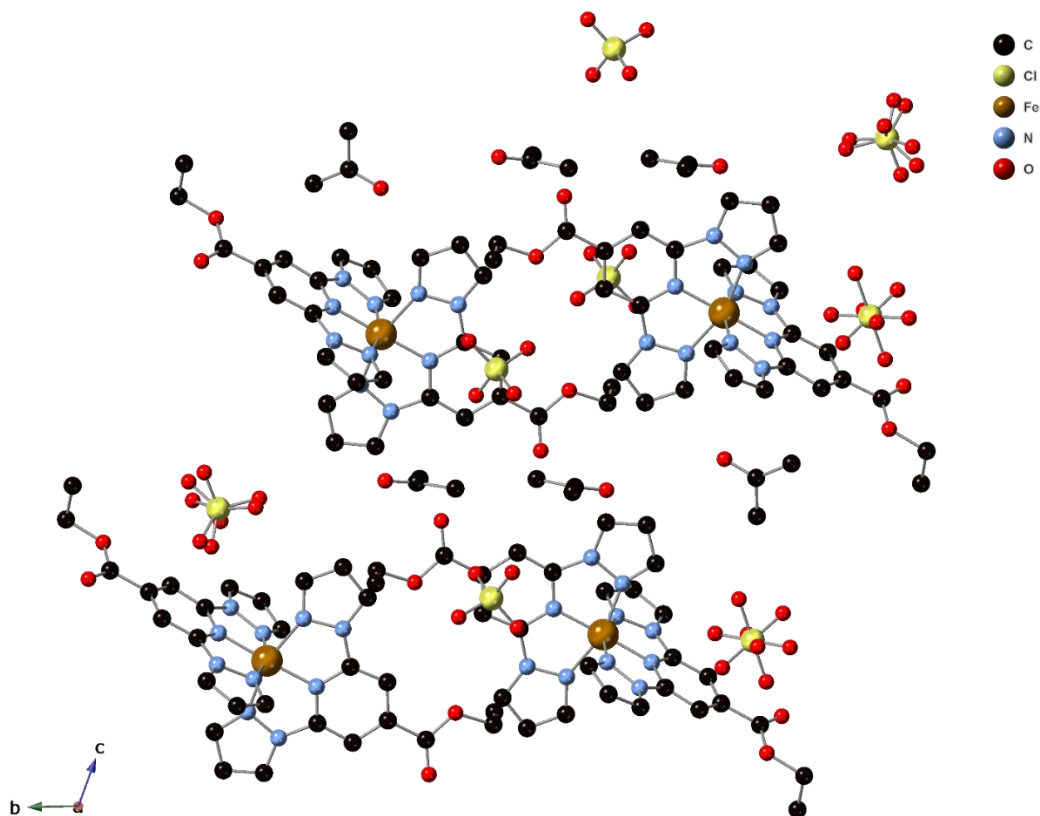


Figure SI. 2.4.18. Projection in the bc plane of the structure of $2(\text{ClO}_4)_2 \cdot y\text{Me}_2\text{CO}$ at 300K. Hydrogen atoms have been omitted for clarity.

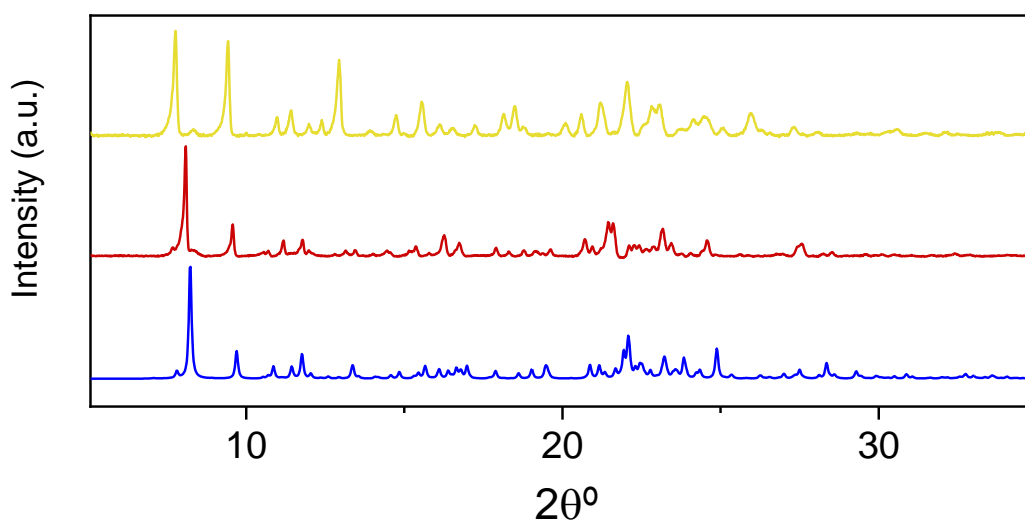


Figure SI. 2.4.19. Simulated PXRD pattern from the structure solved at 300 K (blue), experimental one at 300 K (red) and experimental PXRD pattern of the desolvated sample (yellow) of $2(\text{ClO}_4)_2 \cdot y\text{Me}_2\text{CO}$.

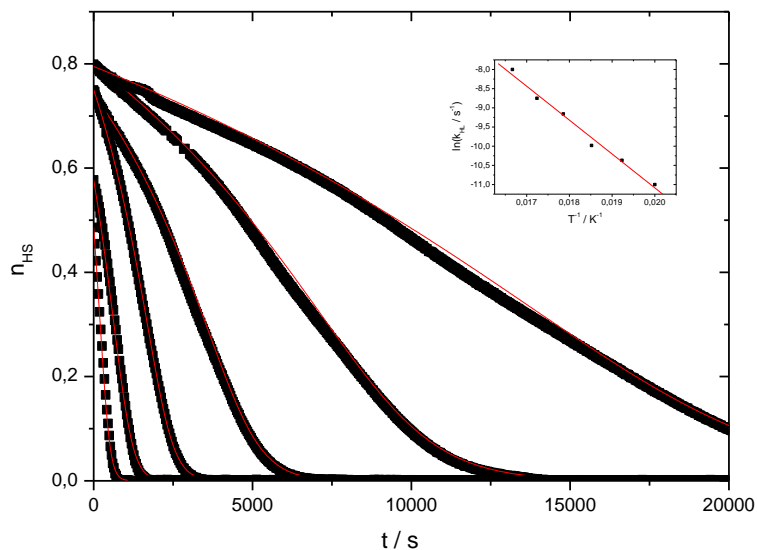


Figure SI. 2.4.20. Kinetics for $1(\text{ClO}_4)_2$.

The kinetics has been fitted using a so-called sigmoidal law. This law describes a self-accelerated process, often associated with cooperative systems. This cooperativity arises from the large difference in metal-ligand bond lengths, resulting in elastic interactions caused by change in internal pressure as the spin transition proceeds.^[46] In this model, the relaxation rate $k_{\text{HL}}(T, n_{\text{HS}})$ depends both on the temperature T and the HS fraction n_{HS} as follows:

$$\frac{d\eta_{\text{HS}}}{dt} = -k_{\text{HL}}^* \eta_{\text{HS}} \quad (1)$$

$$k_{\text{HL}}^*(T, \eta_{\text{HS}}) = k_{\text{HL}}(T) \exp[a(T)(1 - \eta_{\text{HS}})] \quad (2)$$

$$\text{where } a(T) = E_a^*/k_B T \text{ and } k_{\text{HL}}(T) = k_\infty \exp(-E_a/k_B T)$$

$\alpha(T)$ is a self-accelerated factor, E_A the activation energy of the process and k_∞ the frequency factor. For each temperature, the fitting procedure gives a value of $k_{\text{HL}}(T)$ and $\alpha(T)$. Both values are summarized in the

Table S.I. 2.4.2.**Table S.I. 2.4.2.** $k_{HL}(T)$ and $\alpha(T)$ for compound **1(ClO₄)₂**

T (K)	k_{HL} (s⁻¹)	α (T)
50	1.67017E-5	3.012
52	3.14302E-5	3.149
54	4.62833E-5	3.544
56	1.05163E-4	3.417
58	1.58461E-4	3.300
60	3.35463E-4	3.189

An Arrhenius plot allows the determination of the frequency factor and activation energy for the compound: $E_A = 614 \text{ cm}^{-1}$ and $k_\infty = 723 \text{ s}^{-1}$.

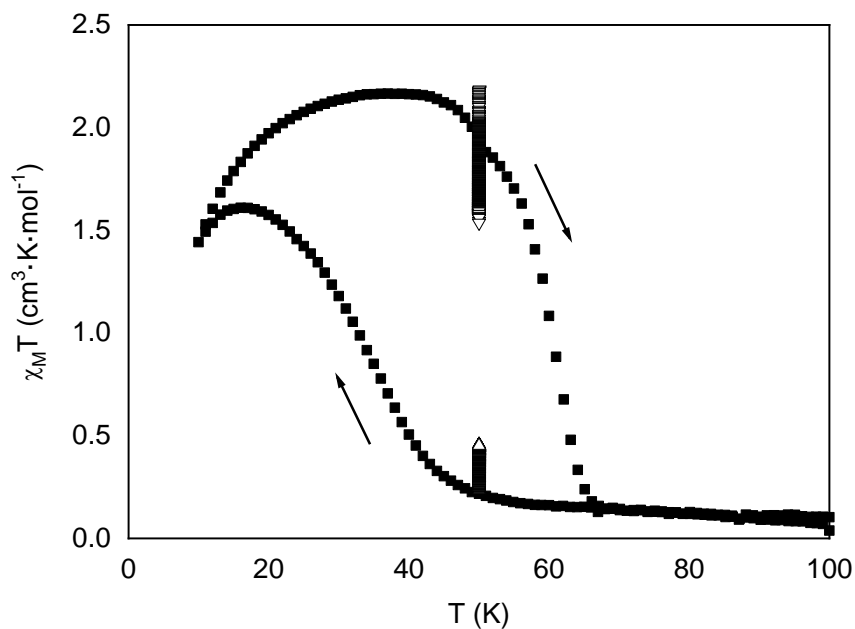


Figure SI. 2.4.21. LITH and static points for $1(\text{ClO}_4)_2$.

A clear LITH hysteresis is observed below 70 K, that is to say that the $\chi_M T$ product is strongly different when recorded decreasing or increasing the temperature. The size and shape of LITH curve is known to be strongly dependent on the temperature sweep rate. In order to search for the possible existence of a static LITH, two kinetics under irradiation have been recorded at 50 K (**Figure SI. 2.4.21**). One kinetic has been recorded first irradiating the sample at 100 K, then decreasing rapidly the temperature to 50 K and starting the kinetic as soon as the temperature is stable at 50 K. The second kinetic has been recorded the same way but first irradiating the compound at 10 K. The two kinetics are also reported below as a function of time (**Figure SI. 2.4.22**).

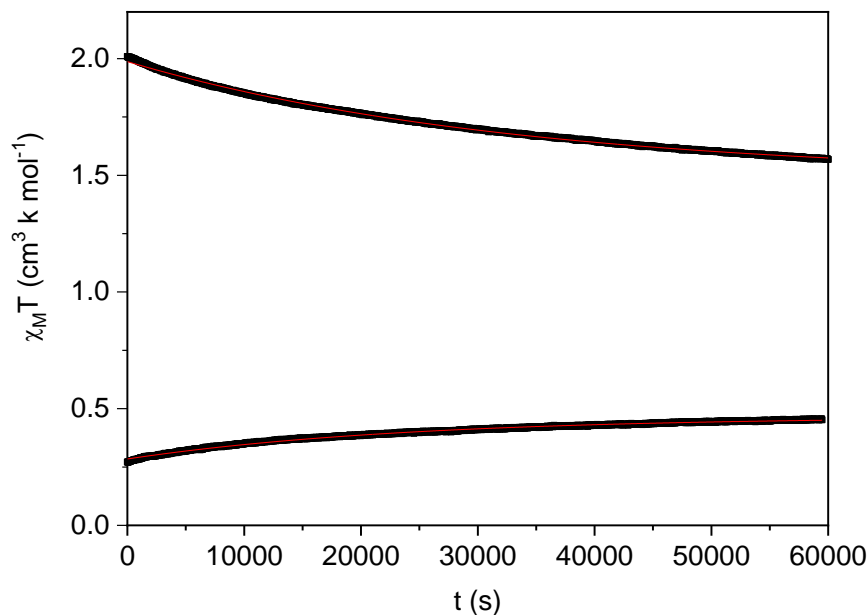


Figure SI. 2.4.22. Kinetics of the static points for $1(\text{ClO}_4)_2$.

The two kinetics at 50 K can be reasonably well fitted by simple exponential functions (red lines of **Figure SI. 2.4.22**). It can be extrapolated that at infinite time the two curves are separated by about $1.0 \text{ cm}^3 \text{ K mol}^{-1}$.

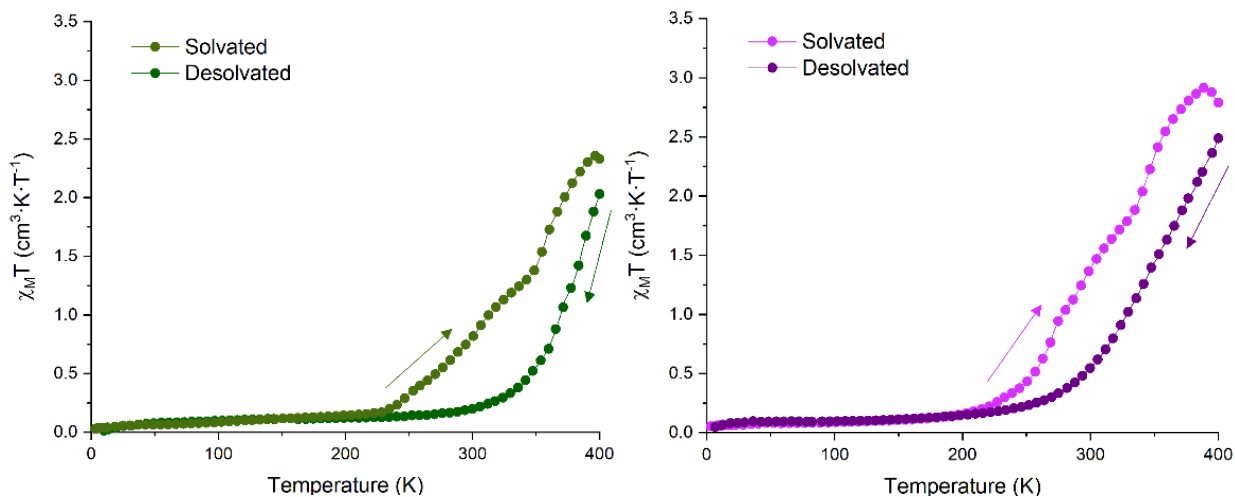


Figure SI. 2.4.23. Thermal dependence of $\chi_M T$ product in the heating mode from 2 – 400 K (light) and subsequent cooling mode from 400 – 2 K (dark) of $1(\text{AsF}_6)_2 \cdot y\text{Me}_2\text{CO}$ (left, green) and $1(\text{SbF}_6)_2 \cdot y\text{Me}_2\text{CO}$ (right, pink).

Table S.I. 2.4.3. Crystallographic data

Compound	1(BF₄)₂	1(BF₄)₂	1(CF₃SO₃)₂·Me₂CO	1(CF₃SO₃)₂·0.5Me₂CO
Empirical formula	C ₂₄ H ₁₈ B ₂ F ₈ FeN ₁₀ O ₄	C ₂₄ H ₁₈ B ₂ F ₈ FeN ₁₀ O ₄	C ₂₉ H ₂₄ F ₆ FeN ₁₀ O ₁₁ S ₂	C ₅₅ H ₄₂ F ₁₂ Fe ₂ N ₂₀ O ₂₁ S ₄
Formula weight	739.95	739.95	922.55	1787.02
Crystal color	Orange	Orange	Orange	Orange
Temperature (K)	120	350	120	300
Wavelength (Å)	0.71073	0.71073	0.71073	0.71073
Crystal system, Z	Monoclinic, 4	Monoclinic, 4	Orthorhombic, 8	Orthorhombic, 4
Space group	<i>C2/c</i>	<i>C2/c</i>	<i>Pcab</i>	<i>Pcab</i>
<i>a</i> (Å)	17.1725(4)	17.3370(10)	14.8997(4)	15.1365(3)
<i>b</i> (Å)	16.0377(4)	16.5488(8)	21.7329(5)	21.8413(4)
<i>c</i> (Å)	10.6830(3)	10.692(5)	22.2566(4)	22.3085(4)
β (°)	106.691(3)	104.976(5)	90	90
<i>V</i> (Å ³)	2818.22(12)	2963.3(14)	7207.0(3)	7375.2(2)
ρ_{calc} (Mg/m ³)	1.744	1.659	1.700	1.609
$\mu(\text{MoK}\alpha)$ (mm ⁻¹)	0.643	0.611	0.640	0.621
θ range (°)	2.92 to 27.53	2.85 to 27.53	3.258 to 27.471	3.342 to 27.497
Reflns collected	36207	33269	30229	25242
Independent reflns, (<i>R</i> _{int})	3248 (0.0905)	3412 (0.0998)	7672 (0.0714)	7655 (0.0290)
L. S. parameters/restraints	225/0	221/0	532/0	532/0
<i>R</i> 1(<i>F</i>), ^[a] $\geq 2\sigma(I)$	0.0347	0.0787	0.0513	0.0501
<i>wR</i> 2(<i>F</i> ²), ^[b] all data	0.0891	0.2521	0.1032	0.1654
<i>S</i> (<i>F</i> ²), ^[c] all data	1.050	1.066	1.029	1.069

[a] $RI(F) = \sum(|F_o| - |F_c|)/\sum|F_o|$; [b] $wR2(F^2) = [\sum w(F_o^2 - F_c^2)^2/\sum wF_o^4]^{1/2}$; [c] $S(F^2) = [\sum w(F_o^2 - F_c^2)^2/(n - p)]^{1/2}$

Compound	1(AsF₆)₂·Me₂CO	1(SbF₆)₂·Me₂CO	1(AsF₆)₂·2Me₂CO	1(SbF₆)₂·2Me₂CO
Empirical formula	C ₂₇ H ₂₄ As ₂ F ₁₂ FeN ₁₀ O ₅	C ₂₇ H ₂₄ F ₁₂ FeN ₁₀ O ₅ Sb ₂	C ₃₀ H ₃₀ As ₂ F ₁₂ FeN ₁₀ O ₆	C ₃₀ H ₃₀ F ₁₂ FeN ₁₀ O ₆ Sb ₂
Formula weight	1002.25	1095.93	1060.33	1153.99
Crystal color	Orange	Orange	Orange	Orange
Temperature (K)	300	300	120	120
Wavelength (Å)	0.71073	0.71073	0.71073	0.71073
Crystal system, Z	Tetragonal, 8	Tetragonal, 8	Tetragonal, 8	Tetragonal, 8
Space group	<i>I</i> ₄ cd	<i>I</i> ₄ cd	<i>I</i> ₄ cd	<i>I</i> ₄ cd
<i>a</i> (Å)	23.4197(9)	23.6034(15)	23.3533(3)	23.4653(2)
<i>c</i> (Å)	14.6422(8)	14.9526(17)	14.3811(3)	14.6485(3)
β (°)	90	90	90	90
<i>V</i> (Å ³)	8031.0(8)	8330.4(14)	7843.1(3)	8065.8(2)
ρ_{calc} (Mg/m ³)	1.658	1.748	1.796	1.901
$\mu(\text{MoK}\alpha)$ (mm ⁻¹)	2.115	1.732	2.173	1.796
θ range (°)	3.282 to 27.540	3.226 to 27.604	3.227 to 27.489	3.279 to 27.530
Reflns collected	21855	19539	15144	65363
Independent reflns, (<i>R</i> _{int})	4345 (0.0905)	4802 (0.1398)	4151 (0.0480)	4631 (0.0745)
L. S. parameters/restraints	330/1	276/1	276/1	276/1
<i>R</i> 1(<i>F</i>), ^[a] $\geq 2\sigma(I)$	0.0609	0.0679	0.0391	0.0315
<i>wR</i> 2(<i>F</i> ²), ^[b] all data	0.1845	0.1825	0.0854	0.0773
<i>S</i> (<i>F</i> ²), ^[c] all data	0.962	0.957	1.046	1.114

[a] $RI(F) = \sum(|F_o| - |F_c|)/\sum|F_o|$; [b] $wR2(F^2) = [\sum w(F_o^2 - F_c^2)^2/\sum wF_o^4]^{1/2}$; [c] $S(F^2) = [\sum w(F_o^2 - F_c^2)^2/(n - p)]^{1/2}$.

Compound	2(ClO₄)₂·Me₂CO	2(ClO₄)₂·Me₂CO
Empirical formula	C ₃₁ H ₃₂ Cl ₂ FeN ₁₀ O ₁₃	C ₃₁ H ₃₂ Cl ₂ FeN ₁₀ O ₁₃
Formula weight	879.41	879.41
Crystal color	Orange	Orange
Temperature (K)	120	293
Wavelength (Å)	0.71073	0.71073
Crystal system, Z	Triclinic, 2	Triclinic, 2
Space group	<i>P</i> -1	<i>P</i> -1
<i>a</i> (Å)	8.4530(4)	8.5577(14)
<i>c</i> (Å)	11.9312(6)	12.0263(17)
α (°)	20.3299(10)	20.578(2)
β (°)	77.745(4)	76.962(10)
γ (°)	82.954(4)	81.395(11)
<i>V</i> (Å ³)	75.170(4)	75.959(13)
ρ_{calc} (Mg/m ³)	1.512	1.467
$\mu(\text{MoK}\alpha)$ (mm ⁻¹)	0.605	0.587
θ range (°)	3.264 to 27.486	3.341 to 26.437
Reflns collected	26171	23761
Independent reflns, (<i>R</i> _{int})	8009 (0.1013)	8144 (0.1369)
L. S. parameters/restraints	539/10	495/0
<i>R</i> 1(<i>F</i>), ^[a] <i>I</i> > 2 σ (<i>I</i>)	0.0910	0.1261
<i>wR</i> 2(<i>F</i> ²), ^[b] all data	0.2806	0.4176
<i>S</i> (<i>F</i> ²), ^[c] all data	1.062	1.005

[a] $RI(F) = \sum(|F_o| - |F_c|) / \sum|F_o|$; [b] $wR2(F^2) = [\sum w(F_o^2 - F_c^2)^2 / \sum wF_o^4]^{1/2}$; [c] $S(F^2) = [\sum w(F_o^2 - F_c^2)^2 / (n - p)]^{1/2}$.

2.5. References

- [1] E. J. Devid, P. N. Martinho, M. V. Kamalakar, I. Šalitroš, Ú. Prendergast, J. F. Dayen, V. Meded, T. Lemma, R. González-Prieto, F. Evers, T. E. Keyes, M. Ruben, B. Doudin, S. J. van der Molen, *ACS Nano* **2015**, *9*, 4496.
- [2] L. Pukenas, Fabrication and Characterisation of SAMs for Spin Crossover and Photocleavable Surfaces, University of Leeds, **2017**.
- [3] I. Capell, Design of New Spin-Crossover Materials for Surface Deposition, University of Leeds, **2019**.
- [4] A. Abhervé, M. Clemente-León, E. Coronado, C. J. Gómez-García, M. López-Jordà, *Dalton Transactions* **2014**, *43*, 9406.
- [5] S. A. Jadhav, *Central European Journal of Chemistry* **2011**, *9*, 369.
- [6] C. Klein, E. Baranoff, M. Grätzel, M. K. Nazeeruddin, *Tetrahedron Letters* **2011**, *52*, 584.
- [7] T. Vermonden, D. Branowska, A. T. M. Marcelis, E. J. R. Sudhölter, *Tetrahedron* **2003**, *59*, 5039.
- [8] M. A. Halcrow, *Coordination Chemistry Reviews* **2005**, *249*, 2880.
- [9] M. A. Halcrow, *Coordination Chemistry Reviews* **2009**, *253*, 2493.
- [10] L. J. Kershaw Cook, R. Mohammed, G. Sherborne, T. D. Roberts, S. Alvarez, M. A. Halcrow, *Coordination Chemistry Reviews* **2015**, *289*, 2.
- [11] N. Bridonneau, L. Rigamonti, G. Poneti, D. Pinkowicz, A. Forni, A. Cornia, *Dalton Transactions* **2017**, *46*, 4075.
- [12] C. Bartual-Murgui, R. Diego, S. Vela, S. J. Teat, O. Roubeau, G. Aromí, *Inorganic Chemistry* **2018**, *57*, 11019.
- [13] A. Hauser, in *Spin Crossover in Transition Metal Compounds II. Top Current Chemistry*, Springer, Berlin, Heidelberg, **2004**, pp. 155–198.
- [14] S. Vela, H. Paulsen, *Inorganic Chemistry* **2018**, *57*, 9478.
- [15] F. Varret, K. Boukheddaden, E. Codjovi, C. Enachescu, J. Linares, **2012**, pp. 199–229.
- [16] C. Carbonera, C. A. Kilner, J. F. Létard, M. A. Halcrow, *Dalton Transactions* **2007**, 1284.

- [17] L. J. Kershaw Cook, F. L. Thorp-Greenwood, T. P. Comyn, O. Cespedes, G. Chastanet, M. A. Halcrow, *Inorganic Chemistry* **2015**, *54*, 6319.
- [18] R. Kulmaczewski, E. Trzop, L. J. Kershaw Cook, E. Collet, G. Chastanet, M. A. Halcrow, *Chemical Communications* **2017**, *53*, 13268.
- [19] C. Carbonera, J. Sánchez Costa, V. A. Money, J. Elhaïk, J. A. K. Howard, M. A. Halcrow, J. F. Létard, *Dalton Transactions* **2006**, *25*, 3058.
- [20] M. A. Halcrow, *Chemical Society Reviews* **2011**, *40*, 4119.
- [21] E. Kónig, G. Ritter, S. K Kulshreshtha, J. Waigel, H. A. Goodwin, *Inorganic Chemistry* **1984**, *23*, 1896.
- [22] J. F. Letard, L. Capes, G. Chastanet, N. Moliner, S. Letard, J.-A. Real, O. Kahn, *Chemical Physics Letters* **1999**, *313*, 115.
- [23] J. F. Létard, P. Guionneau, O. Nguyen, J. S. Costa, S. Marcén, G. Chastanet, M. Marchivie, L. Goux-Capes, *Chemistry - A European Journal* **2005**, *11*, 4582.
- [24] S. Marcen, L. Lecren, L. Capes, H. A. Goodwin, J.-F. Letard, *Chemical Physics Letters* **2002**, *358*, 87.
- [25] J.-F. Létard, P. Guionneau, L. Rabardel, J. A. K. Howard, A. E. Goeta, D. Chasseau, O. Kahn, *Inorganic Chemistry* **1998**, *37*, 4432.
- [26] T. Buchen, P. Gütlich, K. H. Sugiyarto, H. A. Goodwin, *Chemistry A European Journal* **1996**, *2*, 1134.
- [27] J. F. Létard, *Journal of Materials Chemistry* **2006**, *16*, 2550.
- [28] L. Rigamonti, N. Bridonneau, G. Poneti, L. Tesi, L. Sorace, D. Pinkowicz, J. Jover, E. Ruiz, R. Sessoli, A. Cornia, *Chemistry - A European Journal* **2018**, *24*, 8857.
- [29] C. Sánchez-Sánchez, C. Desplanches, J. M. Clemente-Juan, M. Clemente-León, E. Coronado, *Dalton Transactions* **2017**, *46*, 2680.
- [30] S. A. Jadhav, *Central European Journal of Chemistry* **2011**, *9*, 369.
- [31] K. H. Sugiyartoa, H. A. Goodwinb, *Australian Journal of Chemistry* **1988**, *41*, 1645.
- [32] S. A. Barrett, M. A. Halcrow, *RSC Advances* **2014**, *4*, 11240.
- [33] L. J. Kershaw Cook, R. Kulmaczewski, R. Mohammed, S. Dudley, S. A. Barrett, M. A. Little, R. J. Deeth, M. A. Halcrow, *Angewandte Chemie - International Edition* **2016**, *128*, 4399.

- [34] A. Santoro, L. J. Kershaw Cook, R. Kulmaczewski, S. A. Barrett, O. Cespedes, M. A. Halcrow, *Inorganic Chemistry* **2015**, *54*, 682.
- [35] I. Cebula, H. Lu, M. Zharnikov, M. Buck, *Chemical Science* **2013**, *4*, 4455.
- [36] H. Aitchison, R. Ortiz De La Morena, R. Peifer, S. Omar, H. Lu, S. M. Francis, M. Zharnikov, A. Grohmann, M. Buck, *Langmuir* **2018**, *34*, 9654.
- [37] J. A. Barth, M. Rudolph, E. Uhlig, *Zeitschrift für anorganische und allgemeine Chemie* **1986**, *632*, 65.
- [38] B. A. Sexton, N. R. Avery, *Surface Science* **1983**, *129*, 21.
- [39] L. Poggini, M. Milek, G. Londi, A. Naim, G. Poneti, L. Squillantini, A. Magnani, F. Totti, P. Rosa, M. M. Khusniyarov, M. Mannini, *Materials Horizons* **2018**, *5*, 506.
- [40] B. Schäfer, C. Rajnák, M. Ruben, O. Fuhr, D. Klar, C. Schmitz-Antoniak, H. Wende, M. Ruben, *Chemical Communications* **2013**, *49*, 10986.
- [41] N. Giaconi, A. L. Sorrentino, L. Poggini, G. Serrano, G. Cucinotta, E. Otero, D. Longo, H. Douib, F. Pointillart, A. Caneschi, R. Sessoli, M. Mannini, *Magnetochemistry* **2022**, *8*, 1.
- [42] E. C. Wasinger, F. M. F. de Groot, B. Hedman, K. O. Hodgson, E. I. Solomon, *Journal of American Chemical Society* **2003**, *125*, 12894.
- [43] J. S. Costa, S. Rodríguez-Jiménez, G. A. Craig, B. Barth, C. M. Beavers, S. J. Teat, G. Aromí, *Journal of American Chemical Society* **2014**, *136*, 3869.
- [44] V. Jornet-Mollá, Y. Duan, C. Giménez-Saiz, Y. Y. Tang, P. F. Li, F. M. Romero, R. G. Xiong, *Angewandte Chemie - International Edition* **2017**, *56*, 14052.
- [45] L. Pukenas, F. Benn, E. Lovell, A. Santoro, L. J. Kershaw Cook, M. A. Halcrow, S. D. Evans, *Journal of Materials Chemistry C* **2015**, *3*, 7890.
- [46] A. Hauser, P. Gütlich, H. Spiering, *Inorganic Chemistry* **1986**, *25*, 4245.

Chapter 3

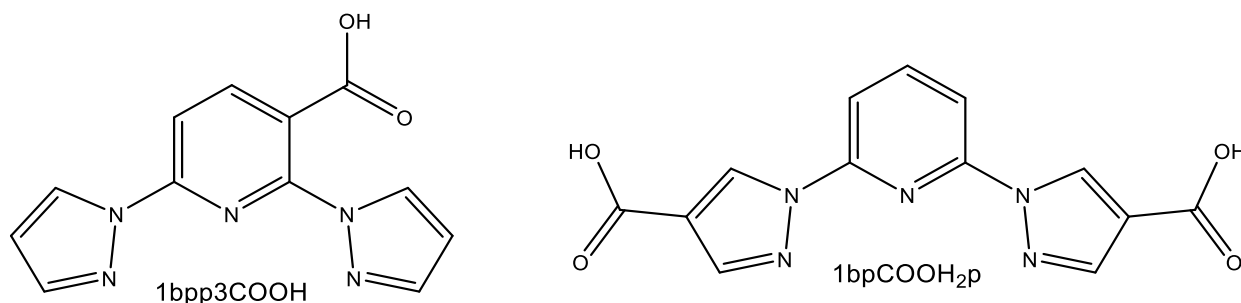
3. Fe(II) SCO complexes of 1bpp derivatives functionalized with carboxylic acid groups in the 3-pyridyl (1bpp3COOH) and 4-pyrazolyl (1bpCOOH_{2p}) positions

V. García-López, M. Palacios-Corella, M. Clemente-León, and E. Coronado, "Fe(II) spin crossover complexes of a derivative of 2,6-bis(pyrazol-1-yl)pyridine (1-bpp) functionalized with a carboxylic acid in the 3-pyridyl position" *Polyhedron*, vol. 170, **2019**, doi: 10.1016/j.poly.2019.05.029.

V. García-López, M. Palacios-Corella, S. Cardona-Serra, M. Clemente-León, and E. Coronado, "Spin-crossover iron(II) complex showing thermal hysteresis around room temperature with symmetry breaking and an unusually high: T (LIESST) of 120 K" *Chemical Communications*, vol. 55, no. 81, **2019**, doi: 10.1039/c9cc05988a.*

3.1. Motivation

In the previous chapter, we have prepared the homoleptic Fe(II) complexes of 1bpp ligand functionalized with a carboxylic acid at the 4-pyridyl position and the ethyl derivative (1bppCOOH and bppCOOEt see Chapter 2). We showed that the solvent-free ClO_4^- and BF_4^- salts of $[\text{Fe}(\text{bppCOOH})_2]^{2+}$ exhibit abrupt thermal and light-induced spin transition related to the presence of a hydrogen-bonded linear network of complexes, whereas the incorporation of solvent molecules in the salts with bulkier counteranions (CF_3SO_3^- , SbF_6^- and AsF_6^-) or ligands (1bppCOOEt) gives rise to solvent-induced SCO, which in some case are reversible. In this chapter, we have prepared the Fe(II) complex of two new derivatives of 1bpp bearing carboxylic acids at the 3-pyridyl position (1bpp3COOH, see **Scheme 3.1.1**, left) and at the 4-positions of the two pyrazolyl groups (1bpCOOH_{2p}, see **Scheme 3.1.1**, right). These ligands were prepared for the first time by us. The aim of this work is to explore the SCO properties induced by the change in position of this functional group, which could offer new possibilities for the preparation of organized assemblies of these SCO units by coordination to other metals or deposition on surfaces. For a better reading, this chapter will be divided into two parts. Each part is dedicated to the different Fe(II) SCO complexes obtained with each ligand.



Scheme 3.1.1. Molecular structure of 1bpp3COOH (left) and 1bpCOOH_{2p} (right).

Since LIESST compounds are photo-activated molecular switches, there is great interest in finding compounds operating at high temperature.^[1] From the theoretical part, mean-field theory predicts an inverse relationship between the thermodynamic thermal SCO temperature $T_{1/2}$ and the lifetime of the photoinduced metastable state. Due to this, with the exception of a few Fe-Co Prussian blue analogues,^[2] there are no reports of Fe coordination compounds combining thermal SCO around room temperature and photo-induced SCO at temperatures above 100 K. Although important deviations from the empirical linear dependence between $T(\text{LIESST})$ and $T_{1/2}$ proposed by Létard in Fe(II) complexes have been found, it is a useful tool to predict the $T(\text{LIESST})$ of many

SCO compounds.^[3] For instance, $T(\text{LIESST})$ of bis-chelated Fe(II) complexes of the tridentate 1bpp^[1,4-7] usually show good agreement with this linear function with $T_0 = 150$ K. This means that the highest values of $T(\text{LIESST})$ for this family of compounds (~ 100 K) correspond in all cases to $T_{1/2}$ values below 200 K, which are far from room temperature.^[4,6-10] In the second part of this chapter, we have shown that the use of a new 1bpp derivative functionalized with carboxylic acid groups in the 4-positions of the two pyrazolyl groups of 1bpp affords the compound $[\text{Fe}(\text{bpCOOH}_2\text{p})_2](\text{ClO}_4)_2 \cdot 3.5\text{Me}_2\text{CO}$ (**2**), which shows an abrupt thermal SCO around room temperature and a photoinduced SCO with an unusually high $T(\text{LIESST})$ of 120 K. This has led to a detailed photo-structural and photomagnetic characterization presented in Part B of this chapter.

3.2. Results and discussion

PART A

*Synthesis of $[\text{Fe}(1\text{bpp}3\text{COOH})_2](\text{ClO}_4)_2 \cdot 0.5\text{EtOH} \cdot 0.5\text{H}_2\text{O}$ (**1**)*

1bpp3COOH was prepared following a similar synthetic procedure to that used with 1bpCOOHp by reacting dichloronicotinic acid and the pyrazolyl radical generated in situ with sodium hydride.^[11] $[\text{Fe}(1\text{bpp}3\text{COOH})_2]^{2+}$ was obtained by slow diffusion of diethyl ether into solutions of $\text{Fe}(\text{ClO}_4)_2 \cdot x\text{H}_2\text{O}$ and 1bpp3COOH in ethanol in a 1:2 molar ratio. After a few days crystals of $[\text{Fe}(1\text{bpp}3\text{COOH})_2](\text{ClO}_4)_2 \cdot 0.5\text{EtOH} \cdot 0.5\text{H}_2\text{O}$ (**1**) suitable for single crystal X-ray diffraction were obtained (see SI for more details). Elemental analysis of an older sample is consistent with the replacement of the EtOH solvent molecules in the structure for water and further absorption in contact with air. This agrees with TG measurements (see **Figure SI. 3.4.1**) and with the small differences observed in the PXRD pattern of a freshly filtered sample of **1** (see **Figure SI. 3.4.2**).

Else, single crystal structure of the compound obtained in methanol showed that, instead of the expected $[\text{Fe}(1\text{bpp}3\text{COOH})_2]^{2+}$ complex, the complex of methyl ester (1bpp3COOMe) was obtained in the compound of formula $[\text{Fe}(1\text{bpp}3\text{COOMe})_2](\text{ClO}_4)_2$. This esterification reaction of the carboxylic acid with the methanol solvent molecules is favored when the ligand is coordinated to the Fe(II) ion since similar conditions in absence of Fe(II) salt did not lead to the formation of the ester. Further characterization of the crystals obtained in different positions of the diffusion tube indicated that the slow reaction of 1bpp3COOH with MeOH in the complex at different methanol/diethyl ether concentrations gave rise to a mixture of compounds containing the

homoleptic $[\text{Fe}(\text{1bpp3COOH})_2]^{2+}$ and $[\text{Fe}(\text{1bpp3COOMe})_2]^{2+}$ and the heteroleptic $[\text{Fe}(\text{1bpp3COOMe})(\text{1bpp3COOH})]^{2+}$ complexes, which are difficult to separate. The optimization of these syntheses to obtain the pure homoleptic and heteroleptic complexes of these ligands in methanol is in progress. Due to the problems to obtain the pure complex in other solvents we have focused our studies in **1**.

*Structure of $[\text{Fe}(\text{1bpp3COOH})_2](\text{ClO}_4)_2 \cdot 0.5\text{EtOH} \cdot 0.5\text{H}_2\text{O}$ (**1**)*

The crystal structure of **1** has been solved at 120 K. It crystallizes in the tetragonal crystal system with the non-centrosymmetric achiral $I-42d$ space group. The asymmetric unit is formed by half $[\text{Fe}(\text{1bpp3COOH})_2]^{2+}$ cation, two half perchlorate anions and one ethanol and water disordered solvent molecules (see **Figure 3.2.1**). The central Fe(II) ion of the complex presents a multiplicity of 0.5 due to the presence of 2-fold and 4-fold rotoinversion axes. It is coordinated by six nitrogen atoms from two tridentate 1bpp3COOH ligands with a distorted octahedral coordination geometry. The short Fe-N bond lengths at 120 K (1.865(10) - 1.992(17) Å) clearly indicate that the complex is in the LS state in agreement with magnetic measurements.

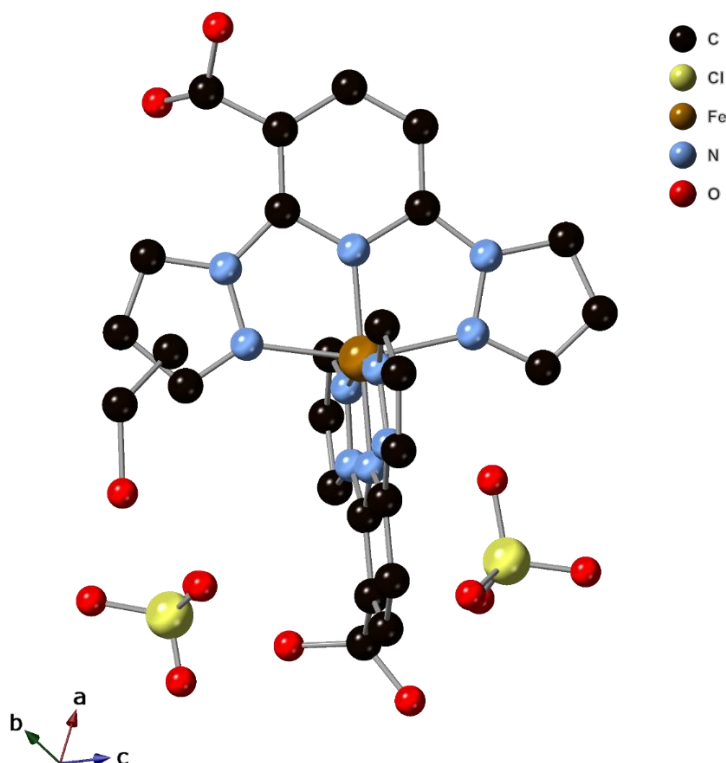


Figure 3.2.1. Structural view of $[\text{Fe}(\text{1bpp3COOH})_2]^{2+}$ complex in **1**; hydrogen atoms have been omitted for clarity; only one of the two possible configurations of disordered carboxylic acid groups is shown for clarity.

The coordination geometry is close to the ideal D_{2d} symmetry associated to a $[\text{Fe}(\text{1bpp})_2]^{2+}$. It presents a (*trans*-N(pyridyl)-Fe-N(pyridyl) angle (ϕ) of 180° and dihedral angle between the least squares planes of the two ligands (θ) close to 88.7° . These values are consistent with those of other LS bpp complexes exhibiting SCO obtained by us (see Chapter 2) and in the literature.^[4,7,12,13] The carboxylic acid group is disordered, which has been solved with two possible configurations with an occupancy of 50% each. The crystal packing of the complexes is shown in **Figure SI. 3.4.3**. $[\text{Fe}(\text{1bpp3COOH})_2]^{2+}$ cations form chains which run along the *c* axis that are surrounded by ClO_4^- anions and disordered solvent molecules. $[\text{Fe}(\text{1bpp3COOH})_2]^{2+}$ complexes interact with each other mainly through $\text{CH}\cdots\text{O}$ contacts between pyrazole groups. The two carboxylic acid groups of $[\text{Fe}(\text{1bpp3COOH})_2]^{2+}$ are involved in hydrogen bonds with two ethanol molecules (see **Figure SI. 3.4.4**). This prevents them from interacting among $[\text{Fe}(\text{1bpp3COOH})_2]^{2+}$, as it has been also seen in $[\text{Fe}(\text{1bppCOOH})_2]^{2+}$ salts of SbF_6^- and AsF_6^- (see Chapter 2).

Magnetic and photomagnetic properties

χ_{MT} of **1** shows a value close to 0 from 300 to 2 K in the cooling and heating modes (see **Figure 3.2.2**). This indicates a diamagnetic LS state of the Fe(II) centers in agreement with short Fe-N bond lengths from the structure at 120 K (see above). At temperatures above 300 K, there is an abrupt increase that upon desolvation of the complex at 400 K reaches a value of *c.a.* $2 \text{ cm}^3\cdot\text{K}\cdot\text{mol}^{-1}$. This value corresponds to around 60% of molecules in the HS state, taking $3.5 \text{ cm}^3\cdot\text{K}\cdot\text{mol}^{-1}$ as the value for pure HS state. This partial SCO is irreversible as χ_{MT} decreases gradually to reach a plateau of $0.5 \text{ cm}^3\cdot\text{K}\cdot\text{mol}^{-1}$ at temperatures below 100 K stabilizing the HS state. The irreversibility of this behavior confirms that it is related to the loss of the solvent molecules observed in the structure at 120 K (EtOH and H_2O). Indeed, PXRD of the desolvated sample shows an irreversible loss of crystallinity (see **Figure SI. 3.4.2**). Therefore, the solvated compound is mostly LS in all the range of temperatures, while the desolvated one shows a gradual and partial SCO from 400 to 100 K related to an irreversible change of structure.

Photomagnetic properties of the solvated (freshly filtered crystals) and desolvated **1** (heated previously at 400 K) were measured after light irradiation at 10 K with a 532 nm laser. A clear increase of the magnetic signal is observed in the two samples (see **Figure 3.2.2**). The maximum χ_{MT} value of solvated **1** after irradiation is $0.6 \text{ cm}^3\cdot\text{K}\cdot\text{mol}^{-1}$, which indicates that about 15% of Fe(II) has been photo-converted with a $T(\text{LIESST})$ of 40 K. On the other hand, an increase of *ca.* $1 \text{ cm}^3\cdot\text{K}\cdot\text{mol}^{-1}$ is observed for the maximum value of χ_{MT} of desolvated **1** after irradiation, which corresponds to about 30 % of LS to HS photoconversion with a $T(\text{LIESST})$ of 50 K. Therefore,

the decrease of the thermal SCO of the desolvated sample gives rise to an increase of T(LIESST) as expected by the “inverse energy gap law”.^[14,15]

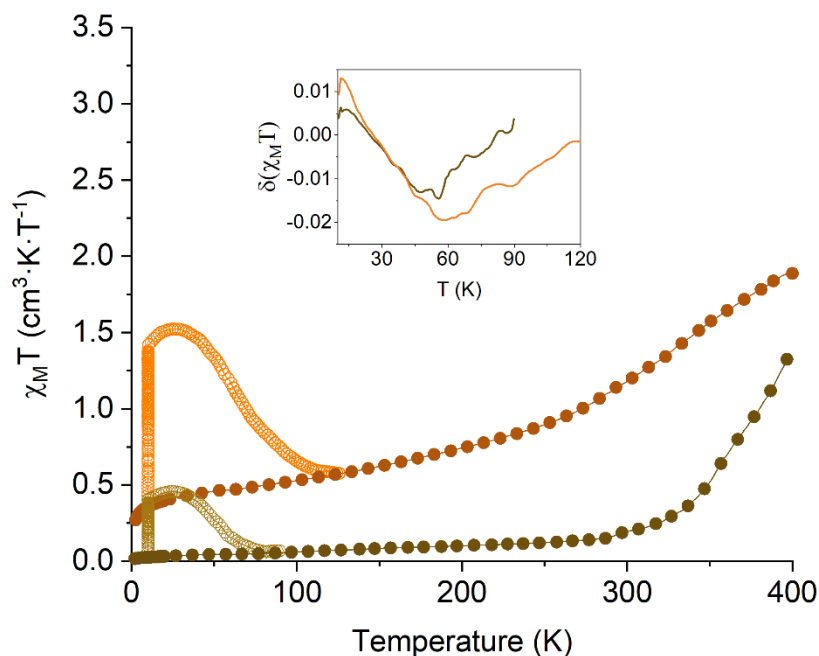


Figure 3.2.2. Temperature dependence of $\chi_M T$ for solvated (dark yellow) and desolvated (orange) **1** before (full circles) and after (empty circles) light irradiation.

Deposition

The procedure for surface deposition was the same as that used in Chapter 2. UV/Vis spectra confirms the stability of the complex in solution with a possible partial decomposition (see **Figure SI. 3.4.5** and associated text). Topographic images confirm the absence of aggregates, and the roughness is consistent with the formation of an ordered monolayer (see **Figure SI. 3.4.6** and associated text). The presence of the ligand was evidenced with MALDI-TOF MS measurements (**Figure SI. 3.4.7** and associated text) and confirmed with XPS spectroscopy semiquantitative analysis (**Figure SI. 3.4.8**, associated text and **Table S.I. 3.4.1**, top). XPS elemental ratios suggest the presence of [Fe(1bpp3COOH)] species, as we have seen in Chapter 2 with [Fe(1bppCOOH)] as well (**Table S.I. 3.4.1**, bot). Finally, the electronic states of our sample were studied by XAS. The spectrum **1-SAM** displays the characteristic Fe(III) shape (see **Figure SI. 3.4.9**). This result was expected since XPS ratios mimics the results obtained previously in Chapter 2.

PART B

*Synthesis of $Fe(1bpCOOH_2p)_2](ClO_4)_2 \cdot 3.5Me_2CO$ (**2**) and $[Fe(1bpCOOCOOHp)(1bpCOOH_2p)Fe(1bpCOOH_2p)(ClO_4)](ClO_4)_2 \cdot H_2O \cdot 1.5Me_2CO$ (**3**)*

1bpCOOH₂p was synthesized by saponification of the 2,6-di[4-(ethylcarboxy)pyrazol-1-yl]pyridine ester precursor.^[12] $[Fe(1bpCOOH_2p)_2]^{2+}$ was obtained by slow diffusion of diethyl ether into solutions of $Fe(ClO_4)_2 \cdot xH_2O$ and 1bpCOOH₂p in acetone in a 1:2 molar ratio. After a few days in inert atmosphere, crystals of $Fe(1bpCOOH_2p)_2](ClO_4)_2 \cdot 3.5Me_2CO$ (**2**) suitable for single crystal X-ray diffraction were obtained (see SI for more details). On the other hand, the coordination polymer $[Fe(1bpCOOCOOHp)(1bpCOOH_2p)Fe(1bpCOOH_2p)(ClO_4)](ClO_4)_2 \cdot H_2O \cdot 1.5Me_2CO$ (**3**) was obtained in the synthesis of **2** if the diffusion tubes were left in air (see **Figure SI. 3.4.11** and **Figure SI. 3.4.12** in the SI and associated text).

Magnetic properties

$\chi_M T$ of **2** below 270 K measured in contact with the mother liquor presents a value close to 0 cm³·K·mol⁻¹, consistent with the diamagnetic LS state ($S = 0$) (see **Figure 3.2.3**). At higher temperatures, $\chi_M T$ shows a sharp increase to a value of 1.6 cm³·K·mol⁻¹ at 300 K, consistent with ca. 50% of conversion of the Fe(II) centers from LS to HS. A thermal hysteresis width (ΔT) of 13 K is observed in heating and cooling modes ($T_{\uparrow} = 292$ K and $T_{\downarrow} = 279$ K) at a scan rate of 0.5 K·min⁻¹. Abrupt thermal hysteretic spin transitions with $\Delta T = 1-4$ K are common in bpp Fe(II) complexes with a particular packing motif, the so-called “terpyridine embrace” one.^[1,4,7,10,16] However, the few examples with wider thermal hysteresis are associated to compounds with distorted octahedral coordination in the HS state, crystallographic phase transitions ($\Delta T = 18$ K^[17]) and/or lattice solvent molecules ($\Delta T = 35$ ^[18] and ~ 100 K^[19]). The hysteretic spin transition was confirmed by differential scanning calorimetry (DSC) measurements in crystals protected with an oil. (**Figure SI. 3.4.13** in the SI) Thus, an exothermic peak at 286 K upon cooling and an endothermic peak at 297 K of the subsequent heating were observed. There is a shift in temperature of around 5 K to higher temperatures with respect to the magnetic measurements (see above), which could be related to the different method used to protect the crystals (oil in DSC and mother liquor in magnetic measurements) and to the different scan rate in both measurements. The average enthalpy and entropy changes associated with these peaks, $\Delta H = 17.0$ kJ·mol⁻¹ and $\Delta S = 60.0$ J·K⁻¹·mol⁻¹, are typical values for Fe(II) SCO solids.^[20] These values are similar to the ones found for other Fe(II) bpp complexes,^[17,21] although they are relatively high if we consider that only half of the Fe(II) centers undergoes spin transition. DSC measurements shows that this LS-HS phase is stable up to 320 K. Then, the second cycle shows a broadening

of the peaks, which is not rare in SCO complexes usually related to fatigue or changes in the structure.^[22] $\chi_{\text{M}}T$ of dried crystals of **2** changes drastically. It increases to a value of $3.6 \text{ cm}^3\cdot\text{K}\cdot\text{mol}^{-1}$ after heating to 400 K corresponding to 100% HS state. The value remains almost constant with a decrease below 30 K due to zero-field-splitting of HS Fe(II) (**Figure SI. 3.4.14** in the SI and associated text). This suggests that desolvation leads to irreversible structural changes that stabilize the HS state as confirmed by PXRD data (see **Figure SI. 3.4.15** in the SI).

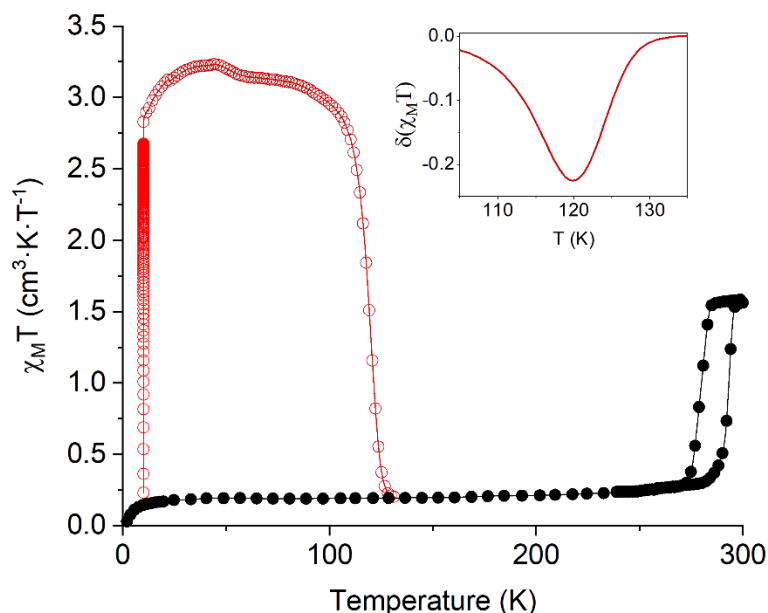


Figure 3.2.3. Thermal variation of $\chi_{\text{M}}T$ of **2** before (black circles) and after (red circles) 660 nm light irradiation. The inset graph shows the temperature dependence of the first derivative of $\chi_{\text{M}}T$ with respect to the temperature.

*Structure of $\text{Fe}(\text{1bpCOOH}_2\text{p})_2(\text{ClO}_4)_2\cdot 3.5\text{Me}_2\text{CO}$ (**2**)*

Single crystal X-ray diffraction experiments from 120 to 300 K show that this thermal SCO is related to a symmetry breaking phase-transition around 280 K. Thus, unit cell parameters and systematic absences change reversibly above this temperature from monoclinic to triclinic space groups (see **Table SI. 3.4.1**, **Figure SI. 3.4.16**, **Figure SI. 3.4.17** and **Figure SI. 3.4.18** in the SI). The structure at 120 K was solved in the monoclinic space group $P2_1/c$ showing a single molecule of $[\text{Fe}(\text{1bpCOOH}_2\text{p})_2]^{2+}$ in the asymmetric unit (see **Figure 3.2.4**, left) with typical LS Fe-N bond lengths ($1.898(2) - 1.977(2) \text{ \AA}$). Above 280 K, the cell parameters α and γ deviate significantly from 90° and the symmetry changes to triclinic, $P-1$. As a result of this, the structure at 300 K shows two molecules of $[\text{Fe}(\text{1bpCOOH}_2\text{p})_2]^{2+}$ in the asymmetric unit (with iron labelled Fe1 and Fe2, see **Figure 3.2.4**, right) with different spin states as shown by Fe-N bond lengths ($1.901(4)$

- 1.981(5) Å for Fe1 and 2.127(4) - 2.180(5) Å for Fe2). The structures at 120 and 300 K present similar packing motifs with important differences: (i) the structure at 300 K shows weaker intrachain contacts for the HS complexes and stronger interchain contacts between HS and LS ones; (ii) ClO_4^- and acetone molecules are disordered at 300 K but not at 120 K (see SI for more details). Therefore, crystal structures at 120 and 300 K and magnetic measurements indicate that there is a SCO of half of the Fe(II) complexes accompanying the structural phase transition. This has also been confirmed by variable temperature PXRD patterns (**Figure SI. 3.4.23** in the SI and associated text). Crystallographic symmetry breaking during SCO is a well-known phenomenon, which often leads to an intermediate crystal phase of lower symmetry containing a mixture of HS and LS molecules.^[23–26] This mixed spin-state phase is usually retained over a temperature range. At lower or higher temperatures, it exhibits a phase change to the full LS or HS state, respectively, with space groups of higher symmetry.^[23,24,27] This re-entrant behavior of the intermediate phase could not be observed in **2** probably due to the irreversible loss of crystallinity caused by the removal of the solvent molecules.

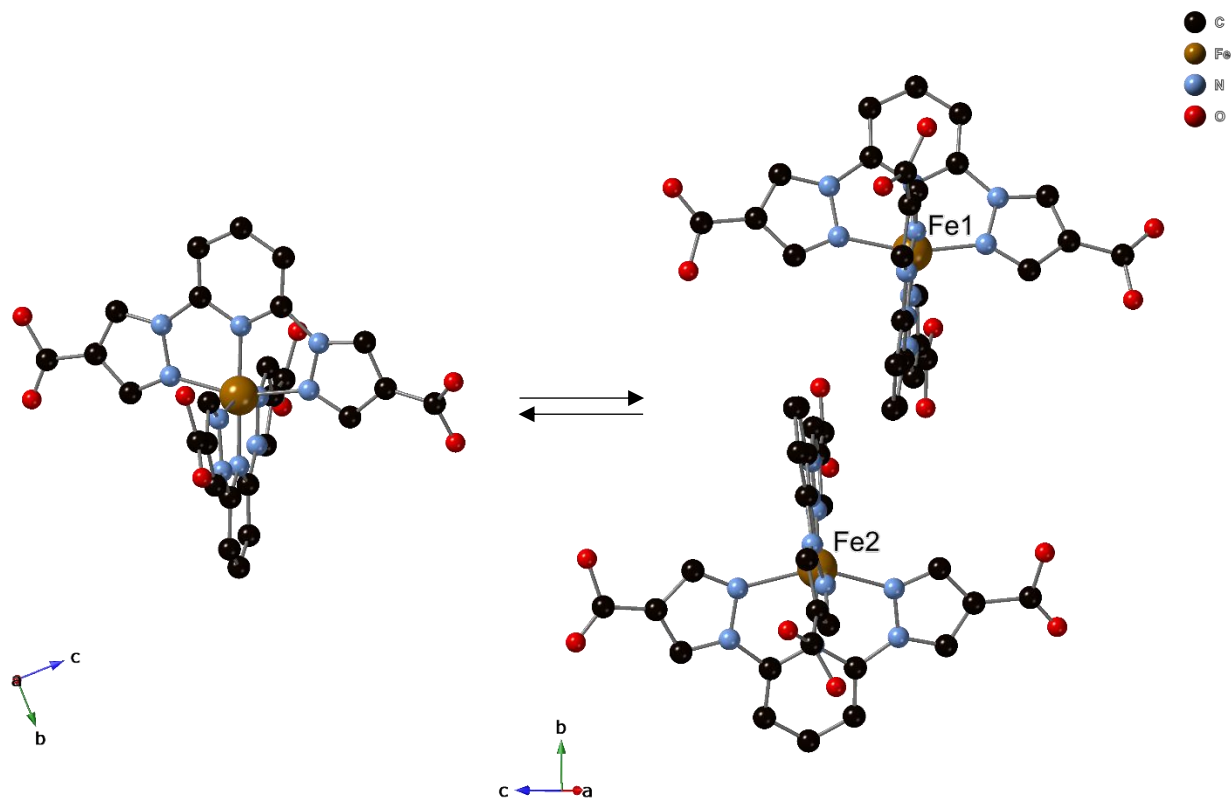


Figure 3.2.4. Asymmetric unit cell of **2** measured at, **left**, 120 K ($P2_1/c$) and, **right**, 300 K ($P-1$).

A more detailed X-ray crystallographic study of a crystal before and after keeping the sample at 300K for two hours, shows a loss of cooperativity and broadening of the spin transition in the evolution of the unit cell parameters with temperature (see **Figure SI. 3.4.18**), in agreement with DSC measurements (see **Figure SI. 3.4.13**). Then, the crystal structure of the same crystal was solved at 120 K showed that the half acetone molecule was lost. This phase was not possible to be measured in the SQUID due to technical problems. Again, the shift of temperatures to higher values of DSC with respect to the evolution of the unit cell parameters could be related to the different method used to protect the crystals (oil in DSC, single crystal under nitrogen stream) and to the different scan rates.

Photomagnetic properties

The LS to HS photoconversion was investigated by irradiating crystals of **2** protected with an oil at 10 K with 660 and 532 nm wavelength lasers. Both lasers give rise to a drastic increase of the magnetic signal at short times followed by a more gradual increase at longer times. The 660 nm red light led to a faster increase of the signal. After irradiation for ca. 16 hours (see **Figure SI. 3.4.24**, top-left

Figure SI. 3.4.24), irradiation was switched off and the temperature was then increased at a rate of 0.3 K min⁻¹. The $\chi_M T$ value after irradiation is higher than the value recorded in the dark at temperatures below 120 K (see empty circles in **Figure 3.2.3**). Interestingly, compound **2** consistently shows a bump, where a small fraction of the sample undergoes partial LIESST relaxation at lower temperature (ca. 50 K, see **Figure 3.2.5**). This is discussed further below. The fraction of Fe(II) photoconverted after irradiation is calculated to be close to 100% in contrast to the LS–HS state reached after heating above 280 K. The abrupt decrease of the LIESST curve above 110 K suggest that the intermediate LS-HS state is not reached after full photoexcitation. The minimum of the $\partial\chi_M T/\partial T$ curve (T(LIESST)) gives a value of 120 K (see inset of **Figure 3.2.5**). Notice that **2** represents one of the few molecular compounds with T(LIESST) well above 100 K^[17,28–30] but, in contrast to these examples, **2** exhibits a $T_{1/2}$ near room temperature. Therefore, $T_{1/2}$ and T(LIESST) values deviate clearly from the linear relationship found for other Fe(II) bpp complexes. The relaxation from the photoinduced HS (HS*) state to the LS state has been investigated from 105 to 115 K close to the T(LIESST). Time dependence of the HS fraction could be fitted to a sigmoidal decay typically found in cooperative systems with a self-accelerated behavior. Therefore, the measurements have been fitted using the mean-field macroscopic model developed by Hauser (see **Figure SI. 3.4.25** and associated text).^[31,32] Parameters obtained from these fittings are in the same range as those of other bpp complexes ($E_a = 2385 \text{ cm}^{-1}$, $k_\infty = 1.2 \times$

10^{11} s^{-1} , $E_a^* = 4.08 \text{ cm}^{-1}$ and $k_0 \leq 9.07 \times 10^{-5} \text{ s}^{-1}$ where E_a is the apparent activation energy, k_∞ is the apparent preexponential factor, E_a^* is the additional activation energy resulting from cooperativity and k_0 is the upper limit of the tunnelling rate constant).^[33–37]

The bump observed in the relaxation curve after photosaturation with 660 nm laser could suggest some structural reorganization since shorter times (ca. 6h), where photosaturation was also reached (see

Figure SI. 3.4.24, top-right), gives rise to a higher fraction of iron centers undergoing LIESST relaxation at the same temperature ($T(\text{LIESST}) = 48 \text{ K}$) giving rise to a step-like behavior (see **Figure 3.2.5**, left).

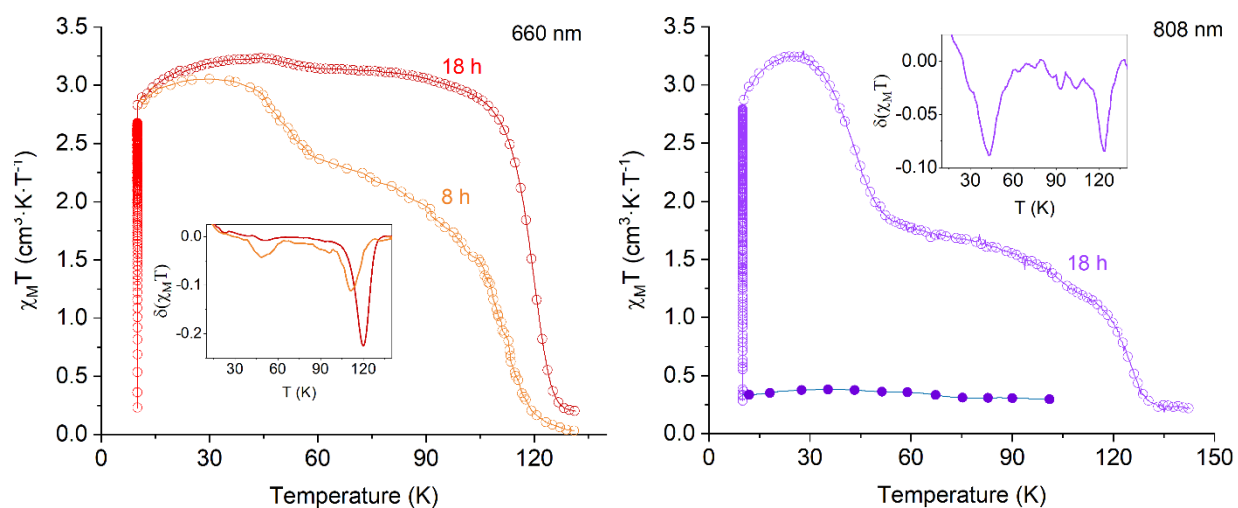


Figure 3.2.5. Left, Thermal variation of $\chi_M T$ after 660 nm light irradiation for 18 hours (red empty circles) and 8 hours (orange empty circles). Right, temperature-dependence of $\chi_M T$ before (full circles) and after (empty circles) 808 nm light irradiation for 18 hours.

Further investigation of the photomagnetic properties were carried out irradiating with an 808 nm wavelength laser for 18 hours (**Figure SI. 3.4.24**, bottom; **Error! No se encuentra el origen de la referencia.**). As in the previous experiment with shorter irradiation time at 660 nm, the two-step relaxation process takes place with two minimums in the $\partial\chi_M T/\partial T$ of ca. 45 and 124 K (see **Figure 3.2.5**, right). This suggests that shorter irradiation times or the same irradiation time but with a lower energy laser, the HS* state is less favored compared to that observed at 660 nm for 16 hours, which is in agreement with PXRD experiments with light (see below).

The thermally induced excited spin-state trapping (TIESST) was not observed after cooling the sample from room temperature to 10 K in a few seconds. This is not unexpected as this effect is usually found in compounds with $T_{1/2}$ below 200 K.^[33]

Low temperature X-ray diffraction studies with light

Investigation of structural changes at low temperature under light irradiation was performed in collaboration with Elzbieta Trzop and Eric Collet from the IPR in Rennes. The structure of **2** was solved at 10 K before and at 20 K after irradiation of a crystal with red laser in the European Synchrotron Radiation Facility (ESRF) at the Swiss-Norwegian beamline BM01 in collaboration with Dmitry Chernyshov and Charlie Mc Monagle (for experimental details go to Appendix). After a few minutes of irradiation, full structural analysis reveals that the symmetry of the complex is unchanged with respect to that of the crystal before irradiation ($P2_1/c$, LS), but the unit cell parameters are slightly bigger (see **Table S.I. 3.4.2** in the SI). Fe-N bond distances and the distortion of the octahedral geometry (see **Table S.I. 3.4.3** and **Table S.I. 3.4.4**) have increased and are consistent with an Fe(II) center in the HS state. All of this confirms that the re-entrant $P2_1/c$ HS* state has been stabilized. Interestingly, by reducing the exposure time with the red laser to a few seconds (ca. 60 s) in a conventional diffractometer at 20 K (see Appendix), a change of symmetry takes place obtaining the photoinduced $P-1$ intermediate LS-HS (LS-HS*) state. The different spin states of the two crystallographically independent iron centers were confirmed with the Fe-N bond distances and distortion parameters see (**Table S.I. 3.4.3** and **Table S.I. 3.4.4**), which are in good agreement with the values obtained at higher temperatures (see above). The space group of both structures were also confirmed by the appearance or disappearance of the systematic absences (see **Figure SI. 3.4.27** and **Figure SI. 3.4.28**). However, the structures are of poor quality due to sample damage induced by the fast cooling and light irradiation. In the light of these results, PXRD studies of **2** were carried out at the ESRF at the Swiss-Norwegian beamline BM01. It was found that the bulk sample was isostructural and interacted with light in the same way as the single crystal described above (see **Figure 3.2.6**), despite of a small fraction of **3** that was also identify (see **Figure SI. 3.4.29** and associated text in the SI).

Indeed, long irradiation times of the sample powder with 660, 782 and 472 nm favors the $P2_1/c$ photoinduced HS state (see **Figure 3.2.6**, and **Figure SI. 3.4.30** and **Figure SI. 3.4.31** in the SI). Such phase transition is more favored with 660 than with 782 nm (see **Figure SI. 3.4.32** and associated text). Irradiation with 1064 nm in the HS* state induces changes in peak position of the pattern. This new pattern is consistent with the simulated LS-HS* state from single crystal (see **Figure SI. 3.4.33**), although small differences may come from the coexistence of other

phases. This result suggests a partial r-LIESST transition from the HS* to the HS-LS* state, as it has been previously observed in other compounds.^[25]

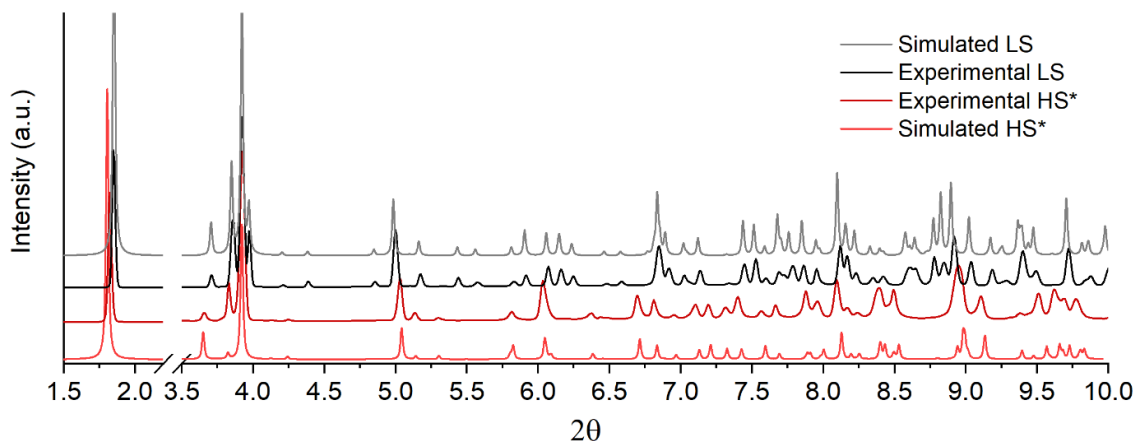


Figure 3.2.6. Simulated PXR D pattern from the structure solved in the dark (grey) and under continuous irradiation with 660 nm for ca. 360 seconds (light red) and experimental PXR D pattern of a powder sample measured in the dark (black) and (red) under continuous light irradiation with 660nm for ca. 1200 seconds at 20 K.

It was possible to qualitatively observe that such intermediate state could also be reached by irradiating with 1064 nm from the LS state; 660 and 782 nm for shorter times; or slightly increasing the temperature (see **Figure 3.2.7**). These results indicate that irradiation from the LS with 1064 nm stabilizes the intermediate *P*-1 faster than from the HS* state (see **Figure SI. 3.4.34**). Light irradiation with relatively high energy lasers (660 and 782 nm) also stabilizes first the low-symmetry *P*-1 phase and then, after further irradiation, the re-entrant higher-symmetry *P*₂₁/*c* phase is stabilized, in agreement with single crystal measurements (see above).

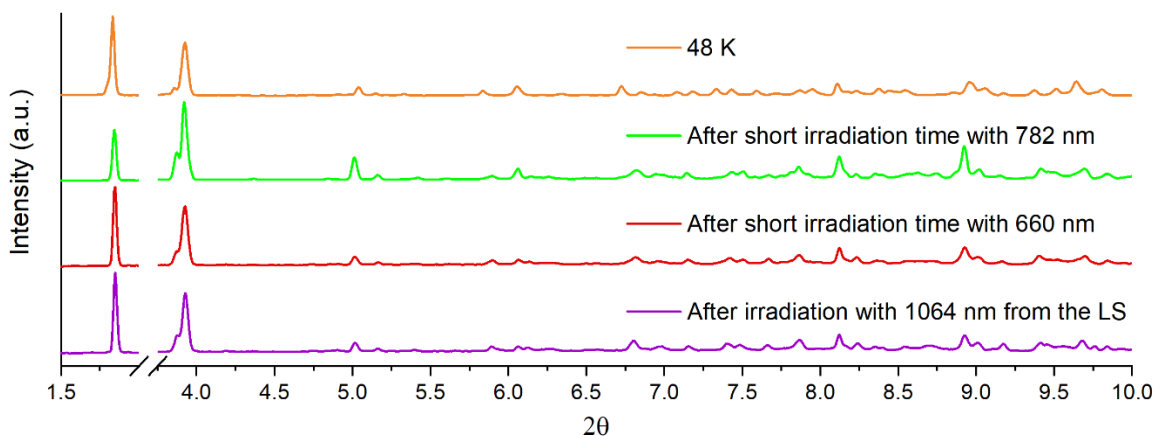


Figure 3.2.7. Experimental PXR D patterns of a powder sample of **2** measured after irradiation with 1064 nm (violet) for ca. 1200 seconds, during a short period of time with 660 nm

(210 s, red) and 782 nm (540 s, green) at low temperature and the average of three spectra collected at 48K from the temperature scan experiment (go to SI for more information).

Further increase in temperature gives rise to the LS phase (**Figure SI. 3.4.35** and associated text). Separately, the use of 472 nm directly induces the monoclinic HS* state (see **Figure SI. 3.4.31** and **Figure SI. 3.4.36**). Full photo-saturation of the different phases was not reached due to the longer exposure times needed (see **Figure SI. 3.4.32**, **Figure SI. 3.4.34** and **Figure SI. 3.4.36**), compared to the single crystal (see above). Nevertheless, these experiments allow understanding the exceptional behavior of our system (see **Figure 3.2.8**).

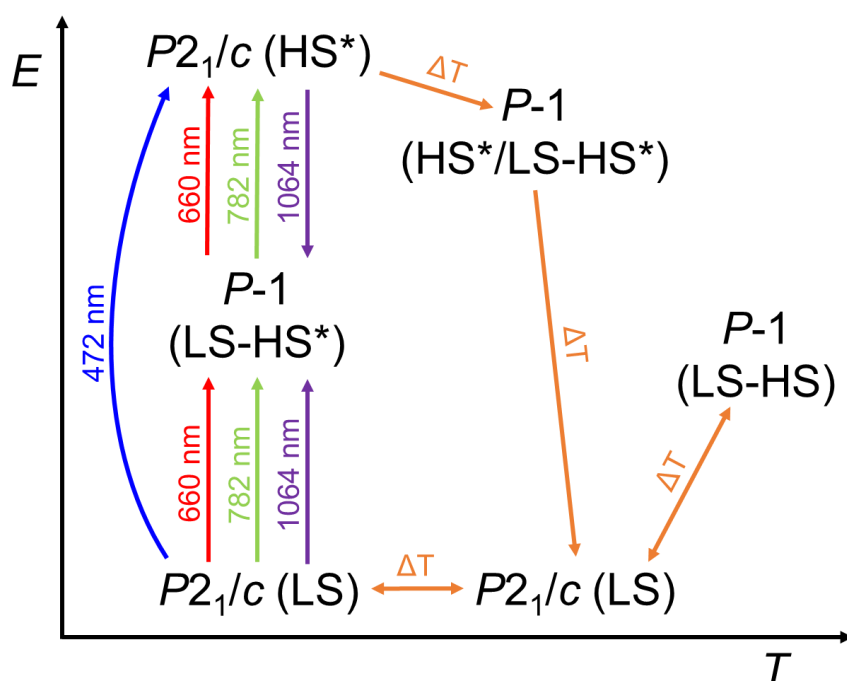


Figure 3.2.8. Schematic representation of the behavior of the different structural phases with light and temperature.

Deposition

We have explored the deposition of **2** on SiO₂ surfaces. Preliminary results indicate that the solubility of the complex is very low and decomposes partially in solution (see **Figure SI. 3.4.37**). Further attempts to improve the solubility and stability of the complex using different solvents could improve these results since XPS and XAS were not conclusive.

3.3. Conclusions

In this chapter we report the preparation and characterization of Fe(II) complexes of two new derivatives of 1bpp, 1bpp3COOH and 1bpCOOH_{2p}, and the structure and SCO properties of their perchlorate salts in the solid state.

In Part A, bulk properties of 1bpp3COOH Fe(II) complex compared with those of 1bppCOOH one from the previous chapter, leads to the following conclusions: (i) the LS state seems to be predominant as observed in [Fe(1bppCOOH)₂]²⁺; (ii) changing the position of the substituent hinders the possibility to form hydrogen-bonds between complexes; (iii) it also prevents the formation of other strong intermolecular interactions such as CH... π and π ... π stacking typical of a “terpyridine embrace” crystal packing seen in other Fe(II) bpp complexes. As a result, a gradual and incomplete SCO is observed. The compound presents LIESST effect. This ligand, as 1bppCOOH, could be a convenient precursor to new bpp derivatives with other functionalities in addition to the SCO properties. Indeed, the reactivity of the Fe(II) complex is enhanced for the esterification reaction. On the other hand, a possible advantage of the change of position of the substituent group of 1bpp is that this could favor the formation of Fe(II) complexes crystallizing in non-centrosymmetric structures as **1**, which would confer new properties such as ferroelectrics. This could be favored by functionalizing the same position with bulkier substituents.

Thanks to the incorporation of the carboxylic acid group, preparation of an organized assembly of SCO complexes could be studied. Several techniques demonstrated that the different position of the carboxylic acid group does not affect the affinity of the 1bpp ligand for metal oxides. However, deposition of **1** gives rise to the same results obtained in Chapter 2 with [Fe(1bppCOOH)₂], oxidation and/or fragmentation upon deposition. Preliminary results have shown that 1bpp3COOH is a suitable ligand for the preparation of SMM complexes using Co(II). The SMM properties and deposition of the Co(II) complex of 1bpp3COOH are in progress and will be presented in future works.

In Part B, the results indicate that in **2**, the combination of a rigid bpp ligand, which leads to distorted HS geometries, and carboxylic acid groups favoring the presence of solvent molecules in the structure, which enable enough free volume for the distorted HS molecules to switch to the undistorted LS state, could be crucial factors to explain the abrupt thermal SCO with hysteresis of **2**. This agrees with that observed in other bpp-based compounds^[17,27] and with the gradual SCO of **3**, which contains the same ligand but with a less distorted octahedral geometry and a

less flexible extended lattice. **2** presents an unexpectedly long-lived photo-induced state for such thermal spin transition. Large trigonal distortions such as that of **2** have been used to explain stabilization of the HS state and increase of T(LIESST).^[3,17] However, this would cause at the same time a decrease of $T_{1/2}$, which is not observed in **2**, in contrast to bpp-based compounds with HS distorted structures.^[1,17,27,29] This suggests that besides the distortion of the octahedral geometry, the photoinduced structural change is the origin of the unexpected behavior of **2**, as it has been seen in $[\text{Fe}(\text{L})_2](\text{BF}_4)_2 \cdot \text{Solv}$ ($\text{L} = 4\text{-(isopropylsulfanyl)-2,6-di(pyrazol-1-yl)pyridine}$), which presents a T(LIESST) lower than the expected one due to a photo-induced crystallographic phase transition.^[29] Indeed, low temperature photo-crystallographic studies of this compound support that a structural change occurs upon light irradiation but in our case, we have the opposite behavior. Low temperature PXRD experiments of **2** show that the photoinduced HS state can be stabilized with high energy lasers such as 472, 633 and 785 nm and the $P2_1/c$ HS phase is reached. Interestingly, shorter irradiation times with 633 and 785 nm leads to mixtures containing the LS-HS* phase, as observed with single crystal experiments with 660nm. This suggests that the intermediate LS-HS* state gets rapidly populated by the 660 and 782 nm wavelengths, and then the HS* starts to be populated since it is more energy accessible from the intermediate $P-1$ phase. On the contrary, irradiation with the 472 nm high energy laser directly stabilizes the HS* phase, even for short irradiation times. The intermediate state can also be stabilized with a lower energy laser such as 1064 nm either from the LS state, either from the HS* with a r-LIESST. It was not possible to access the full LS state through r-LIESST with the lasers used in the experiment. LIESST measurements suggest that by irradiating with red light, the full HS* phase relaxes thermally to the LS state at 120 K, while step-back thermal relaxations are obtained irradiating at higher wavelengths or shorter times. Photocrystallographic measurements with the same single crystal in the temperature range 10-130 K are needed to fully understand the phases corresponding to these spin states. These experiments could also help to understand if the small bump observed in the LIESST experiments with long irradiation times with the 660 nm laser at 10 K corresponds to a phase transition or a residual fraction of LS-HS* crystals relaxing at lower temperatures. These measurements were not possible with the available equipment at this moment. In addition to this, further photo- crystallographic and magnetic experiments under light irradiation with 472 and 1064 nm wavelength lasers at low temperature must be done in order to get a complete understanding of the system since other intermediate state could be involved.

In summary, **2** combines two unexpected properties: SCO around room temperature and a long-lived photoinduced HS state at extraordinary high temperatures, which are associated to a specific crystal structure very sensitive to the presence of solvent molecules.

Photocrystallographic studies have revealed the presence in this compound of at least two different photoinduced metastable states, which can be reached in a controlled way through different wavelengths, irradiation times and temperature. This study represents a step towards the rational design of new SCO complexes with improved properties. In this sense, we are exploring the synthesis of other solvates (nitromethane) and of dilutions of iron with other metals (cobalt) to tune the properties of this interesting family of SCO complexes. These results will be presented in due course.

3.4. Supporting Information

Synthesis of [Fe(1bpp3COOH)₂](ClO₄)₂·4H₂O (1). A solution of Fe(ClO₄)₂·xH₂O (9 mg, 0.025 mmol) in ethanol (1 mL) was added to a solution of 1bpp3COOH (14.3 mg, 0.050 mmol) in ethanol (2 mL) and the mixture was stirred for 15 minutes. An orange solution was formed. Red prismatic crystals of **1** suitable for X-ray diffraction were obtained by slow diffusion of diethyl ether into this solution. The composition of **1**, checked by microanalysis, shows a Fe:Cl ratio close to 1:2. Anal. Calc. for [Fe(1bpp3COOH)₂](ClO₄)₂·4H₂O: C, 34.43; H, 3.13; N, 16.73 %. Found: C, 34.26; H, 2.96; N, 16.49 %.

Synthesis of [Fe(1bpCOOH₂p)₂](ClO₄)₂·3.5Me₂CO (2) and [Fe(1bpCOO·COOHp)(1bpCOOH₂p)Fe(1bpCOOH₂p)(ClO₄)](ClO₄)₂·H₂O·1.5Me₂CO (3).

Fe(ClO₄)₂·xH₂O (9 mg, 0.025 mmol) in acetone (1.5 mL) was added to a solution of 1bpCOOH₂p (15 mg, 0.050 mmol) in acetone (1.5 mL) inside the N₂ atmosphere of a glove box. The mixture was stirred for 15 minutes and filtered. A yellow solution was obtained. Orange prismatic crystals of [Fe(1bpCOOH₂p)₂](ClO₄)₂·3.5Me₂CO (**2**) suitable for X-ray diffraction were obtained by slow diffusion of diethyl ether into this solution after one week inside the glove box. If the diffusion tubes were placed in an air atmosphere after this time, the crystals of **2** dissolved and yellow rectangular crystals of **3** suitable for X-ray diffraction appeared after several weeks. The composition of crystals of **2** and **3**, checked by microanalysis, shows a Fe:Cl ratio close to 1:2 and 2:3, respectively. Elemental analysis of filtered samples of **2** and **3** are more consistent with the presence of four and five water molecules. This suggests loss of acetone molecules and absorption of water molecules after filtering the crystals. [Fe(1bpCOOH₂p)₂](ClO₄)₂·Me₂CO·4H₂O (983.37) (**2**): calcd. C 35.42, N 14.24, H 3.28 %; found C 35.37, N 14.61, H 2.93 %. [Fe(1bpCOOCOOHp)(1bpCOOH₂p)Fe(1bpCOOH₂p)(ClO₄)](ClO₄)₂·5H₂O (1396.835) (**3**): calcd. C 33.53, N 15.04, H 2.60 %; found C 33.53, N 14.98, H 2.50 %.

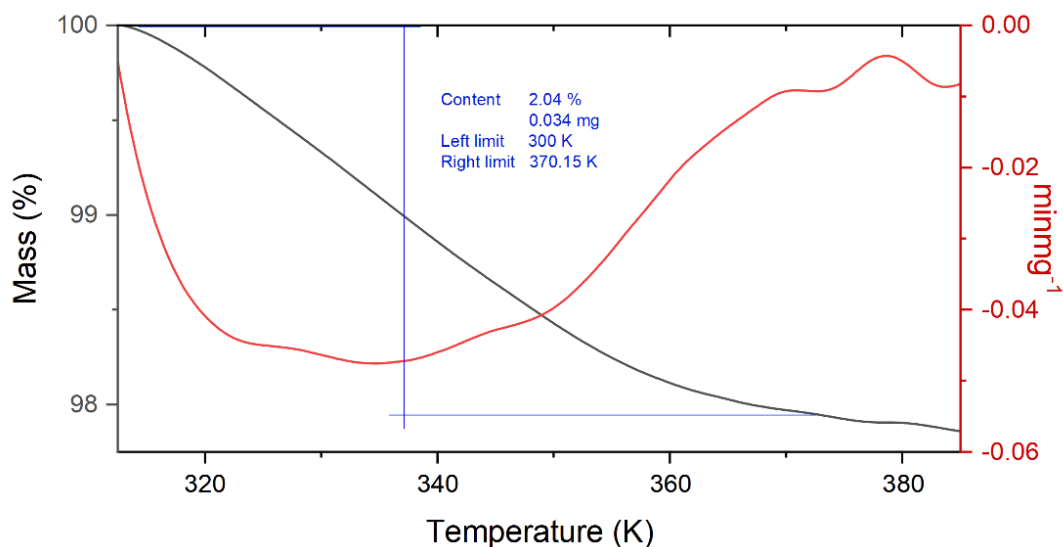


Figure SI. 3.4.1. Thermogravimetric profile of **1** (1.1643 mg, black line) and its derivative (red line) in heating mode from 315 K to 385 K (at 10 °C/min). The mass lost after this ramp corresponds to 2.04 % of the total weight, which is in agreement with the loss of one water molecule (ca. 2 %).

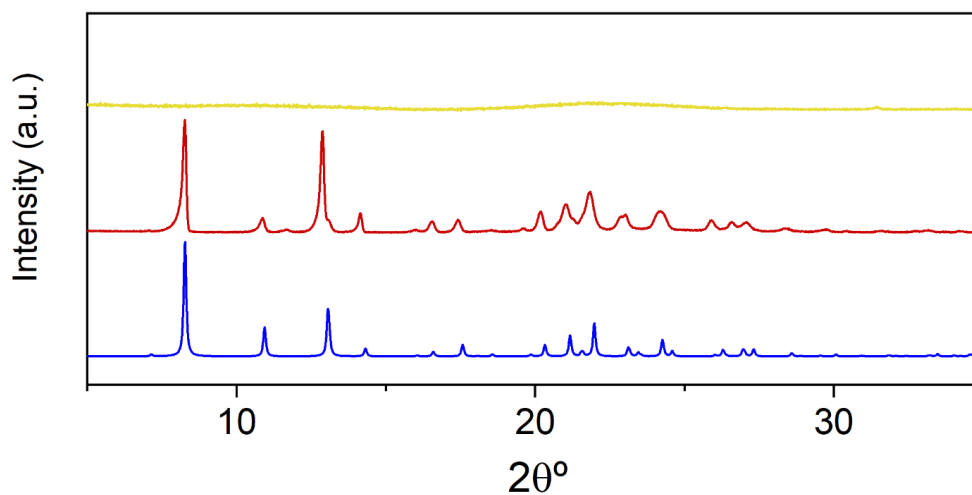


Figure SI. 3.4.2. Simulated PXRD pattern from the structure at 120 K (blue) and experimental ones at 300 K (red) and after heating the sample at 400 K (yellow) of **1**.

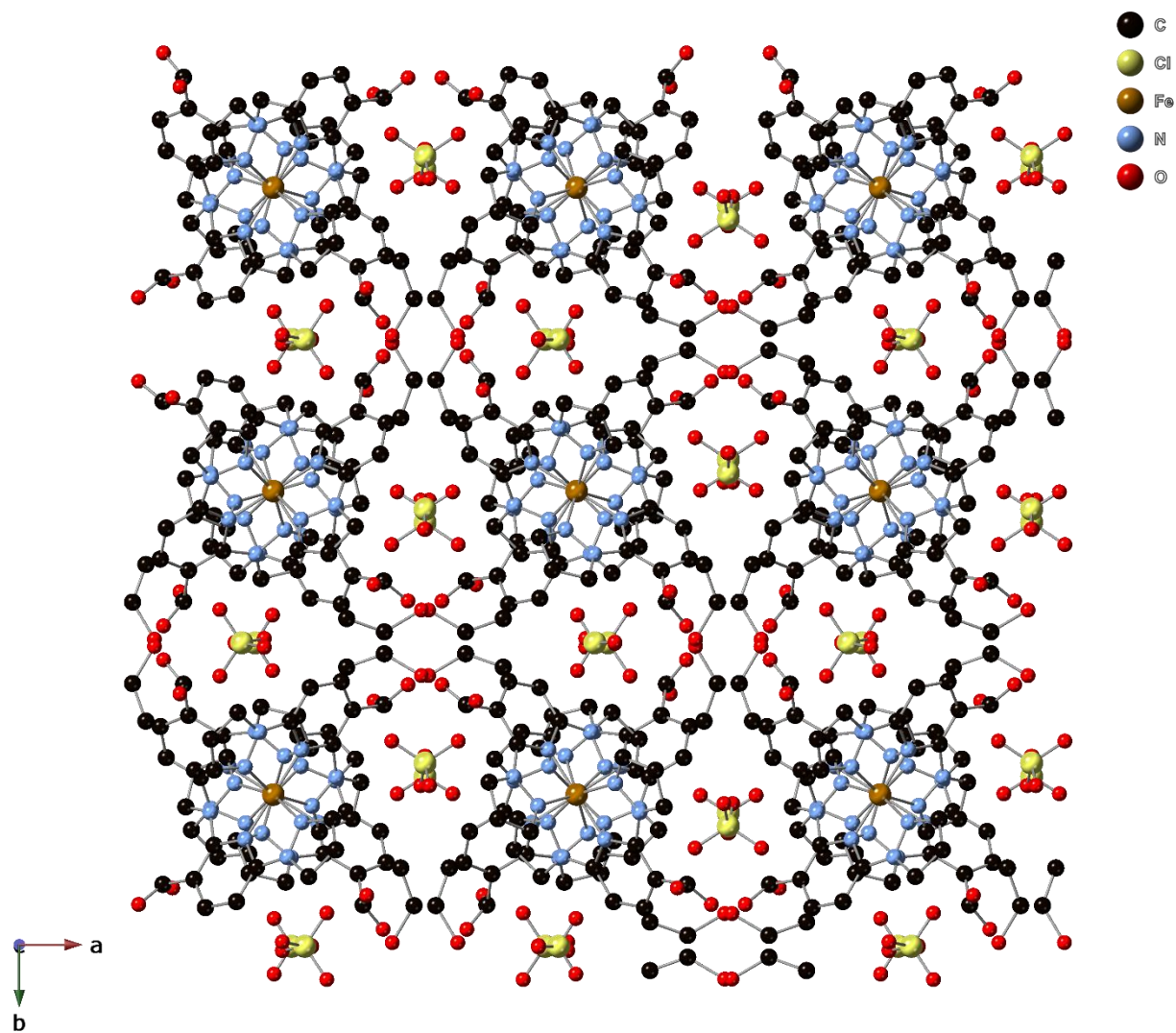


Figure SI. 3.4.3. Projection on the *ab* plane of the structure of **1**. Hydrogen atoms have been omitted for clarity. Only one of the two possible configurations of disordered carboxylic acid groups is shown for clarity.

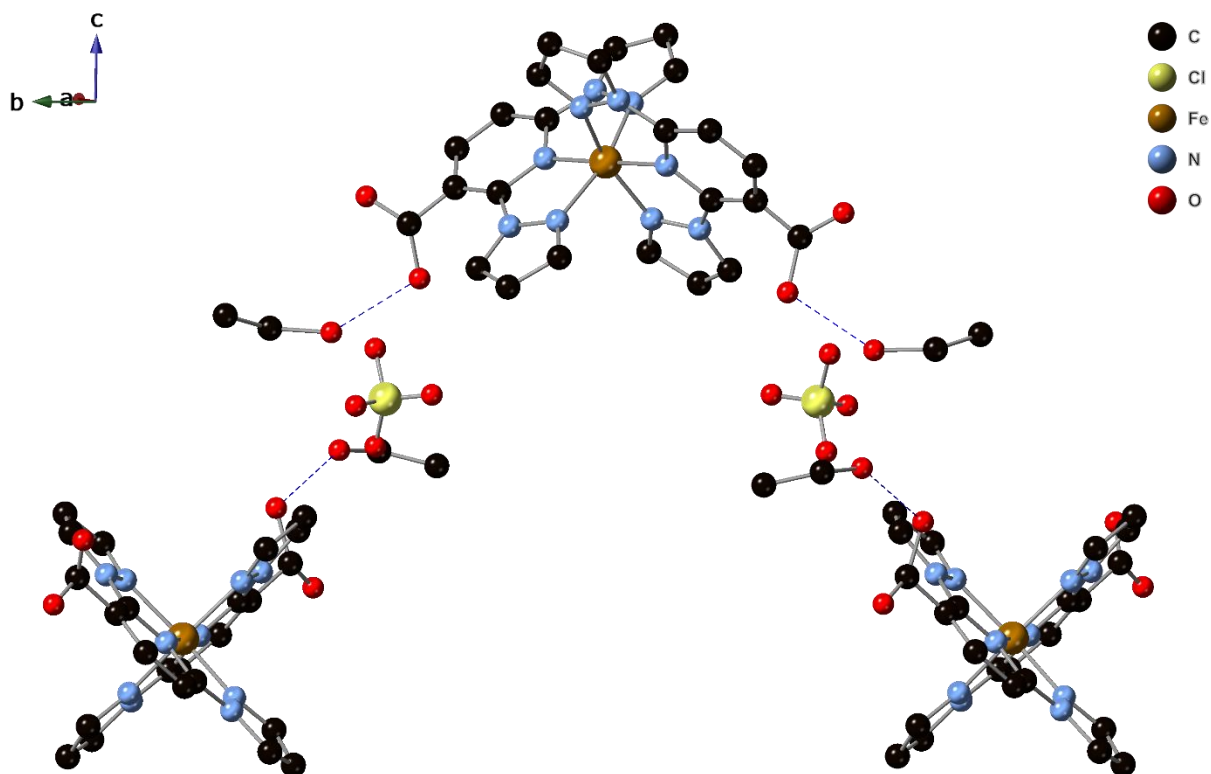


Figure SI. 3.4.4. View of the hydrogen-bonds in the structure of **1** as blue dashed-lines. Hydrogen atoms have been omitted for clarity. Only one of the two possible configurations of disordered carboxylic acid groups is shown for clarity.

Deposition

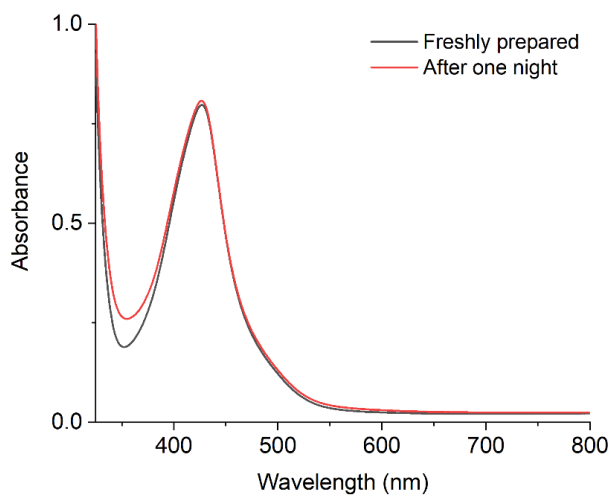


Figure SI. 3.4.5. UV/Vis spectra of a 0.1 mM solution of **1** in MeCN freshly prepared (black line) and after one day in inert atmosphere (red line).

UV/Vis spectroscopy of **1** displays a strong MLCT $t_2-\pi^*$ transition^[38,39] centered at 427 nm ($\epsilon = 8.0 \times 10^3 \text{ L}^{-1}\text{mol}^{-1}\text{cm}^{-1}$), which is indicative of the majority of the species in the LS state,^[40] in contrast to the $\text{Fe}(\text{1bppCOOH})_2$ where only about 50% of the molecules are in the LS state (see Chapter 2). Comparison between the UV/Vis spectrum of freshly prepared and after one night in inert atmosphere shows an increase of the absorbance at around 350 nm (see **Figure SI. 3.4.5**), which could be caused by partial decomposition of the complexes in solution.

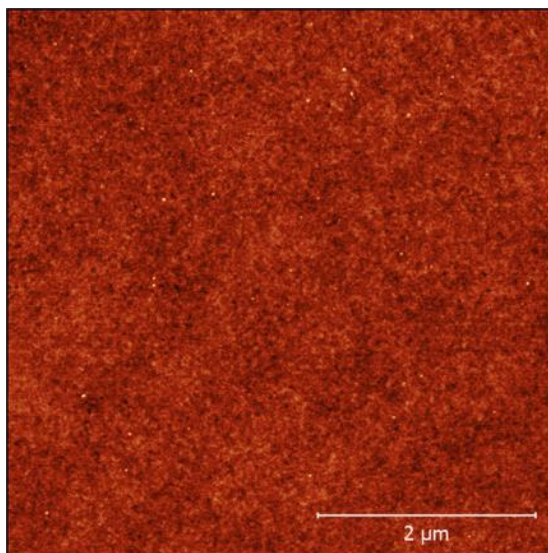


Figure SI. 3.4.6. AFM images of SiO_2 substrates after deposition of **1**.

AFM images confirm the absence of aggregates or multilayers (see **Figure SI. 3.4.6**) as expected, since the first layer is covalently grafted to the surface through the carboxylic acid group while possible additional layers are removed after rinsing with MeCN. The average of the R_{RMS} of the deposit shows no variation from $0.165 \pm 0.006 \text{ nm}$ to $0.164 \pm 0.006 \text{ nm}$ for **1** with respect to the naked substrate, which is consistent with the formation of a monolayer that mimics the roughness of the substrate.

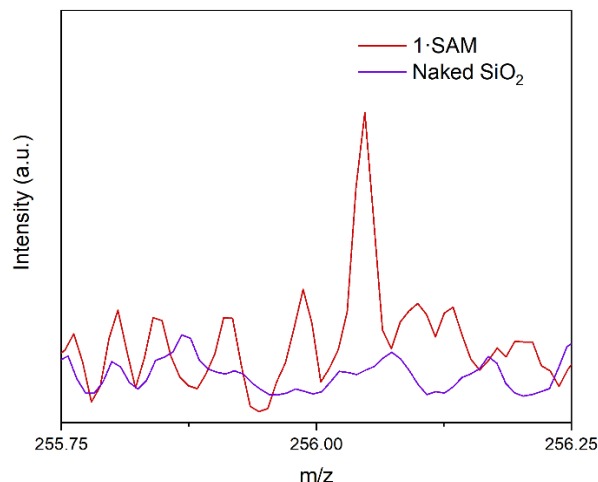


Figure SI. 3.4.7. MALDI-ToF region of the ligand $[1\text{bpp}3\text{COOH}+\text{H}]^+$ (256.08 Da) of **1-SAM** in red and bare SiO_2 substrate as reference in violet.

Peaks corresponding to the protonated ligand $[1\text{bpp}3\text{COOH}+\text{H}]^+$ (Calc. 256.08 Da, Found 256.08 Da, **Figure SI. 3.4.7**) for **1** was obtained confirming the anchoring of the ligand to the metal oxide surface.

XPS was used to get structural and electronic information about the SAMs. $\text{C } 1s$, $\text{N } 1s$, $\text{Cl } 2p$ and $\text{Fe } 2p$ XPS regions were studied to analyze the atomic compositions of the deposits (**Figure SI. 3.4.8**). $\text{C } 1s$ region of **1** features three main components at 285.0, 286.7 and 288.6 eV assigned to the aliphatic and adventitious carbon atoms (orange), heterobonds (green) and carbon atoms of the carboxylate group (blue), respectively.^[41,42] $\text{N } 1s$ region features two components at 401.6 and 399.8 eV assigned to coordinated and uncoordinated nitrogen atoms of the 1bpp moiety.^[43] $\text{Fe } 2p_{3/2}$ regions have been reproduced with 5 components (A–E) along with the corresponding $\text{Fe } 2p_{1/2}$ spin–orbit coupled contributions (A'–E') weighted with the expected 2:1 ratio as well.^[44] Regarding the line shape, we were not able to properly assign an oxidation state based on XPS analysis only. The absence of perchlorate anion signals in both samples is experimental evidence of the absence of physisorbed molecules on the surface (see **Figure SI. 3.4.8**)

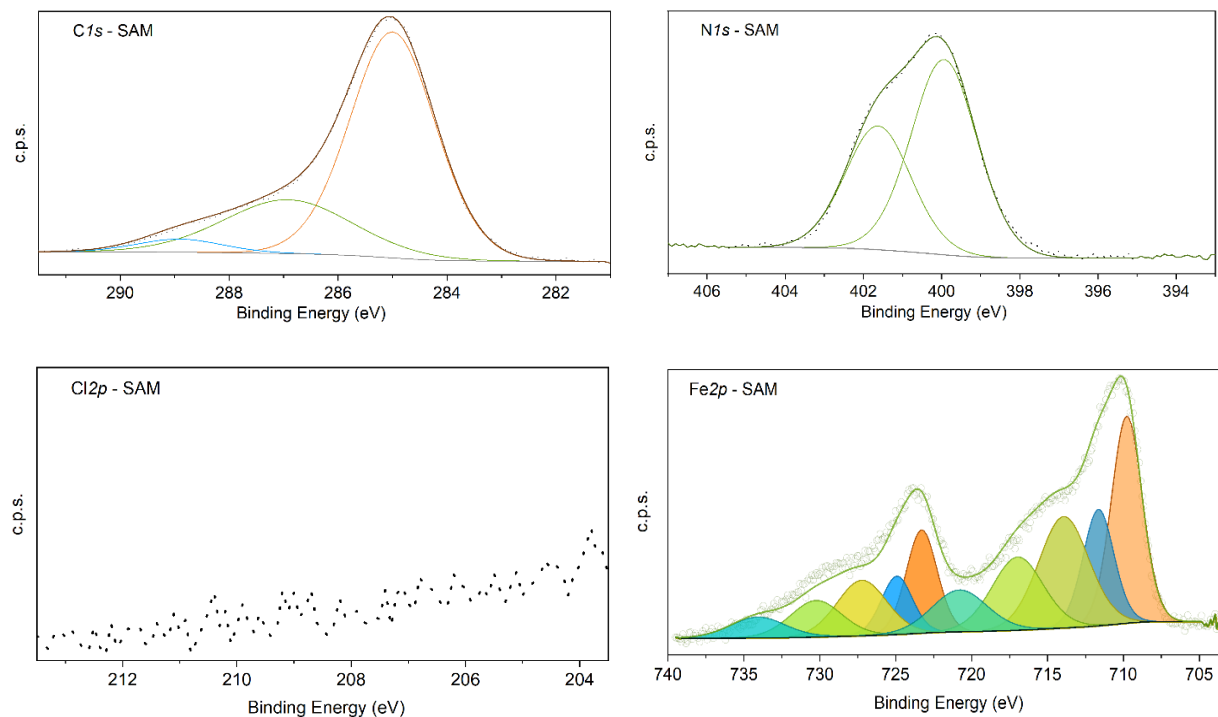


Figure SI. 3.4.8. XPS region of, from top to bottom, C 1s, N 1s, Cl 2p and Fe 2p of **1-SAM**.

Semiquantitative analysis and stoichiometric ratios (**Table S.I. 3.4.1**) show that C component got spoiled by spurious contamination, while N features, which are less likely to get contaminated, are consistent with the presence of the ligand. Metal ratios of **1** suggest only one ligand per Fe atom.

Table S.I. 3.4.1. Theoretical and XPS estimated atomic semiquantitative analysis (top) and ratios (bot) for **1-SAM**. The higher value marked with an asterisk comes from spurious contamination of the adventitious carbon.

	Semiquantitative analysis							
	Fe	N	C	N _{coordinated}	N _{uncoordinated}	C-C	C-N	COO ⁻
Theor. for 1	2.9%	28.6%	68.6%	60.0%	40.0%	42.9%	47.6%	9.5%
1-SAM	4.1%	16.5%	79.4%	61.2%	38.8%	70.6%	25.3%	4.1%

	Iron ratios			Nitrogen ratios		Carbon ratios		
	Fe/Fe	Fe/N	Fe/C	C-N _{coord} /C-N _{coord}	C-N _{coord} /C-N _{uncoord}	C-C/C-N	C-N/C-N	O-C=O/C-N
Theor. for 1	1.00	0.10	0.042	1.00	0.67	0.90	1.00	0.20
1-SAM	1.00	0.25	0.052	1.00	0.63	2.79*	1.00	0.16

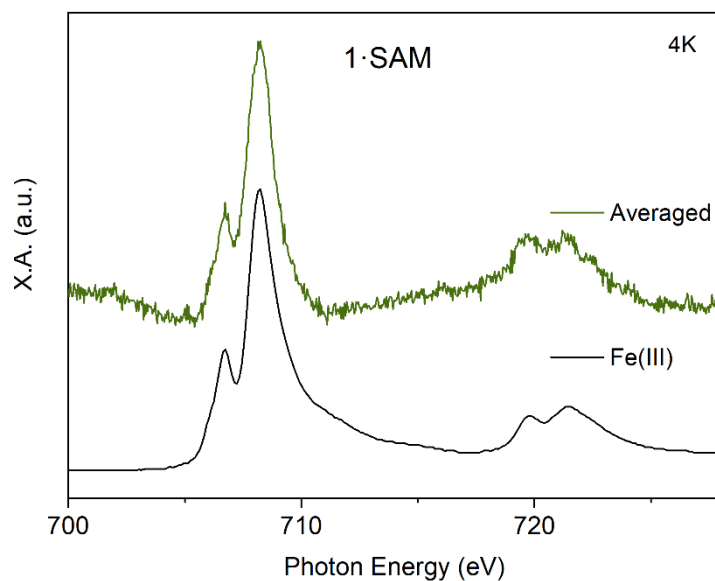


Figure SI. 3.4.9. Left, XAS Fe L_{2,3}-edge spectra of **1·SAM** (red) and an Fe(III) (black) extracted from the literature.^[45]

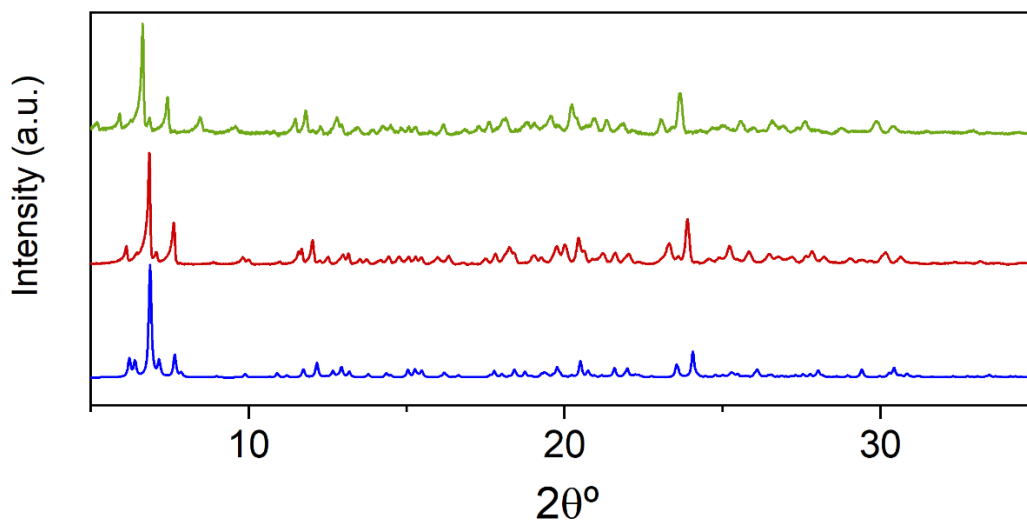


Figure SI. 3.4.10. Simulated PXRD pattern from the structure solved at 120 K (blue), experimental PXRD pattern of a freshly filtered sample (red) and the sample in contact with the mother liquors (green) both at 300K of **3**.

Structure and magnetic properties of 3

The structure of $[\text{Fe}(\text{1bpCOOCOHP})(\text{1bpCOOH}_2\text{p})\text{Fe}(\text{1bpCOOH}_2\text{p})(\text{ClO}_4)](\text{ClO}_4)_2 \cdot \text{H}_2\text{O} \cdot 1.5\text{Me}_2\text{CO}$ (**3**) at 120 K, which belongs to the triclinic space group *P*-1 is formed by cationic chains of formula $[\text{Fe}(\text{1bpCOOH}_2\text{p})(\text{1bpCOOCOHP})\text{Fe}(\text{1bpCOOH}_2\text{p})(\text{ClO}_4)]^{2+}_n$ separated by ClO_4^- counteranions and water and acetone, which in some cases are disordered (see **Figure SI. 3.4.11**). The asymmetric unit contains two iron atoms, two $\text{1bpCOOH}_2\text{p}$ and one 1bpCOOCOHP^- ligands (see below), three ClO_4^- (one of them coordinated to iron), two acetone molecules (one of them with an occupancy of 0.5) and one water molecule. These polymeric chains are formed by two crystallographically independent iron centers (Fe1 and Fe2) with a different coordination environment. Fe1 is coordinated by six nitrogen atoms from two tridentate $\text{1bpCOOH}_2\text{p}$ and 1bpCOOCOHP^- ligands with a distorted octahedral coordination geometry ($\Sigma = 145.8(2)^\circ$, $\Theta = 478.3(5)^\circ$, $\varphi = 173.85(19)^\circ$ and $\theta = 81.8^\circ$) and typical HS Fe-N distances (2.105(5)-2.187(6) Å). We call 1bpCOOCOHP^- to partially deprotonated $\text{1bpCOOH}_2\text{p}$. Thus, one of the two CO bonds of 1bpCOOCOHP^- presents very similar CO distances (1.243(8) and 1.254(8) Å), whereas the carbonyl C=O (1.247(8) Å) and alcoholic C-OH (1.290(9) Å) ends of the other carboxylic acid group can be distinguished. The other ligand linked to Fe1, $\text{1bpCOOH}_2\text{p}$, presents distinguishable C=O (1.217(13) and 1.236(10) Å) and C-OH (1.269(14) and 1.308(10) Å). The O from the C=O group of the carboxylic acid end and one of the two O atoms from the carboxylate end of 1bpCOOCOHP^- are linked to two Fe2 leading to zig-zag chains running along the *c* axis. Therefore, 1bpCOOCOHP^- ligand acts as a bridging ligand to three iron ions. Thus, the carboxylate and carboxylic acid groups of the two sides are coordinated to two Fe2 ions, while the central pyridyl and the two pyrazolyl rings are coordinated to Fe1 in the usual tridentate way of *bpp* (see **Figure SI. 3.4.11**). The remaining four positions of the distorted octahedral coordination of Fe2 are completed with one oxygen from a ClO_4^- anion and one tridentate bpCOOH_2p ligand with distinguishable C=O (1.232(9) and 1.238(9) Å) and C-OH (1.322(9) and 1.255(10) Å) distances. The O atoms belonging to perchlorate and carbonyl groups are in trans, while the carboxylate group is in trans to the N atom from the pyridyl ring. Mossbauer measurements need to be performed to confirm the oxidation state of Fe2. Fe-N and Fe-O distances in Fe2 are typical HS distances ranging from 2.147(6) - 2.204(6) Å for Fe-N and 1.967(5) - 2.223(6) Å for Fe-O as expected for a FeN_3O_3 coordination. Coordinating perchlorate group seems to be important for the stabilization of the structure, as attempts to obtain a similar compound with tetrafluoroborate were unsuccessful. The shortest Fe-O distance corresponds to the carboxylate group in agreement with the more ionic character of this bond.

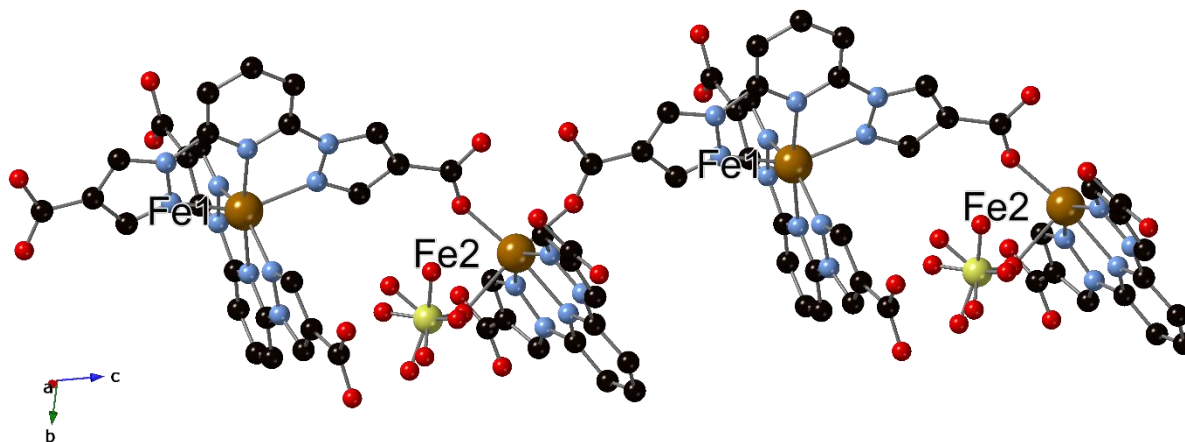


Figure SI. 3.4.11. Structure of the $[\text{Fe}^{\text{II}}(1\text{bpCOOH}_2\text{p})(1\text{bpCOO}^-\text{COOHp})\text{Fe}^{\text{II}}(1\text{bpCOOH}_2\text{p})(\text{ClO}_4)]^{2+}_n$ chains in the structure of **3** at 120 K. Fe (orange) C (black), N (blue), O (red), Cl (yellow). Hydrogen atoms are omitted for clarity.

χ_{MT} of crystals of **3** measured in contact with the mother liquor shows a value of $6.8 \text{ cm}^3 \cdot \text{K} \cdot \text{mol}^{-1}$ at 220 K consistent with the two Fe(II) complexes in the HS state found in the structure at 120 K. This value remains constant at lower temperatures with a decrease below 30 K due to zero-field-splitting (**Figure SI. 3.4.12**). Therefore, the magnetic interactions between Fe(II) centers through the $1\text{bpCOO}^-\text{COOHp}^-$ ligand seem to be negligible. The desolvated sample measured after heating to 400 K in the squid shows a continuous decrease of χ_{MT} from 400 to 80 K, which is more abrupt below 250 K. From 80 to 30 K, χ_{MT} reaches a constant value around $5.0 \text{ cm}^3 \cdot \text{K} \cdot \text{mol}^{-1}$ with the expected abrupt decrease below 30 K due to zero-field-splitting. The χ_{MT} values at 400 and 80 K (6.4 and $5.0 \text{ cm}^3 \cdot \text{K} \cdot \text{mol}^{-1}$, respectively) indicate that 25 % of Fe(II) centers undergo a SCO in the desolvated phase. This corresponds roughly to half of the 50 % of the Fe(II) centers coordinated to $1\text{bpCOOH}_2\text{p}$ and $1\text{bpCOO}^-\text{COOHp}^-$ ligands (with N6 coordination) since SCO is not expected for the remaining 50 % of Fe(II) centers with a N3O3 coordination. Photomagnetic measurements were performed in this desolvated sample, since it is the one showing thermal SCO (see below). A drastic increase of the magnetic signal was observed after irradiation at 532 nm. χ_{MT} after irradiation reaches a maximum value of $6.0 \text{ cm}^3 \cdot \text{K} \cdot \text{mol}^{-1}$, which is close to the value obtained at higher temperatures before irradiation. Therefore, an almost complete photoconversion of the 25 % of LS Fe(II) centers at 10 K is achieved. The $T(\text{LIESST})$ is close to 85 K (see inset in **Figure SI. 3.4.12**), which in this case is consistent with the $T(\text{LIESST})$ vs. $T_{1/2}$ linear relationship with $T_0 = 150 \text{ K}$.

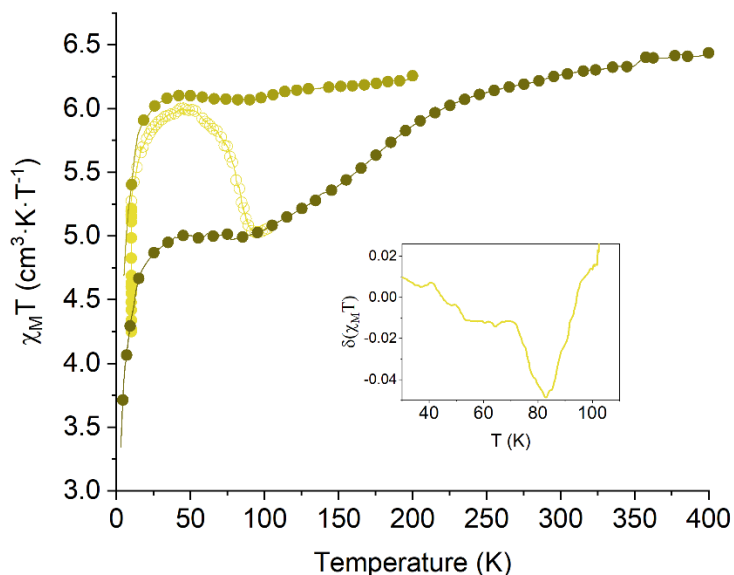


Figure SI. 3.4.12. Thermal dependence of $\chi_M T$ of **3**. Camouflage yellow: Compound measured in contact with the mother liquor. Dark green: data recorded without irradiation after desolvation at 400 K. Yellow: data recorded after irradiation at 10 K for the same desolvated sample. The inset graph shows the temperature dependence of the first derivative of $\chi_M T$ with respect to the temperature.

*Supporting information of $Fe(1bpCOOH_2p)_2](ClO_4)_2 \cdot 3.5Me_2CO$ (**2**)*

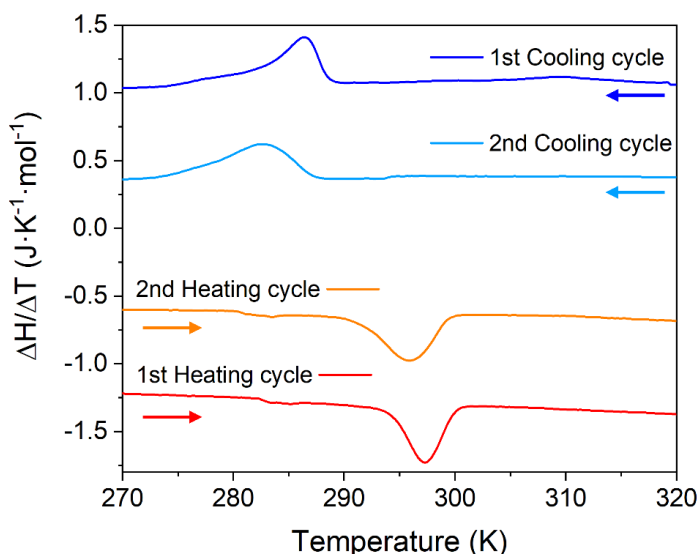


Figure SI. 3.4.13. Differential scanning calorimetry of **2** from 310K to 270K; first cooling (dark blue) and heating mode (red) and second cooling (light blue) and heating (orange) mode after keeping the sample at 310K for 2 hours.

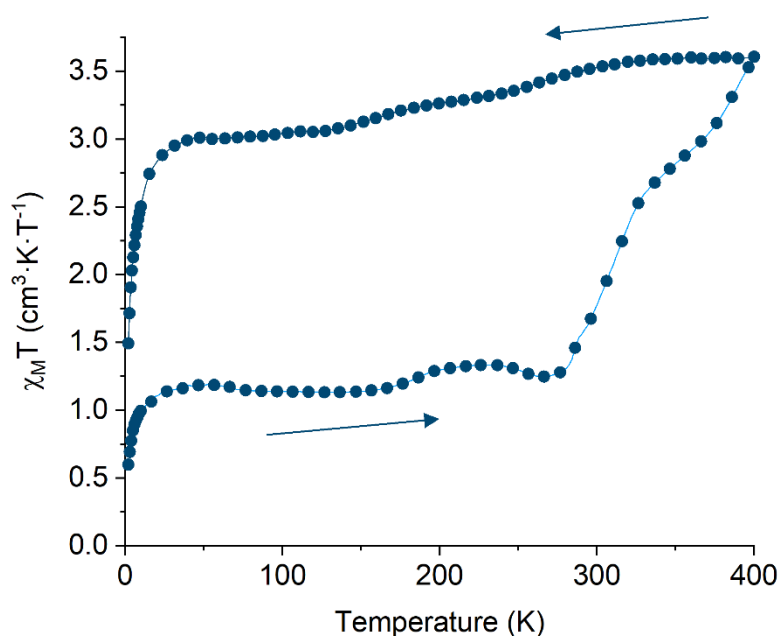


Figure SI. 3.4.14. Thermal variation of $\chi_M T$ of filtered crystals of **2**.

$\chi_M T$ of dried crystals of **2** shows a value close to $1.2 \text{ cm}^3 \cdot \text{K} \cdot \text{mol}^{-1}$ from 50 to 300 K. Above this temperature, it increases abruptly and irreversibly to reach a value of $3.6 \text{ cm}^3 \cdot \text{K} \cdot \text{mol}^{-1}$ at 400 K, which corresponds to 100 % of the molecules in the HS state. This value remains almost constant when the sample is successively cooled from 400 to 2 K with a decrease below 30 K due to zero-field-splitting of HS Fe(II). This suggests that desolvation leads to irreversible structural changes that stabilize the HS state as confirmed by powder X-ray diffraction (PXRD) data (see **Figure SI. 3.4.15**). On the other hand, the value of $1.1 \text{ cm}^3 \cdot \text{K} \cdot \text{mol}^{-1}$ obtained before heating to 400 K could indicate a mixture of different solvates and/or partially desolvated crystals. We have to take into account that PXRD of dried crystals shows a loss of crystallinity (see **Figure SI. 3.4.15**). Furthermore, elemental analysis of dried crystals is more consistent with the presence of one Me_2CO and four H_2O per molecule instead of the $3.5 \cdot \text{Me}_2\text{CO}$ molecules found in the structure (see above).

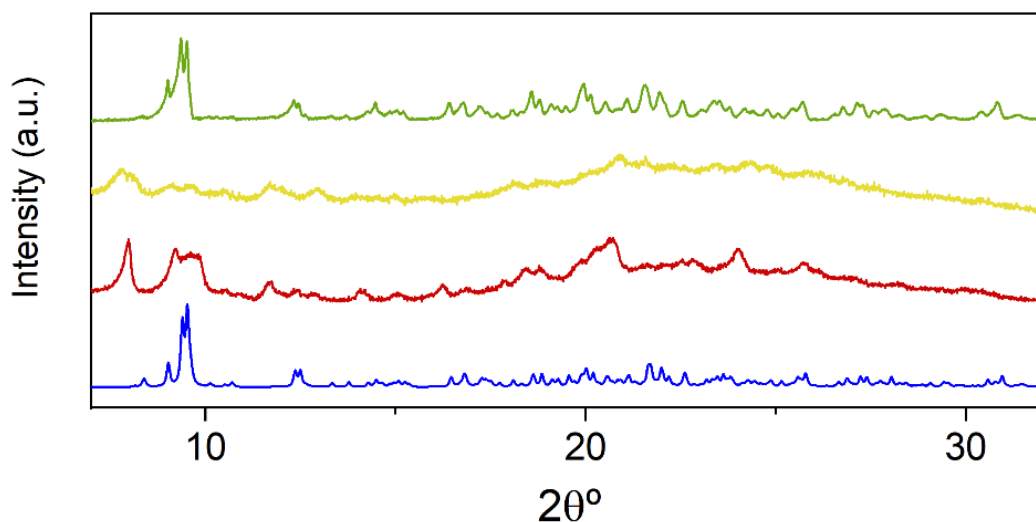


Figure SI. 3.4.15. Simulated PXRD pattern from the structure solved at 300 K (blue), experimental PXRD pattern of a freshly filtered sample (red), desolvated sample (yellow) and the sample in contact with the mother liquors (green) at 300K of **2**.

PXRD pattern at room temperature of filtered crystals presents important differences with respect to the simulated one confirming that the loss of crystallinity observed in single crystal measurements above 300 K is related to the loss of solvent molecules (**Figure SI. 3.4.15**). Indeed, elemental analysis of a filtered sample of **2** is more consistent with the presence of one acetone and four water molecules (see above). This suggests partial loss of acetone molecules and absorption of water molecules after filtering the crystals.

Table SI. 3.4.1. Unit cell parameters of a single crystal before and after thermal spin transition.

T (K)	120	270	290	260	300
a (Å)	12.846(5)	13.032(7)	12.878(11)	13.048(9)	12.863(14)
b (Å)	17.964(5)	18.040(6)	18.404(8)	18.035(7)	18.416(11)
c (Å)	19.297(13)	19.381(6)	19.631(10)	19.401(7)	19.635(12)
α (°)	90	90	88.74(4)	90	88.85(5)
β (°)	91.56(4)	90.76(4)	88.75(4)	90.70(4)	88.64(7)
γ (°)	90	90	89.74(5)	90	89.87(7)
V (Å ³)	4451(4)	4556(3)	4651(5)	4565(4)	4649(7)
	<i>P2₁/c</i>	<i>P2₁/c</i>	<i>P-1</i>	<i>P2₁/c</i>	<i>P-1</i>

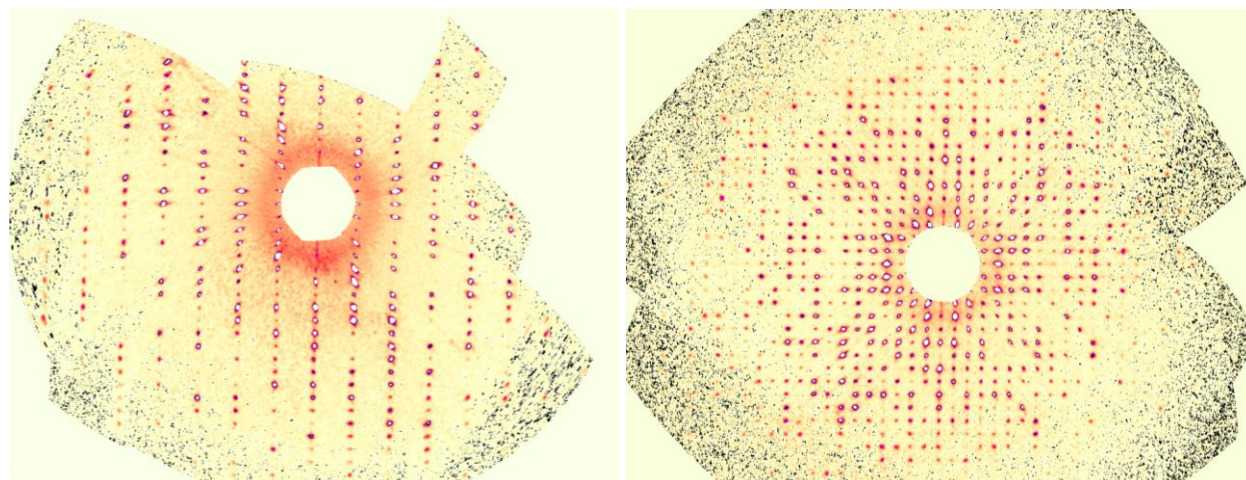


Figure SI. 3.4.16. Bragg peaks from the $h0l$ plane of the structure of **2** solved at 120K (left) and 300K (right). Doubling of the number of peaks take place.

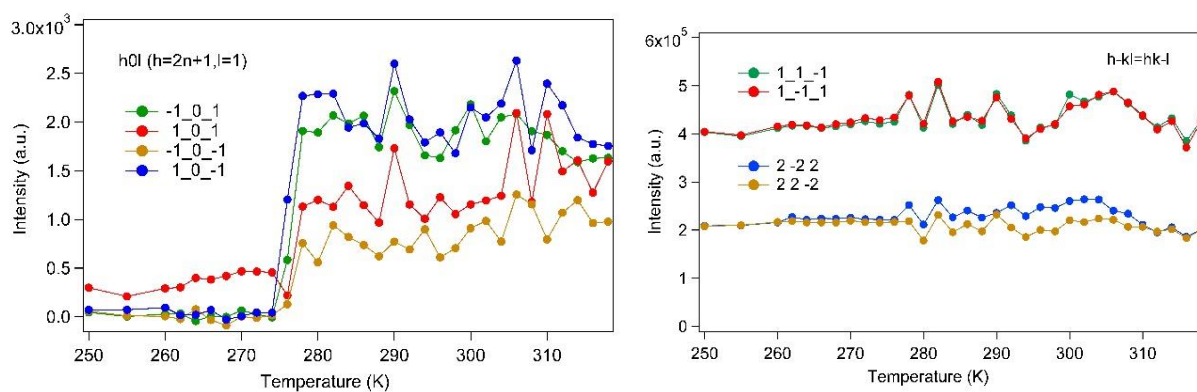


Figure SI. 3.4.17. Left, systematic absences from the $h0l$ plane that fulfill the $h=2n+1, l=m$ condition. Right, equivalent reflections from the $Ok0$ plane that fulfill the $k=2n+1$ condition. Values of the intensity extracted from the hkl file at the different temperatures.

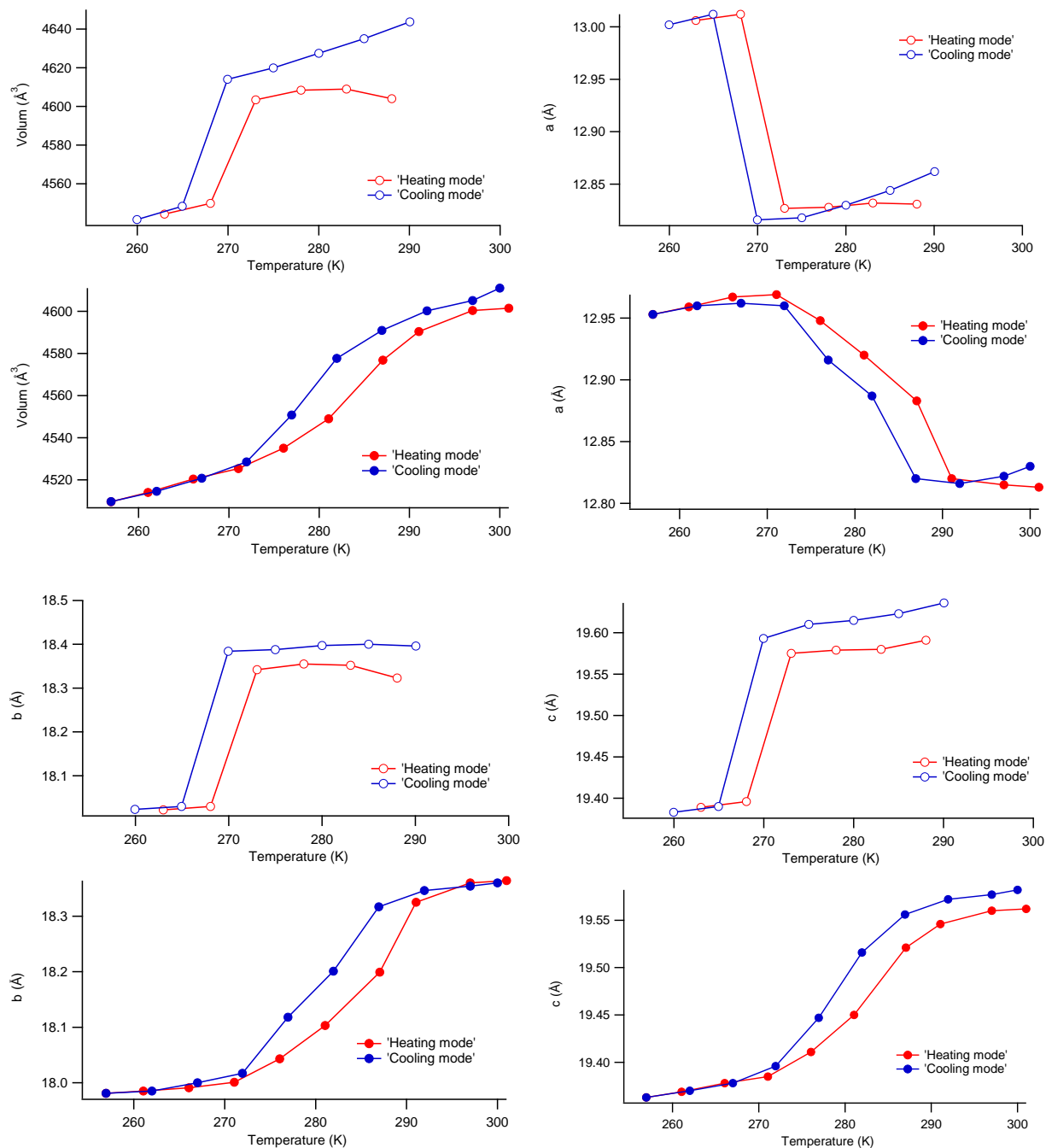


Figure SI. 3.4.18. Temperature dependence of the unit cell parameters of a crystal of **2** extracted directly from the mother liquors before (empty dots) and after heating the crystal at 300K for 2 hours (full dots) under the nitrogen stream.

After the second cycle the crystal was frozen, and the structure was solved at 120K in order to confirm the presence of **2·3Me₂CO** solvate.

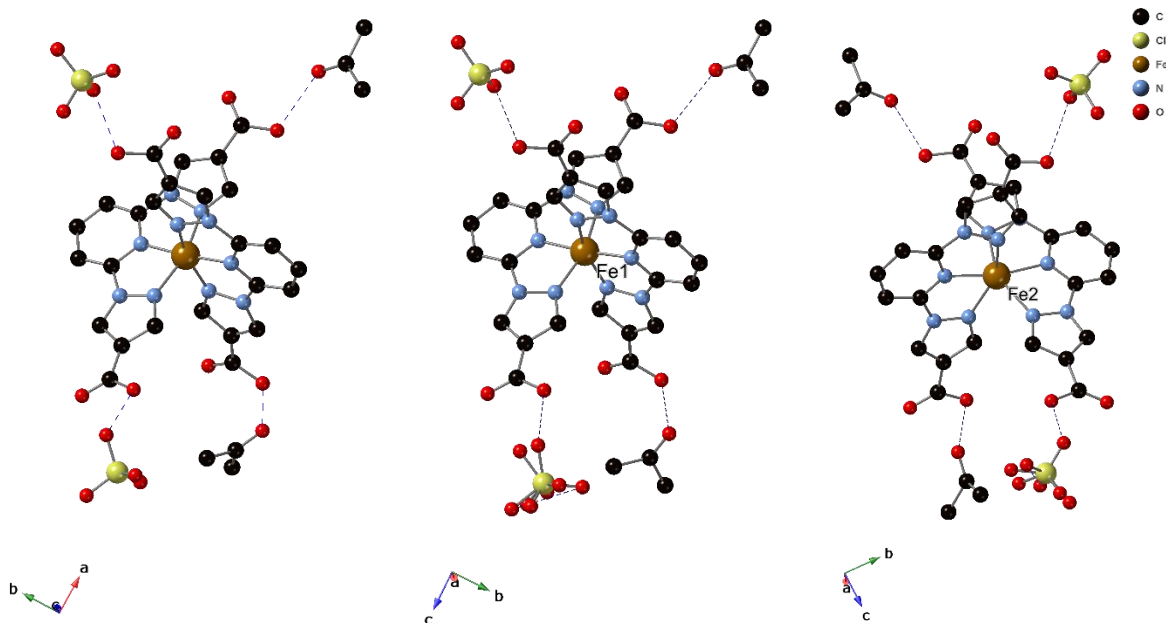


Figure SI. 3.4.19. Hydrogen bond interactions of $[\text{Fe}(\text{1bpCOOH}_2\text{p})_2]^{2+}$ complexes (blue-dashed lines) in the structure of **2** at 120 K (left) and 300 K (mid and right). Hydrogen atoms have been omitted for clarity.

The unit cell of **2** contains one crystallographically independent $[\text{Fe}(\text{1bpCOOH}_2\text{p})_2]^{2+}$ cation, two perchlorate counteranions and four acetone molecules (one of them with an occupancy of 0.5) at 120 K. At 300 K, there are two crystallographically independent $[\text{Fe}(\text{1bpCOOH}_2\text{p})_2]^{2+}$ cations (with Fe1 and Fe2, see **Figure SI. 3.4.20**), four perchlorate counteranions and six acetone molecules. One of these acetone and perchlorate molecules are disordered at 300 K. Furthermore, in the structure of **1** at 300 K, there are solvent accessible voids. The subroutine SQUEEZE was used to calculate the diffracting component of disordered solvents resulting in a void of ca. 186 \AA^3 and 28 electrons/cell.^[46] This corresponds to ca. one acetone molecule per cell. This molecule has been included in the molecular formula of the cif file leading to the same formula obtained in the structure at 120 K.

The Fe(II) ion of the complex coordinated by two tridentate 1bpCOOH₂p ligands presents a distorted octahedral geometry, which has been evaluated using Σ and Θ parameters ($\Sigma = 88.1(2)^\circ$ and $\Theta = 278.5(1)^\circ$ at 120 K and $\Sigma = 90.4(1)^\circ$ and $\Theta = 282.9(2)^\circ$ for Fe1 and $\Sigma = 152.7(2)^\circ$ and $\Theta = 495.9(2)^\circ$ for Fe2 at 300 K).^[47] These values are similar to those obtained in other bpp complexes with hysteretic spin transitions.^[17] Another remarkable aspect is that the HS complexes exhibit a strong Jahn–Teller distortion. Thus, the *trans*-N(pyridyl)–Fe–N(pyridyl) angles (φ) are $175.70(11)^\circ$ at 120 K and $174.80(18)^\circ$ (Fe1) and $167.93(17)^\circ$ (Fe2) at 300 K, whereas the dihedral

angles between the least squares planes of the two ligands (θ) are 80.2° at 120 K and 79.4° (Fe1) and 77.7° (Fe2) at 300 K. HS complexes deviating more strongly from the ideal values of θ and φ (90° and 180° , respectively) are less likely to transform to their LS state upon cooling.^[27] Indeed, most of the SCO active bpp based compounds exhibited Jahn–Teller distortion parameters with $\theta \geq 76^\circ$ and $\varphi \geq 172^\circ$. However, several examples of active SCO ones with parameters outside this range have been reported recently exhibiting hysteretic spin transitions.^[7,17,19] This seems to be the case in **2**, with a low φ value of 167.93° .

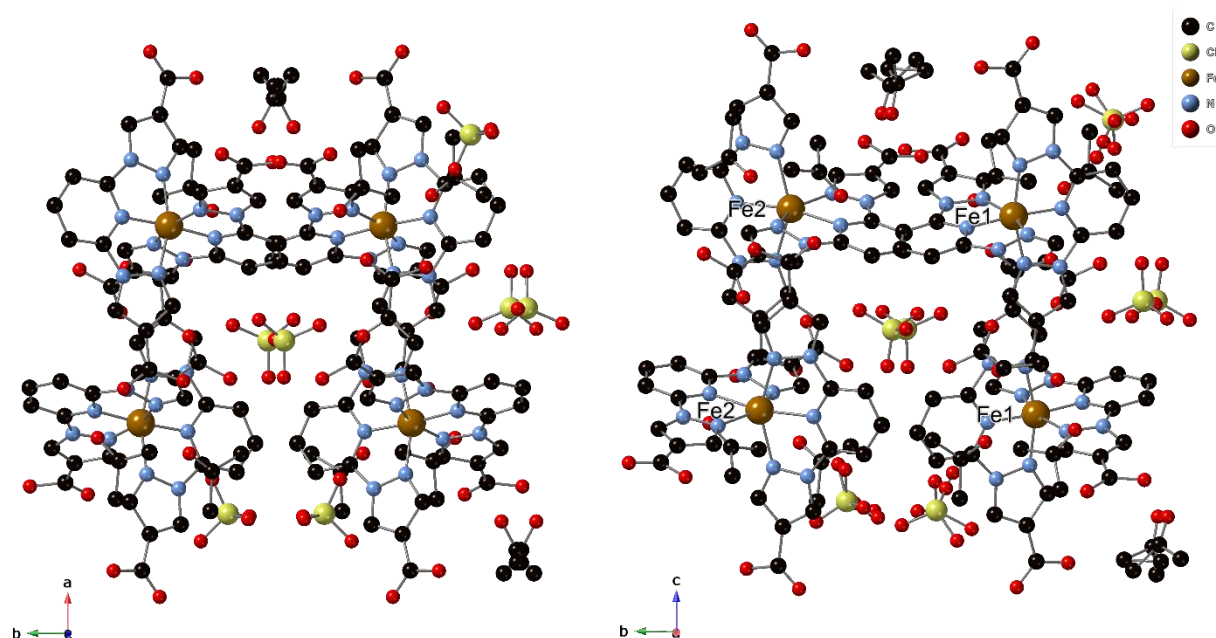


Figure SI. 3.4.20. Projection of the structure of **2** in the *ab* plane at 120 K (top) and in the *bc* plane at 300 K (bottom). Hydrogen atoms have been omitted for clarity.

The 1bpCOOH₂p ligands form hydrogen bonds with one acetone molecule and one ClO₄⁻ (see **Figure SI. 3.4.19**). This prevents formation of hydrogen-bonded chains of complexes as in other Fe(II) complexes of bpp functionalized with carboxylic acid, see Chapter 2. At 120 K, neighboring [Fe(1bpCOOH₂p)₂]²⁺ cations present $\pi \cdots \pi$ interactions between the pyrazolyl rings and several short contacts involving the CO groups. This gives rise to chains of complexes along the *c* axis (**Figure SI. 3.4.21**, top). These chains are linked at 120 K through several contacts involving O atoms from carboxylic acid groups and CH groups from pyridine and pyrazole (see **Figure SI. 3.4.22**) leading to a double layer of complexes in the *bc* plane (see **Figure SI. 3.4.20**, left). At 300 K, there are two types of chains, which now run along the *a* axis. Chains of LS [Fe(1bpCOOHp)₂]²⁺ cations with Fe1 present similar features in the *ab* plane to those at 120 K (see **Figure SI. 3.4.21**, mid).

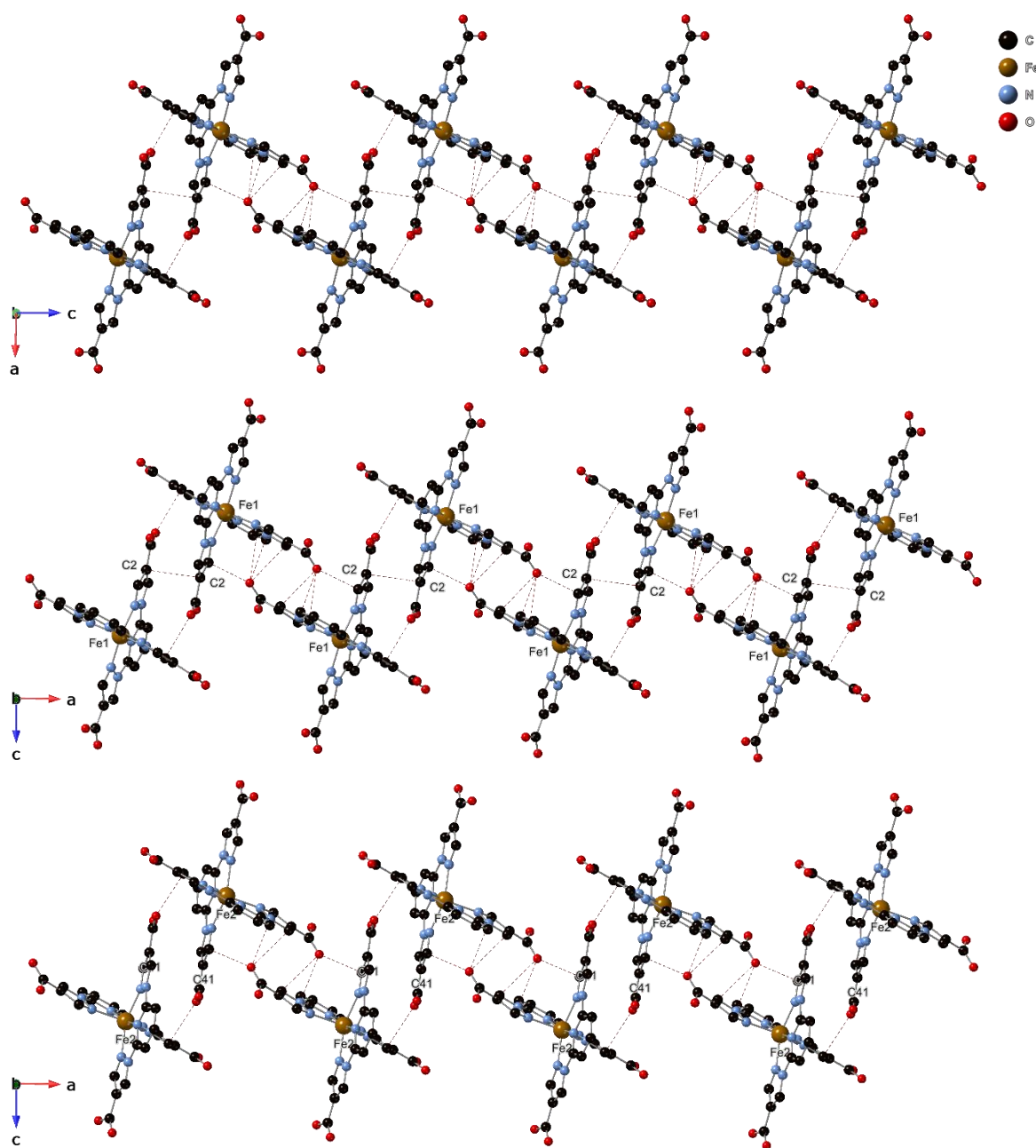


Figure SI. 3.4.21. Chains of $[\text{Fe}(\text{1bpCOOH}_2\text{p})_2]^{2+}$ complexes linked through intermolecular interactions (red-dashed lines) in the structure of **2** at 120 K (top) and 300 K (mid and bot). Hydrogen atoms and perchlorate counteranions have been omitted for clarity.

The HS $[\text{Fe}(\text{1bpCOOH}_2\text{p})_2]^{2+}$ cations with Fe2 form chains with a smaller number of intermolecular interactions. Thus, $\pi\cdots\pi$ interactions are not observed due to an increase of the C \cdots C distances between pyrazolyl rings of neighboring complexes related by an inversion center

(C41...C41 = 3.416 Å for HS complexes and C2...C2 = 3.288 Å for LS complexes). At the same time, the number of short contacts involving the CO groups decreases (see **Figure SI. 3.4.21**, bot). In contrast to this, complexes with Fe1 and Fe2 belonging to different chains present stronger intermolecular interactions (see **Figure SI. 3.4.22**).

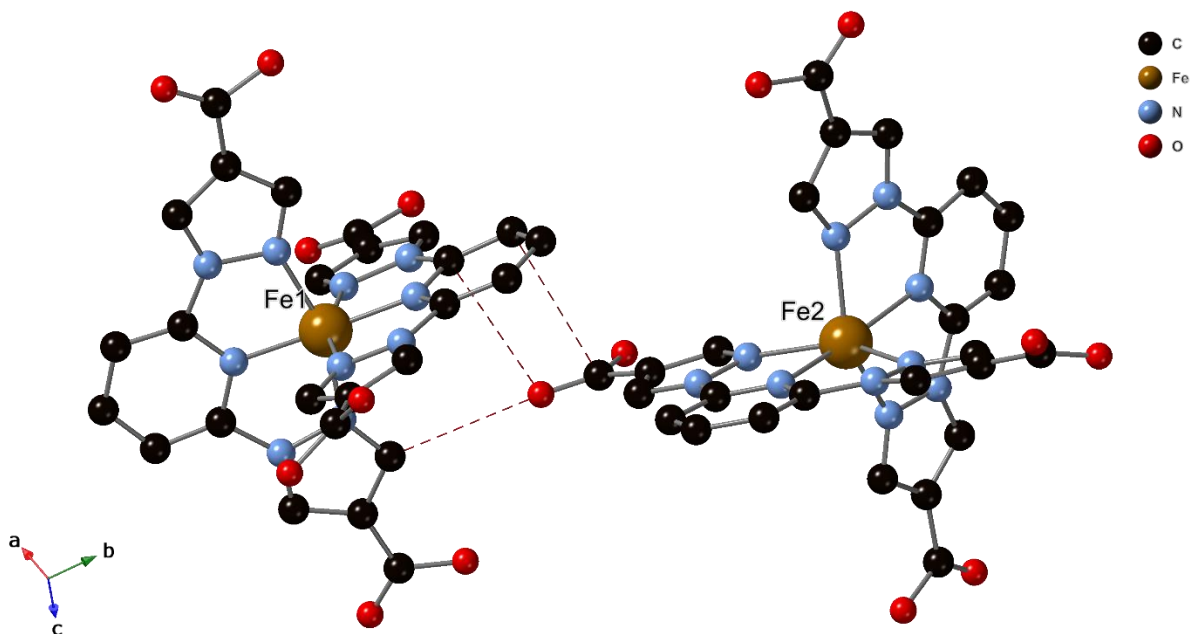


Figure SI. 3.4.22. Interchain interactions between $[\text{Fe}(\text{1bpCOOH}_2\text{p})_2]^{2+}$ complexes (red-dashed lines) in the structure of **2** at 300 K. Hydrogen atoms and perchlorate counteranions have been omitted for clarity.

PXRD pattern before and after thermal spin transition were measured in contact with the mother liquors. The two diffractograms at 250 K and that at 300 K are in good agreement with simulated powder patterns for the $P2_1/c$ and $P-1$ phases, respectively (see **Figure SI. 3.4.23**, left). The reversibility of the crystallographic symmetry breaking was monitored by PXRD experiments. Thus, the sample was first measured at 300 K and then cooled to 250 K to reach the LS phase, then another PXRD pattern was collected again at 300 K (**Figure SI. 3.4.23**, right).

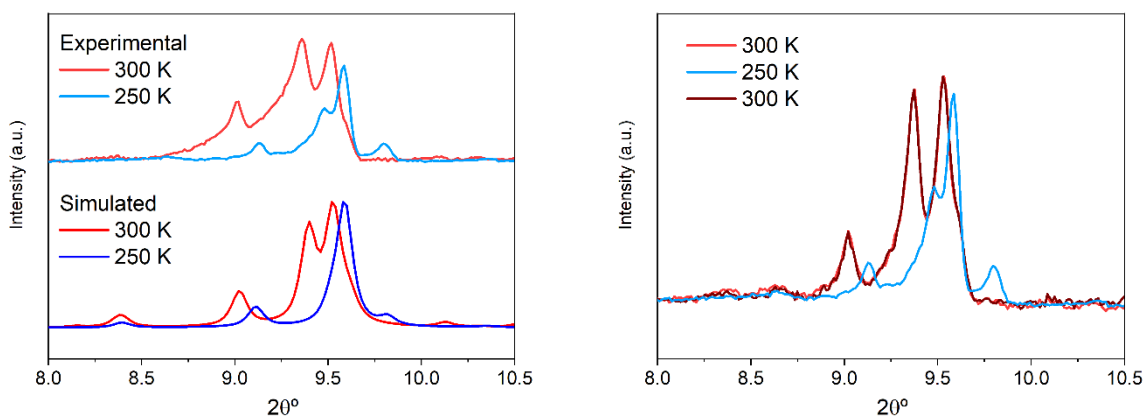


Figure SI. 3.4.23. PXRD patterns of **2**; **left**, simulated at 300 K (blue) and 250 K (red) and experimental at 300 K (light blue) and 250 K (light red); **right**, experimental at 300 K (light blue) and 250 K (light red) and 300 K after cooling to 250 K (dark red) to confirm reversibility of the crystallographic symmetry breaking.

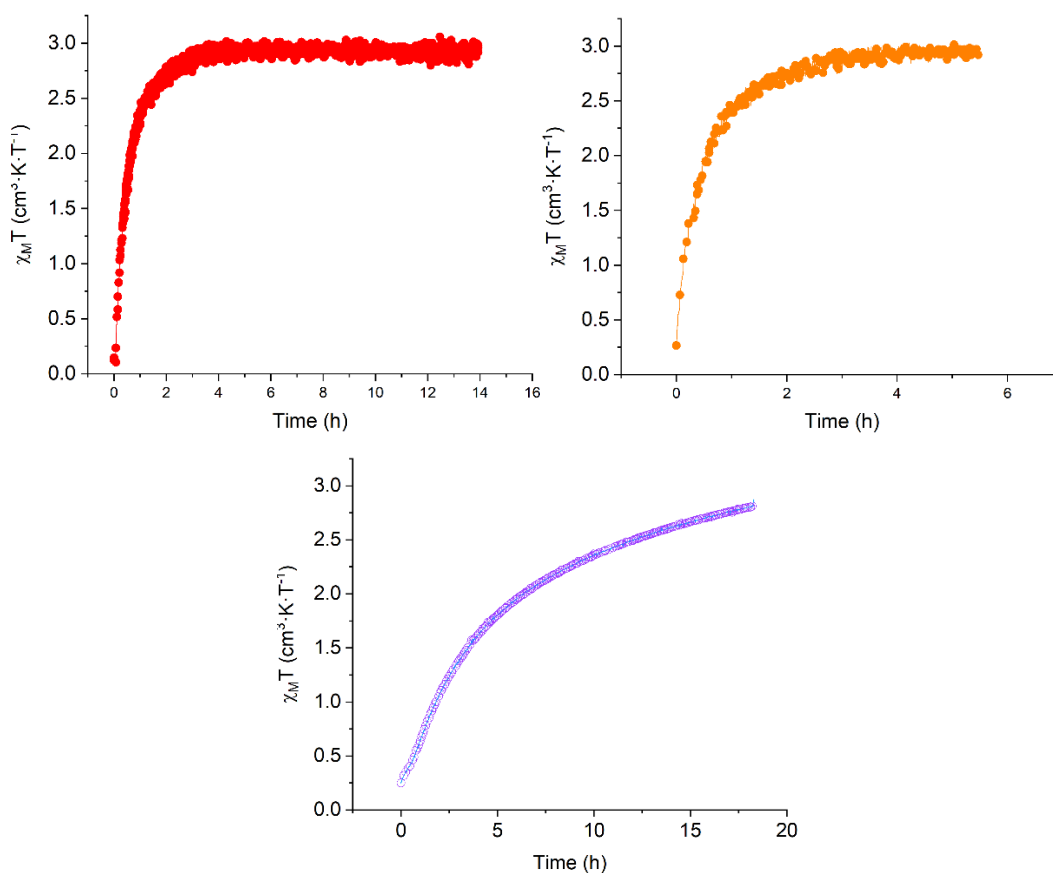


Figure SI. 3.4.24. Time dependence of $\chi_M T$ of **2** under light irradiation with a 660 nm wavelength laser for ca. 16 h (top-left), 6 h (top-right) and under light irradiation with a 1064 nm wavelength laser for ca. 18 h (bottom) at 10 K

Relaxation of the metastable state in 2

In order to determine the kinetic mechanism that govern the magnetic relaxation of the photoexcited HS state we have used the model proposed by Hauser et al for a cooperative system.^[31,32]

$$\frac{d\gamma_{\text{HS}}}{dt} = -k_{\text{HL}} * \gamma_{\text{HS}} \quad (1)$$

$$k_{\text{HL}}*(T, \gamma_{\text{HS}}) = k_{\text{HL}}(T)\exp[a(T)(1 - \gamma_{\text{HS}})] \quad (2)$$

$$\text{where } a(T) = E_a^*/k_B T \text{ and } k_{\text{HL}}(T) = k_{\infty}\exp(-E_a/k_B T)$$

Using these set of equations, we have programmed an IGOR Pro 8 (Wavemetrics software, Lake Oswego, OR, USA) procedure to perform the fitting of the photoexcited relaxation for a range of temperatures between 105 and 120K (see **Figure SI. 3.4.25**, left). These fittings run over two main parameters for each curve: $k_{\text{HL}}(T)$ and $\alpha(T)$, with the boundaries of $k_{\text{HL}}(0)$. From the exponential definition of $k_{\text{HL}}(T)$, it is possible to define a typical Arrhenius law to extract the activation energy of the transition E_a and the preexponential factor k_{∞} . (see **Figure SI. 3.4.25**, right). In this latter case, the 105K measurement has been rejected due to the long relaxation rate at the measured times and the uncertainties in the extrapolation.

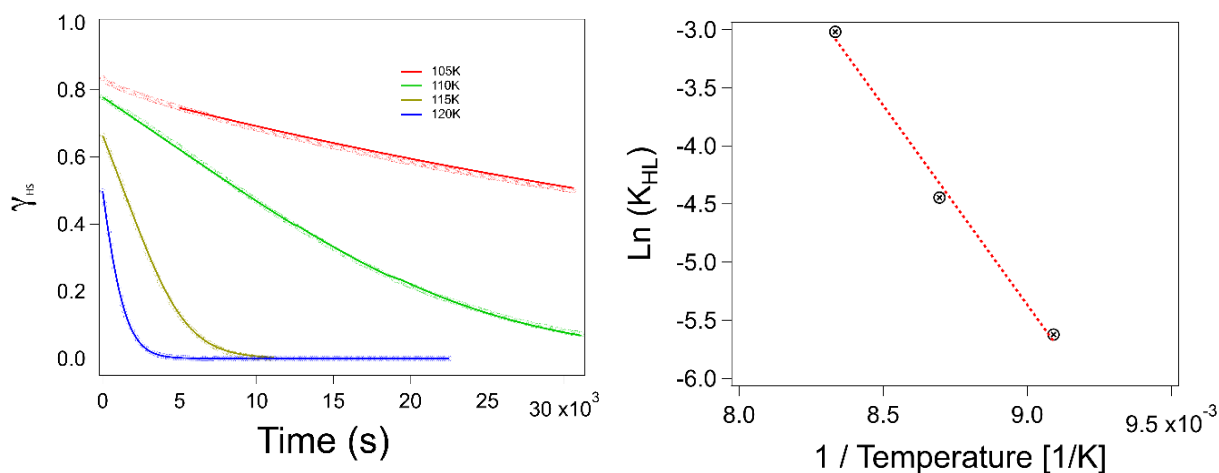


Figure SI. 3.4.25. Left, time dependence at various temperatures of the photoinduced HS molar fraction. The relaxation curves are fitted according to sigmoidal behavior (see text for more details). Right, Arrhenius fitting of the activate process (the measurement at 105K has been removed from the fitting, see text).

The values of the k_{∞} and E_a obtained from these fittings are higher than those reported in the literature. Furthermore, the low value of E_a^* could indicate a low level of cooperativity. However, these values must be taken with caution since they are obtained with a limited number of experiments so they could be considered as preliminary. It was not possible to perform a complete set of relaxations at different temperatures for practical reasons, which are related mainly to the long irradiation times needed to reach saturation (8 hours). An additional problem is that it was not possible to reuse the same sample for relaxations at different temperatures. Thus, if the same sample was re-irradiated after being heated above 120 K to erase the metastable state obtained in the first irradiation, slightly faster relaxations were obtained (see **Figure SI. 3.4.26**). This could be related to irreversible damage of part of the sample related to loss of solvent molecules or other structural changes. As a result of this, it was necessary to use a fresh sample for a relaxation at a given temperature.

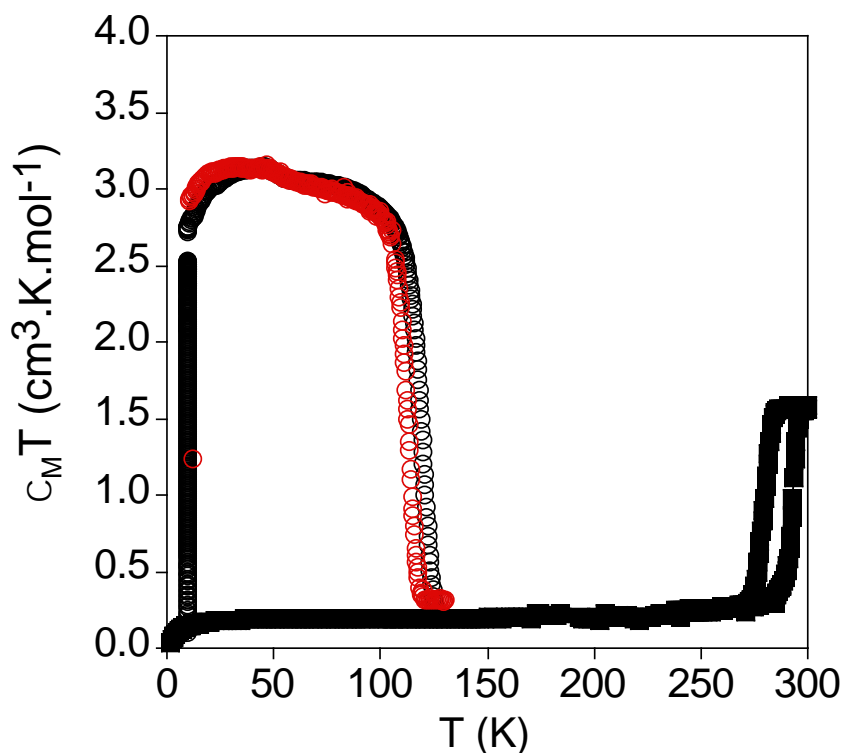


Figure SI. 3.4.26. Thermal dependence of χ_{MT} of **1**. Full squares: data recorded without irradiation; Black empty circles: data recorded after the first irradiation at 10 K and; Red empty circles: data recorder after second irradiation at 10 K.

Table S.I. 3.4.2. Unit cell parameters of single crystals of **2** measured before and after irradiation with 660 for different periods of time.

	10 K in the dark (LS)	20 K + 660 nm for ca. 60 s (LS-HS*)	20 K + 660 nm for ca. 360 s (HS*)
Symmetry	$P2_1/c$	$P-1$	$P2_1/c$
a (Å)	19.161(5)	12.5149(19)	19.328(2)
b (Å)	17.895(2)	18.2722(16)	18.460(2)
c (Å)	12.769(2)	19.323(4)	12.2091(7)
α (°)	90	91.247(10)	90
β (°)	91.790(14)	89.772(14)	90.150(9)
γ (°)	90	90.259(9)	90
V (Å³)	4376.3(15)	4417.5(11)	4356.13(8)

Table S.I. 3.4.3. Fe-N bond distances of the single crystals of **2** measured before and after irradiation with 660 for different periods of time.

LS ($P2_1/c$)			HS* ($P2_1/c$)		
Bond		Length (Å)	Bond		Length (Å)
Fe1	N1	1.954(19)	Fe1	N1	2.121(14)
Fe1	N3	1.916(18)	Fe1	N3	2.101(11)
Fe1	N5	1.991(16)	Fe1	N5	2.138(12)
Fe1	N6	1.991(19)	Fe1	N6	2.090(15)
Fe1	N8	1.900(18)	Fe1	N8	2.119(13)
Fe1	N10	1.972(18)	Fe1	N10	2.096(15)
LS-HS* ($P-1$)					
Fe1			Fe2		
Bond		Length (Å)	Bond		Length (Å)
Fe1	N1	2.13(2)	Fe2	N11	1.99(2)
Fe1	N3	2.095(18)	Fe2	N13	1.966(19)
Fe1	N5	2.147(17)	Fe2	N15	1.89(2)
Fe1	N6	2.181(18)	Fe2	N16	1.976(18)
Fe1	N8	2.05(2)	Fe2	N18	1.882(18)
Fe1	N10	2.110(19)	Fe1	N20	1.961(19)

Table S.I. 3.4.4. Distortion parameters of the single crystals of **2** measured before and after irradiation with 660 for different periods of time at low temperature.

	10 K in the dark (LS)	20 K + 660 nm for ca. 60 s (LS-HS*)		20 K + 660 nm for ca. 360 s (HS*)
		<i>Fe1</i> (HS)	<i>Fe2</i> (LS)	
Σ (°)	95.01	163.16	95.47	153.55
φ (°)	174.47	166.91	170.88	165.37
θ (°)	80.94	76.89	78.38	76.27

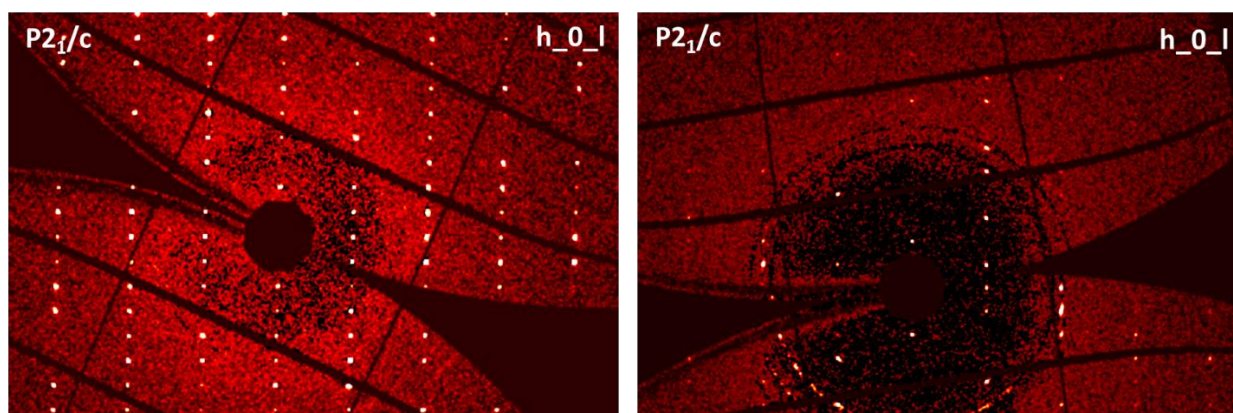


Figure SI. 3.4.27. Bragg peaks from the $h0l$ plane of the structure of **2** before (left) and after (right) irradiation with 660 nm for ca. 360 s. The systematic absences $h0l$ ($h = 2n + 1$, $l = m$) are fulfilled.

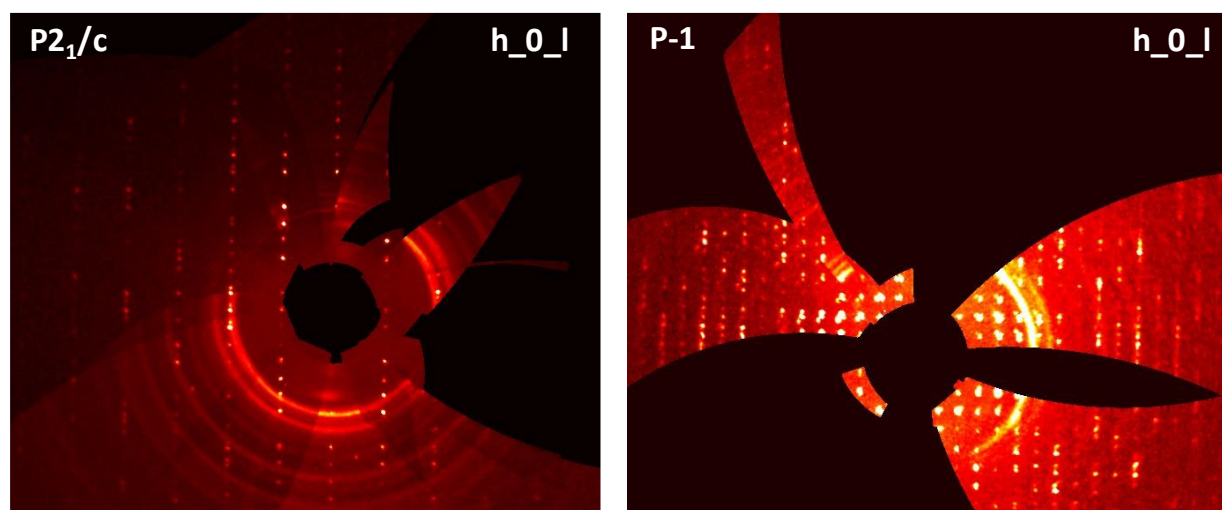


Figure SI. 3.4.28. Bragg peaks from the $h0l$ plane of the structure of **2** before (left) and after (right) irradiation with 660 nm ca. 60 s. Doubling of the number of peaks take place.

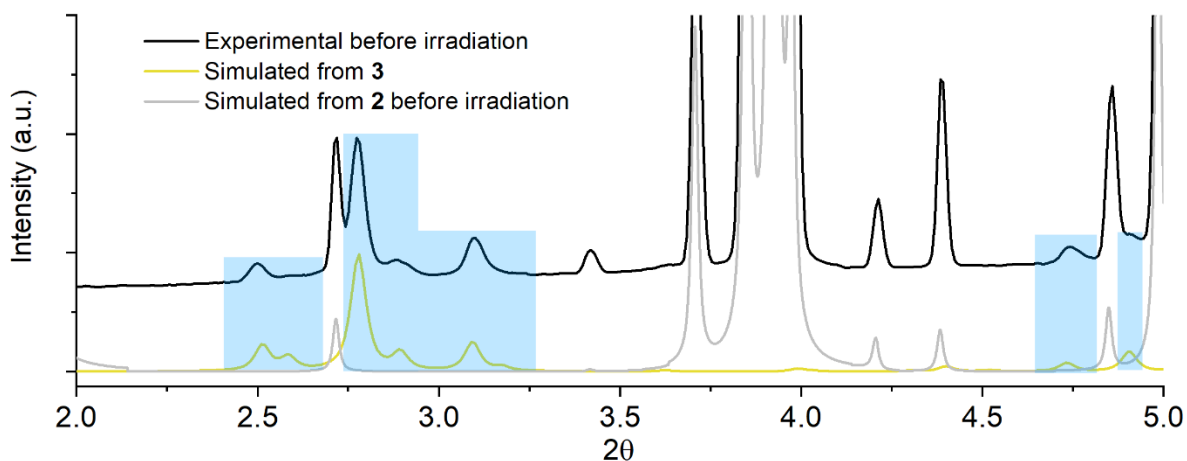


Figure SI. 3.4.29. Simulated PXRD pattern of **3** (yellow), **2** (grey) and experimental PXRD pattern of a powder sample of **2** (black) before irradiation in the 2 - 5 2θ range at low temperature. Areas highlighted in blue are guides to the eye.

The small fraction of **3** present in the powder sample has been calculated to be less than ~10% of the polymeric phase present in the spectra (see **Figure SI. 3.4.29**), probably due to the exposure to the atmosphere of the diffusion tubes from our in-house glovebox to the synchrotron facilities (see SI). Fine analysis of the spectra with the refined PXRD patterns from the single crystal structure are in progress and will be reported in due course.

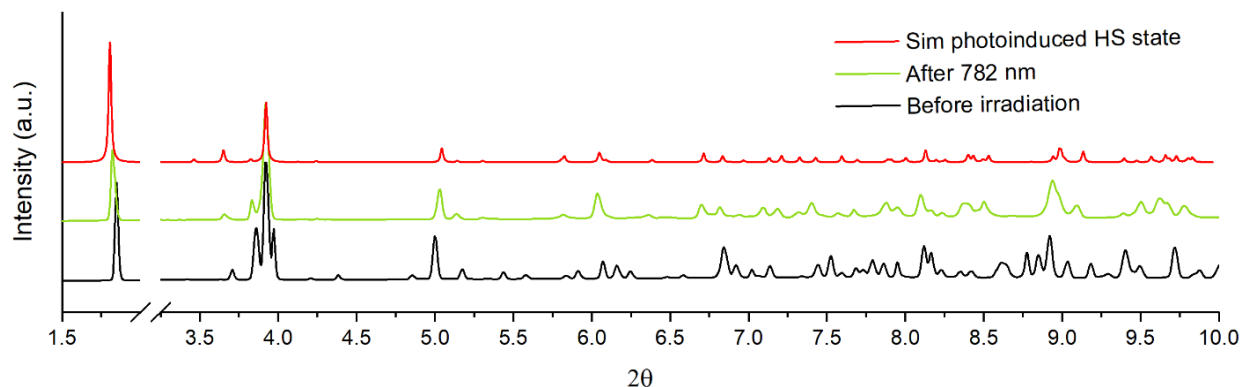


Figure SI. 3.4.30. Experimental PXRD patterns of a powder sample of **2** measured before (black) and after (green) irradiation with 782 nm at 20 K for *ca.* 4800 seconds. In red, the PXRD pattern of a powder sample measured with 660 nm for comparison purposes.

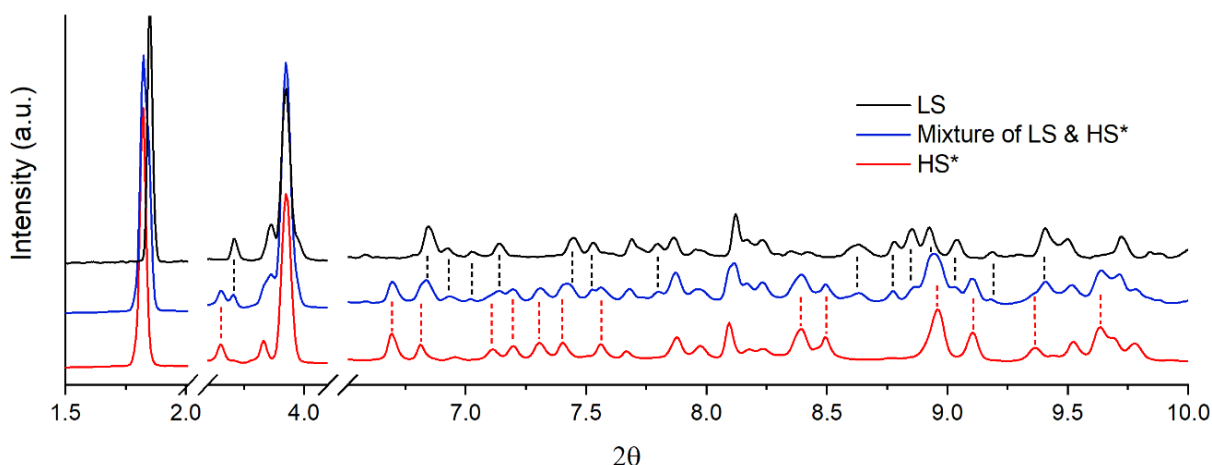


Figure SI. 3.4.31. Experimental PXRD patterns of a powder sample of **2** measured before (black) and after (blue) irradiation with 472 nm at low temperature. In red, experimental PXRD of the HS* is shown for comparison purposes. Dashed lines are a guide to eye.

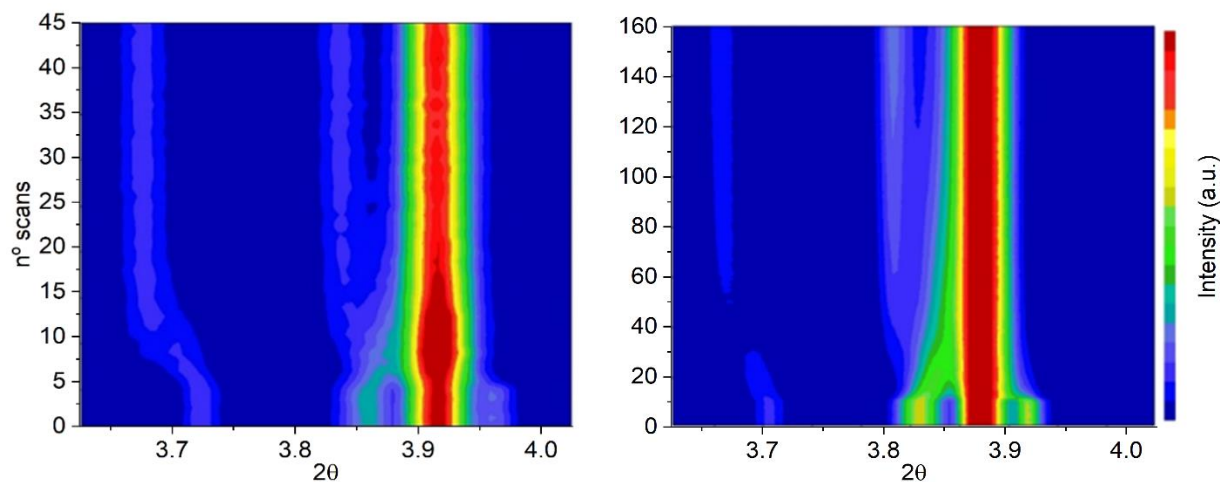


Figure SI. 3.4.32. Time dependent 3D surface maps of a spin and symmetry dependent peaks in the 3.6 – 4 2θ range of a powder sample of **2** under light irradiation with 660 nm (left) and 782 nm (right). The first spectra are collected in the dark as a reference.

A gradual evolution of the peaks is observed in the 3D surface maps. It is clear by the larger number of spectra that the 782 nm laser has less effect inducing the HS* state compared to the 660 nm, taking into account that each spectra takes ca. 30 seconds to record.

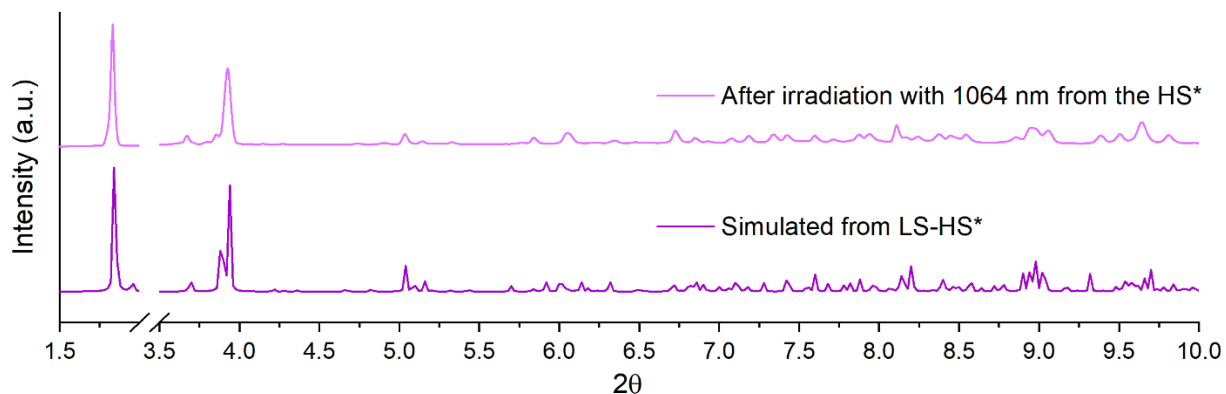


Figure SI. 3.4.33. Simulated PXRD pattern of a single crystal (violet) after irradiation for 60 seconds and a powder sample in the HS* state (pink) of **2** under continuous irradiation for ca. 4500 seconds with 1064 nm at 20 K.

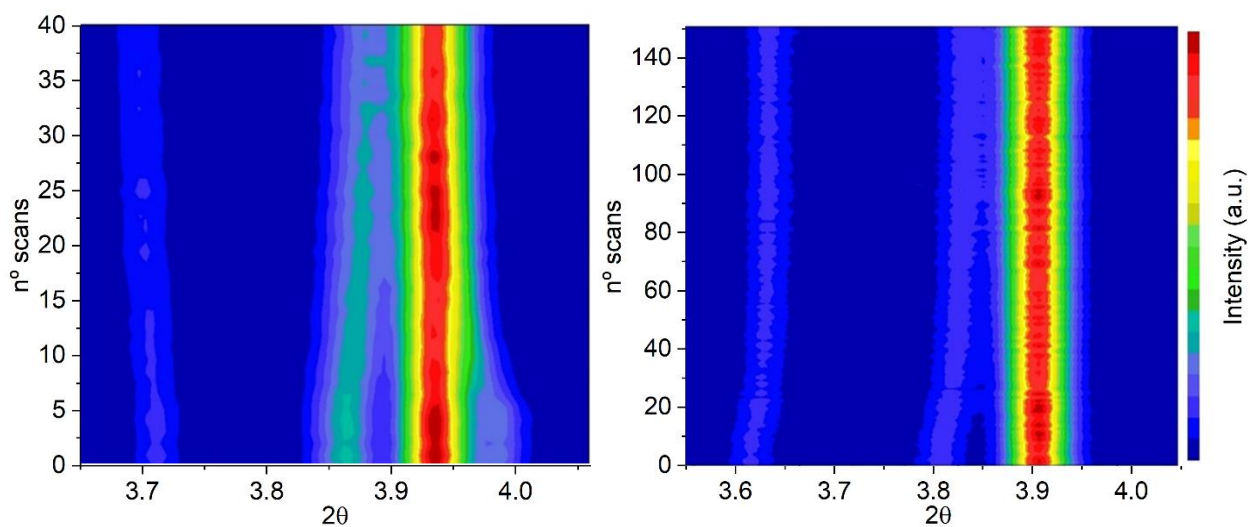


Figure SI. 3.4.34. Time dependent 3D surface maps of a spin and symmetry dependent peaks in the 3.6 – 4 2θ range of a powder sample of **2** under light irradiation with 1064 nm from the HS* state (left) and LS state (right). The first spectra are collected in the dark as a reference.

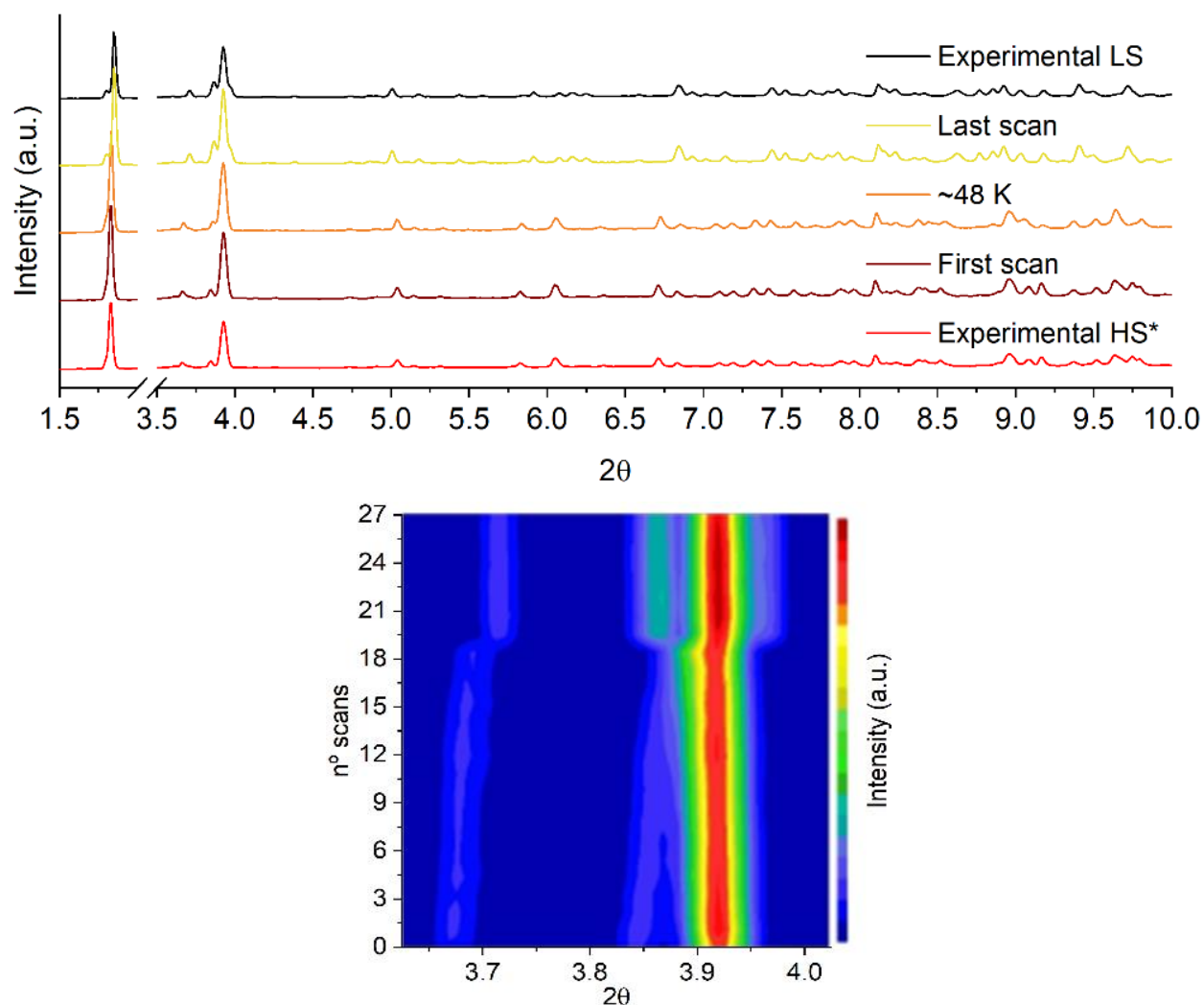


Figure SI. 3.4.35. Top, experimental PXR D of the first (wine), 48 K averaged spectrum (yellow) and last scan (yellow) of the temperature variation experiment of a powder sample of **2**. Experimental PXR D of the LS and HS* phases are also included for comparison purposes. **Bottom**, Temperature dependent 3D surface maps of a spin and symmetry dependent peaks in the 3.6 – 4 2θ range of the powder sample. Each scan represents a step of $\Delta T = 1$ K.

The temperature scan experiment was performed as follows: first, the cryogenic set up was set to increase the temperature 30 K above from base temperature (*ca.* 40 K). A single scan was done to check that the PXR D phase was the same than the one at base temperature. Then, the temperature controller was programmed to do steps of $\Delta T = 1$ K and collect three single scans after stabilization of the temperature. The average of those three scans were used as a single temperature point. Then they were compared on by one with the experimental after 1064 nm irradiation. The best fit was obtained with the averaged spectrum number 8th (*ca.* 48 K), which is

in agreement with the $T(\text{LIESST})$ obtained from LIESST experiments, ca. 43 K. Then, due to the cryogenic set up used, a spike in temperature in scan number 20th caused an abrupt stabilization of the $P2_1/c$ LS phase.

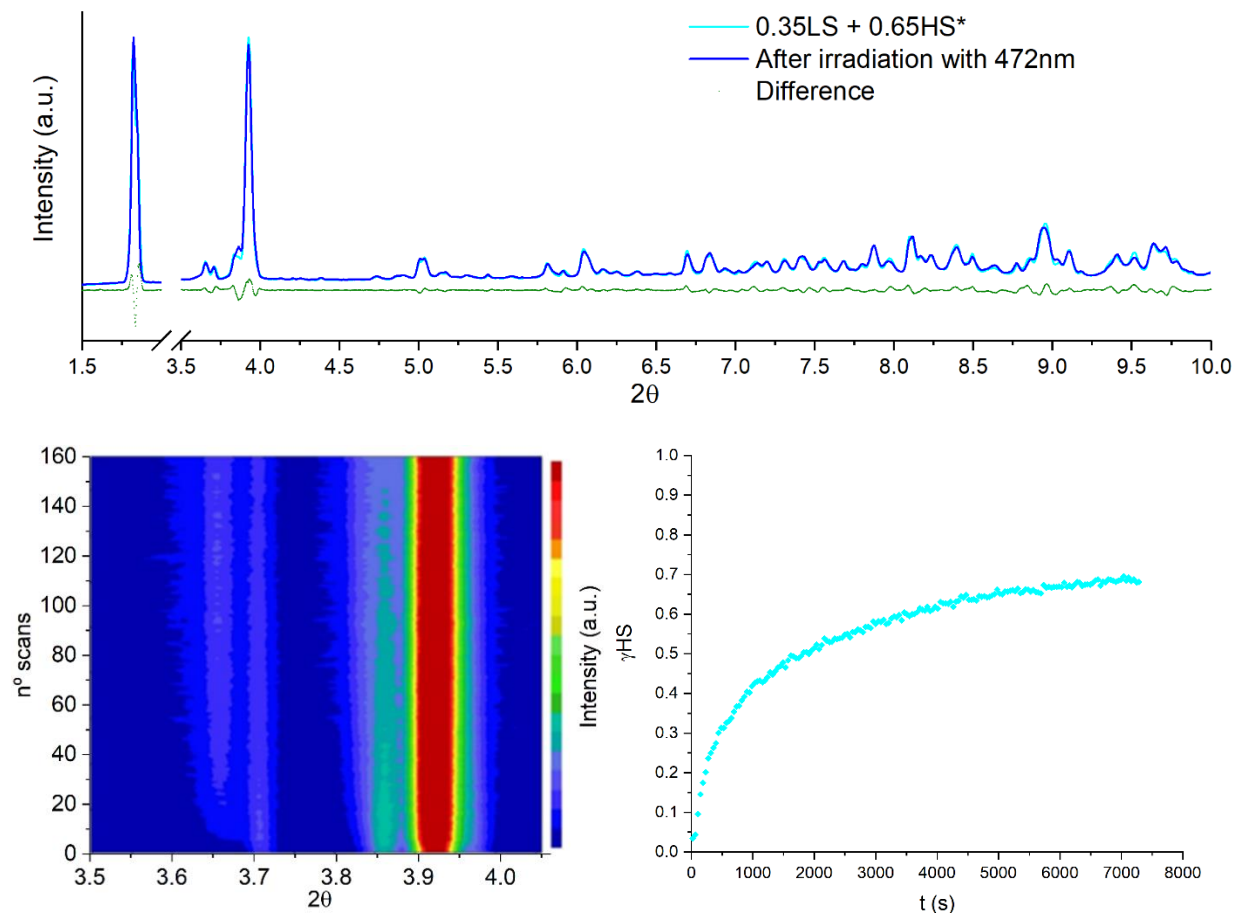


Figure SI. 3.4.36. Top, experimental PXRD patterns of a powder sample of **2** measured before (black), after irradiation with 472 (blue) and 660 nm (red) at low temperature. **Bottom-left**, Time dependent 3D surface maps of a spin and symmetry dependent peaks in the 3.6 – 4 2θ range of the powder sample under light irradiation with 472 nm. **Bottom-right**, time distribution of the HS photoinduced molar fraction obtained from the linear regression fit of the single spectra with the experimental LS and HS* used as references.

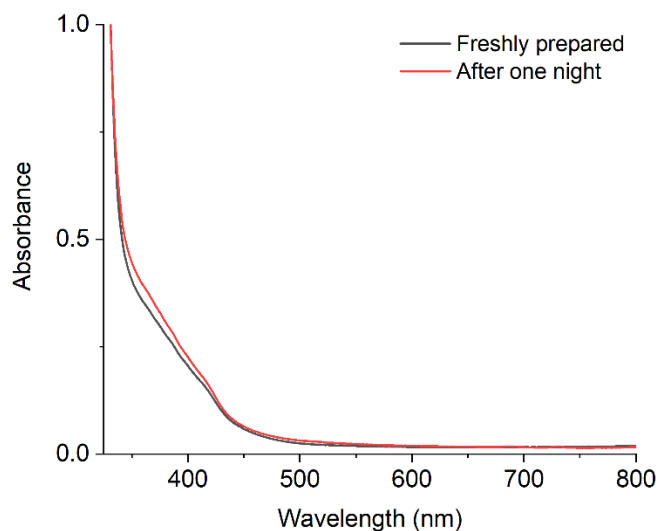
Deposition of **2**

Figure SI. 3.4.37. UV/Vis spectra of a 0.1 mM solution of **2** in MeCN freshly prepared (black line) and after one day in inert atmosphere (red line).

UV/Vis spectroscopy of **2** does not display the typical MLCT $t_2-\pi^*$ transition for bpp complexes, suggesting a HS state in agreement with the yellow color of the solution of the compound.^[38,39] Comparison between the UV/Vis spectrum of freshly prepared and after one night in inert atmosphere shows an increase of the absorbance at around 400 nm, which could be caused by partial decomposition of the complexes in solution as observed in the solid state.

Table S.I. 3.4.5. Crystallographic tables.

Compound	1	2	2
Empirical formula	C ₅₀ H ₃₂ N ₂₀ O ₂₆ Cl ₄ Fe ₂	C ₇₃ H ₇₈ Cl ₄ Fe ₂ N ₂₀ O ₃₉	C ₃₅ H ₃₆ Cl ₂ FeN ₁₀ O ₁₉
Formula weight	1582.45	2113.05	1027.49
Temperature/K	120.15(10)	120.00(10)	300.05(10)
Crystal system	tetragonal	monoclinic	triclinic
Space group	<i>I</i> -42 <i>d</i>	<i>P</i> 2 ₁ / <i>c</i>	<i>P</i> -1
<i>a</i> /Å	21.359(3)	19.2527(3)	12.8517(4)
<i>b</i> /Å	21.359(3)	17.9600(3)	18.4107(4)
<i>c</i> /Å	15.1623(19)	12.8378(2)	19.5908(4)
α /°	90	90	88.715(2)
β /°	90	91.571(2)	88.876(2)
γ /°	90	90	89.761(2)
Volume/Å ³	6917.4(19)	4437.37(12)	4633.2(2)
Z	4	2	4
ρ_{calc} /cm ³	1.519	1.581	1.473
μ /mm ⁻¹	0.666	0.552	0.525
F(000)	3200.0	2176.0	2112.0
Crystal size/mm ³	0.03 x 0.03 x 0.32	0.4 x 0.35 x 0.04	0.72 x 0.41 x 0.09
Radiation	MoK α (λ = 0.71073)	MoK α (λ = 0.71073)	MoK α (λ = 0.71073)
2 Θ range for data collection/°	6.59 to 53.118	6.638 to 55.032	6.636 to 55.072
Index ranges	-26 \leq h \leq 26, -26 \leq k \leq 26, -18 \leq l \leq 18	-17 \leq h \leq 24, -23 \leq k \leq 23, -14 \leq l \leq 16	-16 \leq h \leq 16, -23 \leq k \leq 23, -25 \leq l \leq 25
Reflections collected	48871	32411	64980
Independent reflections	3571 [R _{int} = 0.2168, R _{sigma} = 0.1044]	9404 [R _{int} = 0.0466, R _{sigma} = 0.0614]	19501 [R _{int} = 0.0904, R _{sigma} = 0.1387]
Data/restraints/parameters	3571/37/225	9404/2/631	19501/43/1260
Goodness-of-fit on F ²	1.031	1.040	1.056
Final R indexes [<i>I</i> \geq 2 σ (<i>I</i>)]	R ₁ = 0.1299, wR ₂ = 0.3230	R ₁ = 0.0515, wR ₂ = 0.1116	R ₁ = 0.0814, wR ₂ = 0.1848
Final R indexes [all data]	R ₁ = 0.2449, wR ₂ = 0.3960	R ₁ = 0.0805, wR ₂ = 0.1291	R ₁ = 0.1881, wR ₂ = 0.2574
Largest diff. peak/hole / e Å ⁻³	0.42/-0.35	0.71/-0.49	0.84/-0.42

Compound	2 in the dark	2 + 660 nm ca. 60 s	2 + 660 nm ca. 360 s
Empirical formula	C _{36.5} H ₃₉ Cl ₂ FeN ₁₀ O _{19.5}	C _{36.5} H ₃₉ Cl ₂ FeN ₁₀ O _{19.5}	C ₃₅ H ₃₅ Cl ₂ FeN ₁₀ O ₁₉
Formula weight	1056.52	1056.52	2052.96
Temperature/K	10.0	20.0(1)	10.0
Crystal system	monoclinic	triclinic	monoclinic
Space group	P2 ₁ /c	P-1	P2 ₁ /c
a/Å	19.161(5)	12.5149(19)	19.328(2)
b/Å	17.895(2)	18.2722(16)	18.460(2)
c/Å	12.769(2)	19.323(4)	12.2091(7)
α/°	90	91.247(10)	90
β/°	91.790(14)	89.772(14)	90.150(9)
γ/°	90	90.259(9)	90
Volume/Å ³	4376.3(15)	4417.5(11)	4356.0(8)
Z	4	4	2
ρ _{calc} /cm ³	1.604	1.589	1.565
μ/mm ⁻¹	0.559	0.554	0.390
F(000)	2176.0	2176.0	2108.0
Crystal size/mm ³	0.558 × 0.226 × 0.011	0.35 × 0.25 × 0.025	0.04 × 0.04 × 0.02
Radiation	MoKα (λ = 0.71073)	MoKα (λ = 0.71073)	Synchrotron irradiation (λ = 0.62241)
2θ range for data collection/°	5.918 to 49.998	5.892 to 49.998	3.69 to 52.792
Index ranges	-18 ≤ h ≤ 22, -21 ≤ k ≤ 15, -14 ≤ l ≤ 14	-14 ≤ h ≤ 14, -21 ≤ k ≤ 21, -20 ≤ l ≤ 22	-26 ≤ h ≤ 26, -25 ≤ k ≤ 25, -9 ≤ l ≤ 9
Reflections collected	11911	14795	26697
Independent reflections	5587 [R _{int} = 0.3768, R _{sigma} = 0.5064]	14795 [R _{int} = ?, R _{sigma} = 0.4291]	8172 [R _{int} = 0.3879, R _{sigma} = 0.3758]
Data/restraints/parameters	5587/359/627	14795/654/1243	8172/0/592
Goodness-of-fit on F ²	0.975	1.058	0.900
Final R indexes [I ≥ 2σ(I)]	R ₁ = 0.1428, wR ₂ = 0.2971	R ₁ = 0.1481, wR ₂ = 0.3678	R ₁ = 0.1204, wR ₂ = 0.2685
Final R indexes [all data]	R ₁ = 0.3425, wR ₂ = 0.3911	R ₁ = 0.2929, wR ₂ = 0.4318	R ₁ = 0.3753, wR ₂ = 0.4183
Largest diff. peak/hole / e Å ⁻³	0.94/-0.73	1.26/-1.11	0.78/-0.34

Compound	3
Empirical formula	$C_{87}H_{74}Cl_6Fe_4N_{30}O_{53}$
Formula weight	2823.86
Temperature/K	120.00(10)
Crystal system	triclinic
Space group	<i>P</i> -1
<i>a</i> /Å	14.6268(6)
<i>b</i> /Å	15.0615(6)
<i>c</i> /Å	15.2862(6)
α /°	96.056(3)
β /°	112.125(4)
γ /°	104.778(4)
Volume/Å ³	2939.0(2)
Z	1
ρ_{calc} /cm ³	1.595
μ /mm ⁻¹	0.728
F(000)	1436.0
Crystal size/mm ³	0.12 × 0.09 × 0.04
Radiation	MoK α (λ = 0.71073)
2 θ range for data collection/°	6.612 to 56.02
Index ranges	-19 ≤ <i>h</i> ≤ 19, -19 ≤ <i>k</i> ≤ 19, -19 ≤ <i>l</i> ≤ 20
Reflections collected	43662
Independent reflections	12366 [<i>R</i> _{int} = 0.0880, <i>R</i> _{sigma} = 0.1527]
Data/restraints/parameters	12366/8/917
Goodness-of-fit on <i>F</i> ²	1.032
Final <i>R</i> indexes [<i>I</i> ≥ 2 σ (<i>I</i>)]	<i>R</i> ₁ = 0.0950, <i>wR</i> ₂ = 0.2355
Final <i>R</i> indexes [all data]	<i>R</i> ₁ = 0.1859, <i>wR</i> ₂ = 0.3048
Largest diff. peak/hole / e Å ⁻³	3

3.5. References

- [1] M. A. Halcrow, *Coordination Chemistry Reviews* **2009**, 253, 2493.
- [2] N. Shimamoto, S. I. Ohkoshi, O. Sato, K. Hashimoto, *Inorganic Chemistry* **2002**, 41, 678.
- [3] G. Chastanet, C. Desplanches, C. Baldé, P. Rosa, M. Marchivie, P. Guionneau, C. Baldé, *Chemistry Squared - Chem2* **2018**, 2, 1.
- [4] M. A. Halcrow, *Coordination Chemistry Reviews* **2005**, 249, 2880.
- [5] M. G. Cowan, J. Olguín, S. Narayanaswamy, J. L. Tallon, S. Brooker, *Journal of American Chemical Society* **2012**, 134, 2892.
- [6] M. A. Halcrow, *New Journal of Chemistry* **2014**, 38, 1868.
- [7] L. J. Kershaw Cook, R. Mohammed, G. Sherborne, T. D. Roberts, S. Alvarez, M. A. Halcrow, *Coordination Chemistry Reviews* **2015**, 289, 2.
- [8] V. A. Money, J. S. Costa, S. Marcén, G. Chastanet, J. Elhaïk, M. A. Halcrow, J. A. K. Howard, J. F. Létard, *Chemical Physics Letters* **2004**, 391, 273.
- [9] J. F. Létard, P. Guionneau, O. Nguyen, J. S. Costa, S. Marcén, G. Chastanet, M. Marchivie, L. Goux-Capes, *Chemistry - A European Journal* **2005**, 11, 4582.
- [10] J. Olguín, S. Brooker, *Coordination Chemistry Reviews* **2011**, 255, 203.
- [11] C. Klein, E. Baranoff, M. Grätzel, M. K. Nazeeruddin, *Tetrahedron Letters* **2011**, 52, 584.
- [12] R. Pritchard, C. A. Kilner, S. A. Barrett, M. A. Halcrow, *Inorganica Chimica Acta* **2009**, 362, 4365.
- [13] J. Olguín, S. Brooker, *Coordination Chemistry Reviews* **2011**, 255, 203.
- [14] A. Hauser, *Coordination Chemistry reviews* **1991**, 111, 275.
- [15] S. Marcen, L. Lecren, L. Capes, H. A. Goodwin, J.-F. Letard, *Chemical Physics Letters* **2002**, 358, 87.
- [16] A. Aliprandi, D. Genovese, M. Mauro, L. de Cola, *Chemistry Letters* **2015**, 44, 1152.
- [17] L. J. Kershaw Cook, F. L. Thorp-Greenwood, T. P. Comyn, O. Cespedes, G. Chastanet, M. A. Halcrow, *Inorganic Chemistry* **2015**, 54, 6319.
- [18] H. Douib, L. Cornet, J. F. Gonzalez, E. Trzop, V. Dorcet, A. Gouasmia, L. Ouahab, O. Cador, F. Pointillart, *European Journal of Inorganic Chemistry* **2018**, 2018, 4452.

- [19] K. Senthil Kumar, B. Heinrich, S. Vela, E. Moreno-Pineda, C. Bailly, M. Ruben, *Dalton Transactions* **2019**, 48, 3825.
- [20] S. Rat, J. Sánchez Costa, S. Bedoui, W. Nicolazzi, G. Molnár, L. Salmon, A. Bousseksou, in *Pure and Applied Chemistry*, **2015**, pp. 261–270.
- [21] A. Abhervé, M. Clemente-León, E. Coronado, C. J. Gómez-García, M. López-Jordà, *Dalton Transactions* **2014**, 43, 9406.
- [22] N. Suryadevara, A. Mizuno, L. Spieker, S. Salamon, S. Sleziona, A. Maas, E. Pollmann, B. Heinrich, M. Schleberger, H. Wende, S. K. Kuppusamy, M. Ruben, *Chemistry - A European Journal* **2022**, 28.
- [23] N. Ortega-Villar, M. C. Muñoz, J. A. Real, *Magnetochemistry* **2016**, 2.
- [24] M. Shatruk, H. Phan, B. A. Chrisostomo, A. Suleimenova, *Coordination Chemistry Reviews* **2015**, 289–290, 62.
- [25] W. Phonsri, C. G. Davies, G. N. L. Jameson, B. Moubaraki, J. S. Ward, P. E. Kruger, G. Chastanet, K. S. Murray, *Chemical Communications* **2017**, 53, 1374.
- [26] H. Hang, B. Fei, X. Q. Chen, M. L. Tong, V. Ksenofontov, I. A. Gural'Skiy, X. Bao, *Journal of Materials Chemistry C* **2018**, 6, 3352.
- [27] I. Capel Berdiell, R. Kulmaczewski, O. Cespedes, A. Halcrow, C. J. Eur, *Chemistry A European Journal* **2018**, 24, 5055.
- [28] S. Marcén, L. Lecren, L. Capes, H. A. Goodwin, J. F. Létard, *Chemical Physics Letters* **2002**, 358, 87.
- [29] R. Kulmaczewski, E. Trzop, L. J. Kershaw Cook, E. Collet, G. Chastanet, M. A. Halcrow, *Chemical Communications* **2017**, 53, 13268.
- [30] J. S. Costa, C. Balde, C. Carbonera, D. Denux, A. Wattiaux, C. Desplanches, J. P. Ader, P. Gütllich, J. F. Létard, *Inorganic Chemistry* **2007**, 46, 4114.
- [31] A. Hauser, *Chemical Physics Letters* **1992**, 192, 65.
- [32] A. Hauser, J. Jeftic, H. Romstedt, R. Hinek, H. Spiering, *Coordination Chemistry Reviews* **1999**, 190, 471.
- [33] L. J. Kershaw Cook, F. Tuna, M. A. Halcrow, *Dalton Transactions* **2013**, 42, 2254.
- [34] P. Guionneau, *Dalton Transactions* **2014**, 43, 382.

- [35] R. Pritchard, H. Lazar, S. A. Barrett, C. A. Kilner, S. Asthana, C. Carbonera, J. F. Létard, M. A. Halcrow, *Dalton Transactions* **2009**, 6656.
- [36] C. Carbonera, J. Sánchez Costa, V. A. Money, J. Elhaïk, J. A. K. Howard, M. A. Halcrow, J. F. Létard, *Dalton Transactions* **2006**, 25, 3058.
- [37] V. A. Money, C. Carbonera, J. Elhaïk, M. A. Halcrow, J. A. K. Howard, J. F. Létard, *Chemistry - A European Journal* **2007**, 13, 5503.
- [38] K. H. Sugiyartoa, H. A. Goodwinb, *Australian Journal of Chemistry* **1988**, 41, 1645.
- [39] S. A. Barrett, M. A. Halcrow, *RSC Advances* **2014**, 4, 11240.
- [40] A. Santoro, L. J. Kershaw Cook, R. Kulmaczewski, S. A. Barrett, O. Cespedes, M. A. Halcrow, *Inorganic Chemistry* **2015**, 54, 682.
- [41] I. Cebula, H. Lu, M. Zharnikov, M. Buck, *Chemical Science* **2013**, 4, 4455.
- [42] H. Aitchison, R. Ortiz De La Morena, R. Peifer, S. Omar, H. Lu, S. M. Francis, M. Zharnikov, A. Grohmann, M. Buck, *Langmuir* **2018**, 34, 9654.
- [43] J. A. Barth, M. Rudolph, E. Uhlig, *Zeitschrift für anorganische und allgemeine Chemie* **1986**, 632, 65.
- [44] L. Poggini, M. Milek, G. Londi, A. Naim, G. Poneti, L. Squillantini, A. Magnani, F. Totti, P. Rosa, M. M. Khusniyarov, M. Mannini, *Materials Horizons* **2018**, 5, 506.
- [45] E. C. Wasinger, F. M. F. de Groot, B. Hedman, K. O. Hodgson, E. I. Solomon, *Journal of American Chemical Society* **2003**, 125, 12894.
- [46] A. L. Spek, *Journal of Applied Crystallography* **2003**, 36, 7.
- [47] M. Marchivie, P. Guionneau, J.-F. Èois, L. Âtard, D. Chasseau, *Acta Cryst* **2003**, 59, 479.

Chapter 4

4. Heteroleptic Fe(II) SCO complexes based on 1bppCOOH

V. García-López, M. Palacios-Corella, V. Gironés-Pérez, C. Bartual-Murgui, J. A. Real, E. Pellegrin, J. Herrero-Martín, G. Aromí, M. Clemente-León, E. Coronado, "Heteroleptic Iron(II) Spin-Crossover Complexes Based on a 2,6-Bis(pyrazol-1-yl)pyridine-type Ligand Functionalized with a Carboxylic Acid" *Inorganic Chemistry*, vol. 58, no. 18, **2019**, doi: 10.1021/acs.inorgchem.9b01526.

4.1. Motivation

Aromí et al. discovered that the mixture of an Fe(II) salt with two different 3bpp ligands of varying length led to the quantitative crystallization of the heteroleptic complex out of all the possible combinations of two ligands per metal.^[1] Later on, this investigation was expanded to other 3bpp derivatives in combination with the 2,6-bis(pyridin-2-yl)pyridine (tpy) and the 2,6-bis(benzimidazol-2-yl)pyridine (2bbp) ligands,^[2] confirming a marked tendency of the Fe(II) ion to form heteroleptic $[\text{Fe}(\text{L})(\text{L}')](\text{ClO}_4)_2$ complexes from pairs of chelating tris-imine ligands. This quasi-exclusive formation of heteroleptic adducts has been proven as a prolific source of new compounds with very diverse properties,^[3,4] which has been explored in this chapter.

In Chapter 2, we have shown that the solvent-free perchlorate and tetrafluoroborate salts of the homoleptic Fe(II) complex of the ligand 1bppCOOH exhibit a hysteretic (3 K) abrupt thermal spin transition at high temperatures (380 and 340 K, respectively) affected by the presence of a linear network of hydrogen-bonded complexes. Besides, the homoleptic complex formed by the related 1bppCOOEt ligand presents two solvates: $[\text{Fe}(\text{1bppCOOEt})_2](\text{ClO}_4)_2 \cdot 0.75\text{Me}_2\text{CO}$, obtained in this thesis (see Chapter 2), shows an abrupt LS-to-HS solvent-induced SCO around 330 K that becomes irreversible once the complex loses the solvent molecules remaining in the HS state; $[\text{Fe}(\text{1bppCOOEt})_2](\text{ClO}_4)_2 \cdot \text{MeCN}$ exhibits solvent-dependent thermal SCO in the temperature range 180-290 K with a thermal hysteresis ca. 100 K wide, for the first cooling and heating cycle.^[5]

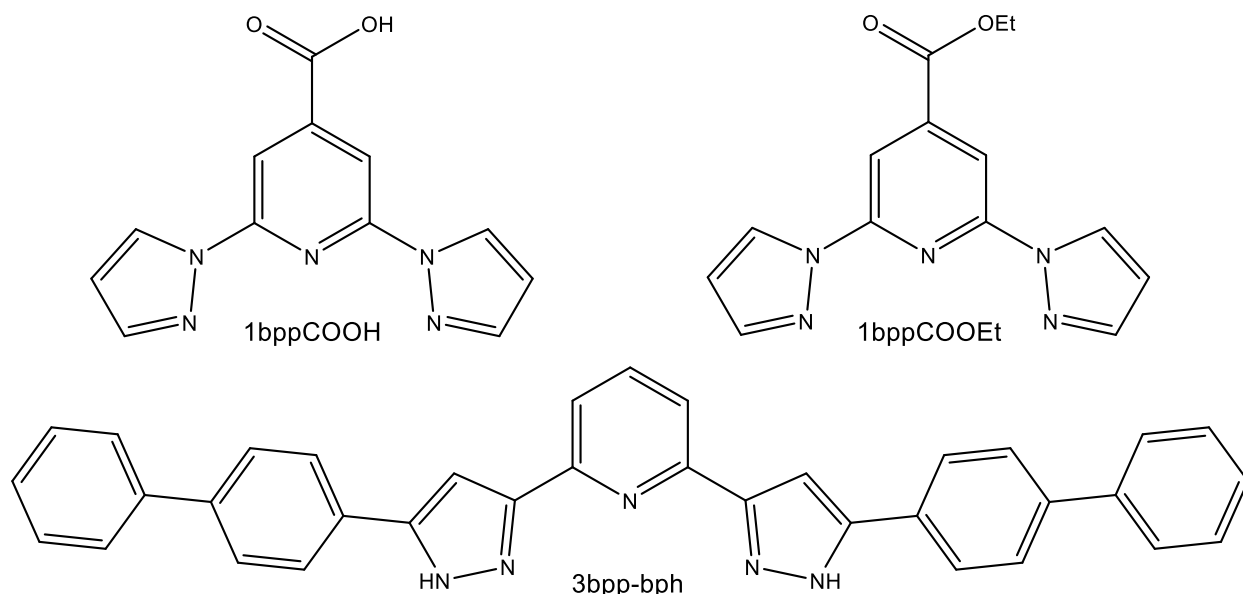
In this work, we intend to take advantage of the properties of the 1bppCOOH ligand while incorporating additional features to its SCO materials by extending its family of Fe(II) SCO complexes to heteroleptic species. We have thus combined it with ligands 3bpp-bph (2,6-bis(5-([1,1'-biphenyl]-4-yl)-1H-pyrazol-3-yl)pyridine) or 1bppCOOEt yielding, respectively, the corresponding heteroleptic complexes $[\text{Fe}(\text{1bppCOOH})(\text{3bpp-bph})](\text{ClO}_4)_2 \cdot \text{solv}$ (**1-solv**, solv = various solvents) and $[\text{Fe}(\text{1bppCOOH})(\text{1bppCOOEt})](\text{ClO}_4)_2 \cdot 0.5\text{Me}_2\text{CO}$ (**2-0.5Me₂CO**). In compound **1-solv**, the 3bpp-bph ligand has been selected with two main goals: i) decreasing the SCO temperature with respect to the homoleptic $[\text{Fe}(\text{1bppCOOH})_2](\text{ClO}_4)_2$ counterpart by exploiting a ligand with a potentially weaker crystal field; ii) increasing the number of $\pi \cdots \pi$ and C-H $\cdots\pi$ interactions through the biphenyl groups in order to improve the connectivity between Fe(II) centers and, therefore, the cooperativity of the system. Concerning compound **2-0.5Me₂CO**, it represents, to the best of our knowledge, the first example of a heteroleptic complex formed by two 1bpp-type ligands. On the other hand, these two complexes are suitable for anchoring on

metal-oxide surfaces thanks to the presence of a grafting ligand (1bppCOOH), while the second ligand, in the case of **1**, could favor $\pi \cdots \pi$ and C–H $\cdots\pi$ interactions among the deposited complexes on the surface. The spin-crossover properties, structural characterization and LIESST effect behaviors of **1·solv**, **2·0.5Me₂CO** and their desolvated counterparts are discussed here together with a preliminary characterization of their deposition.

4.2. Results and discussion

Synthesis

1bppCOOH and 1bppCOOEt ligands were prepared according to literature methods.^[6,7] The synthesis of 3bpp-bph was prepared for the first time by us. The synthesis is performed in two steps (for more information go to SI).



Scheme 4.2.1. Representation of the ligands used in this chapter

The liquid-to-liquid or vapor-to-liquid diffusion of diethyl ether into solutions of $\text{Fe}(\text{ClO}_4)_2 \cdot x\text{H}_2\text{O}$ and equimolar mixtures of 1bppCOOH/3bpp-bph or 1bppCOOH/1bppCOOEt in acetone led to the corresponding heteroleptic compounds $[\text{Fe}(1\text{bppCOOH})(3\text{bpp-bph})](\text{ClO}_4)_2 \cdot 2\text{Me}_2\text{CO} \cdot 0.5\text{Et}_2\text{O}$ (**1·2Me₂CO·0.5Et₂O**) and $[\text{Fe}(1\text{bppCOOH})(3\text{bpp-bph})](\text{ClO}_4)_2 \cdot \text{Me}_2\text{CO}$ (**1·Me₂CO**) or $[\text{Fe}(1\text{bppCOOH})(1\text{bppCOOEt})](\text{ClO}_4)_2 \cdot 0.5\text{Me}_2\text{CO}$ (**2·0.5Me₂CO**), respectively.

*Structure of [Fe(1bppCOOH)(3bpp-bph)](ClO₄)₂·2Me₂CO·0.5Et₂O (**1·2Me₂CO·0.5Et₂O**) and [Fe-(1bppCOOH)(3bpp-bph)](ClO₄)₂·Me₂CO (**1·Me₂CO**)*

1·2Me₂CO·0.5Et₂O and **1·Me₂CO** systematically co-crystallize within the crystallization vial (for more information go to SI). The structures of both compounds were successfully determined by single-crystal X-ray diffraction of a crystal transferred directly to the cold nitrogen stream of the diffractometer from the mother liquor at 120 K (see below). It is important to note that PXRD pattern of a filtered sample composed by a mixture of the two solvatomorphs at room temperature is consistent with the simulated pattern of **1·Me₂CO** (see **Figure SI. 4.4.1**). This observation indicates that partial desolvation of crystals of **1·2Me₂CO·0.5Et₂O** leads to compound **1·Me₂CO** out of the mother liquors. Indeed, the crystal structure of **1·Me₂CO** obtained at 300 K confirms that its acetone molecule is not lost at room temperature. After several minutes at 400 K, compound **1·Me₂CO** undergoes a complete loss of crystallinity due to desorption of the acetone molecules as confirmed by elemental analysis (see SI). Therefore, it was not possible to determine the structure of the SCO-active desolvated phase **1** (see below). PXRD of the SCO phase **1** shows some changes in the position of the peaks with respect to the solvated form (see **Figure SI. 4.4.1**), which suggests important structural modifications upon desolvation.

Both structures belong to the triclinic *P*-1 space group and present, in the asymmetric unit, one crystallographically independent [Fe(1bppCOOH)(3bpp-bph)]²⁺ cation, two ClO₄⁻ anions, and the corresponding solvent molecules (of acetone and diethyl ether), which in some cases are disordered. [Fe(1bppCOOH)(3bpp-bph)]²⁺ complex features an Fe(II) center coordinated to both mutually perpendicular tridentate ligands (**Figure 4.2.1**) with typical Fe–N bond lengths of a HS Fe(II) (2.130(3) - 2.211(4) Å at 120 K for **1·2Me₂CO·0.5Et₂O** and 2.131(3) - 2.201(3) Å at 120 K and 2.129(3) - 2.197(3) Å at 300 K for **1·Me₂CO**). At 120K, the asymmetric unit of **1·2Me₂CO·0.5Et₂O** contains two acetone molecules and one diethyl ether molecule with a 0.5 occupancy. Hydrogen bonds between the two N-H groups of 3bpp-bph are involved in hydrogen bonds with an acetone molecule and a ClO₄⁻ anion, while the -OH group of the ligand 1bppCOOH is hydrogen bonded with the O atom of the diethyl ether molecule (see **Figure 4.2.1, left**). Pairs of [Fe(1bppCOOH)(3bpp-bph)]²⁺ complexes form dimers linked through two symmetrical interactions between the CO group of 1bppCOOH from one complex and one N-H moiety of 3bpp-bph from the other (see **Figure 4.2.2, left**). Neighboring dimers of [Fe(1bppCOOH)(3bpp-bph)]²⁺ present CH...π interactions between the terminal phenyl groups and the central pyridyl rings of 3bpp-bph or the pyrazolyl rings of 1bppCOOH (see **Figure SI. 4.4.2**).

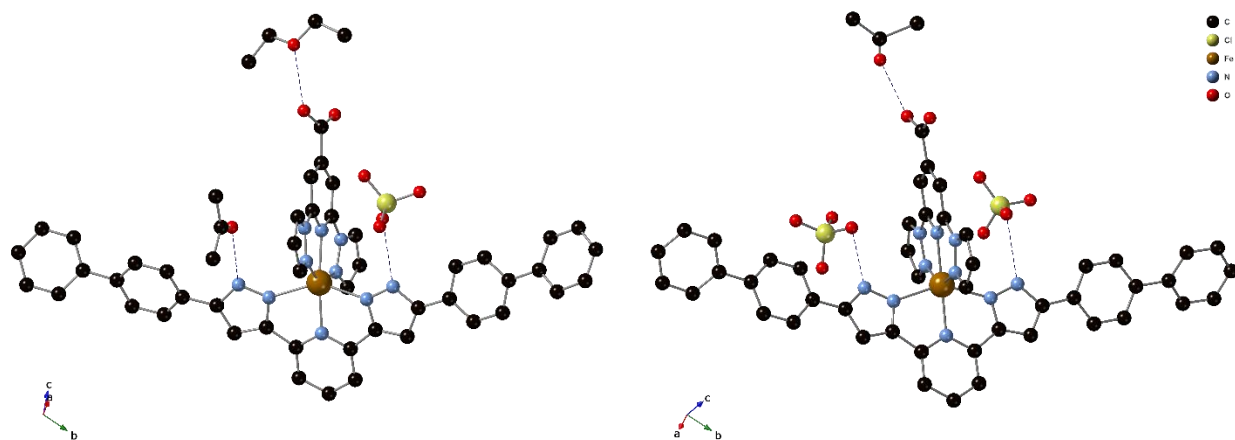


Figure 4.2.1. Representation of the molecular units of **1·2Me₂CO·0.5Et₂O** (left) and **1·Me₂CO** (right) at 120 K. Hydrogen bonds shown with blue dashed lines. Half of the disordered acetone molecules were omitted for clarity.

This leads to chains of dimers running along the *b* axis (see **Figure SI. 4.4.3**). ClO₄⁻ anions and the acetone molecule occupy the holes between [Fe(1bppCOOH)(3bpb-bph)]²⁺ complexes.

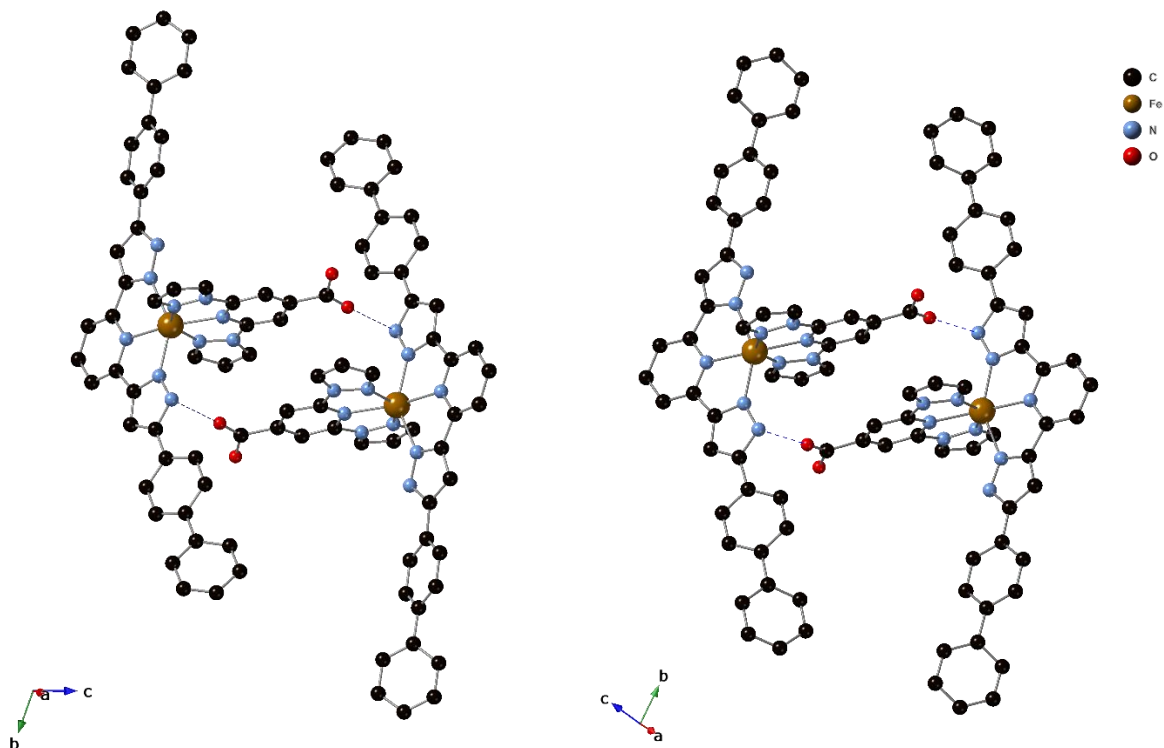


Figure 4.2.2. Dimers of [Fe(1bppCOOH)(3bpb-bph)]²⁺ complexes in the structure of **1·2Me₂CO·0.5Et₂O** (left) and **1·Me₂CO** (right) at 120 K. Hydrogen atoms have been omitted for clarity.

The hydrogen-bond interactions of $[\text{Fe}(\text{1bppCOOH})(\text{3bpp-bph})]^{2+}$ complexes of **1·Me₂CO** change with respect to those of **1·2Me₂CO·0.5Et₂O**. On one hand, in **1·Me₂CO**, hydrogen bonds between the two N-H groups of 3bpp-bph and the two ClO_4^- anions are present. One of the two ClO_4^- anions of **1·Me₂CO** is disordered at 300 K and has been modelled with two configurations of three out of four oxygen atoms with occupancy fractions close to 0.5 per set. On the other hand, the -OH group from 1bppCOOH is involved in a hydrogen bond with a disordered acetone molecule (see **Figure 4.2.1, right**). The disorder has been solved with two possible configurations with close to 0.5 occupancies of the two methyl groups and O atom twisted around the central carbonyl C atom. Pairs of $[\text{Fe}(\text{1bppCOOH})(\text{3bpp-bph})]^{2+}$ complexes form dimers as those of **1·2Me₂CO·0.5Et₂O** (see **Figure 4.2.2, right**), exhibiting a more compact packing due to the loss of solvent molecules, which results in an decrease of the unit cell volume (see **Figure SI. 4.4.4**).

*Structure of $[\text{Fe}(\text{1bppCOOH})(\text{1bppCOOEt})](\text{ClO}_4)_2 \cdot 0.5\text{Me}_2\text{CO}$ (**2·0.5Me₂CO**)*

This compound crystallizes in the orthorhombic *Pbca* space group. Its structure was solved at 120 and 400 K. The asymmetric unit is construct by one $[\text{Fe}(\text{1bppCOOH})(\text{1bppCOOEt})]^{2+}$ cation, three ClO_4^- anions (two of them disordered with a 0.5 occupancy), and one acetone molecule with half occupancy. Elemental analysis of **2·0.5Me₂CO** indicates the persistence of the acetone of crystallization found in the structure and also that half water molecule is likely absorbed in contact to air (see SI). Besides, the PXRD pattern of **2·0.5Me₂CO** at room temperature is in good agreement with the diagram simulated from the single-crystal X-ray diffraction data (see **Figure SI. 4.4.5**).

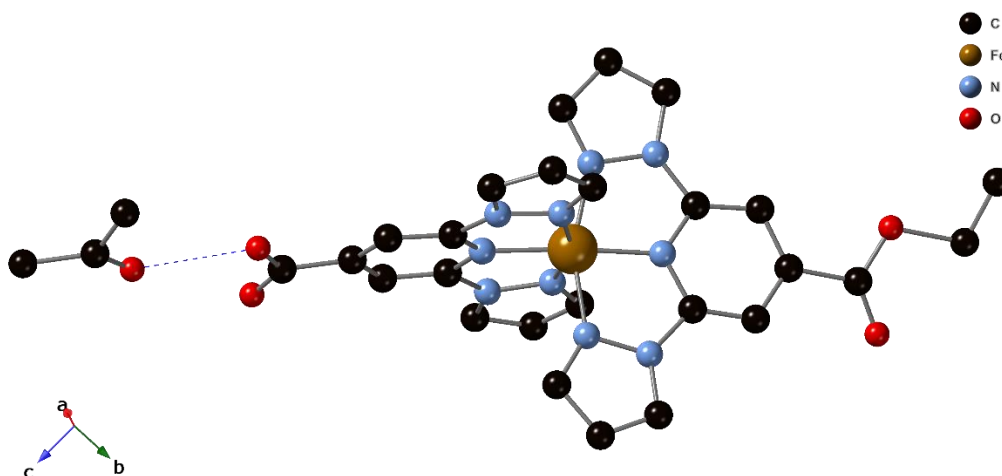


Figure 4.2.3. Representation of $[\text{Fe}(\text{1bppCOOH})(\text{1bppCOOEt})]^{2+}$ and acetone molecule in **2·0.5Me₂CO** at 120 K. Hydrogen bonds are shown with blue dashed lines. Hydrogen atoms and half of the disordered acetone molecules have been omitted for clarity.

The central Fe(II) ion of the complex is coordinated by six nitrogen atoms from the two tridentate 1bppCOOH and 1bppCOOEt ligands, furnishing a distorted octahedral geometry, confirming the formation of the heteroleptic complex (see **Figure 4.2.3**). Fe-N bond lengths at 120 K range 1.893(6) - 1.967(7) Å, which are typical LS Fe-N distances for an octahedral Fe(II) complex. At 400 K, an increase in the Fe-N bond lengths, which lie in the range 1.956(8) - 2.037(9) Å, is observed. These distances are intermediate between the expected LS and HS ones, confirming the partial spin crossover observed in the magnetic measurements (see below). Also, the disorder on the ClO₄⁻ anions, carboxylic acid substituents of 1bppCOOH and ethyl carboxylate groups of 1bppCOOEt increases at this temperature, as expected. Because of this, the use of restraints is needed to model the acetone molecules and perchlorate counteranions, giving rise to a low-quality structure. The acetone molecules interact through hydrogen bonds with the carboxylic acid group of 1bppCOOH (O2...O15 = 2.68 Å at 120 K, see **Figure 4.2.3**) preventing the formation of hydrogen bonds between neighboring complexes, as it has been seen in other compounds from previous chapters. Neighboring [Fe(1bppCOOH)(1bppCOOEt)]²⁺ complexes present CH...π contacts between CH groups and aromatic rings from the pyrazolyl groups of 1bppCOOH ligand. This gives rise to chains of complexes running along the *a* axis (see **Figure SI. 4.4.6**). They are connected through short contacts involving CO groups from 1bppCOOH and 1bppCOOEt and CH groups from pyridine and pyrazolyl groups from both ligands (see **Figure SI. 4.4.7**). These chains are surrounded by ClO₄⁻ anions and acetone molecules.

*Magnetic and photomagnetic properties of [Fe(1bppCOOH)(3bpp-bph)](ClO₄)₂·2Me₂CO·0.5Et₂O (**1·2Me₂CO·0.5Et₂O**) and [Fe-(1bppCOOH)(3bpp-bph)](ClO₄)₂·Me₂CO (**1·Me₂CO**)*

χ_{MT} of a mixture of filtered crystals of **1·2Me₂CO·0.5Et₂O** and **1·Me₂CO** is shown in **Figure 4.2.4**. Although, as mentioned above, PXRD pattern at room temperature indicates that the structure of this sample is that of **1·Me₂CO**. The same behavior is obtained in the first cooling and heating cycle from 300 to 2 K and from 2 to 400 K, respectively. The value is close to 3.4 - 3.6 cm³·K·mol⁻¹ in the 50 - 400 K range, consistent with the HS state of **1·Me₂CO** at 120 and 300 K, also observed in the Fe-N distances from the molecular structure (see above). The sharp decrease below 50 K is due to zero-field splitting as expected for Fe(II) ions in the HS state. Interestingly, after being heated to 400 K, the desolvated phase (**1**) shows a completely different behavior. Thus, when it is cooled from 400 to 250 K, a gradual decrease of χ_{MT} from 3.6 cm³·K·mol⁻¹ at 400 K to 2.75 cm³·K·mol⁻¹ at 250 K is registered. When further cooled, an abrupt decrease of the magnetic signal is observed down to 0.9 cm³·K·mol⁻¹ at 220 K. Below this temperature, χ_{MT} product decreases gradually registering a value of 0.5 cm³·K·mol⁻¹ at 50 K. This

value indicates that $\sim 85\%$ of the Fe(II) centers undergo spin transition. The latter behavior is observed persistently upon repeated cycles in the heating and cooling modes with a small thermal hysteresis of 13 K ($T_{1/2\downarrow} = 234$ K and $T_{1/2\uparrow} = 247$ K). The presence of this thermal hysteresis loop demonstrates the existence of a significant level of cooperativity in the desolvated sample. Although it is difficult to rationalize this behavior without knowing the structure of the desolvated phase, several explanations are possible. On one hand, removal of the acetone solvent molecule could change the hydrogen bonding to the NH groups of 3bpp-bph as observed with the partial desolvation from $1 \cdot 2\text{Me}_2\text{CO} \cdot 0.5\text{Et}_2\text{O}$ to $1 \cdot \text{Me}_2\text{CO}$. This would change the crystal field around Fe(II), considering that the spin state of 3bpp Fe(II) complexes is very sensitive to hydrogen-bonded solvent molecules or counteranions.^[8-11] On the other hand, the larger chemical pressure induced by the decrease in unit cell volume after removal of the solvent molecules could stabilize the LS state.

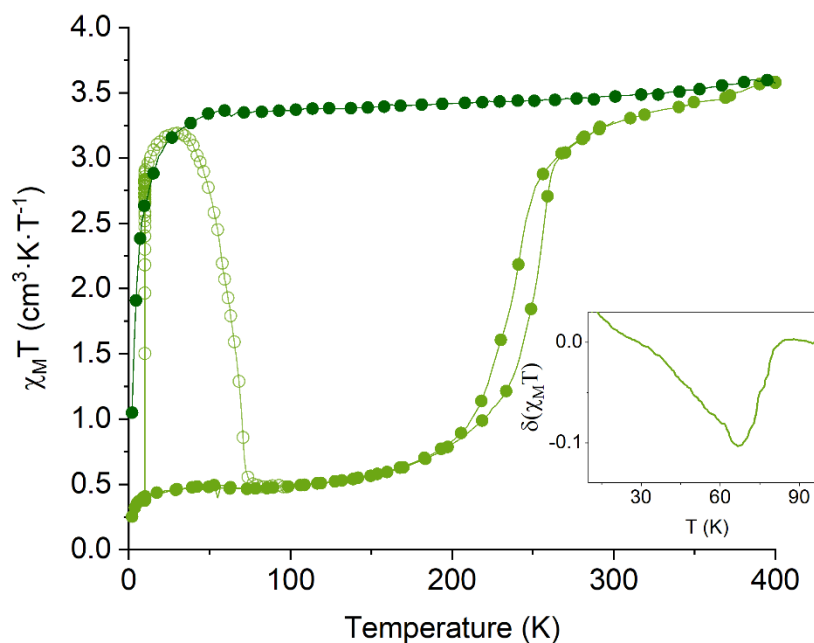


Figure 4.2.4. Temperature dependence of the product of the molar magnetic susceptibility times temperature ($\chi_M T$) for solvated (dark green) and desolvated (green) **1** before (full circles) and after (empty circles) light irradiation.

After previous desolvation at 400 K in the SQUID spin device, **1** was irradiated with a 532 nm laser at 10 K, causing a drastic increase of the magnetic signal. After the irradiation was switched off, the temperature was increased at a scan rate of $0.3 \text{ K} \cdot \text{min}^{-1}$. In the 10 - 31 K

temperature range, an increase of $\chi_M T$ to reach a maximum value of $3.4 \text{ cm}^3 \cdot \text{K} \cdot \text{mol}^{-1}$ at 31 K was observed, reflecting a zero-field splitting of HS Fe(II), suggesting an almost quantitative LS to HS photoconversion. Then, it displays an abrupt relaxation curve with a minimum in the $\partial\chi_M T/\partial T$ (T(LIESST)) at 71 K.

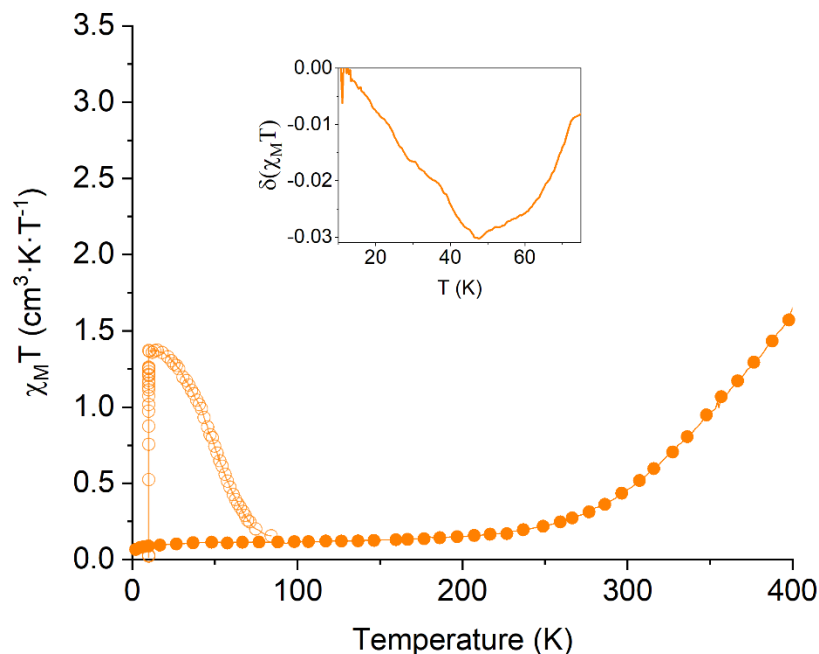


Figure 4.2.5. Temperature dependence $\chi_M T$ for solvated **2·0.5Me₂CO** before (full circles) and after (empty circles) light irradiation.

Temperature dependence of $\chi_M T$ product of **2·0.5Me₂CO** is shown in **Figure 4.2.5**. From 2 to 300 K, $\chi_M T$ values are lower than $0.4 \text{ cm}^3 \cdot \text{K} \cdot \text{mol}^{-1}$, consistent with Fe(II) ions being in the LS state, in agreement with the Fe-N distances found at 120 K (see above). At higher temperatures, a gradual increase of the magnetic signal to reach a $\chi_M T$ value of $1.6 \text{ cm}^3 \cdot \text{K} \cdot \text{mol}^{-1}$ at 400 K is recorded. Therefore, the $T_{1/2}$ of this compound with a well above 300 K and close to 400 K that is not completed at the latter temperature (the highest measured). This behavior is almost reversible in the cooling cycle after heating to 400 K (see **Figure Si. 4.4.8**). Heating at longer times or higher temperatures would be needed to confirm the reversibility. A complete photoconversion of **2·0.5Me₂CO** is not achieved. Thus, a maximum $\chi_M T$ value of $1.4 \text{ cm}^3 \cdot \text{K} \cdot \text{mol}^{-1}$ at 15 K is observed, consistent with a *ca.* 40% photoconversion and a T(LIESST) of 52 K. The gradual relaxation curve could be attributed to the weaker intermolecular interactions of this last compound and/or to the incomplete photoswitching. **2·0.5Me₂CO** presents an important deviation, being T(LIESST) around 40 K higher than expected. It is however consistent with the behavior observed in other compounds with $T_{1/2}$ well above room temperature, which also deviate from this formula.^[12–15]

Deposition of the heteroleptic complexes

For comparison purposes, the procedure for surface deposition was maintained the same than previous chapters 2 and 3. Thermally grown SiO₂ substrates were immersed overnight in a 1 mM MeCN solution of **1** and **2**. They were thoroughly rinsed with MeCN and dried under a N₂ stream. The stability of the solution was studied by means of UV/Vis and the deposited complexes were preliminarily characterized by AFM, MALDI-TOF, XPS and XAS (see SI). XPS spectra of **2** are consistent with the absence of the 1bppCOOEt ligand after deposition as [Fe(1bppCOOH)(solvent)] species are detected. This gives rise to oxidation of the complex and the detection of a clear Fe(III) signal by XAS as observed in homoleptic complexes deposited in chapters 2 and 3. In **1**, MALDI-TOF shows the presence of both ligands but the quality of XPS data does not allow a proper identification of the deposited species. However, XAS experiments at 4 K of **1** suggest a mixture of HS and LS Fe(II) species and Fe(III). The different behavior of **2** compared to **1** could indicate that the deposition of **1** does not lead only to [Fe(1bppCOOH)(solvent)] species as in **2** but to mixtures of species, which could contain the heteroleptic complexes. Further characterization is needed to confirm these results.

4.3. Conclusions

The preparation of two new heteroleptic complexes [Fe(1bppCOOH)(L)](ClO₄)₂ (L = 3bpp-bph (**1**) or 1bppCOOEt (**2**)), in addition to those previously reported, confirms a clear tendency for the formation of the mixed ligand species over the homoleptic ones. This constitutes a rich resource in the search of better performing SCO complexes. The combination in compound **1** of 1bppCOOH and 3bpp-bph ligands has resulted in an improvement of the SCO properties with respect to the homoleptic [Fe(1bppCOOH)₂]²⁺ compound since a hysteretic thermal SCO closer to room temperature has been achieved. Besides, compound **2** represents the first heteroleptic complex based on two 1bpp type ligands. In this case, the combination of 4' substituted 1bpp type ligands stabilizes, as it occurs in the corresponding homoleptic compounds ([Fe(1bppCOOH)₂](ClO₄)₂ and [Fe(1bppCOOEt)₂](ClO₄)₂), the LS state. Moreover, both **1** and **2** complexes exhibit the LIESST effect at 10 K with a 532 nm laser, which further proves that the preparation of heteroleptic complexes is a suitable strategy for obtaining new SCO materials with improved properties.

Finally, an interesting feature of these heteroleptic complexes is the presence of 1bpp ligands functionalized with a carboxylic acid group in the 4-pyridyl position. Although characterization of the SAMs obtained with these heteroleptic molecules suggests an oxidation

to Fe(III) of the deposited complexes as observed with the 1bppCOOH homoleptic complexes, this paves the way for the preparation of new heteroleptic SCO complexes combining different properties in the two ligands by exploiting the chemical versatility of 1bpp, which can be functionalized in this position with a variety of functional substituents without perturbing significantly the SCO properties.

4.4. Supporting information

Synthesis

Synthesis of (2,6-bis(5-([1,1'-biphenyl]-4-yl)-1H-pyrazol-3-yl)pyridine) (3bpp-bph)

Step I: Synthesis of the precursor 2,6-bis(1-([1,1'-biphenyl]-4-yl)-3-oxopropanoyl)-pyridine (**3bpp-bph-prec**). A 60% oil dispersion of NaH (2.09 g, 52.2 mmol) was washed for 20 min under N₂ with hexane. The solvent was extracted using a filter cannula, and tetrahydrofuran (THF, 25 mL) was added. Then, 1-([1,1'-biphenyl]-4-yl)ethan-1-one (1.77 g, 9.03 mmol) and dimethyl-2,6-pyridinedicarboxylate (1.01 g, 4.5 mmol) were dissolved in THF (25 mL) under a nitrogen atmosphere. This mixture was added dropwise with stirring over the NaH suspension. After the addition was completed, the reaction mixture was heated to reflux, turning from yellow to orange after a few hours, and left overnight. The mixture was then left to cool to room temperature, and some drops of EtOH were added to quench any remaining NaH, followed by careful addition of 100 mL of water. HCl 37% (20 mL) was then added changing the pH from 14 to 3 that resulted in the precipitation of a light-yellow solid, which was filtered, washed with diethyl ether, and dried in air. The yield was 1.2 g (44%). ¹H NMR (400 MHz, ppm in CDCl₃): 8.25 (d, 2H), 8.15–8.05 (m, 4H), 8.05–7.95 (m, 1H), 7.76–7.65 (m, 6H), 7.63–7.55 (m, 2H), 7.47–7.32 (m, 6H), 2.30 (s, 2H), 1.8 (s, 2H).

Step II: Preparation of 2,6-bis(5-([1,1'-biphenyl]-4-yl)-1H-pyrazol-3-yl)-pyridine (**3bpp-bph**). Solid **3bpp-bph-prec** (0.45 g, 0.86 mmol) was refluxed overnight with hydrazine monohydrate (0.27 g, 8.6 mmol) in MeOH (40 mL). After it cooled to room temperature, the off-white suspension was filtered and washed with diethyl ether giving place to a white precipitate, which was dried in air. The yield was 0.41 g (92%). ¹H NMR (400 MHz, ppm in deuterated dimethyl sulfoxide (DMSO-*d*₆)): 13.60 (broad s, 2H), 8.20–7.90 (broad m, 5H), 7.90–7.70 (broad m, 9H), 7.65–7.42 (broad m, 6H), 7.45–7.25 (m, 3H).

*Synthesis of [Fe(1bppCOOH)(3bpp-bph)](ClO₄)₂·2Me₂CO·0.5Et₂O (**1·2Me₂CO·0.5Et₂O**), [Fe(1bppCOOH)(3bpp-bph)](ClO₄)₂·Me₂CO (**1·Me₂CO**) and [Fe(1bppCOOH)(1bppCOOEt)](ClO₄)₂·0.5Me₂CO (**2·0.5Me₂CO**)*

A solution of Fe(ClO₄)₂·xH₂O (7.64 mg, 0.03 mmol) in acetone (1.5 mL) was added to a solution of 1bppCOOH (7.68 mg, 0.03 mmol) and 3bpp-bph (15.42 mg, 0.03 mmol) for **1** or 1bppCOOEt (8.52 mg, 0.03 mmol) for **2** in acetone (1.5 mL) obtaining an orange solution that was stirred for 15 min and filtered. This solution was put in contact with diethyl ether vapors or layered with diethyl ether in a test tube yielding a mixture of orange blocks crystals of **1·2Me₂CO·0.5Et₂O**

and orange prisms crystals of **1·Me₂CO** after a few days or orange prisms of **2·0.5Me₂CO** after one week. Anal. Calcd for Fe(C₁₂H₉O₄N₅)(C₃₅N₅H₂₅)(ClO₄)₂ (**1**): C 53.38, N 13.24, H 3.24% Found: C 53.36, N 13.84, H 3.36 % Anal. Calcd for Fe(N₅C₁₂H₉O₂)(N₅C₁₄H₁₃O₂)(ClO₄)₂(CH₃COCH₃)_{0.5}(H₂O)_{0.5} (**2·0.5Me₂CO·0.5H₂O**): C, 39.73; H, 3.15; N, 16.85%. Found: C, 39.96; H, 3.37; N, 16.17%.

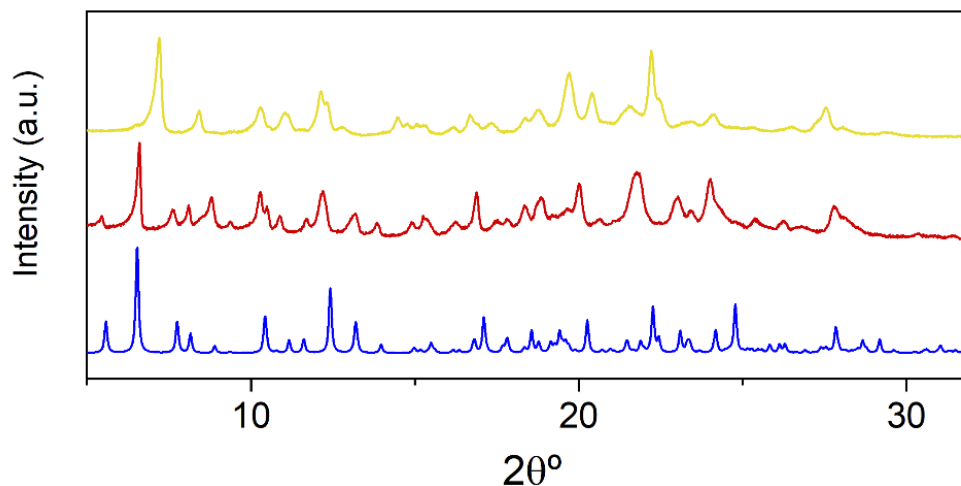


Figure SI. 4.4.1. Simulated PXRD pattern from single crystal measured at 120 K (blue), a mixture of **1·2Me₂CO·0.5Et₂O** and **1·Me₂CO** after filtering (red) and after desolvation at 400 K in the squid (yellow).

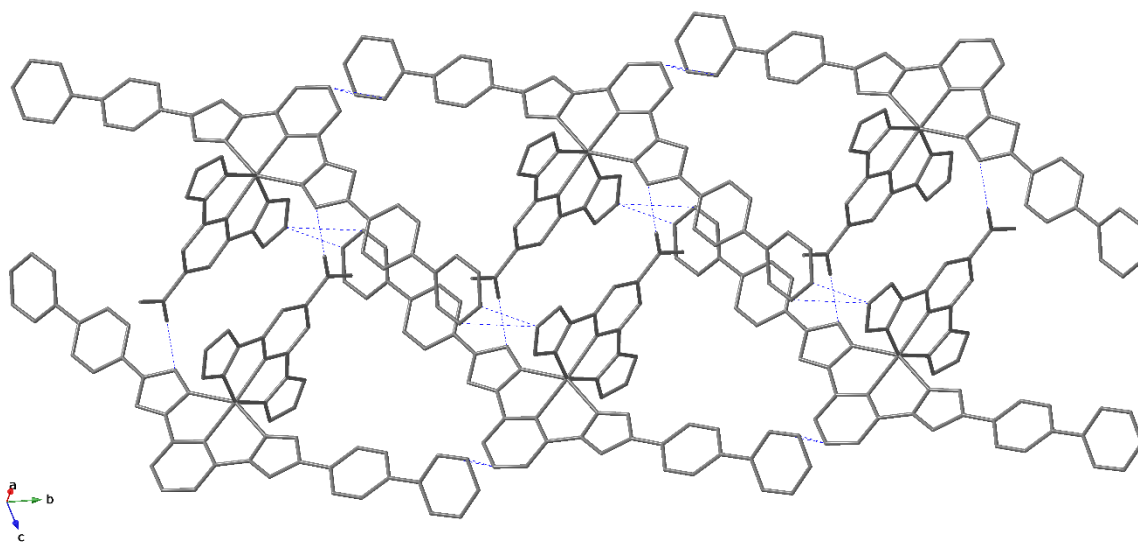


Figure SI. 4.4.2. Intermolecular contacts between [Fe(1bppCOOH)(3bpp-bph)]²⁺ complexes shown with blue dashed lines.

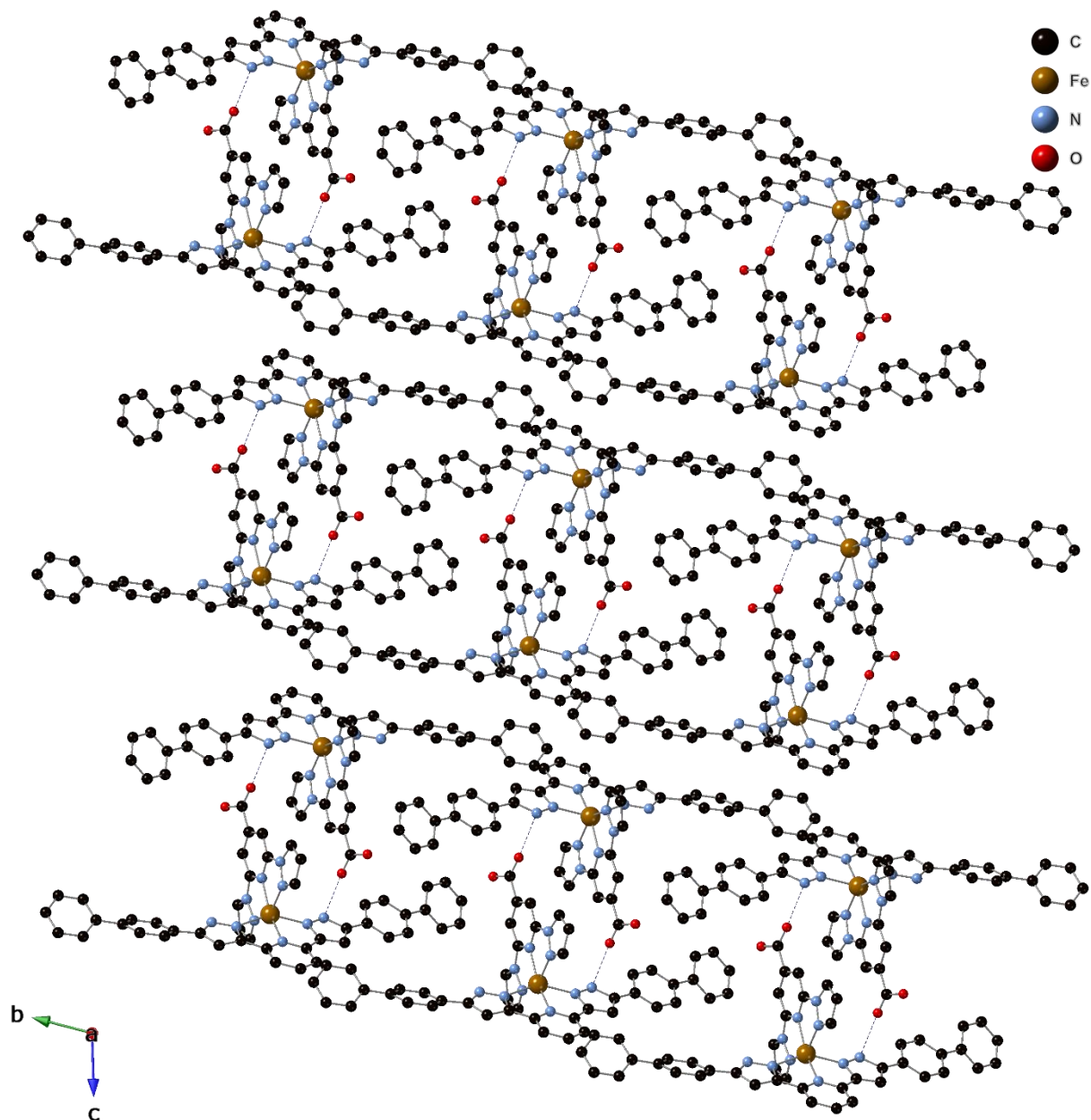


Figure SI. 4.4.3. Chains of $[\text{Fe}(\text{1bppCOOH})(\text{3bpp-bph})]^{2+}$ dimers running along the b axis in the structure of $\text{1}\cdot\text{2Me}_2\text{CO}\cdot\text{0.5Et}_2\text{O}$ at 120 K. Hydrogen atoms have been omitted for clarity.

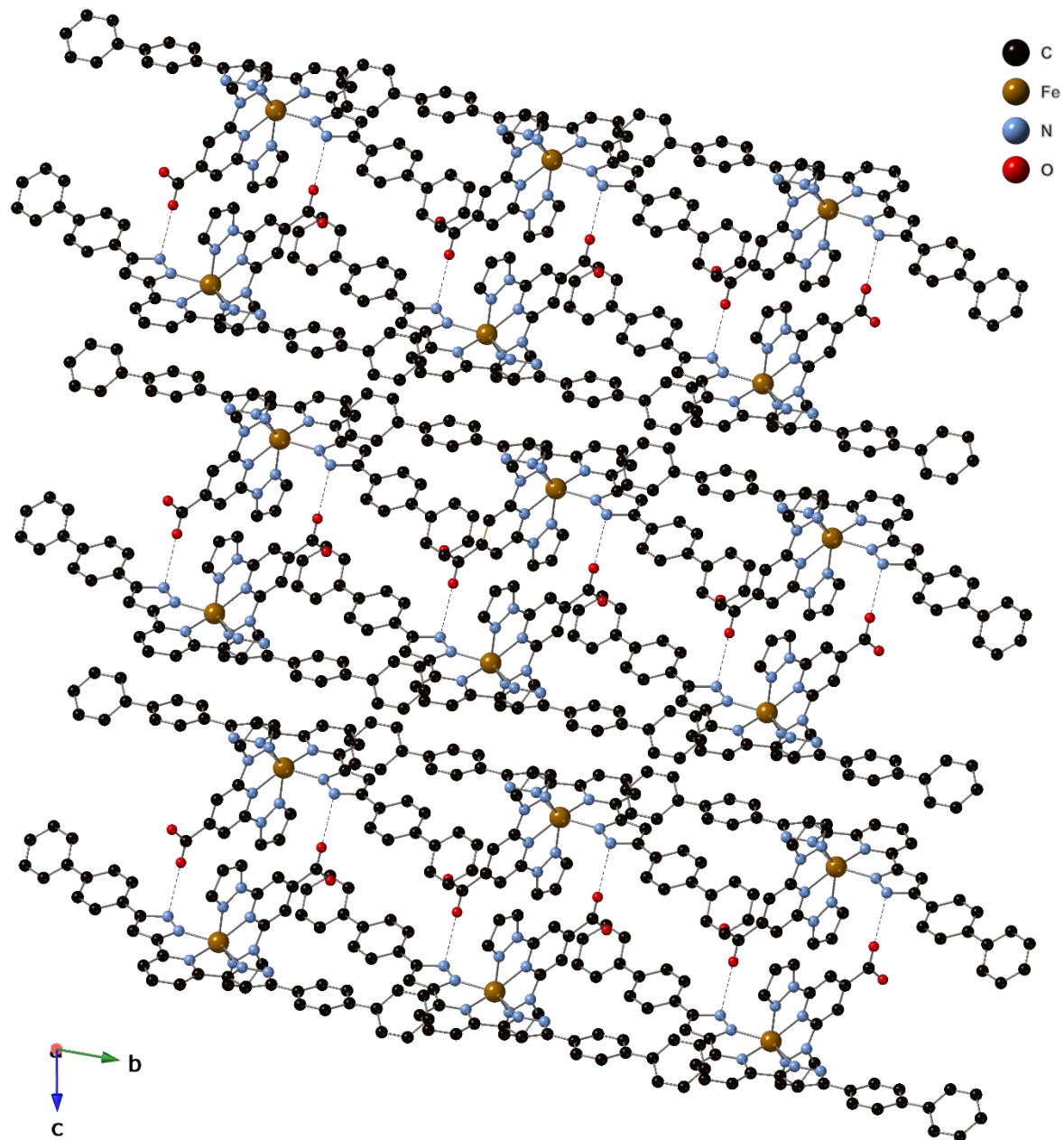


Figure SI. 4.4.4. Chains of $[\text{Fe}(\text{1bppCOOH})(\text{3bpp-bph})]^{2+}$ dimers running along the *b* axis in the structure of $\mathbf{1} \cdot \text{Me}_2\text{CO}$ at 120 K displaying a more compact crystal packing. Hydrogen atoms have been omitted for clarity.

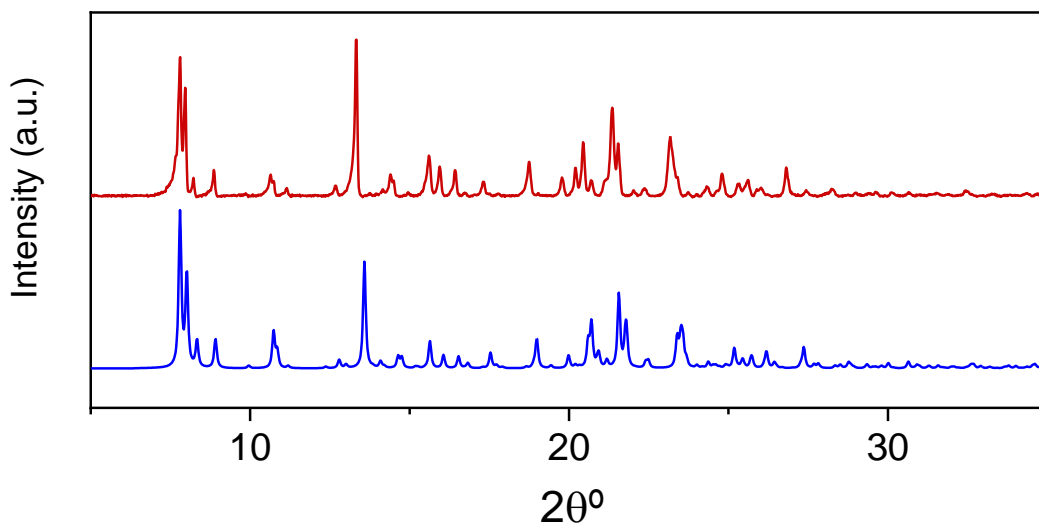


Figure SI. 4.4.5. Simulated PXRD pattern at 120 K (blue) and experimental at room temperature (red) of **2·0.5Me₂CO**.

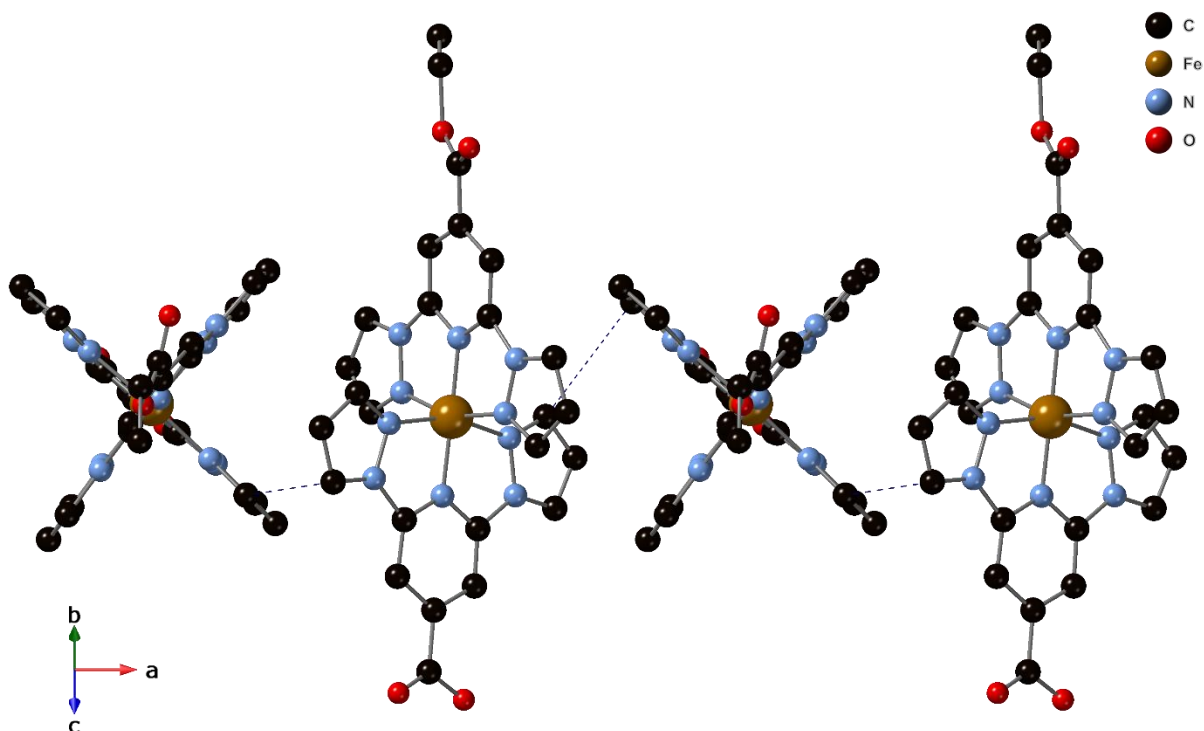


Figure SI. 4.4.6. View of chains of [Fe(1bppCOOH)(1bppCOOEt)]²⁺ complexes running in the *a* axis in the structure of **2·0.5Me₂CO** at 120 K. Intermolecular contacts shown with blue dashed lines. Hydrogen atoms, perchlorate counteranions and disordered acetone molecules have been omitted for clarity.

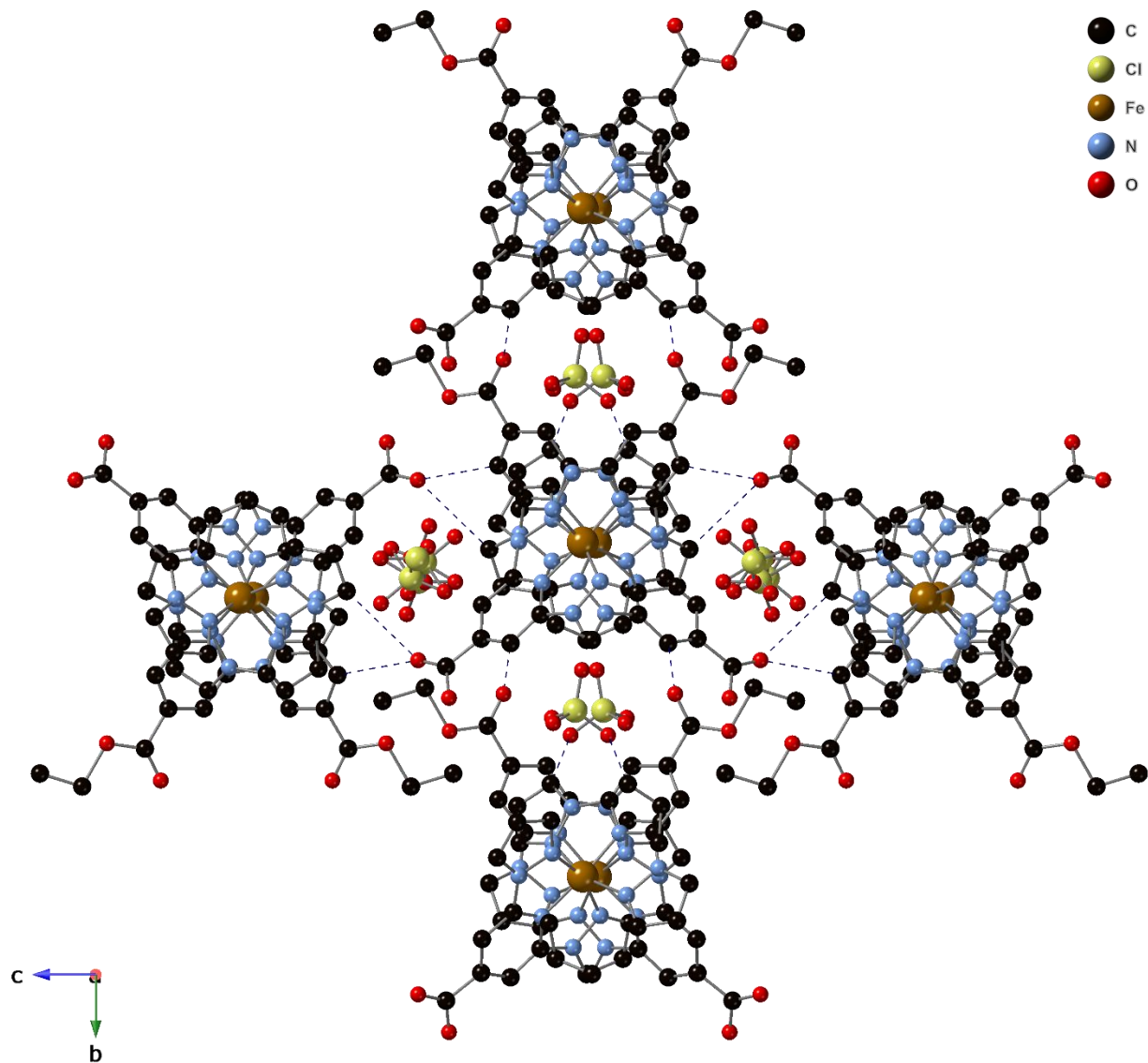


Figure SI. 4.4.7. View of chains of $[\text{Fe}(\text{1bppCOOH})(\text{1bppCOOEt})]^{2+}$ complexes in the bc plane of the structure of $2 \cdot 0.5\text{Me}_2\text{CO}$ at 120 K. Intermolecular contacts shown with blue dashed lines. Hydrogen atoms and disordered acetone molecules have been omitted for clarity.

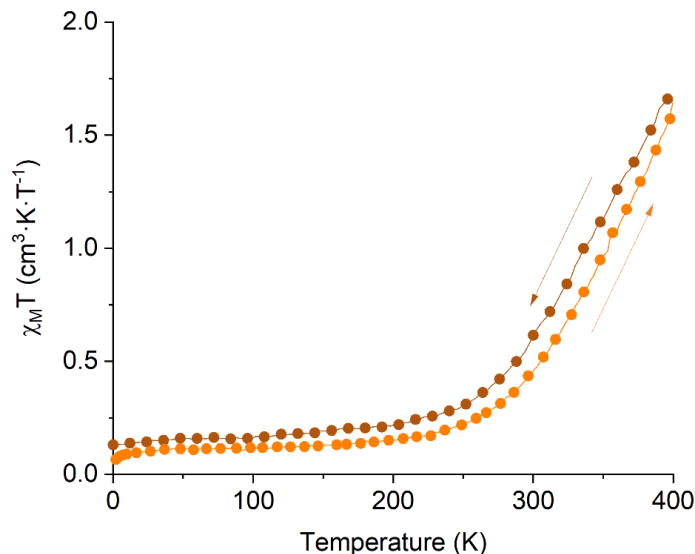


Figure SI. 4.4.8. Thermal variation of $\chi_{\text{M}}T$ for **2**·0.5Me₂CO. Orange circles: first heating cycle; brown circles: first cooling after heating to 400 K.

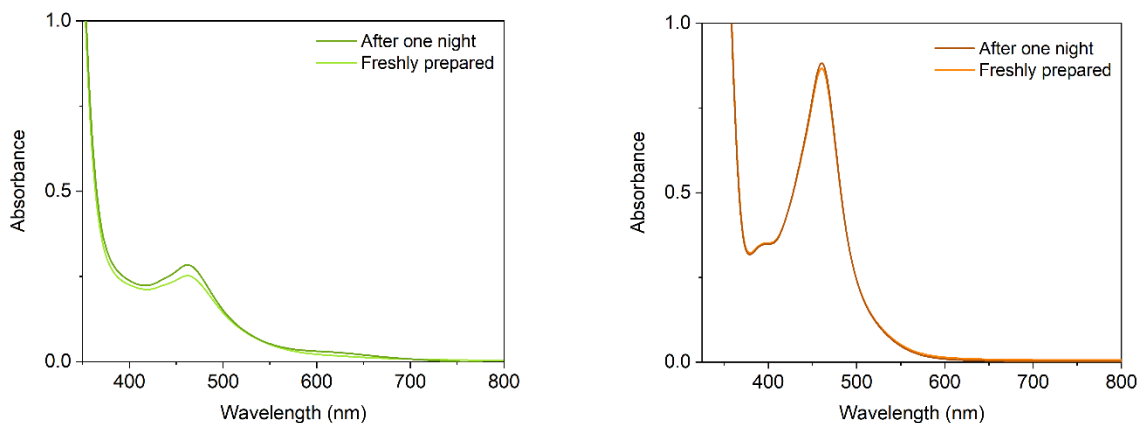


Figure SI. 4.4.9. UV/Vis spectra of a 0.1 mM solution of, left, **1** and, right, **2** in MeCN freshly prepared and after one day in inert atmosphere.

UV/Vis spectroscopy of **1** and **2** display the classical MLCT $t_2-\pi^*$ transition band also seen in their previous derivatives (see chapters 2 and 3). **1** displays a band centered at 464 nm ($\epsilon = 2.5 \times 10^3 \text{ L}^{-1}\text{mol}^{-1}\text{cm}^{-1}$), indicating that around 50% of Fe(II) centers are in the HS, as it has been seen in the homoleptic 1bppCOOH analogous, while **2** present a strong band at 461 nm ($\epsilon = 8.6 \times 10^3 \text{ L}^{-1}\text{mol}^{-1}\text{cm}^{-1}$) for **2**, which means that the LS species are predominant.^[16] The UV/Vis spectrum after one night of both complexes does not present any changes, confirming the stability of the solutions (**Figure SI. 4.4.9**). The slight increase in intensity is due to normal evaporation of the solvent.

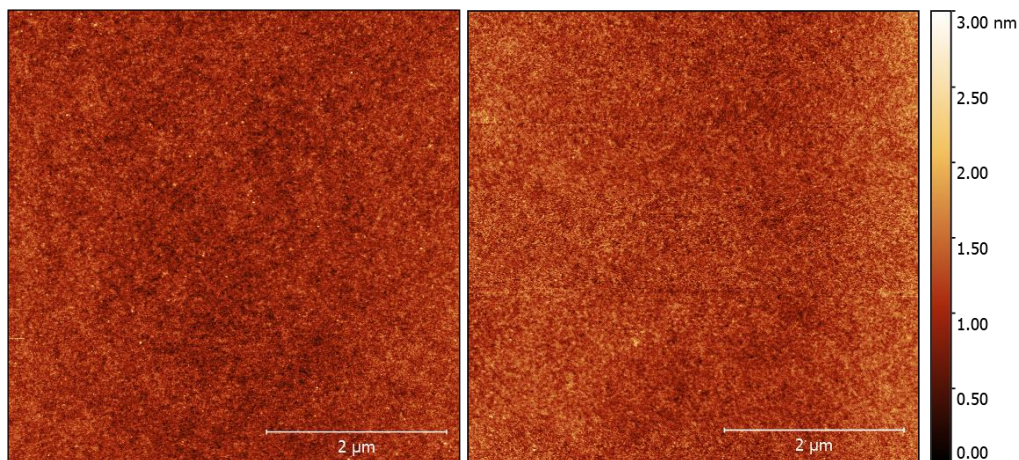


Figure SI. 4.4.10. AFM images of SiO₂ substrates after deposition of **1** (left) and **2** (right).

AFM images confirm the absence of aggregates or multilayers (see **Figure SI. 4.4.10**) as expected. The average of the R_{RMS} of the deposit obtained from 15 measurements in different points of the surface, show a small increase from 0.203 ± 0.010 nm to 0.202 ± 0.004 nm for **1** and to 0.203 ± 0.008 nm for **2** with respect to the naked substrate. Both are consistent with the formation of a continuous monolayer of complexes.

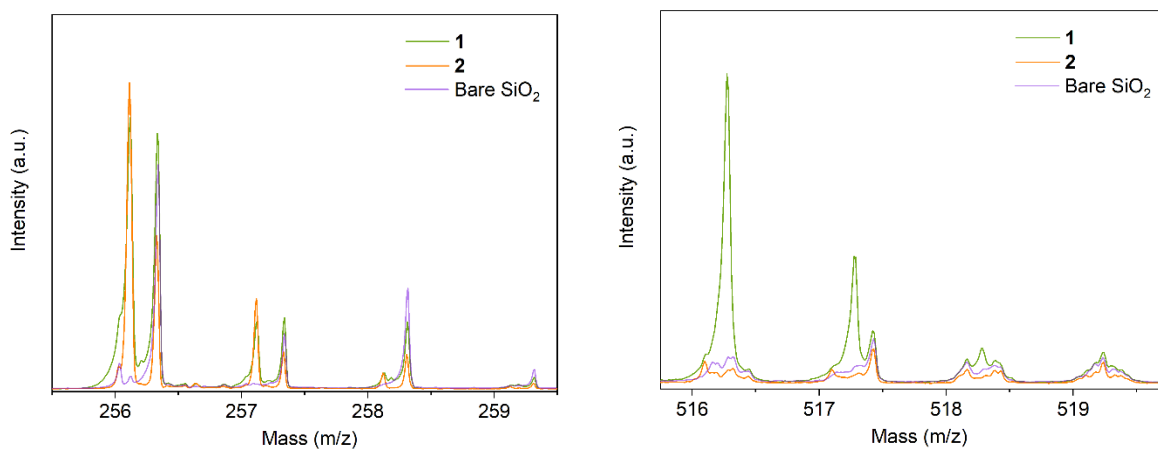


Figure SI. 4.4.11. MALDI-TOF region of 1bppCOOH (**left**) and 3bpp-bph (**right**) of **1** (green), **2-SAM** (orange) and bare SiO₂ (light purple).

Fragments of the complex were detected with MALDI-ToF measurements. Peaks corresponding to the protonated ligands $[1\text{bppCOOH}+\text{H}]^+$ (Calc. 256.08 Da, Found 256.11 Da) and $[3\text{bpp-bph}+\text{H}]^+$ (Calc. 516.22 Da, Found 516.27 Da) were obtained (**Figure SI. 4.4.11**). In the case of the 1bppCOOEt, it could not be clearly identified without ambiguity since it presents peaks at the same position as those of the matrix used to ionize the deposited complexes.

In order to investigate structural and electronic properties of the SAM, XPS has been performed. C1s, N1s, Cl2p and Fe2p XPS regions were studied to analyze the atomic compositions of the deposit (**Figure SI. 4.4.12**). C1s region features three main components at 285.0 (285.0), 286.7 (286.4) and 288.9 (288.6) eV assigned to the aliphatic carbon atoms (orange), heterobonds (green) and carbon atoms of the carboxylate group (blue), respectively.^[17,18] N1s region features two components at 401.4 (401.5) and 399.9 (399.8) eV assigned to nitrogen atoms of the pyridine and pyrazolyl groups coordinated and non-coordinated to the iron atom (brown)^[19]. Fe2p_{3/2} regions have been reproduced with 5 components (A–E) along with the corresponding Fe2p_{1/2} spin-orbit coupled contributions (A'–E') weighted with the expected 2:1 ratio as well.^[20] In the Fe2p region, the signal to noise ratio of **1** is too low to get some information, while **2** shows a very similar spectra to those of the homoleptic 1bpp derivatives seen in this work, which corresponds to an Fe(III) oxidation state (see chapters 2 and 3). Again, the low signal to noise ratio coming from compound **1** makes it harder to conclude anything from the semiquantitative analysis and elemental stoichiometric ratios. In **2**, we observe the formation of [Fe(1bppCOOH)] species as observed previously with [Fe(1bppCOOH)] and [Fe(1bpp3COOH)] in chapters 2 and 3, respectively (see **Table S.I. 4.4.1**).

Table S.I. 4.4.1. Theoretical and XPS estimated atomic semiquantitative analysis (top) and ratios (bot) for **1-SAM** and **2-SAM**.

	Semiquantitative analysis							
	Fe	N	C	N _{coordinated}	N _{uncoordinated}	C-C	C-N	COO-
Theor. for 1	1.7%	17.2%	81.0%	60.0%	40.0%	67.7%	29.0%	3.2%
1-SAM@SiO₂	1.4%	3.3%	95.3%	68.9%	31.1%	63.3%	32.4%	4.3%
Theor. for 2	2.7%	27.0%	70.3%	60.0%	40.0%	45.5%	45.5%	9.1%
2-SAM@SiO₂	4.2%	19.4%	76.3%	58.3%	41.7%	57.2%	36.5%	6.3%

	Iron ratios			Nitrogen ratios		Carbon ratios		
	Fe/Fe	Fe/N	Fe/C	C-N _{coord} /C-N _{coord}	C-N _{coord} /C-N _{uncoord}	C-C/C-N	C-N/C-N	O-C=O/C-N
Theor. for 1	1.00	0.10	0.021	1.00	0.67	2.33	1.00	0.11
1-SAM@SiO₂	1.00	0.41	0.014	1.00	0.45	1.95	1.00	0.13
Theor. for 2	1.00	0.10	0.038	1.00	0.67	1.00	1.00	0.20
2-SAM@SiO₂	1.00	0.22	0.055	1.00	0.72	1.57	1.00	0.17

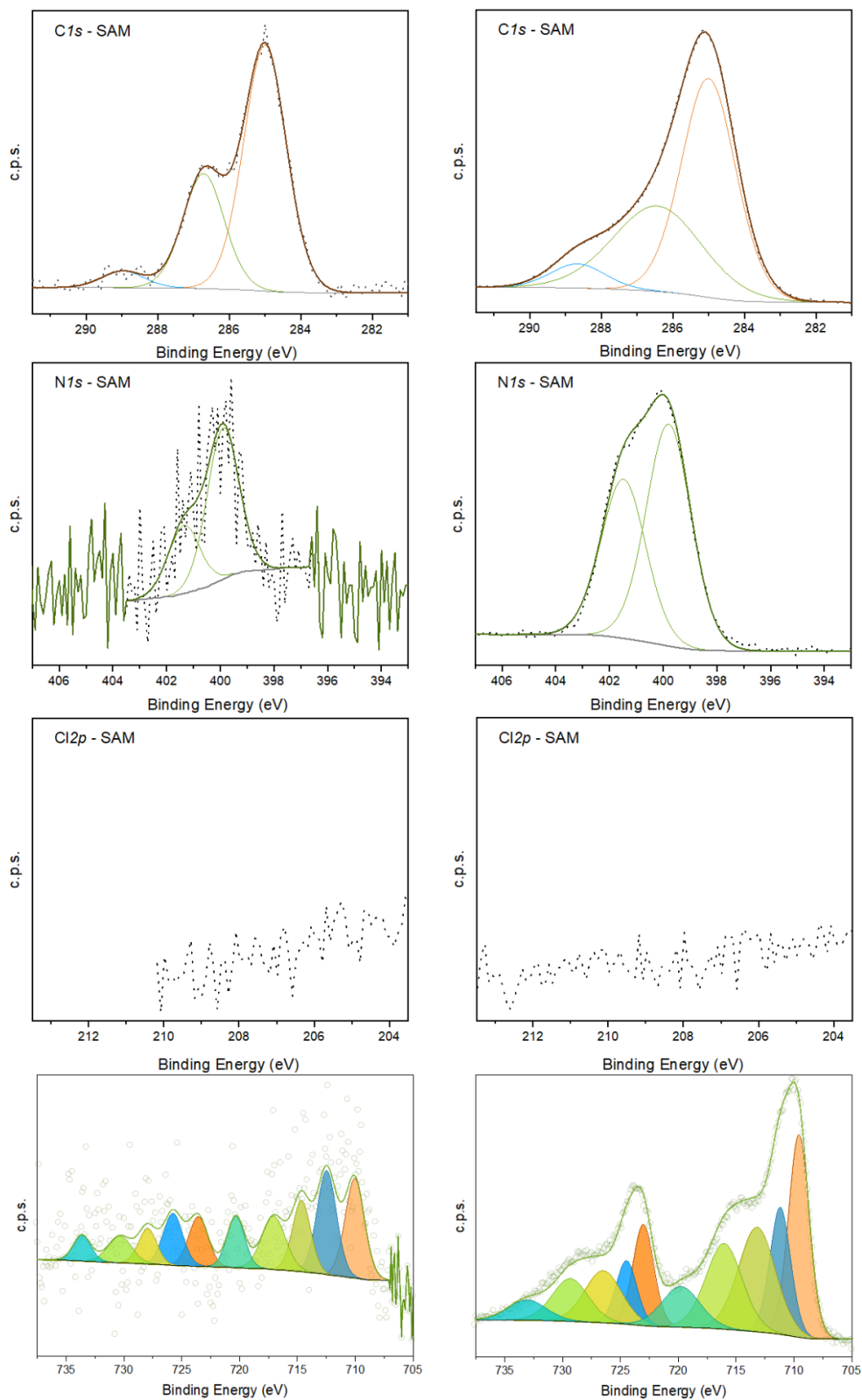


Figure SI. 4.4.12. XPS C1s, N1s, Cl2p and Fe2p regions of **1-SAM** (left) and **2-SAM** (right).

The spin state of our deposits was further investigated with XAS. **Figure SI. 4.4.13** shows the XAS Fe $L_{2,3}$ -edge spectra of **1** and **2** on top of SiO_2 . Compound **1** presents a mixture of spin states, which is consistent with a mixture of LS and HS Fe(II) species and HS Fe(III). As the temperature increases, the photoreduction effect becomes more important. On the other hand, **2** displays the characteristic Fe(III) HS state^[21] at all temperatures as expected from XPS and previous results for a $[\text{Fe}(\text{1bppCOOH})]$ specie on the surface (see chapters 2 and 3).

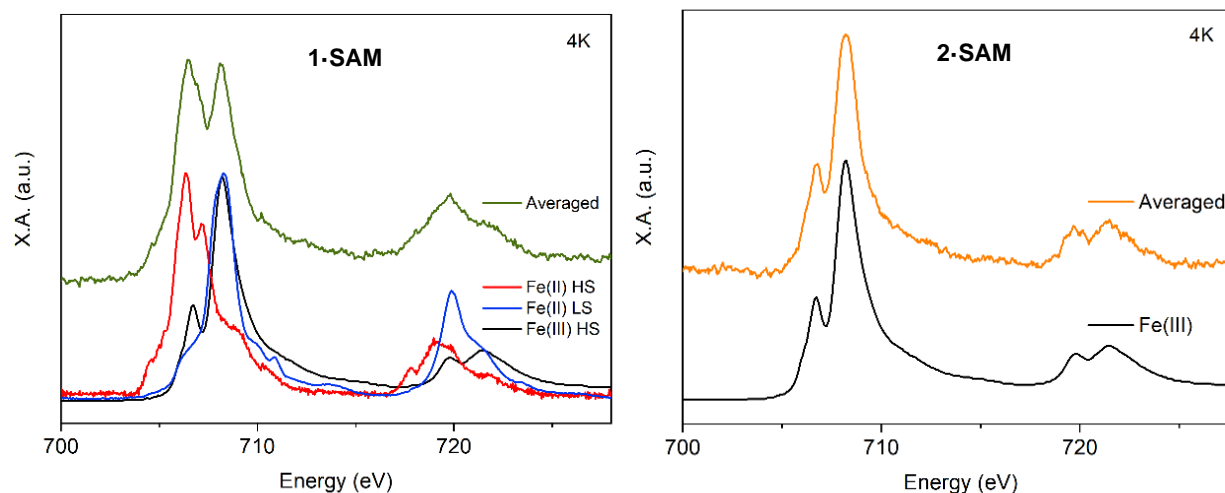


Figure SI. 4.4.13. Left, XAS Fe $L_{2,3}$ -edge spectra of **1-SAM** (green), $\text{Fe(III)}^{[21]}$ (black) and Fe(II) HS (red) and Fe(II) LS (blue) obtained from the bulk of $[\text{Fe}(\text{1bppCOOH})_2](\text{BF}_4)_2$ from Chapter 2 used as a reference. Right, XAS Fe $L_{2,3}$ -edge spectra of **2-SAM** and an $\text{Fe(III)} L_{2,3}$ -edge extracted from the literature.^[21]

Table S.I. 4.4.2. Crystallographic tables.

Identification code	1·2Me₂CO·0.5Et₂O	1·Me₂CO	1·Me₂CO	2·0.5Me₂CO	2·0.5Me₂CO
Empirical formula	C ₁₁₀ H ₁₀₂ Cl ₄ Fe ₂ N ₂₀ O ₂₅	C ₅₀ H ₄₀ Cl ₂ FeN ₁₀ O ₁₁	C ₅₀ H ₄₀ Cl ₂ FeN ₁₀ O ₁₁	C ₅₅ H ₅₀ Cl ₄ Fe ₂ N ₂₀ O ₂₅	C ₅₅ H ₅₀ Cl ₄ Fe ₂ N ₂₀ O ₂₅
Formula weight	2357.61	1083.67	1083.67	1644.65	1644.65
Temperature/K	120.00(10)	120.00(10)	300.00(10)	120(2)	399.95(10)
Crystal system	triclinic	triclinic	triclinic	orthorhombic	orthorhombic
Space group	P-1	P-1	P-1	Pbca	Pbca
a/Å	10.9594(3)	11.0678(5)	11.2137(6)	14.2991(17)	14.7845(7)
b/Å	15.2064(5)	13.7755(6)	13.7063(6)	22.0531(11)	22.2028(11)
c/Å	18.1301(8)	16.4761(9)	16.6716(10)	22.6493(11)	22.5899(13)
α°	104.480(3)	79.015(4)	79.292(4)	90	90
β°	94.555(3)	78.125(4)	79.181(5)	90	90
γ°	103.052(3)	88.209(4)	86.777(4)	90	90
Volume/Å ³	2820.15(18)	2413.1(2)	2472.4(2)	7142.2(10)	7415.3(7)
Z	1	2	2	4	4
ρ _{calc} /cm ³	1.388	1.491	1.456	1.529	1.473
μ/mm ⁻¹	0.433	0.497	0.485	0.647	0.624
F(000)	1222.0	1116.0	1116.0	3360.0	3360.0
Crystal size/mm ³	0.28 × 0.21 × 0.16	0.67 × 0.08 × 0.04	0.55 × 0.25 × 0.12	0.540 × 0.070 × 0.020	0.7 × 0.15 × 0.07
Radiation	MoKα (λ = 0.71073)	MoKα (λ = 0.71073)	MoKα (λ = 0.71073)	MoKα (λ = 0.71073)	MoKα (λ = 0.71073)
2θ range for data collection/°	6.758 to 55.038	6.89 to 56.17	6.786 to 55.988	6.54 to 55.016	6.622 to 49.468
Index ranges	-14 ≤ h ≤ 14, -19 ≤ k ≤ 19, -23 ≤ l ≤ 23	-13 ≤ h ≤ 13, -18 ≤ k ≤ 17, -21 ≤ l ≤ 21	-13 ≤ h ≤ 14, -17 ≤ k ≤ 17, -21 ≤ l ≤ 21	-18 ≤ h ≤ 12, -27 ≤ k ≤ 28, -29 ≤ l ≤ 27	-17 ≤ h ≤ 17, -26 ≤ k ≤ 24, -25 ≤ l ≤ 26
Reflections collected	38786	32418	35597	25324	23547
Independent reflections	11731 [R _{int} = 0.0609, R _{sigma} = 0.0837]	10175 [R _{int} = 0.0639, R _{sigma} = 0.0858]	10402 [R _{int} = 0.0370, R _{sigma} = 0.0449]	8178 [R _{int} = 0.1448, R _{sigma} = 0.2037]	6306 [R _{int} = 0.1065, R _{sigma} = 0.1486]
Data/restraints/parameters	11731/0/730	10175/5/669	10402/3/658	8178/1/508	6306/131/509
Goodness-of-fit on F ²	1.044	1.031	1.046	1.025	1.000
Final R indexes [I > 2σ(I)]	R ₁ = 0.0679, wR ₂ = 0.1756	R ₁ = 0.0556, wR ₂ = 0.1147	R ₁ = 0.0672, wR ₂ = 0.1827	R ₁ = 0.1199, wR ₂ = 0.2828	R ₁ = 0.1098, wR ₂ = 0.2895
Final R indexes [all data]	R ₁ = 0.1219, wR ₂ = 0.2186	R ₁ = 0.1013, wR ₂ = 0.1414	R ₁ = 0.1035, wR ₂ = 0.2145	R ₁ = 0.2392, wR ₂ = 0.3590	R ₁ = 0.2735, wR ₂ = 0.3981
Largest diff. peak/hole / e Å ⁻³	1.36/-0.41	1.04/-0.58	1.22/-0.59	1.21/-0.67	0.37/-0.27

4.5. References

- [1] J. S. Costa, S. Rodríguez-Jiménez, G. A. Craig, B. Barth, C. M. Beavers, S. J. Teat, G. Aromí, *Journal of American Chemical Society* **2014**, *136*, 3869.
- [2] L. A. Barrios, C. Bartual-Murgui, E. Peyrecave-Lleixà, B. le Guennic, S. J. Teat, O. Roubeau, G. Aromí, *Inorganic Chemistry* **2016**, *55*, 4110.
- [3] C. Bartual-Murgui, R. Diego, S. Vela, S. J. Teat, O. Roubeau, G. Aromí, *Inorganic Chemistry* **2018**, *57*, 11019.
- [4] G. Aromí, C. M. Beavers, J. Sánchez Costa, G. A. Craig, G. Mínguez Espallargas, A. Orera, O. Roubeau, *Chemical Science* **2016**, *7*, 2907.
- [5] K. Senthil Kumar, B. Heinrich, S. Vela, E. Moreno-Pineda, C. Bailly, M. Ruben, *Dalton Transactions* **2019**, *48*, 3825.
- [6] C. Klein, E. Baranoff, M. Grätzel, M. K. Nazeeruddin, *Tetrahedron Letters* **2011**, *52*, 584.
- [7] T. Vermonden, D. Branowska, A. T. M. Marcelis, E. J. R. Sudhölter, *Tetrahedron* **2003**, *59*, 5039.
- [8] M. del C. Giménez-López, M. Clemente-León, C. Giménez-Saiz, *Dalton Transactions* **2018**, *47*, 10453.
- [9] T. D. Roberts, F. Tuna, T. L. Malkin, C. A. Kilner, M. A. Halcrow, *Chemical Science* **2012**, *3*, 349.
- [10] G. A. Craig, O. Roubeau, G. Aromí, *Coordination Chemistry Reviews* **2014**, *269*, 13.
- [11] S. Marcén, L. Lecren, L. Capes, H. A. Goodwin, J.-F. Létard, *Chemical Physics Letters* **2002**, *358*, 87.
- [12] R. Pritchard, H. Lazar, S. A. Barrett, C. A. Kilner, S. Asthana, C. Carbonera, J. F. Létard, M. A. Halcrow, *Dalton Transactions* **2009**, *33*, 6656.
- [13] C. Sánchez-Sánchez, C. Desplanches, J. M. Clemente-Juan, M. Clemente-León, E. Coronado, *Dalton Transactions* **2017**, *46*, 2680.
- [14] N. Bridonneau, L. Rigamonti, G. Poneti, D. Pinkowicz, A. Forni, A. Cornia, *Dalton Transactions* **2017**, *46*, 4075.
- [15] V. García-López, M. Palacios-Corella, A. Abhervé, I. Pellicer-Carrenõ, C. Desplanches, M. Clemente-León, E. Coronado, *Dalton Transactions* **2018**, *47*, 16958.

- [16] A. Santoro, L. J. Kershaw Cook, R. Kulmaczewski, S. A. Barrett, O. Cespedes, M. A. Halcrow, *Inorganic Chemistry* **2015**, *54*, 682.
- [17] I. Cebula, H. Lu, M. Zharnikov, M. Buck, *Chemical Science* **2013**, *4*, 4455.
- [18] H. Aitchison, R. Ortiz De La Morena, R. Peifer, S. Omar, H. Lu, S. M. Francis, M. Zharnikov, A. Grohmann, M. Buck, *Langmuir* **2018**, *34*, 9654.
- [19] J. A. Barth, M. Rudolph, E. Uhlig, *Zeitschrift für anorganische und allgemeine Chemie* **1986**, *632*, 65.
- [20] L. Poggini, M. Milek, G. Londi, A. Naim, G. Poneti, L. Squillantini, A. Magnani, F. Totti, P. Rosa, M. M. Khusniyarov, M. Mannini, *Materials Horizons* **2018**, *5*, 506.
- [21] E. C. Wasinger, F. M. F. de Groot, B. Hedman, K. O. Hodgson, E. I. Solomon, *Journal of American Chemical Society* **2003**, *125*, 12894.

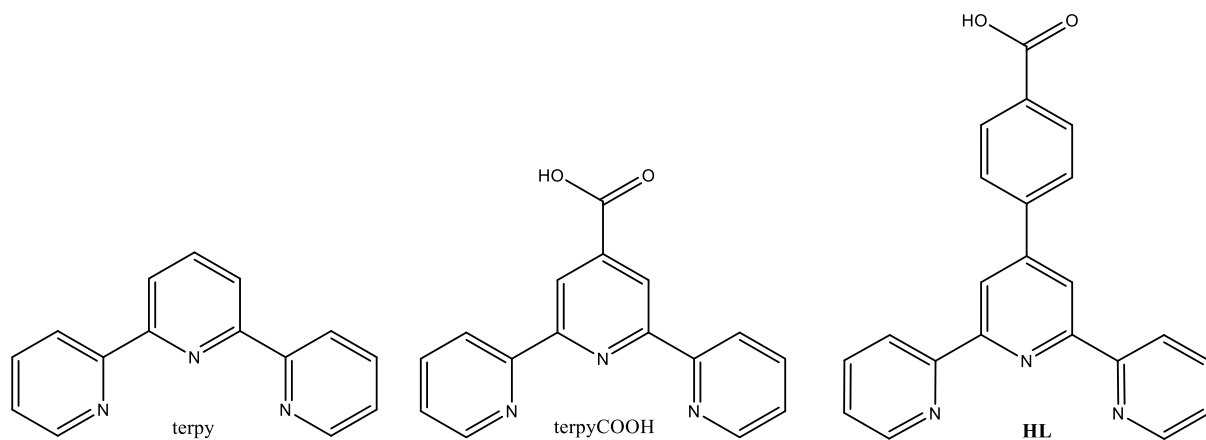
Chapter 5

5. Self-assembled monolayer of active SCO molecules based on a Co(II) terpyridine derivative bearing carboxylic acid groups

5.1. Motivation

In previous chapters, we have used the archetypical family of Fe(II) SCO complexes of the tridentate ligand 2,6-bis(pyrazol-1-yl)pyridine (1bpp) functionalized with carboxylic acid groups. This strategy gave rise to homoleptic 1bppCOOH and 1bppCOOEt, and 1bpp3COOH and 1bpCOOH₂p based Fe (II) SCO complexes in chapters 2 and 3, respectively. They present thermal-, light- and solvent-induced spin transitions highly dependent on the intermolecular interaction and solvent content. In chapter 4, the combination of 1bppCOOH with bppCOOEt or the bulkier 3bpp-bhp resulted in two heteroleptic Fe(II) SCO complexes; the first example of a 1bpp-based heteroleptic complex and a better performing SCO system, respectively. They all showed interesting properties in the solid state, unfortunately, preliminary results of their deposition suggested oxidation or decomposition of the iron (II) after deposition. In order to overcome this problem, Co(II) SCO complexes of tridentate ligands have been chosen in this work due to its robustness against oxidation compared to iron. Co(II) complexes of 1bppCOOH and 1bpp3COOH ligands from chapters 2 and 3, respectively, were synthesized but they did not give rise to SCO complexes. Such complexes stabilized the HS state in all the range of temperature showing interesting single molecule magnet properties. For the shake of the reader, this work will not be presented here (for more information go to the literature^[1]). Nonetheless, deposition of the complexes was studied. Preliminary results showed that [Co(1bppCOOH)] or [Co(1bpp3COOH)] species were present in the surface but, unexpectedly, the oxidation and electronic states were found to be the same as in the bulk, HS-Co(II). Therefore, a Co(II) terpy derivative complex showing SCO properties suitable for surface deposition was chosen (see Chapter 1). Separately, despite the Co(II) ion maintained its oxidation upon deposition, the ligand non-interacting with the surface was lost, as in Fe(II) complexes. Therefore, the use of the expanded ligand of the terpy functionalized with a carboxylic acid group, 4'-(4-carboxyphenyl)-2,2':6',2''-terpyridine (see **Scheme 5.1.1**), was used as a spacer to decouple the switching core of the molecule from the surface, which is known to be an effective strategy.^[2]

As already mentioned in Chapter 1, the crystal structure of the neutral Co(II) complex of the deprotonated expanded ligand **L**, [Co(L)₂]-5H₂O was reported in the literature by Yang *et al.*^[3] but the magnetic properties were not studied. In this chapter, we have synthesized the salt of the protonated ligand in order to optimize its processability towards surface deposition. Thus, we prepared the [Co(LH)₂](ClO₄)₂·4DMA (**1**) compound, which has been structurally and magnetically characterized in the solid state, and studied its behavior upon surface deposition.



Scheme 5.1.1. Schematic representation of, **left**, terpy = 2,2':6',2''-terpyridine, **mid**, terpyCOOH = 4'-carboxyl-2,2':6',2''-terpyridine and, **right**, HL = 4'-(4-carboxyphenyl)-2,2':6',2''-terpyridine.

5.2. Results and discussion

Synthesis of $[\text{Co}(4'-(4\text{-carboxyphenyl})-2,2':6',2''\text{-terpyridine})_2](\text{ClO}_4)_2 \cdot 4\text{DMA}$, (**1**)

1 was obtained by slow diffusion of diethyl ether into solutions of $\text{Co}(\text{ClO}_4)_2 \cdot x\text{H}_2\text{O}$ and **HL** in a 1:2 molar ratio in dimethylacetamide (DMA). After a few weeks, big prismatic dark-orange crystals of **1** suitable for single crystal diffraction were obtained. Purity and stability of the complex was checked with elemental analysis and PXRD (see SI and **Figure SI. 5.4.1**).

Structure of $[\text{Co}(4'-(4\text{-carboxyphenyl})-2,2':6',2''\text{-terpyridine})_2](\text{ClO}_4)_2 \cdot 4\text{DMA}$, (**1**)

The crystal structure of **1** was solved by single-crystal X-ray diffraction at 120 K, 300 K and 340 K in the non-centrosymmetric *P*-1 space group. The asymmetric unit cell is composed of one $[\text{Co}(\text{LH})_2]^{2+}$ cation, two ClO_4^- anions and four DMA solvent molecules (**Figure 5.2.1** and SI for more information). The metal center adopts an octahedral coordination sphere with the six N of the two terpy moieties giving rise to a distorted octahedral geometry. Co-N bond lengths display four longer equatorial Co-N bond that lie in the range of 2.010(2)-2.162(2) Å at 120K and 2.096(4)-2.146(4) Å at 340K for the external pyridine rings and two shorter Co-N axial bond distances to the central pyridine rings from 1.872(2)-1.928(2) Å at 120K and 1.965(4)-1.970(3) Å at 340K (go to [Error! No se encuentra el origen de la referencia.](#) for all distances in the SI). This subtle increase in bond lengths with temperature indicates that the number of molecules in the HS state is increasing with temperature, as it has been already seen in other compounds,^[4] and agrees with magnetic properties (see below). Neighboring $[\text{Co}(\text{LH})_2]^{2+}$ cations are weakly organized in pairs through $\pi \cdots \pi$ and $\text{CH} \cdots \pi$ interactions between phenyl and one of the two lateral pyridyl groups of neighboring complexes

(**Figure SI. 5.4.2**). In addition, $[\text{Co}(\text{LH})_2]^{2+}$ present numerous short contacts with perchlorate anions and DMA solvent molecules. The OH groups are involved in hydrogen bonds with the carbonyl groups from two of the four DMA solvent molecules that avoid the formation of 1D chains of hydrogen-bonded $[\text{Co}(\text{LH})_2]^{2+}$ cations through carboxylic acid groups (see **Figure 5.2.1**), as it has been seen in other bis-trisquelated 4-substituted pyridine derivatives.^[5,6] O atoms of one ClO_4^- are disordered. They have been modelled as six O atoms for 120 K and eight O atoms for 300 K and 340 K with 50% occupancy. At 300 K and 340 K, two DMA solvent molecules are disordered as well. They have been solved as four molecules with an occupancy of 50% each.

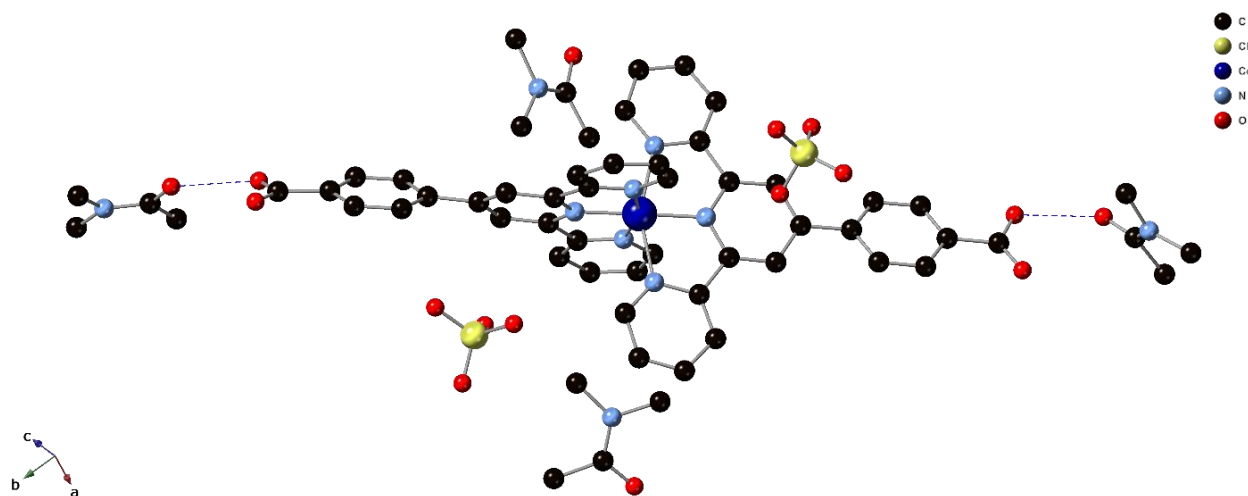


Figure 5.2.1. X-ray structure of the complex **1**. Hydrogen atoms are omitted for clarity. Hydrogen bonds are represented with dashed blue lines.

Magnetic properties

Temperature dependence of the product $\chi_{\text{M}}T$ of **1** in contact with mother liquor presents a gradual increase from typical LS values below 150 K ($0.48 \text{ cm}^3 \cdot \text{K} \cdot \text{mol}^{-1}$) to $1.85 \text{ cm}^3 \cdot \text{K} \cdot \text{mol}^{-1}$ at 350 K suggesting an incomplete and non-cooperative spin transition (**Figure 5.2.2**). Magnetic measurements on the filtered sample before and after heating to 400 K shows a similar behavior with a more incomplete spin transition reaching a maximum value of $1.72 \text{ cm}^3 \cdot \text{K} \cdot \text{mol}^{-1}$ at 400K. This value corresponds to around 60% of molecules in the HS state, taking $2.5 \text{ cm}^3 \cdot \text{K} \cdot \text{mol}^{-1}$ as the value for pure HS state. In contrast, the Co(II) neutral complex with the deprotonated ligand **L**, $[\text{Co}(\text{L})_2] \cdot 5\text{H}_2\text{O}$, shows an abrupt SCO upon dehydration (see **Figure SI. 5.4.3** and associated text in the Supporting Information) This suggests that the absence of strong intermolecular interactions between the complexes in **1**, probably due to the presence of ClO_4^- counteranions and DMA solvent molecules in the structure, could explain the gradual spin transition of **1**, while

the absence of these molecules in the dehydrated $[\text{Co}(\text{L})_2]$ compound would involve closer contacts between complexes leading to a cooperative and abrupt SCO.

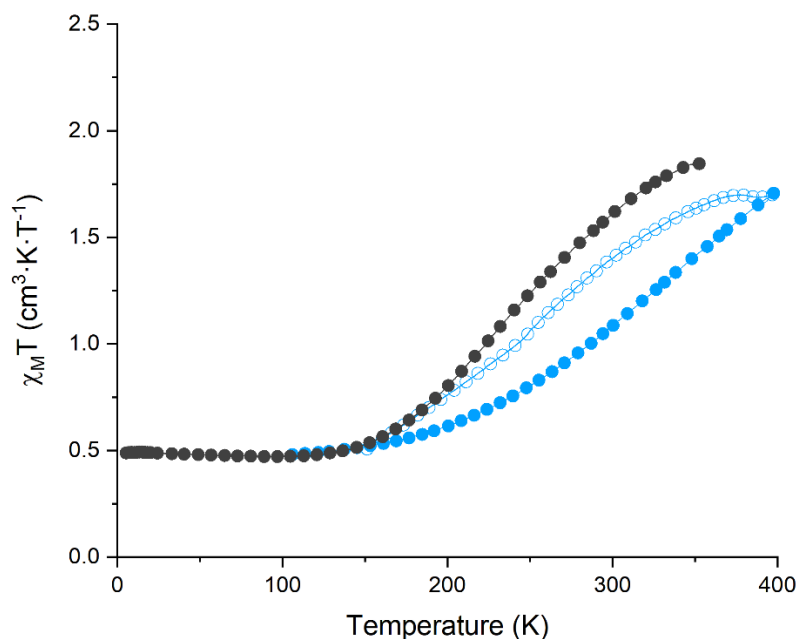


Figure 5.2.2. $\chi_{\text{M}}T$ vs temperature for **1** in contact with mother liquor (grey circles), filtered (blue empty circles) and after desolvation (blue circles).

Deposition

1-SAM were prepared following the same procedure than previous chapters but with some minor changes. Substrates of thermally grown SiO_2 and evaporated silver were immersed for 6h in a 1mM anhydrous DMA solution of **1**. After that, they were washed and rinsed thoroughly with clean DMA to remove any physisorbed material and dried under N_2 stream. Silver was chosen due to the possibility to form SAMs with carboxylic acid groups^[7] and because it has been reported that is possible to obtain at room temperature, within a short time, large domains of well-ordered 2D structures.^[8] XPS measurements demonstrated that different substrates and different deposition times ranging from 6 h to 96 h gave the same results. Therefore, our efforts will be focused on Ag because of all the advantages that it entails.

The stability of the solution was studied by means of UV/Vis and the deposited complexes were characterized by AFM, MALDI-TOF, Raman, XPS and XAS.

UV/Vis spectroscopy of **1** display the classical charge-transfer $t_2-\pi^*$ transition broad bands ranging from 400 to 550 nm also seen in other derivatives.^[9] The most intense band is centered at 524 nm ($\epsilon = 1.9 \times 10^3 \text{ L}^{-1} \text{ mol}^{-1} \text{ cm}^{-1}$). The UV/Vis spectrum after one night of the complex does

not change, confirming the stability of the solution in air (**Figure 5.2.3**). The slight increase in intensity is due to normal evaporation of the solvent.

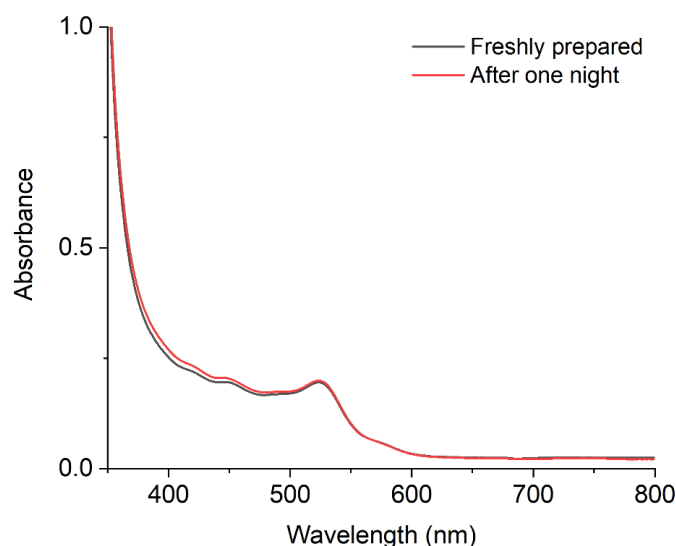


Figure 5.2.3. UV/Vis spectra of a 0.1 mM solution of **1** in DMA freshly prepared (black) and after one day stored in air (red).

Topographic images of **1-SAM** confirmed the absence of aggregates or multilayers (see **Figure 5.2.4**) This result was expected considering that the carboxylic acid group bonds the first layer of molecules to the surface and additional layers, not chemically bonded, would be removed after the washing steps. Due to the high RMS of the naked silver it was not possible to study the effect of the monolayer deposit with accuracy, instead, a SAM of the ligand **HL** (**L-SAM**) was also done for comparison purposes.

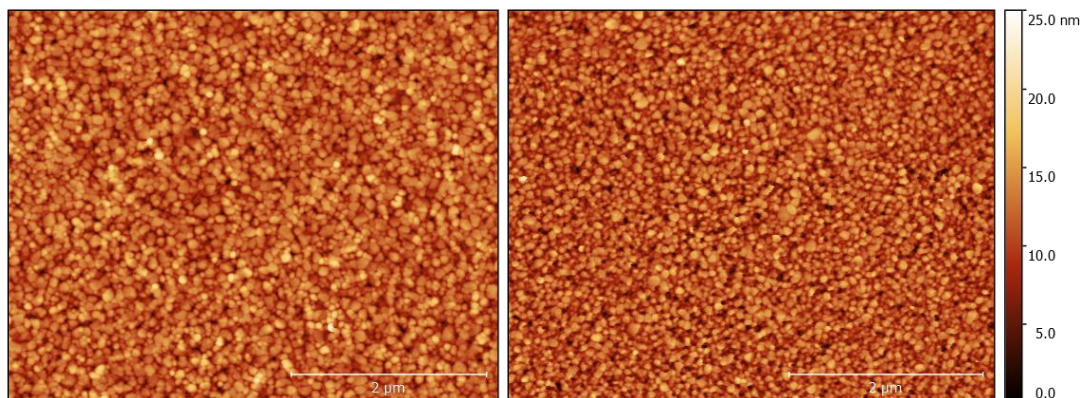


Figure 5.2.4. AFM topographic images of silver substrates of **1-SAM** (left) and **L-SAM** (right). The scale bar represents 2 μm.

Integrity of the molecules in 1-SAM was checked with MALDI-TOF MS. A comparative analysis between bulk and SAM is shown in **Figure 5.2.5**. Peaks of m/z corresponding to $[\text{Co}(\text{LH})_2]^+$ are present in bulk and monolayer spectra (764.16 m/z). On one hand, further proof of the formation of a single layer of molecules is supported by the presence of molecular fragments bonded to silver atoms such as $[\text{L}+\text{H}+\text{Ag}]^+$, $[\text{Co}(\text{LH}+\text{H}+\text{Na})(\text{L}+\text{Ag})]$ and $[\text{Co}(\text{LH}-\text{COOH}+\text{H})(\text{L}+\text{Ag})]^+$ that are not present in the bulk sample. This result has also been observed previously in other systems assembled on Au,^[10,11] where a molecule-substrate bonding is expected. It also suggests that deprotonation of the carboxylic acid group upon contact with the surface takes place. Separately, the lack of molecular fragments in the monolayer sample with the counteranion, such as $[\text{Co}(\text{LH})(\text{ClO}_4)]^+$, that are present in the bulk sample, also confirms the absence of aggregates or any physisorbed material in agreement with AFM measurements (for further information go to **Table S.I. 5.4.1** in the SI).

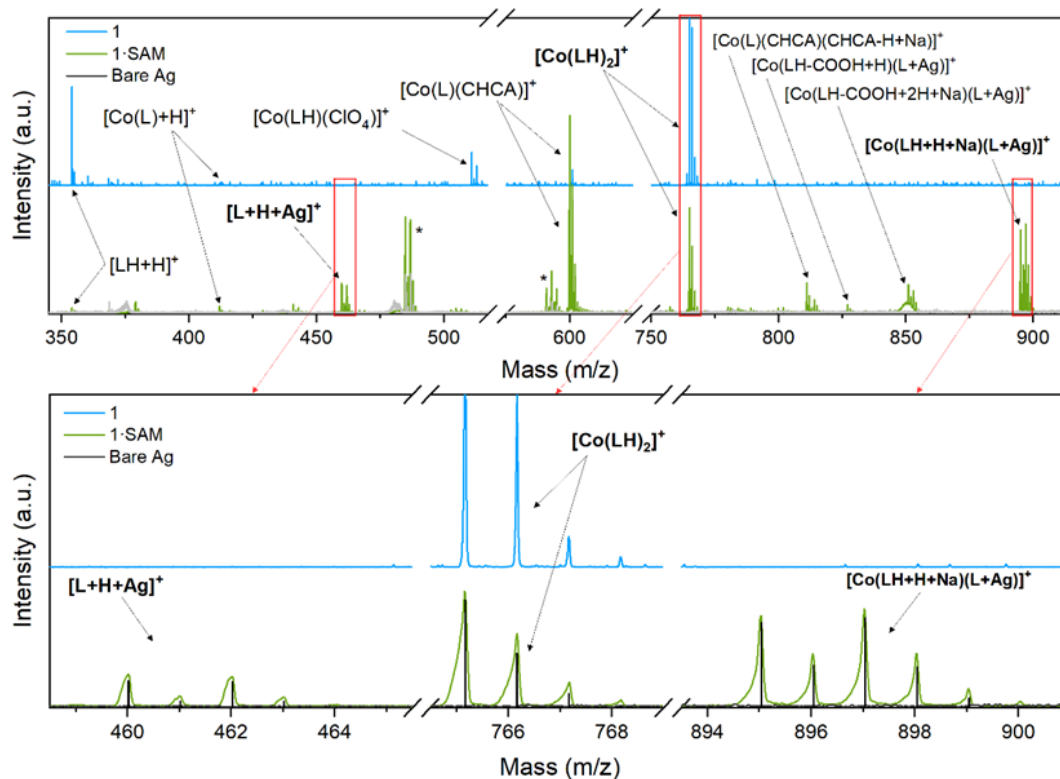


Figure 5.2.5. MALDI-TOF spectra of **1** (blue), **1-SAM** (green) and bare Ag (grey). Magnification of the $[\text{L}+\text{H}+\text{Ag}]^+$, $[\text{Co}(\text{LH})_2]^+$ and $[\text{Co}(\text{LH}+\text{H}+\text{Na})(\text{L}+\text{Ag})]^+$ (enclosed in red rectangles). The expected isotopic distribution pattern for each fragment is reported as black lines. Peaks coming from the matrix used for calibration are marked with an asterisk and are also present in bare Ag. CHCA is abbreviation for α -cyano-4-hydroxycinnamic acid and is present in the matrix used for MALDI-TOF MS measurements (see Experimental Section).

It was possible to study the deposits with Raman spectroscopy on top of a mechanically roughened silver substrate. The nature of the imposed silver defects and their small separation leads to a plasmon absorbance, which is resonant with the 532 nm light used to excite the samples.^[12,13] Therefore, the Raman spectrum of the deposits is expected to be magnified in the “hot-spots” by the SERS effect.

The structural integrity of the complex in **1-SAM** is evident from the fact that SERS spectra of the monolayer and conventional Raman spectra of the bulk are found to be very similar (**Figure 5.2.6** and SI for more information). The most important difference between both samples is the replacement of the band at 783 cm^{-1} in the bulk for a band at 814 cm^{-1} in the monolayer. This band is assigned to the deformation vibration of carboxylate groups and is sensitive to the protonation/deprotonation state.^[14] Such band is also present in the Raman spectra of the complex of the deprotonated ligand $[\text{Co}(\text{L})_2]\cdot 5\text{H}_2\text{O}$ ^[3] (**Figure 5.2.6**) measured as reference. The presence of only one band indicates that both carboxylic acid groups of the deposited complexes are deprotonated.^[15] This is in agreement with MALDI-TOF MS experiments (see above), Raman spectra of a monolayer of the ligand also measured as a reference (**L-SAM**, see **Figure SI. 5.4.6** in the Supporting Information), the absence of Cl from ClO_4^- counteranion in XPS experiments of **1-SAM** (see below) and with literature experiments performed on similar ligands on Ag.^[16]

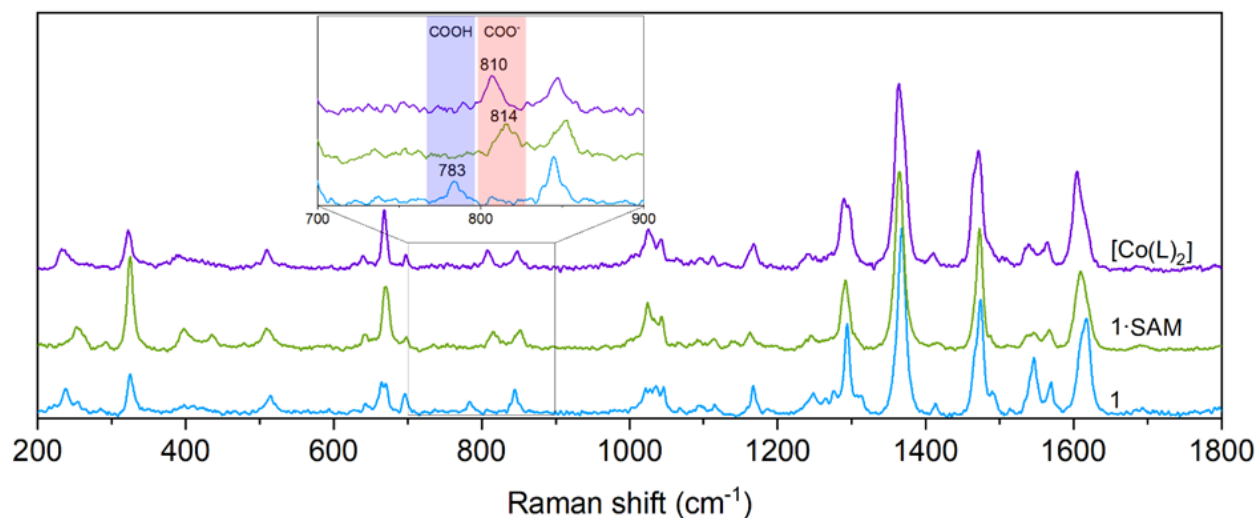


Figure 5.2.6. Raman fingerprints of **1** (blue), **1-SAM** (green) and $[\text{Co}(\text{L})_2]\cdot 5\text{H}_2\text{O}$ (purple) in the $200\text{-}1800\text{ cm}^{-1}$ at 100K. Inset of the $700\text{-}900\text{ cm}^{-1}$ region.

The most characteristic feature of terpy systems is the asymmetric breathing vibration of pyridine rings and is located at *ca.* 991 cm^{-1} . It is known to be independent of the 4-substituted position but not to metal coordination.^[17] Therefore, the shift observed in the breathing mode

above 1020cm^{-1} in the bulk and monolayer samples of **1** with respect to the monolayer of the ligand was expected. Such shift is also observed in the Raman spectra of $[\text{Co}(\text{L})_2]\cdot 5\text{H}_2\text{O}$.^[3] No big differences are seen in the $200 - 900\text{ cm}^{-1}$ region except for the carboxylic/carboxylate bands already mentioned in the manuscript. Based on the literature, the stretching vibration region is known to be mainly governed by coordinative terpy modes such as ring-stretching and in plane deformation modes,^[4,5] although a small contribution of modes coming from the carboxylic/carboxylate groups is also expected.^[6] Nevertheless, we were able to identify the peak at $\text{ca. } 1365\text{ cm}^{-1}$ assigned to the 4-substituted position of the pyridine ring which has been taken as a weak temperature-dependent mode.^[2]

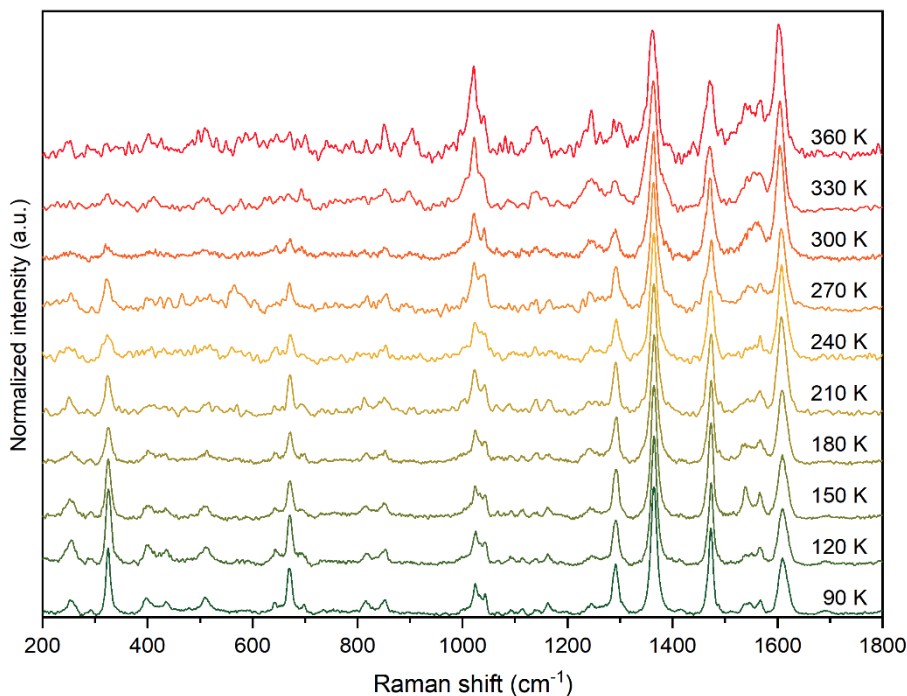


Figure 5.2.7. Temperature dependent Raman spectra of **1-SAM** in the $200\text{-}1800\text{ cm}^{-1}$ range.

Temperature dependent Raman spectroscopy has been used to monitor the spin state of the $\text{Co}(\text{II})$. In the bulk sample, changes in intensity ratios and Raman shifts are observed at the same temperature range of the spin transition, especially in the coordinative terpy modes (**Figure SI. 5.4.4**). Nevertheless, the most notably feature is the increase of intensity of the peak located at 1020 cm^{-1} at increasing temperature. This peak is assigned to the pyridine ring breathing mode,^[17] which is strongly coupled to the Co-N stretch and, in consequence, to the spin state. Similar Raman spectral changes of this peak accompanying spin transition are observed in a related $\text{Co}(\text{II})$ complex reported in the literature.^[18] To get a more quantitative insight, the

normalized intensity of such feature (integrated against the weak temperature-dependent mode of the 4-substituted position of the pyridine ring at 1365 cm^{-1})^[17] is plotted against temperature (**Figure SI. 5.4.5**). It displays a curve in excellent agreement with the bulk data extracted from conventional magnetometry measurements. Therefore, these Raman spectral changes can be attributed to spin transition and used to monitor the spin state.

SERS spectra of **1-SAM** display similar changes with temperature (**Figure 5.2.7**). These changes are not observed in **L-SAM** (**Figure SI. 5.4.6**). Therefore, we can conclude that the spin state of **1-SAM** changes with temperature. A comparison of the spin transition of the bulk with that of the monolayers of **1** and **L** using the spin state-dependent marker from the bulk, suggests that **1** and **1-SAM** undergo spin transition in the same temperature range (150-300 K), while **L-SAM** does not display any changes (**Figure 5.2.8**).

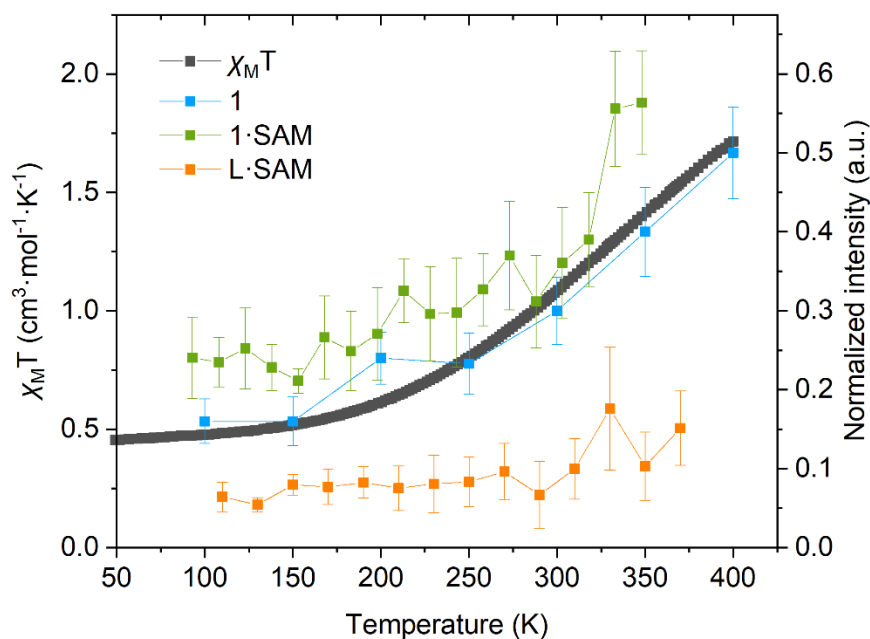


Figure 5.2.8. Temperature-dependence of the normalized intensity of the 1020 cm^{-1} features for **1** (blue squares), **1-SAM** (green circles) and **L-SAM** (orange circles) together with the $\chi_M T$ product (black). The lines are a guide to the eye. Error bars have been calculated from the median absolute deviation.

The fraction of HS molecules seems to be higher in **1-SAM**. These results are confirmed by XPS and XAS measurements, which enables a more accurate estimation of the LS/HS fraction (see below). To prove stability and reproducibility of the spin transition various measurements were done heating and cooling the sample after one week stored in air (see **Figure 5.2.9**). They

confirm that the spin transition in the monolayer is reversible in the temperature range 100 – 360 K. Further increase in temperature leads to irreversible changes in the spectra and blocking of the spin state (see **Figure SI. 5.4.7**). **L-SAM** exhibits the same irreversible changes (see **Figure SI. 5.4.8** associated text) suggesting that the irreversibility of the spin transition at temperatures above 360 K is related to structural changes of the SAMs.^[19,20] Indeed, the irreversibility of the spin transition above 360 K was confirmed by XAS (see below).

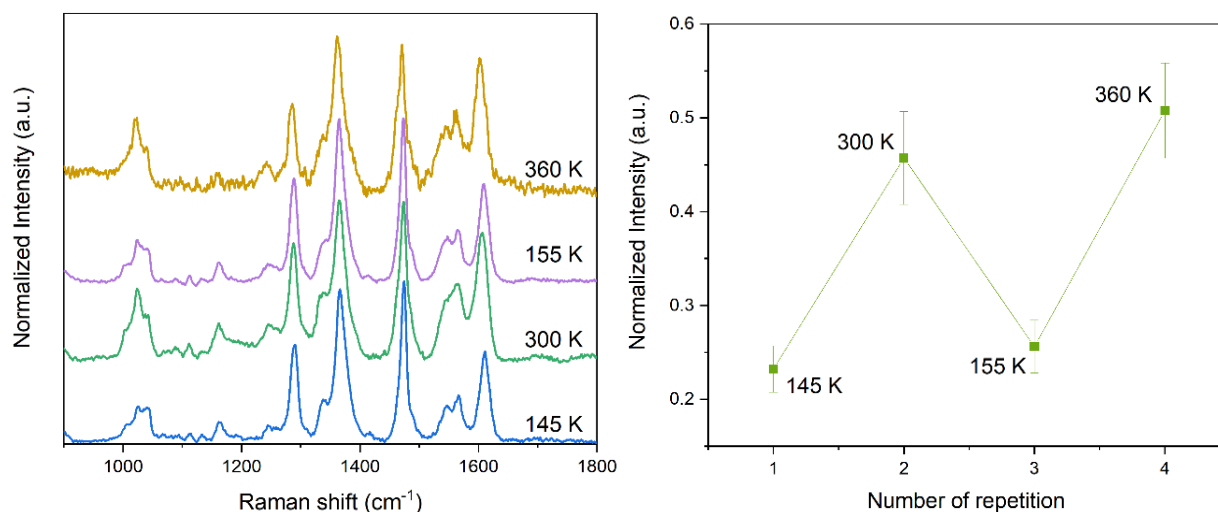


Figure 5.2.9. **Left**, temperature dependent Raman spectra of the same sample after being stored in air for one week in the 900-1800 cm^{-1} range. **Right**, subsequent normalized intensity of the 1020 cm^{-1} features at the given temperatures. The lines are a guide to the eye. Error bars have been calculated from the median absolute deviation.

Structural and electronic properties of the powder and monolayer sample were also investigated by means of XPS. $\text{C}1s$, $\text{N}1s$, $\text{Cl}2p$ and $\text{Co}2p$ XPS regions of **1** (**1-SAM**) were analyzed. The line shape of the $\text{C}1s$ band features three main components; two at lower energies at 285.0 (285.0) and c.a. 286.5 (286.4) eV corresponding to heterobonds such as C-N/C=N and C-C/C=C atoms, respectively,^[7] and the third component at 288.9 (288.1) eV assigned to the O-C=O carbon atoms.^[21] The shift to lower binding energy of the third component of the monolayer respect to the bulk is indicative of the presence of the carboxylate moiety in the deposited molecule and it is also present in **L-SAM** (see **Figure 5.2.10** and **Table S.I. 5.4.2**). $\text{N}1s$ region shows only one component at 399.7 (399.7) eV assigned to the coordinated nitrogen atoms of the pyridine rings.^[22] $\text{Cl}2p$ spectrum of **1** features the typical shape of perchlorate anion centered at 208 eV,^[23] while **1-SAM** does not display such band (**Figure 5.2.10**). This is further

experimental evidence of the absence of physisorbed molecules on the surface and deprotonation of the carboxylic acid groups upon deposition that compensates the +2 charge of the complexes. These results are in agreement with the conclusion drawn from C 1s, MALDI-TOF, Raman and with the literature.^[16]

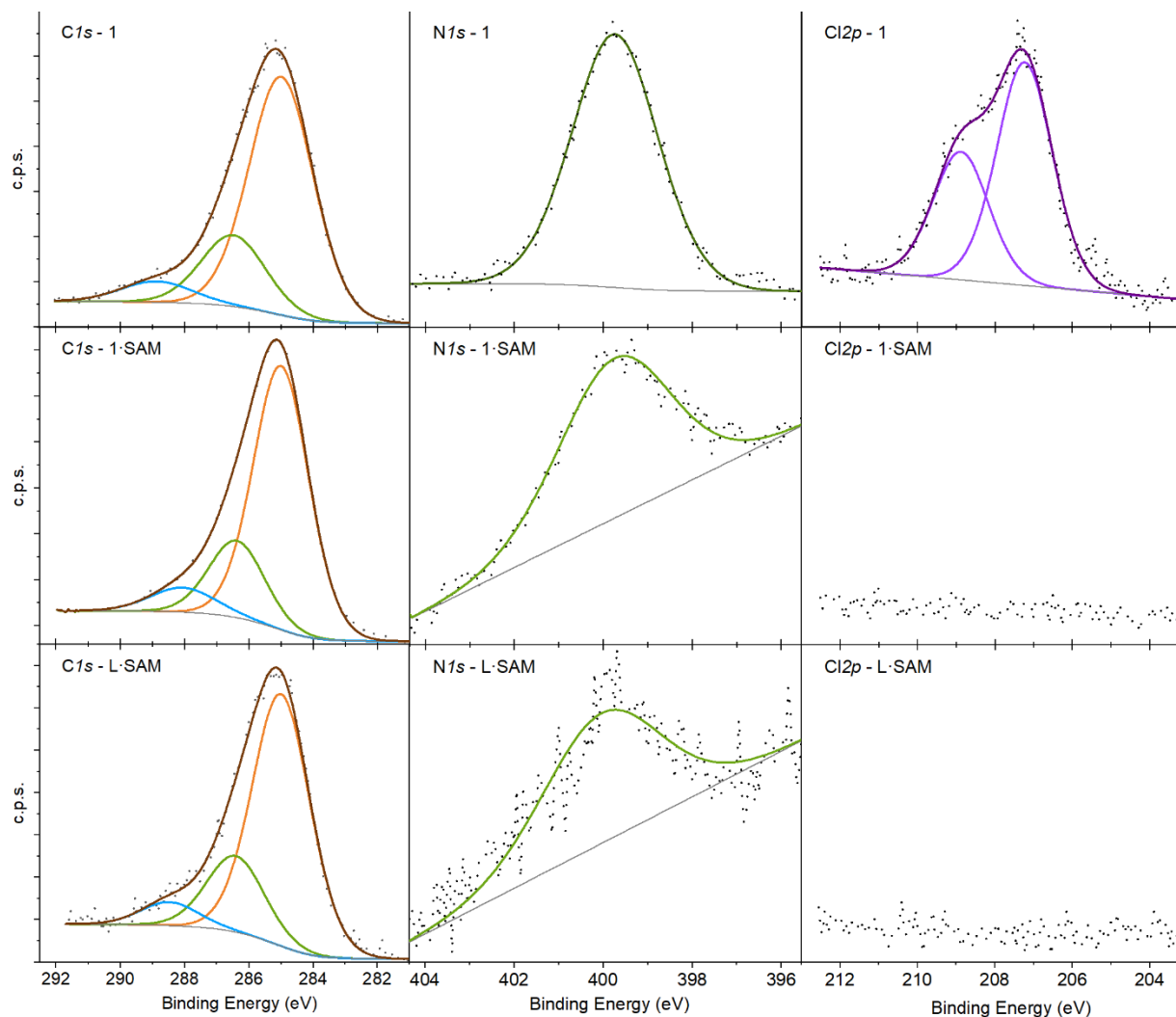


Figure 5.2.10. C 1s, N 1s and Cl 2p XPS regions of **1**, **1-SAM** and **L-SAM** along with the best fitting model.

The Co2p_{3/2} region of the bulk and monolayer display the expected lineshape of a Co(II) photoemission (see **Figure 5.2.11**).^[24,25] In order to get qualitative information about the SCO properties, it was fitted with a similar procedure previously reported for HS/LS-Co(II), where the intensity of the satellites is directly correlated to the paramagnetism, i.e. to the spin state of the metal ion.^[11] In our approach, the line shapes have been reproduced with 5 components (A–E) along with the corresponding Co2p_{1/2} spin–orbit (SO) coupled contributions (A'–E') weighted by

the expected 2:1 ratio. **1(1•SAM)** components are composed by a main peak A at 780.4(780.9) eV, integrating about 23.7(21.7)% of the overall signal at 170 K and 18.7(17.6) % at 300 K, and the satellites B, C, D and E at 782.4(782.2), 784.7 (784.4), 787.3 (787.2) and 790.3(789.8), respectively (see **Table S.I. 5.4.4**). Else, a sixth component (F) appears at low binding energies for both samples. We attribute this to an LMM Auger line coming from the Co ion. Nevertheless, the fraction of this component is almost negligible (less than 6%). Semiquantitative analysis and stoichiometric ratios (see **Table S.I. 5.4.2** and

Table S.I. 5.4.3) are in good agreement with the expected values. This suggests that most of the molecules covering the surface retain the molecular structure found in the bulk.

XPS was also used to get an insight of the electron level population and so of the spin state. On one hand, experimental results^[24,26,27] confirm that SO splitting increases with the number of unpaired 3d-electrons, being closer to 15 or 16 eV for diamagnetic Co(III) or paramagnetic cobalt(II) compounds, respectively. Thus, a change in Δ SO upon spin transition is expected due to different orbital populations in the two spin states, being larger for the HS-Co(II) than for the LS-Co(II). Therefore, the occurrence of SCO can be followed by SO shift.^[28] On the other hand, the percentage of the different components is also indicative of the spin state, an increase in the number of unpaired atomic electrons causes an increase in the satellite intensity in XPS^[11,29]. Therefore, the intensity ratio ($\Sigma I_{\text{sat}}/I_{\text{Co}2p_{3/2}}$) is directly related to the intensity of the satellites and has been selected as the most sensitive parameter to follow the spin transition.^[24]

Co $2p_{3/2}$ XPS region was measured at 170K and 300K to analyze the differences between low and high temperature species. At low temperatures, **1 (1•SAM)** presents a SO value of 15.1 (15.2), which is the expected one for a LS-Co(II) and is in agreement with magnetic properties (Raman spectroscopy) (see above). It evidences an increase in the SO from 15.1 (15.2) at low temperature to 15.2 (15.3) at room temperature (Δ SO = 0.1 (0.1), see **Table S.I. 5.4.4**; **Error! No se encuentra el origen de la referencia.**). To confirm the spin transition, together with the high-energy shift of the metal lines, a satellite magnification is also expected. Indeed, the significantly increased intensities of the Co $2p_{3/2}$ satellites from 1.70 (1.91) to 2.42 (2.66), $\Delta(\Sigma I_{\text{sat}}/I_{\text{Co}2p_{3/2}}) = 0.72$ (0.75) (**Table S.I. 5.4.4**), provides further prove of thermal spin transition in both, bulk, and monolayer samples. This confirms that our complexes maintain the SCO properties under X-ray irradiation in high vacuum conditions as well and that a higher HS-Co(II) fraction seems to be present in the monolayer, which is in agreement with Raman and confirmed by XAS measurements (see below).). It must be taken into consideration that the higher intensity of the main peak in **1•SAM** compare to **1** could be indicative of a small fraction of Co(III) molecules present in the sample, also seen

in XAS (see below). Therefore, the higher HS fraction of molecules observed in XPS may be underrated.

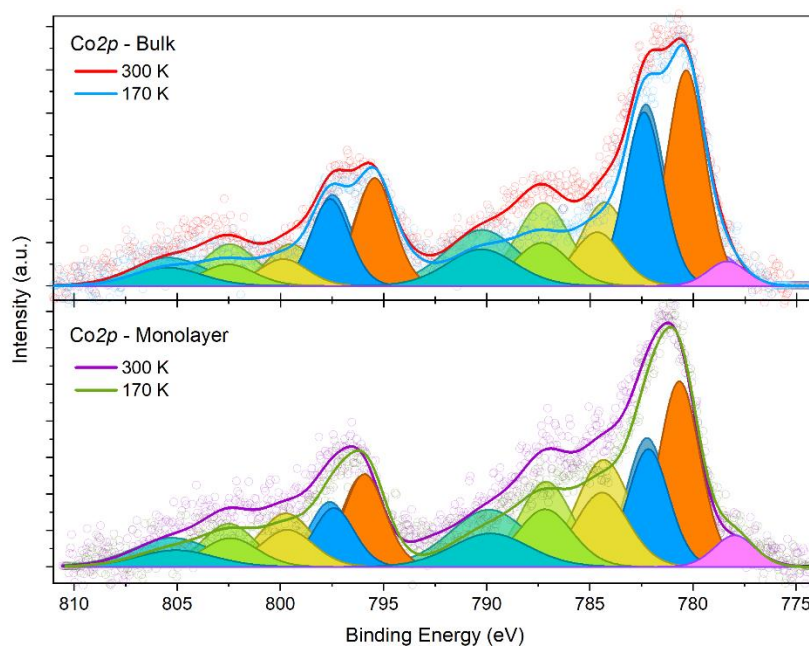


Figure 5.2.11. Comparison of XPS Co2p spectra of **1** (top) and **1-SAM** (bot) along with deconvolution of the peaks and corresponding best fitting lines.

XAS spectra at CoL_{2,3}-edges were recorded at different temperatures for **1-SAM**. **Figure 5.2.12a** shows the temperature dependent XAS spectra of the monolayer in the 125-310K range. Evolution of the signal under soft X-rays irradiation was excluded at all temperatures (see **Figure SI. 5.4.9**). However, a fraction of molecules was altered by the beam. Such effect was also observed in the bulk and could be removed by reducing the photon flux (see **Figure SI. 5.4.10a**; Error! No se encuentra el origen de la referencia.). In **1-SAM**, however, it was still present at the minimum photon flux. We then tried to evaluate the signal coming from the altered molecules (see **Figure SI. 5.4.10b**). Theoretical calculations supports that this component comes from oxidation of Co(II) to Co(III) in a terpy environment. To provide a better quantitative insight on the temperature-dependence HS-Co(II) profile, **1-SAM** CoL₃ XAS spectra was fitted using the simulated HS and Co(III) and the experimental LS spectra of the bulk, since it is highly dependent on the distortion parameters (see **Figure SI. 5.4.11** and associated text in the SI for more details). The results, shown in **Figure 5.2.12b** (see **Figure SI. 5.4.12** and **Figure SI. 5.4.13** in the SI for all the fitted curves for the first and second cycles, respectively), evidence a constant *c.a.* 0.20(0.04) fraction of altered molecules while the rest undergoes spin transition above 150 K. If we do not take into account such fraction, these results indicate that the monolayer present a

higher HS content than the bulk in the same range of temperatures. Thus, warming from 125 to 310 K, the HS fraction goes from *ca.* 60 to 90 % for the monolayer and from *ca.* 0 to 30 % for the bulk.

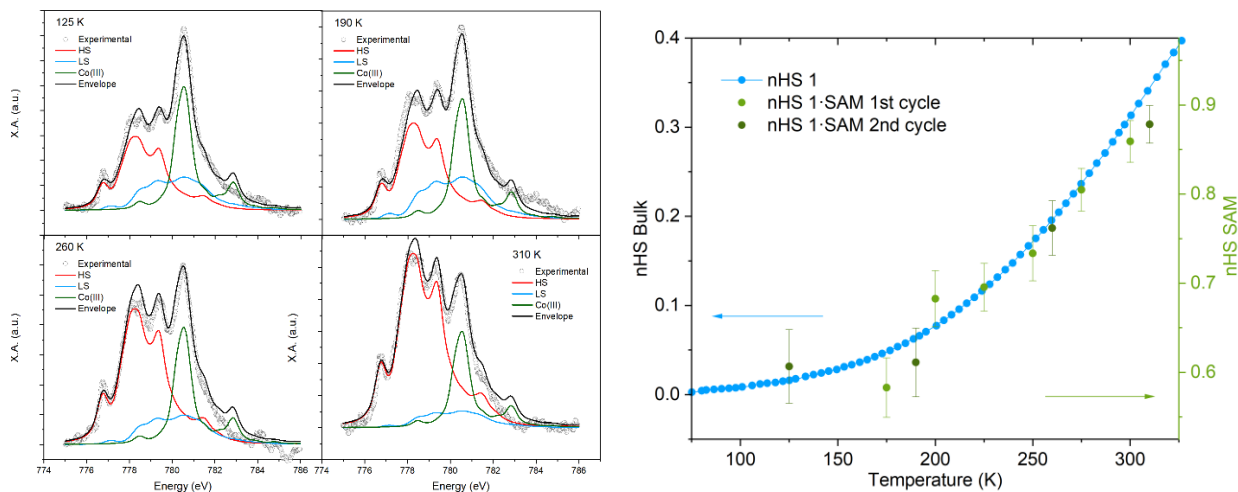


Figure 5.2.12. a) XAS CoL_3 -edge of **1-SAM** at each temperature (empty circles) together with experimental LS Co(II) (blue curves) and theoretical HS Co(II) (red curves) and LS Co(III) (green curve) components. Black line is the best fitting curve with the sum of the three components. **b)** Co(II) HS molar fraction thermal distribution obtained from magnetic measurements of the bulk and from the one extracted from the XAS fitting of the monolayer in the first and second warming cycles.

These results confirm a thermal spin transition comparable with that observed in the bulk in the same temperature range, with a fraction of molecules (*ca.* 60%) remaining in the HS state on the monolayer, as observed in Raman and XPS experiments. A second warming cycle was done confirming reversibility of the spin transition in the monolayer (**Figure 5.2.12b**). At 370K, XAS spectra of **1-SAM** is consistent with the Co(II)-HS state extracted from the bulk (**Figure SI. 5.4.14**). The subsequent cooling does not affect the spin state and remains blocked in the HS (see **Figure SI. 5.4.14b**). This result is also in agreement with Raman spectroscopy.

5.3. Conclusions

In this chapter, synthesis and characterization of a new Co(II) SCO complex based on (4'-(4-carboxyphenyl)-2,2':6',2''-terpyridine ligand has been studied. The chemical functionalization of the system with a functional group that provides a versatile anchoring point and the processability enabled by the higher solubility of the salt allowed us to prepare SAMs of intact molecules from a diluted solution within a short period of time. AFM, MALDI-TOF MS, Raman spectroscopy and XPS evidences the formation of the deprotonated specie upon surface deposition and confirms the absence of physisorbed material. Thermal SCO properties of the monolayer have been confirmed with a total of three different techniques: Raman spectroscopy, XPS and XAS pointing to a gradual SCO behavior similar to that observed in the solid state for the protonated complex, which suggest the absence of a cooperative spin transition on the surface as observed previously for monolayers of evaporated SCO complexes. This represents, as far as we are aware, the first example of a SAM of active SCO complexes anchored to a metallic substrate. Finally, our contribution opens the door to the construction of SCO nanostructure-based devices through soft methodologies compared to the high-cost conventional ultra-high vacuum techniques largely employed for this purpose. Further improvements such as a more abrupt SCO and higher stability could be achieved by expanding the aromaticity of the ligand to enhance the intermolecular interactions between the deposited molecules.

5.4. Supporting Information

Synthesis of of [CoII(4'-(4-carboxyphenyl)-2,2':6',2''-terpyridine)2](ClO4)2·4DMA, (1)

A solution of $\text{Co}(\text{ClO}_4)_2 \cdot x\text{H}_2\text{O}$ (36.6 mg, 0.10 mmol) in DMA (3 mL) was added dropwise to a suspension of **HL** (70.6 mg, 0.15 mmol) in DMA (3 mL) and the mixture was stirred for 15 minutes. A red-dark solution was formed. Red-dark prismatic crystals of **1** suitable for X-ray diffraction were obtained by slow diffusion of diethyl ether into this solution. Microanalysis shows a Co:Cl ratio of 1:2. Anal. Calcd for **1** ($\text{C}_{60}\text{H}_{67}\text{Cl}_2\text{CoN}_{10}\text{O}_{16}$): C, 54.84; H, 5.14; N, 10.66 %. Found: C, 50.69; H, 3.83; N, 8.48 %. Anal. Calcd for $[\text{Co}(\text{HL})_2](\text{ClO}_4)_2 \cdot 1\text{DMA} \cdot 5(\text{H}_2\text{O})$ ($\text{C}_{48}\text{H}_{44}\text{Cl}_2\text{CoN}_7\text{O}_{18}$): C, 50.72; H, 3.90; N, 8.62 %. Found: C, 50.69; H, 3.83; N, 8.48 %.

Elemental analysis results of **1** indicate that two solvent molecules present in the structure are replaced by five water molecules in contact with ambient air. For this reason, experimental PXRD presents small differences with respect to the simulated one from the structure solved under nitrogen steam.

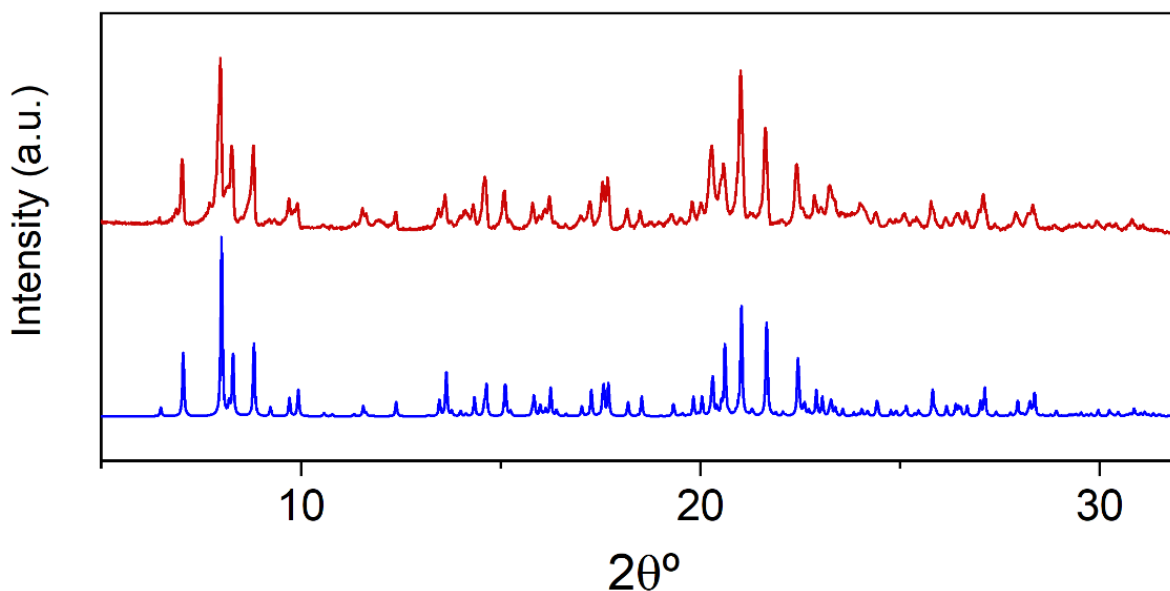


Figure SI. 5.4.1. Simulated PXRD pattern from single crystal of **1** measured at 300 K (blue) and experimental (red).

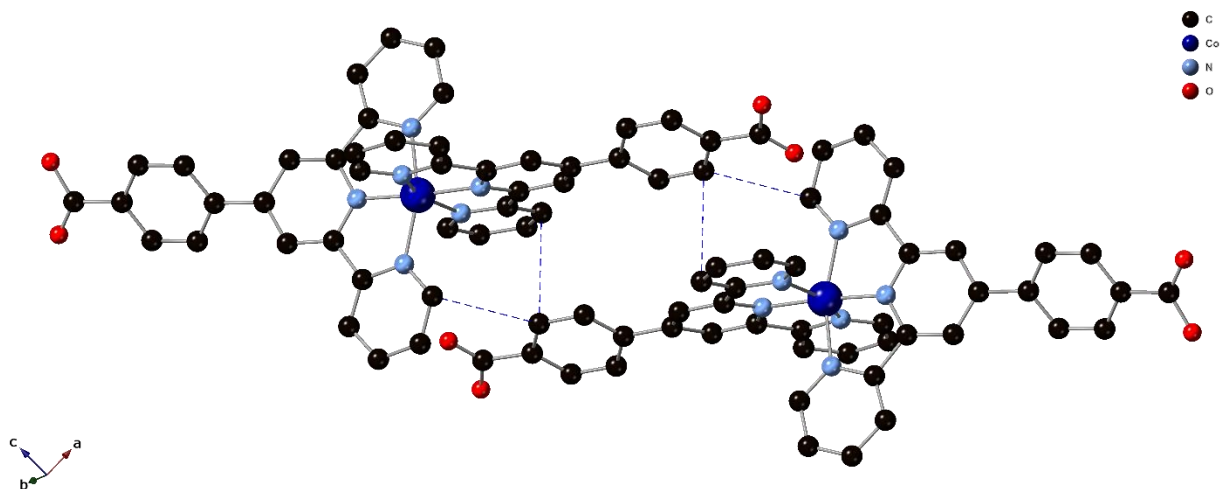


Figure SI. 5.4.2. View of the supramolecular $\pi\cdots\pi$ and $\text{CH}\cdots\pi$ interactions between pairs of molecules of **1** (C (black), N (blue), O (red), Co (dark blue)). $\pi\cdots\pi$ interactions are represented with dashed red lines. Counter ions, solvent molecules, and hydrogen atoms are omitted for clarity.

Magnetic properties of $[\text{Co}(\text{L})_2]\cdot 5\text{H}_2\text{O}$

Temperature dependence of $\chi_{\text{M}}T$ of $[\text{Co}(\text{L})_2]\cdot 5\text{H}_2\text{O}$ shows values close to $0.5 \text{ cm}^3\cdot\text{K}\cdot\text{mol}^{-1}$ from 5 to 250 K typical of LS Co(II). At higher temperature there is a gradual increase to reach a maximum at 360 K of $1.21 \text{ cm}^3\cdot\text{K}\cdot\text{mol}^{-1}$. Interestingly, at higher temperatures there is a decrease of $\chi_{\text{M}}T$ to reach a minimum at 374 K ($0.75 \text{ cm}^3\cdot\text{K}\cdot\text{mol}^{-1}$). This is a clear indication that a reverse spin transition takes place in this temperature range. At higher temperatures there is an abrupt increase of $\chi_{\text{M}}T$ to reach values close to 2.2 at 388 K. On lowering the temperature, the abrupt spin transition is shifted to lower temperatures with a thermal hysteresis of 30 K. Again, there is a partial reverse spin transition from 340 to 300 K. Reverse spin transition in Co(II) complexes have been reported and have been related to structural phase transitions.^[1] In this case, preliminary variable-temperature PXRD experiments suggest the presence of several phases; the initial hydrate one (**phase I**), which is lost above 350 K; the dehydrated **phase III**, which present an abrupt spin transition from 340 to 400 K in cooling and heating modes; and the intermediate **phase II** at around 310 K in the first heating and cooling cycle undergoing a gradual spin transition. The structural phase transitions from **phases II and III** could explain the reverse spin transition.

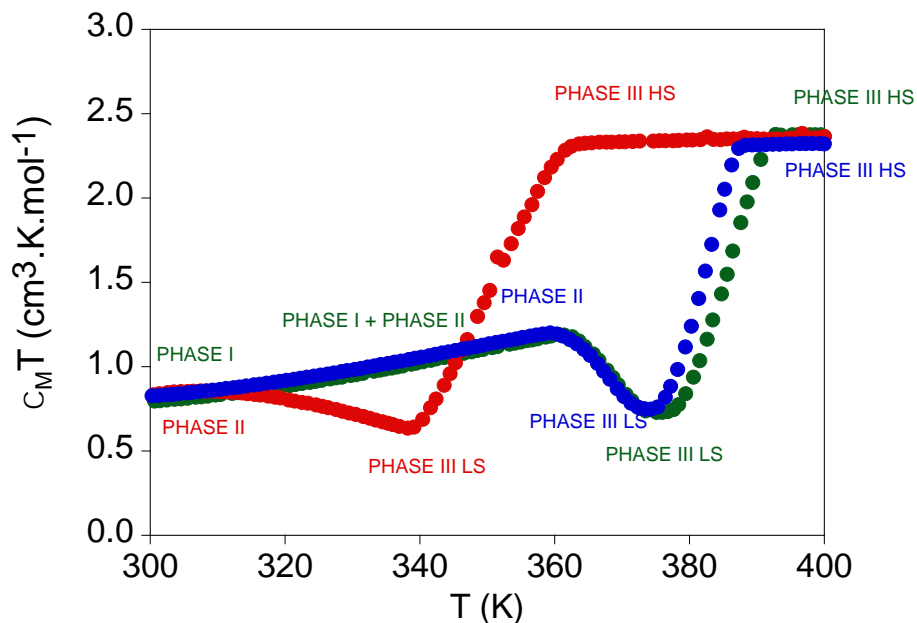


Figure SI. 5.4.3. Temperature dependence of the product of the molar magnetic susceptibility and the temperature ($\chi_M T$) of $\text{Co}(\text{L}_2)$ (green, first heating, red, first cooling and blue, second heating). Scan rates 2 Kmin^{-1} for the first heating and cooling and 1 Kmin^{-1} for the second heating.

Deposition of $[\text{Co}(\text{L}_2)] \cdot 5\text{H}_2\text{O}$

Table S.I. 5.4.1. MALDI-TOF peaks expected and experimentally found for **1** and **1-SAM**.

Fragment	Theor. (<i>m/z</i>)	1 (<i>m/z</i>)	1-SAM (<i>m/z</i>)
$[\text{Co}(\text{LH})_2]^+$	764.17	764.16	764.15
$[\text{Co}(\text{LH}+\text{H}+\text{Na})(\text{L}+\text{Ag})]^+$	895.06	n/d	895.01
$[\text{LH}+\text{H}]^+$	354.12	354.11	354.12
$[\text{L}+\text{Ag}+\text{H}]^+$	460.02	n/d	460.03
$[\text{Co}(\text{LH})]^+$	412.05	412.00	412.04
$[\text{Co}(\text{L})(\text{CHCA}^{\text{a}})]^+$	600.07	600.08	600.07
$[\text{Co}(\text{L})(\text{CHCA})(\text{CHCA}-\text{H}+\text{Na})]^+$	811.11	n/d	811.09
$[\text{Co}(\text{LH}-\text{COOH}+\text{H})(\text{L}+\text{Ag})]^+$	827.07	n/d	827.07
$[\text{Co}(\text{LH}-\text{COOH}+2\text{H}+\text{Na})(\text{L}+\text{Ag})]^+$	851.07	n/d	851.03
$[\text{Co}(\text{LH})(\text{ClO}_4)]^+$	511.0	510.99	n/d

a) CHCA is abbreviation for α -cyano-4-hydroxycinnamic acid and is present in the matrix used for MALDI-TOF MS measurements (for more information go to Appendix).

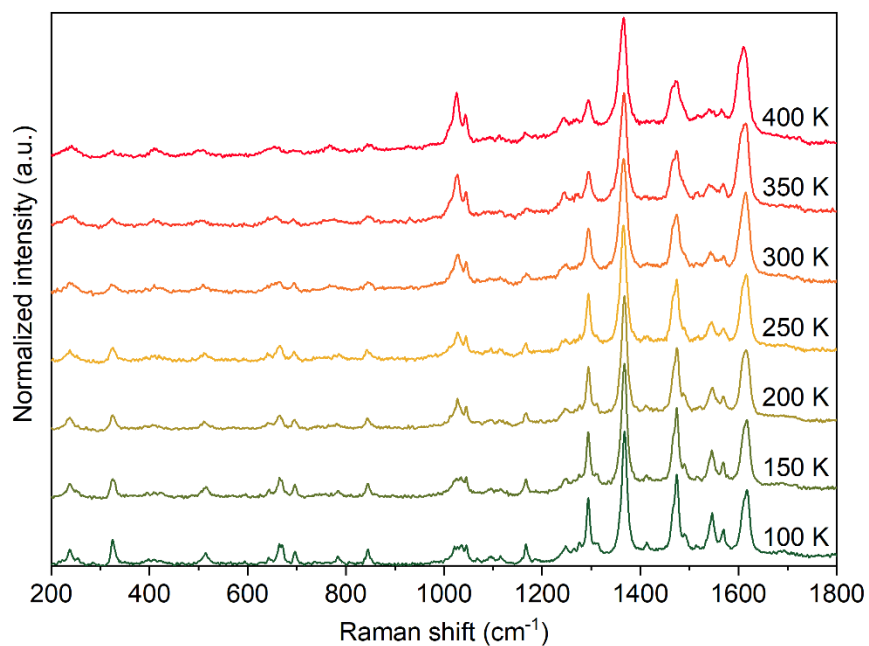


Figure SI. 5.4.4. Temperature-dependent Raman spectra of 1.

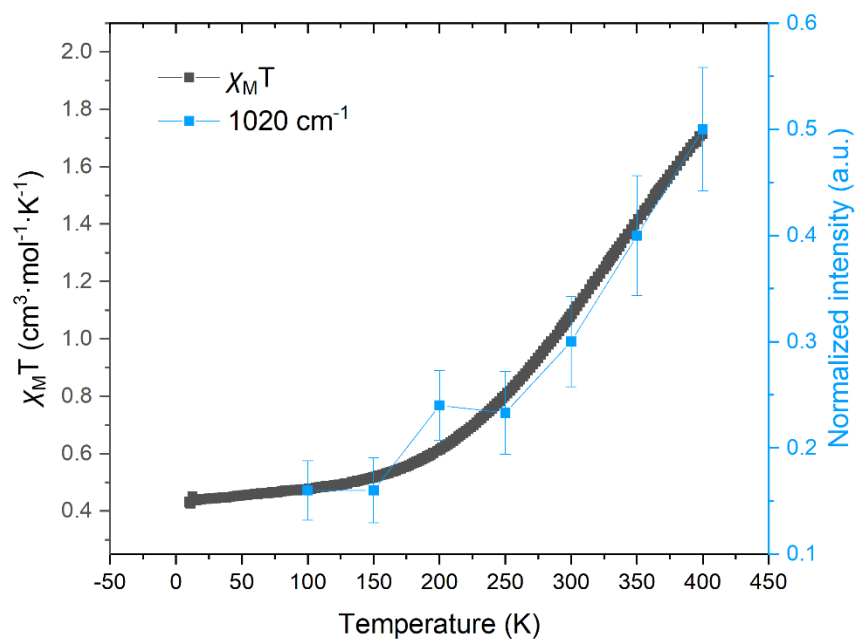


Figure SI. 5.4.5. $\chi_M T$ vs temperature (black) and normalized intensity value of the pyridine ring breathing mode at 1020 cm^{-1} (blue squares) for desolvated 1.

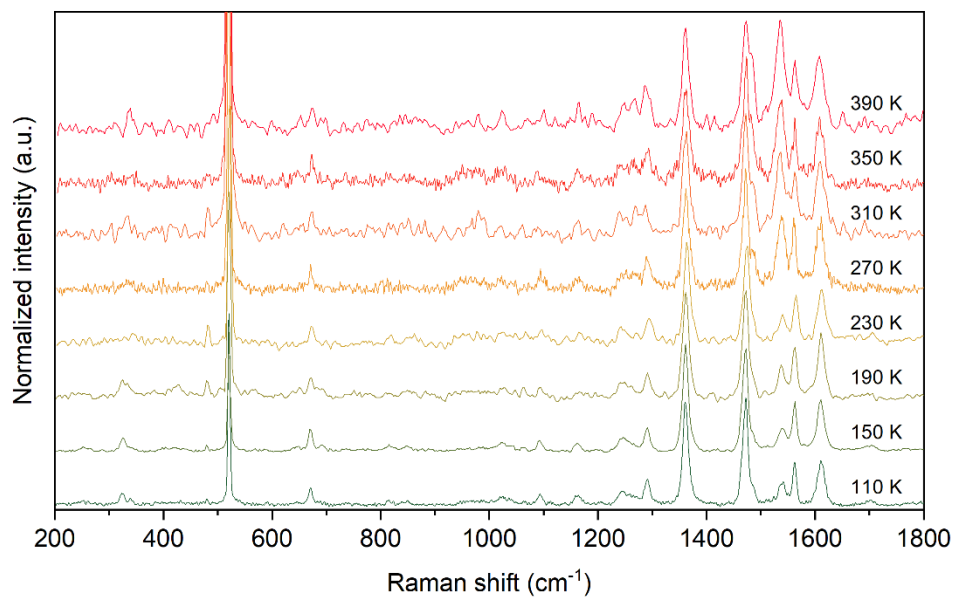


Figure SI. 5.4.6. Temperature dependent Raman spectra of **L-SAM**.

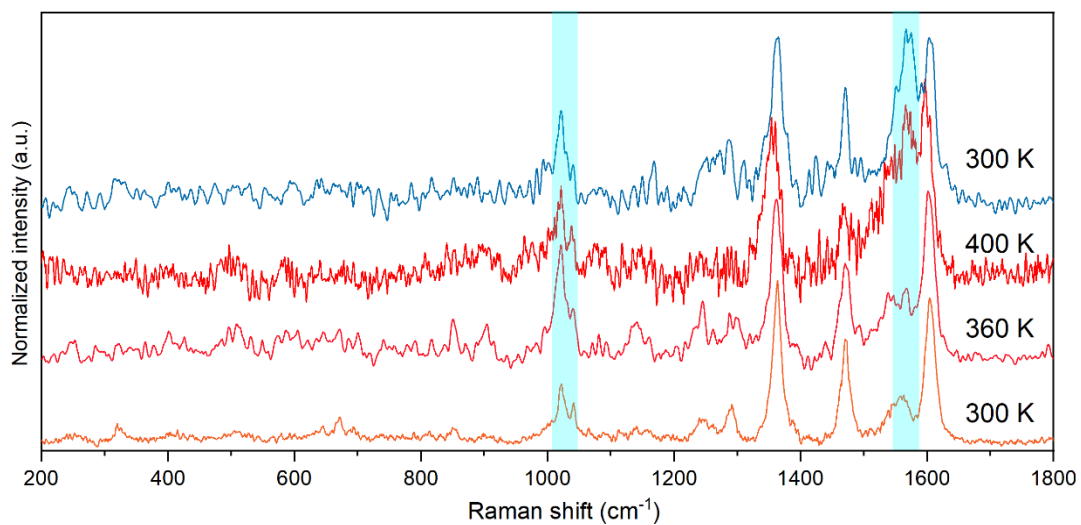


Figure SI. 5.4.7. Raman spectra of **1-SAM** before and after heating the sample at 400 K. Irreversible changes in the spectra at 1567 cm^{-1} and 1020 cm^{-1} (highlighted in cyan) take place.

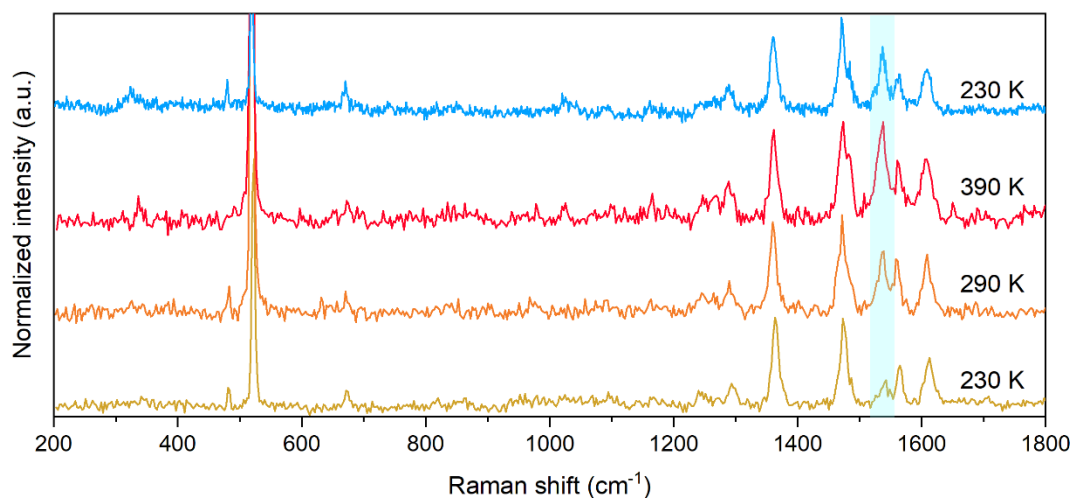


Figure SI. 5.4.8. Raman spectra of **L-SAM** before and after heating the sample at 390 K. Irreversible changes in the spectra at ca. 1550 cm^{-1} (highlighted in cyan) take place.

Table S.I. 5.4.2. XPS peak position and estimated and theoretical percentages (relative error about 5%) of C 1s and N 1s elements for compound **1**, **1-SAM** and **L-SAM**.

Element	1	1-SAM	L-SAM	Theory
	B. E. (%)	B. E. (%)	B. E. (%)	(%)
C	285.0 (71.6)	285.0 (71.4)	284.9 (71.8)	(73.3)
	286.5 (21.4)	286.4 (20.8)	286.3 (21.7)	(20.0)
	288.9 (7.0)	288.1 (7.7)	288.3 (6.7)	(6.7)
N	399.7 (100)	399.7 (100)	399.9 (100)	(100)
Cl	207.2/208.9 (100)	-	-	-

Table S.I. 5.4.3. Theoretical and XPS estimated atomic semiquantitative analysis and ratios for bulk and monolayer of **1**.

	Semiquantitative analysis			Element ratios			Carbon ratios		
	Co	N	C	Co/Co	Co/N	Co/C	Co/C-C	Co/C-N	Co/COO ⁻
Theoretical	2.0%	11.8%	86.3%	1	0.17	0.023	0.03	0.09	0.27
1	1.6%	6.4%	92.1% ^a	1	0.24	0.017	0.02	0.07	0.22
1-SAM	2.0%	11.4%	86.6%	1	0.18	0.024	0.03	0.10	0.26

a) Although a homogeneous coverage of all the surface was done spreading a thick layer of powder, the higher value of the carbon semiquantitative analysis of **1** is probably coming from the carbon tape used to attach the powder to the sample holder.

Table S.I. 5.4.4. Peak position of the spectral components employed for least squares fitting of the Co2p XPS binding energies (B.E.) for **1** and **1-SAM** at 170 K and 300 K. Integrated areas are reported in percentages for each component in brackets. Spin-orbit splitting (Δ SO) and intensity ratios of the satellites ($\Sigma I_{\text{sat}}/I_{\text{Co}2p_{3/2}}$) are also gathered.

	Co 2p					Δ SO eV	$I_{\text{sat}}/I_{\text{Co}2p_{3/2}}$
	A B.E. (%)	B B.E. (%)	C B.E. (%)	D B.E. (%)	E B.E. (%)		
1 (170 K)	780.4 (23.7)	782.4 (19.1)	784.7 (7.4)	787.3 (6.6)	790.3 (7.2)	15.1	1.70
1 (300 K)	780.4 (18.7)	782.3 (16.3)	784.3 (9.2)	787.2 (10.3)	790.2 (9.5)	15.2	2.42
1-SAM (170 K)	780.7 (21.7)	782.2 (13.8)	784.4 (11.2)	787.2 (9.0)	789.8 (7.4)	15.3	1.91
1-SAM (300 K)	780.9 (17.6)	782.4 (12.4)	784.6 (13.6)	787.3 (10.4)	790.1 (10.3)	15.4	2.66

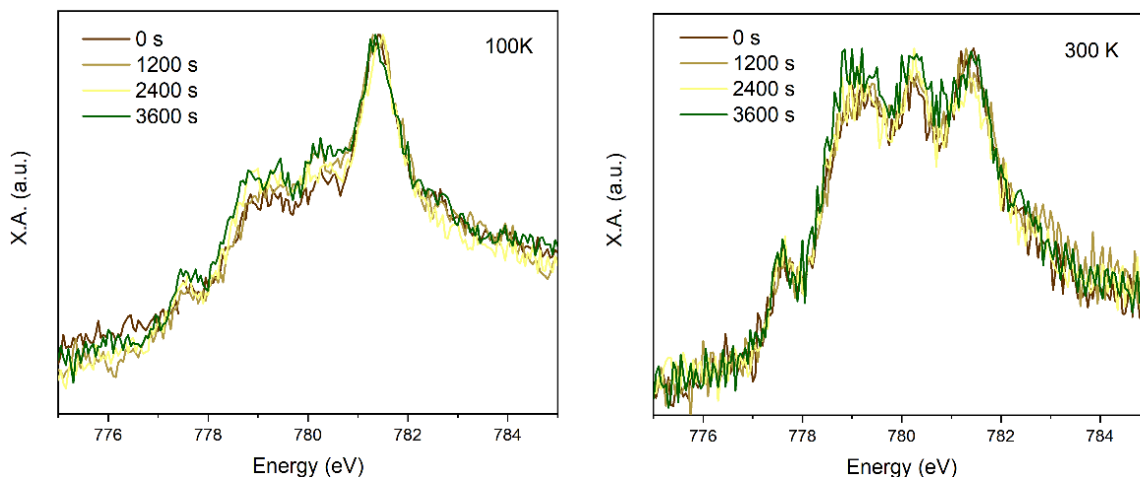


Figure SI. 5.4.9. Time evolution of Co_L3-edge XAS spectra of **1-SAM** at 100 K and 300 K.

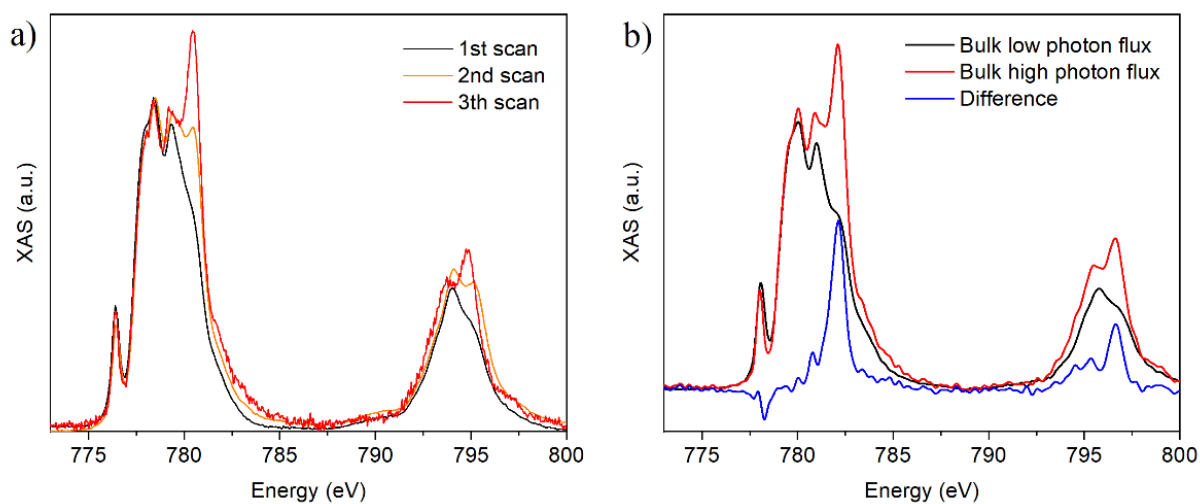


Figure SI. 5.4.10.a) Time-dependence XAS spectra of the Co_L2,3-edges acquired on the same spot in the bulk sample with a high photon flux at 300K. **b)** Difference between the XAS spectra of the Co_L2,3-edges acquired at high and low photon flux conditions for the bulk.

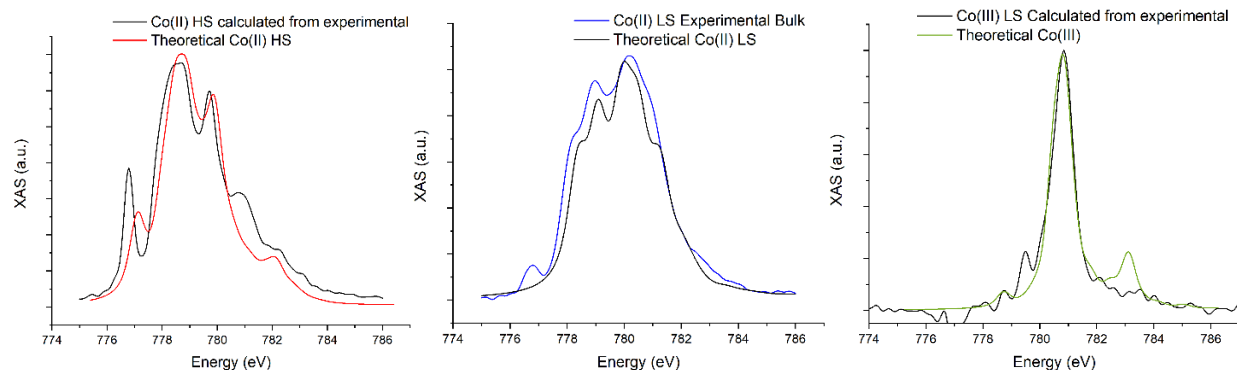


Figure SI. 5.4.11. XAS CoL_3 -edge of the desolvated bulk at 100 K in the LS state (left), at the highest available temperature (370 K) after subtracting a 0.4 fraction of the LS spectra (middle) and the calculated difference of the altered molecules together with the theoretical calculated spectra. The references used for the fitting procedure are highlighted in colours.

The HS spectra used as a reference was obtained after subtracting a 0.4 contribution of the low temperature spectrum (LS state), according to magnetic measurements, to the 370 K XAS spectrum of the bulk.

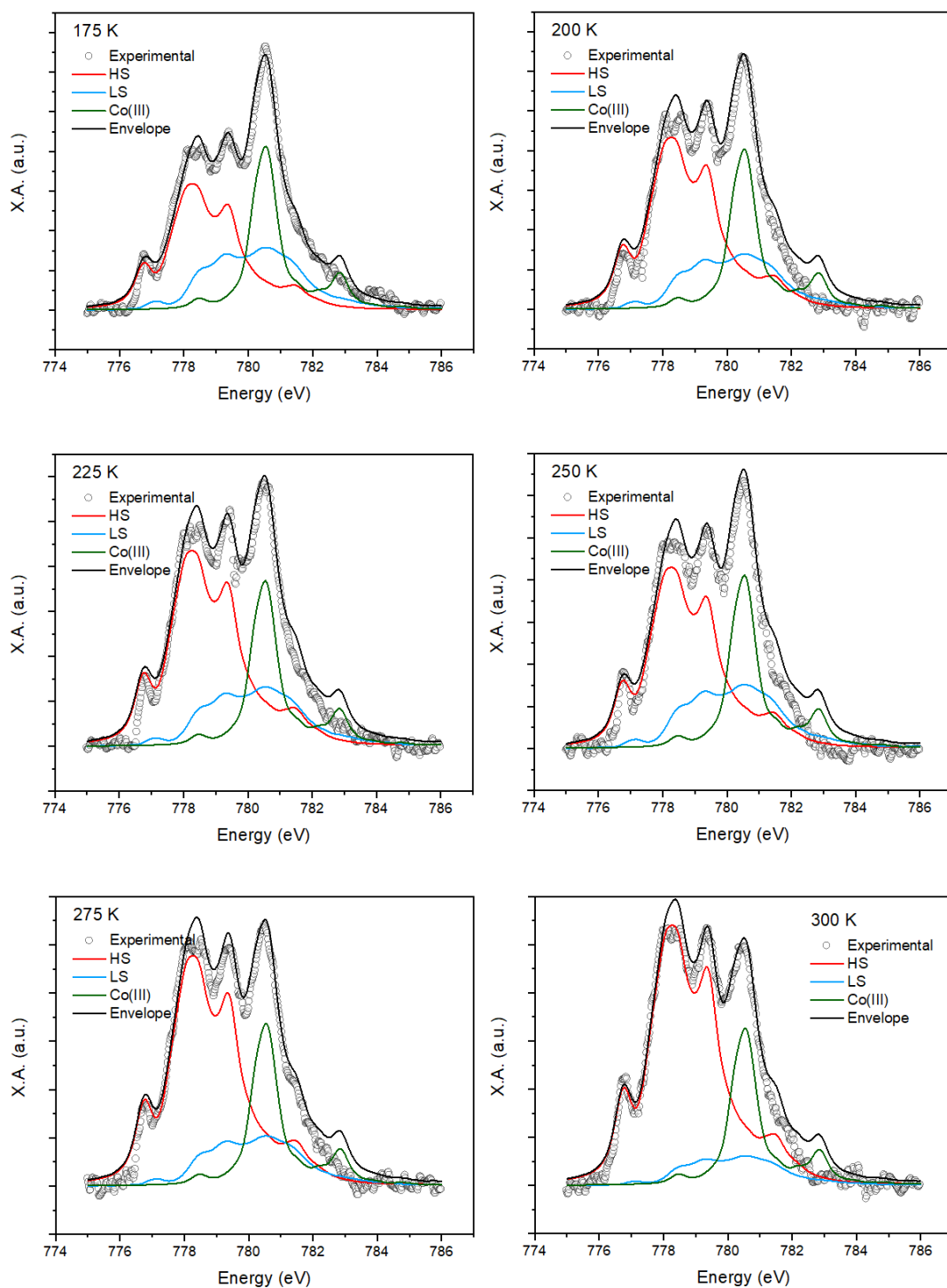


Figure SI. 5.4.12. XAS CoL_{2,3}-edge of **1-SAM** (empty circles) together with the reference HS Co(II) (red curves), LS Co(II) (blue curves) and LS Co(III) (green curve) at each temperature for the first cycle. Black line is the best fitting curve with the sum of the three components.

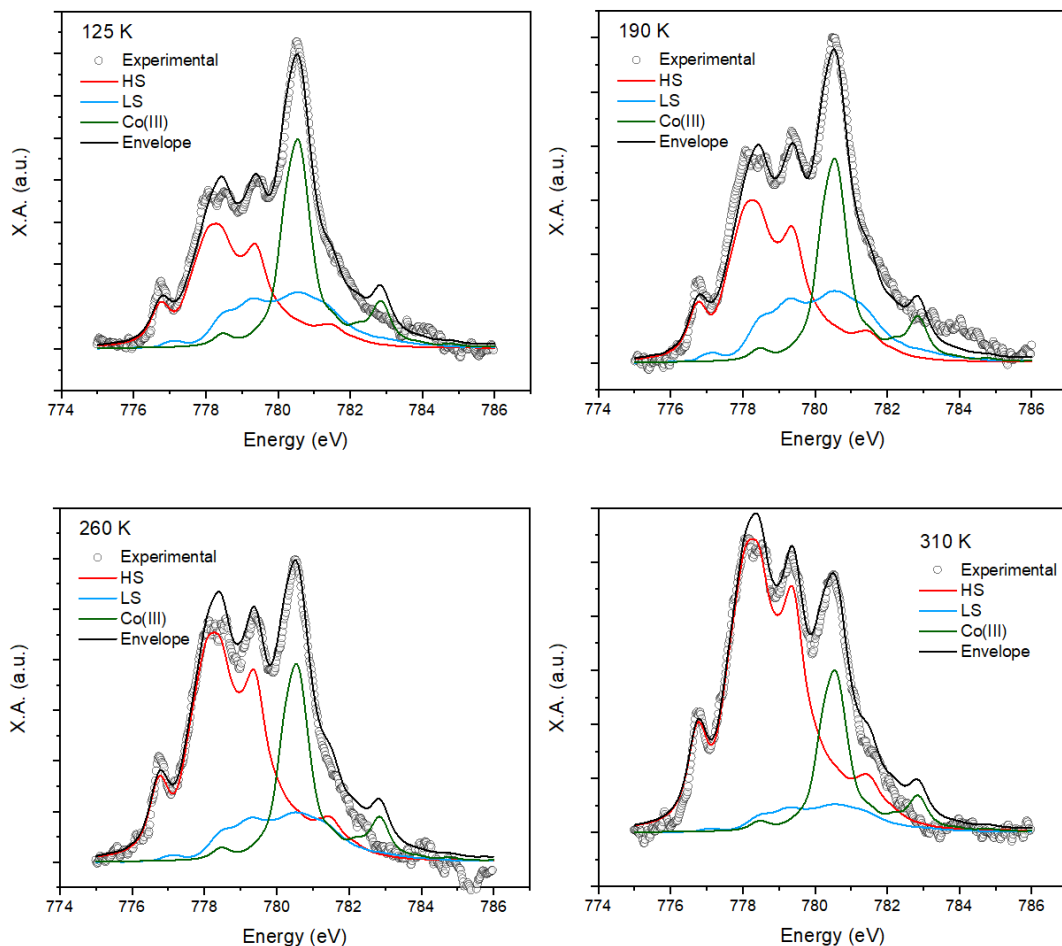


Figure SI. 5.4.13. XAS $\text{Co}_{L_{2,3}}$ -edge of **1-SAM** (empty circles) together with the reference HS Co(II) (red curves), LS Co(II) (blue curves) and LS Co(III) (green curve) at each temperature for the second cycle. Black line is the best fitting curve with the sum of the three components.

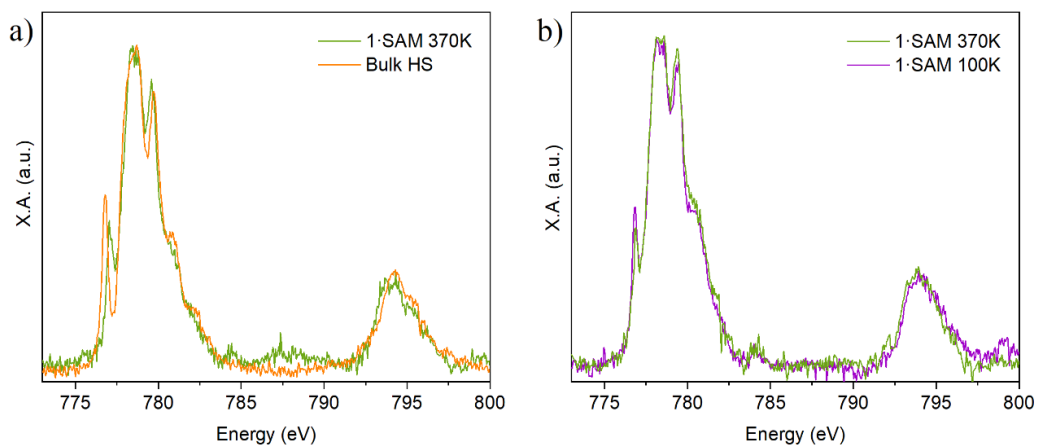


Figure SI. 5.4.14. $\text{Co}_{L_{2,3}}$ -edge XAS comparison of the spectra of **a) 1-SAM** and calculated HS state of the bulk and **b) 1-SAM** at 370K and its subsequent cooling down to 100K.

Table S.I. 5.4.5. Crystallographic tables.

Identification code	1	1	1
Empirical formula	C ₆₀ H ₆₆ Cl ₂ CoN ₁₀ O ₁₆	C ₆₀ H ₆₆ Cl ₂ CoN ₁₀ O ₁₆	C ₆₀ H ₆₆ Cl ₂ CoN ₁₀ O ₁₆
Formula weight	1313.05	1313.05	1313.05
Temperature/K	120.00(10)	299.4(10)	340(4)
Crystal system	triclinic	triclinic	triclinic
Space group	P-1	P-1	P-1
a/Å	12.3368(4)	12.5846(5)	12.6608(6)
b/Å	13.5063(5)	13.6472(4)	13.6988(5)
c/Å	18.0712(5)	18.2438(6)	18.2866(5)
α/°	90.221(2)	91.119(3)	91.312(3)
β/°	94.068(2)	93.664(3)	93.524(3)
γ/°	94.159(3)	94.085(3)	94.057(3)
Volume/Å ³	2995.49(17)	3118.03(19)	3156.5(2)
Z	2	2	2
ρ _{calc} /cm ³	1.456	1.399	1.382
μ/mm ⁻¹	0.455	0.437	0.432
F(000)	1370.0	1370.0	1370.0
Crystal size/mm ³	0.45 × 0.35 × 0.2	0.45 × 0.35 × 0.2	0.45 × 0.35 × 0.2
Radiation	MoKα (λ = 0.71073)	MoKα (λ = 0.71073)	MoKα (λ = 0.71073)
2θ range for data collection/°	6.478 to 60.124	6.604 to 58.24	6.426 to 58.3
Index ranges	-16 ≤ h ≤ 16, -18 ≤ k ≤ 18, -25 ≤ l ≤ 24	-17 ≤ h ≤ 16, -17 ≤ k ≤ 18, -23 ≤ l ≤ 24	-17 ≤ h ≤ 17, -17 ≤ k ≤ 18, -23 ≤ l ≤ 24
Reflections collected	48487	48421	48772
Independent reflections	15595 [R _{int} = 0.0504, R _{sigma} = 0.0628]	14990 [R _{int} = 0.0676, R _{sigma} = 0.1082]	15181 [R _{int} = 0.0708, R _{sigma} = 0.1160]
Data/restraints/parameters	15595/31/840	14990/59/960	15181/53/840
Goodness-of-fit on F ²	1.056	1.034	1.039
Final R indexes [I >= 2σ (I)]	R ₁ = 0.0666, wR ₂ = 0.1621	R ₁ = 0.0698, wR ₂ = 0.1415	R ₁ = 0.0816, wR ₂ = 0.1853
Final R indexes [all data]	R ₁ = 0.0911, wR ₂ = 0.1831	R ₁ = 0.1699, wR ₂ = 0.2014	R ₁ = 0.1988, wR ₂ = 0.2698
Largest diff. peak/hole / e Å ⁻³	2.06/-0.73	0.40/-0.40	0.53/-0.45

5.5. References

- [1] V. García-López, F. J. Orts-Mula, M. Palacios-Corella, J. M. Clemente-Juan, M. Clemente-León, E. Coronado, *Polyhedron* **2018**, *150*, 54.
- [2] T. G. Gopakumar, M. Bernien, H. Naggert, F. Matino, C. F. Hermanns, A. Bannwarth, S. Mühlenberend, A. Krüger, D. Krüger, F. Nickel, W. Walter, R. Berndt, W. Kuch, F. Tuczek, *Chemistry - A European Journal* **2013**, *19*, 15702.
- [3] J. Yang, R. X. Hu, M. B. Zhang, *Journal of Solid State Chemistry* **2012**, *196*, 398.
- [4] P. Gütllich, H. A. Goodwin, *Spin Crossover in Transition Metal Compounds*, Springer, Berlin, Heidelberg, **2004**.
- [5] A. Abhervé, M. Clemente-León, E. Coronado, C. J. Gómez-García, M. López-Jordà, *Dalton Transactions* **2014**, *43*, 9406.
- [6] V. García-López, M. Palacios-Corella, A. Abhervé, I. Pellicer-Carreño, C. Desplanches, M. Clemente-León, E. Coronado, *Dalton Transactions* **2018**, *47*, 16958.
- [7] H. Aitchison, R. Ortiz De La Morena, R. Peifer, S. Omar, H. Lu, S. M. Francis, M. Zharnikov, A. Grohmann, M. Buck, *Langmuir* **2018**, *34*, 9654.
- [8] A. Krzykawska, J. Ossowski, T. Zaba, P. Cyganik, *Chemical Communications* **2017**, *53*, 5748.
- [9] L. J. Kershaw Cook, F. Tuna, M. A. Halcrow, *Dalton Transactions* **2013**, *42*, 2254.
- [10] P. Totaro, L. Poggini, A. Favre, M. Mannini, P. Sainctavit, A. Cornia, A. Magnani, R. Sessoli, *Langmuir* **2014**, *30*, 8645.
- [11] G. Poneti, L. Poggini, M. Mannini, B. Cortigiani, L. Sorace, E. Otero, P. Sainctavit, A. Magnani, R. Sessoli, A. Dei, *Chemical Science* **2015**, *6*, 2268.
- [12] Z. Starowicz, R. Wojnarowska-Nowak, P. Ozga, E. M. Sheregii, *Colloid and Polymer Science* **2018**, *296*, 1029.
- [13] S. Luo, A. Mancini, F. Wang, J. Liu, S. A. Maier, J. C. de Mello, *ACS Nano* **2022**, *16*, 7438.
- [14] N. F. L. Machado, M. P. M. Marques, L. A. E. Batista de Carvalho, J. L. Castro, J. C. Otero, *Journal of Raman Spectroscopy* **2017**, *48*, 413.
- [15] A. Królikowska, J. Bukowska, *Journal of Raman Spectroscopy* **2007**, *38*, 936.

- [16] H. Aitchison, R. Ortiz De La Morena, R. Peifer, S. Omar, H. Lu, S. M. Francis, M. Zharnikov, A. Grohmann, M. Buck, *Langmuir* **2018**, *34*, 9654.
- [17] J. Kožíšek, J. Svoboda, J. Zedník, B. Vlčková, I. Šloufová, *Journal of Physical Chemistry B* **2021**, *125*, 12847.
- [18] M. G. Cowan, J. Olgúin, S. Narayanaswamy, J. L. Tallon, S. Brooker, *Journal of American Chemical Society* **2012**, *134*, 2892.
- [19] J. Ling, Y. Lu, L. Liu, X. Liu, L. Wang, *Physica E: Low-Dimensional Systems and Nanostructures* **2016**, *81*, 19.
- [20] D. Jiang, Y. Lu, J. Ling, X. Leng, X. Liu, L. Wang, *Surface Review and Letters* **2016**, *23*, DOI 10.1142/S0218625X1650061X.
- [21] I. Cebula, H. Lu, M. Zharnikov, M. Buck, *Chemical Science* **2013**, *4*, 4455.
- [22] J. A. Barth, M. Rudolph, E. Uhlig, *Zeitschrift für anorganische und allgemeine Chemie* **1986**, *632*, 65.
- [23] B. C. Beard, *Surface Science Spectra* **1993**, *2*, 97.
- [24] T. Ivanova, A. Naumkin, A. Sidorov, I. Eremenko, M. Kiskin, *Journal of Electron Spectroscopy and Related Phenomena* **2007**, *156–158*, 200.
- [25] G. Poneti, M. Mannini, B. Cortigiani, L. Poggini, L. Sorace, E. Otero, P. Sainctavit, R. Sessoli, A. Dei, *Inorganic Chemistry* **2013**, *52*, 11798.
- [26] D. Frost, C. McDowell, I. Woolsey, *Evidence for Multiplet Splitting of 2p Photoelectron Lines of Transition Metal Complexes*, **1972**.
- [27] D. C. Frost, C. A. McDowell, I. S. Woolsey, *Molecular Physics* **1974**, *27*, 1473.
- [28] D. Briggs, V. A. Gibson, *Chemical Physics Letters* **1974**, *25*, 493.
- [29] Yu. G. Borod'ko, S. I. Vetchinkin, S. L. Zimont, I. N. Ivleva, Yu. M. Shul'Ga, *Chemical Physics Letters* **1976**, *42*, 264.

Chapter 6

6. General conclusions

6.1. Conclusions

After our exhaustive study about the molecular functionalization of SCO complexes and its implementation in surfaces, several aspects can be highlighted as main conclusions of this thesis.

First, in chapters 2 and 3 we explored the use of homoleptic Fe(II) SCO complexes based on 1bppCOOH and 1bppCOOEt, and 1bpp3COOH and 1bpCOOH_{2p} ligands, respectively. All of them display thermal-, light- and solvent-induced spin transition, confirming the well-known capability of the 1bpp moiety to give rise to SCO complexes. In the case of 1bppCOOH with carboxylic acid in the 4-position of the pyridine ring (Chapter 2), it has been found that in the salts with smaller counteranions (BF₄⁻ or ClO₄⁻) the packing of the complexes is directed by the hydrogen bonds between the carboxylic acid groups leading to chains of complexes that display an abrupt SCO as a result of the cooperativity provided by these intermolecular interactions. In contrast to this, bulkier counteranions (such as CF₃SO₃, AsF₆ and SbF₆), bulkier substituents (1bppCOOEt) or changing the position of the functional group to one of the two pyrazolyl rings (1bpp3COOH, Chapter 3 – Part A), give rise to a less dense crystal packing compared to the solvent free [Fe(1bppCOOH)₂]X₂ (X = ClO₄ and BF₄) resulting in the incorporation of solvent molecules in the structure. SCO properties of these compounds are highly dependent on such molecules and their intermolecular interactions but, in general, gradual thermal SCO or solvent-dependent spin transitions and LIESST effect are obtained. Interestingly, in Chapter 3 – Part B, the addition of carboxylic substituents in the two pyrazolyl rings (1bpCOOH_{2p}) results in the incorporation of solvent molecules in the structure but they participate in CH...π and π...π interactions leading to chains of interacting complexes that strongly define the magnetic and structural properties giving rise to a SCO compound that shows an abrupt thermal spin transition close to room temperature and an unusually high T(LIESST). Low temperature X-ray diffraction experiments with light have demonstrated that these properties are related to structural reorganization of the system between different crystallographic phases, which can be controlled with light and temperature. Thus, the interplay between the flexibility of the complexes, provided by the solvent molecules and carboxylic acid substituents, and the stiffness of the coordination provided by the bpp, are key factors to induce structural changes¹ that give rise to unexpectedly long-lived photo-induced spin state.

In Chapter 4, we studied the formation of heteroleptic Fe(II) SCO complexes. Combination of 1bppCOOH with 1bppCOOEt or the bulkier 3bpp-bhp ligand resulted in the first example of a heteroleptic complex made of two 1bpp-type ligands and a better-performing SCO system. While

the first one presents gradual and incomplete thermal- and light-induced SCO, the latter shows a hysteretic thermal spin transition closer to room temperature and a complete photo-conversion at low temperatures. Again, the CH $\cdots\pi$ and $\pi\cdots\pi$ interactions provided in this case by the bulkier 3bpp-bhp ligand are crucial to obtain an abrupt thermal SCO. These results open the door for the preparation of new heteroleptic SCO complexes that combine different properties coming from each ligand by exploiting the chemical versatility of 1bpp, which can be easily functionalized with different functional groups without significantly perturbing the SCO properties.

Finally, we can conclude that the incorporation of carboxylic acid groups to 1bpp ligand has been shown as a prolific source of compounds with interesting SCO properties in the solid state. Lateral functionalization of this ligand in the pyrazolyl groups and the use of a 3bpp derivative with lateral expanded aromaticity have been the most successful strategies to obtain abrupt thermal spin transitions close to room temperature.

All the SCO complexes obtained in this thesis are suitable for surface deposition thanks to the anchoring point provided by the carboxylic acid group. Deposition studies of the homoleptic Fe(II) 1bppCOOH and 1bpp3COOH complexes from chapters 2 and 3 – Part A, confirm the affinity of the functionalized ligand for metal oxides. Unfortunately, the loss of the ligand not bonded to the surface and oxidation of the Fe(II) to Fe(III) takes place. Heteroleptic complexes were then employed to understand the role played by the ligand non-interacting with the surface. The similar molecular structure of the 1bppCOEt heteroleptic complex compared to the homoleptic 1bppCOOH analogue, gave rise to the same outcome. On the other hand, preliminary results with the bulkier 3bpp-bhp ligand in the heteroleptic $[\text{Fe}(\text{1bppCOOH})(\text{3bpp-bhp})]^{2+}$ complex seems to increase the stability of the molecules deposited on the surface. If these results were confirmed, this could be a promising strategy to achieve the deposition of this family of SCO complexes.

Therefore, from chapters 2, 3, 4, and previous attempts of other authors,²⁻⁴ Fe(II) 1bpp moiety does not seem to be suitable to form switching SAMs, although other strategies such as the use of shorter deposition periods of time, different solvents, or expanded ligands, like the one used in Chapter 5, are yet to be investigated.

In Chapter 5, chemical functionalization of the terpy system with a functional group that provides a versatile anchoring point and the processability enabled by the higher solubility of the salt, compared to the neutral complex, allowed us to prepare SAMs of intact molecules from solution on different surfaces. These results confirm the affinity of the terpy ligand functionalized with a carboxylic acid group on metal oxides and noble metal surfaces. It has been proven that the formation of the deprotonated specie upon surface deposition takes place. Thermal SCO

properties of the monolayer have been confirmed with three different techniques. It displays a gradual SCO behavior, which suggests the absence of strong intermolecular interactions on the surface, representing, as far as we are aware, the first example of a SAM of active SCO molecules in direct contact to the surface from solution. This work opens the door for the construction of SCO nanostructure-based devices through soft methodologies compared to the high-cost conventional ultra-high vacuum techniques largely employed for this purpose. The effect in the stability of the SAMs of a family of complexes with different distances between the surface and the metal center, like the one presented in Chapter 5, and the possibility of increasing the cooperativity of the SAM spin transition by using bulkier ligands, are unresolved questions that will guide the future of our research.

6.2. References

- 1 M. Nadeem, J. Cruddas, G. Ruzzi and B. J. Powell, *Journal of American Chemical Society*, 2022, **144**, 9138–9148.
- 2 L. Pukenas, F. Benn, E. Lovell, A. Santoro, L. J. Kershaw Cook, M. A. Halcrow and S. D. Evans, *Journal of Materials Chemistry C*, 2015, **3**, 7890–7896.
- 3 I. Capell, University of Leeds, 2019.
- 4 L. Pukenas, University of Leeds, 2017.

7. Appendix

7.1. Characterization techniques.

Scanning Electron Microscopy - Energy Dispersive X-ray spectroscopy. Heavy elements ratios were measured with a Philips ESEM XL30 scanning electron microscope equipped with an EDAX DX-4 microsonde.

Elemental analyses (C, H, N, and S) were performed *ex-situ* in the Universidad Complutense de Madrid with a CE Instruments EA 1110 CHNS Elemental analyzer.

Single crystal diffraction. Single crystals all complexes were mounted on glass fibers using a viscous hydrocarbon oil to coat the crystal and then transferred directly to the cold nitrogen stream for data collection at the selected temperature on a Supernova diffractometer. The CrysAlisPro program, Oxford Diffraction Ltd., was used for unit cell determinations and data reduction. Empirical absorption correction was performed using spherical harmonics, implemented in the SCALE3 ABSPACK scaling algorithm. The structures were solved with the ShelXT structure solution program¹ and refined with the SHELXL-2013 program,² using Olex2.³ All non-hydrogen atoms were refined anisotropically except as noted and hydrogen atoms were placed in calculated positions and refined isotropically with a riding model. They have been included in chemical formula in the cif file and crystallographic tables. CCDC references containing the supplementary crystallographic data for the structures are summarized in **Table 7.1.1**. These data can be obtained free of charge from The Cambridge Crystallographic Data Centre via www.ccdc.cam.ac.uk/data_request/cif.

Single crystal diffractometer for photocrystallographic experiments. Crystallographic data at 20 K, before and after irradiation of the crystal, were measured using an Xcalibur 3 four-circle diffractometer (Oxford Diffraction) equipped with a 2D Sapphire3 CCD detector and monochromatic Mo-K α radiation source ($\lambda = 0.71073 \text{ \AA}$). The diffractometer was fitted with a Helijet Oxford Diffraction helium cryostat. A total of 10 crystals were tested upon irradiation with 660nm (at 0.7mW, 1.0mW, 1.1mW, 2mW, and 3.5mW for 1 to 8 minutes). To reduce damage of the crystal upon irradiation to the minimum, the crystal was mounted in the diffractometer upon irradiation with 660nm at 1.1mW directly at 20K. Full data collection was taken only on the crystal which did not get too damaged

while exposed to 660nm. No system change has been seen upon irradiation with 800nm, nor crystal trapping while inserting directly into 20K, has been observed.

Similar experiment has been performed at 85K by means of 700Plus nitrogen flow cryojet of Oxford Cryosystems. Irradiation with 660nm has been unsuccessful here.

Table 7.1.1. CCDC numbers of each structure.

Chapter	Compound	CCDC number
2	1(ClO ₄) ₂	1856814
	1(BF ₄) ₂	1856804
	1(BF ₄) ₂	1856805
	1(CF ₃ SO ₃) ₂ ·Me ₂ CO	1856809
	1(CF ₃ SO ₃) ₂ ·0.5Me ₂ CO	1856812
	1(AsF ₆) ₂ ·Me ₂ CO	1856806
	1(AsF ₆) ₂ ·2Me ₂ CO	1856807
	1(SbF ₆) ₂ ·Me ₂ CO	1856808
	1(SbF ₆) ₂ ·2Me ₂ CO	1856811
	2(ClO ₄) ₂ ·Me ₂ CO	1856813
2(ClO ₄) ₂ ·Me ₂ CO	1856810	
3	1	1910175
	[Fe(1bpp3COOMe) ₂](ClO ₄) ₂	1910176
	2 120 K	1944602
	2 300 K	1944601
	2 in the Dark	2191827
	2 + 660nm 60 s	2191828
	2 + 660 nm 360 s	2191829
	3	1944600
	1·2Me ₂ CO·0.5Et ₂ O	1917750
	1·Me ₂ CO 120 K	1917751
4	1·Me ₂ CO 300K	1917752
	2·0.5Me ₂ CO	1917753
	2·0.5Me ₂ CO	1917754
	1 120 K	2191823
5	1 300 K	2191824
	1 340 K	2191825

Powder X-ray Diffraction. A 0.7 or 1 mm glass capillary was filled with a freshly filtered or in contact with the mother liquor polycrystalline sample and mounted and aligned on an Empyrean PANalytical powder diffractometer, using CuK α radiation ($k = 1.54177 \text{ \AA}$). A total of 3 scans were collected at room temperature in the 2θ range $5\text{-}40^\circ$. For the temperature variable PXRD experiments, a liquid nitrogen-based device controller was set at the extreme of the capillary allowing to control the temperature in the 150 - 400 K range. After letting the temperature stabilize for 10 minutes, the same data acquisition program was used.

Differential scanning calorimetry (DSC). DSC measurements were done under nitrogen atmosphere in a Mettler Toledo DSC 821e apparatus with warming and cooling rates equal to $5 \text{ K}\cdot\text{min}^{-1}$. A correction from the sample holder was automatically applied. The heat flow thus measured ($\Delta H/\Delta t$) was used in the calculation of the approximate specific heat function as follows:

$$\frac{\Delta H}{\Delta T} = \frac{\Delta H}{\Delta t} \cdot \frac{M}{\beta \cdot m}$$

where m is the mass of the sample, M its molecular weight and β the heating (cooling) rate.

Thermogravimetric analyses (TG): Samples were measured using a TGA 550 (TA Instruments) at a heating rate of $5 \text{ }^\circ\text{C}/\text{min}$ from $25\text{-}700 \text{ }^\circ\text{C}$ under nitrogen.

Magnetic and photomagnetic properties. Magnetic measurements were performed with a Quantum Design MPMS-XL-5 SQUID magnetometer in the 2 to 400 K temperature range with an applied magnetic field of 0.1 T at a scan rate of $1 \text{ K}\cdot\text{min}^{-1}$ on a polycrystalline sample with a given mass. Photomagnetic measurements were performed irradiating with a Diode Pumped Solid State Laser DPSS-532-20 from Chylas coupled via an optical fibre to the cavity of the SQUID magnetometer. The optical power at the sample surface was adjusted to $3.4 \text{ mW}\cdot\text{cm}^{-2}$, and it was verified that it resulted in no significant change in magnetic response due to heating of the sample. The photomagnetic samples consisted of a thin layer of compound whose weight was obtained by comparison of a thermal spin crossover curve with that of a more accurately weighted sample of the same compound.

UV/Vis Spectroscopy: UV-vis absorption spectra are recorded on a Jasco V-670 spectrophotometer in baseline mode from 400 to 800 nm range, using 1.0 cm optical path quartz cuvettes. **Molar extinction coefficients were calculated using the Lambert-Beer equation.**

Atomic Force Microscopy (AFM). AFM measurements were performed with a Digital Instruments Veeco Nanoscope IVa AFM microscope in tapping mode, using silicon tips with a natural resonance frequency of 300 kHz and with an equivalent constant force of 40 N/m.

Matrix Assisted Laser Desorption Ionization – Time-Of-Flight Mass Spectrometry (MALDI-TOF MS). The samples were analyzed in a 5800 MALDI TOF/TOF (ABSciex) in positive reflection mode (3000 shots every position; LASER INTENSITY 4200) in a mass range of 200–1500 m/z. Previously, the sample and the acquisition method were externally calibrated with a Bruker PSCII solution. In order to do so, 0.5 μL of Bruker PSCII dissolution was spotted on a corner of the sample and allowed to air-dry at room temperature. After this, 0.5 μL of matrix (10mg/mL CHCA (Bruker) in 70% MeCN, 0.1% TFA) was spotted on the previous drop and allowed to air-dry at room temperature. On the diagonal opposite corner 0.5 μL of matrix solution was spotted and allowed to air-dry at room temperature.

Raman Spectroscopy/Surface-Enhance Raman Spectroscopy. Spectroscopical characterization was carried out on a LabRAM HR Evolution confocal Raman microscope (Horiba). The measurements were conducted with an excitation wavelength of 532 nm from a Helium Neon Laser source. The laser was focused using a 50 \times objective (0.8 NA), thus leading to a laser spot with a diameter of ca. 300 μm . An exposure time of 3s with 6 accumulations was employed. A CCD camera was used to collect the backscattered light that was dispersed by a 600 grooves per mm grating providing a spectral resolution of $\sim 1 \text{ cm}^{-1}$. The corresponding Raman spectra were then constructed by processing the data using Lab Spec 5 software. For temperature dependent Raman spectroscopy, a Linkam Scientific THMS600 temperature stage controlled with liquid nitrogen was employed. The measurements were performed after first cooling the sample to the lowest available temperature and then warming it up to the selected temperatures. After reaching the desired temperature, the sample was thermalized for 5 minutes before each measurement. Background correction was applied after averaging several scans across the substrate. Then, the intensities were normalized against a temperature-independent feature at 1365 cm^{-1} .

Room temperature X-ray Photoelectron Spectroscopy (XPS). XPS measurements at room temperature were performed on a Thermo Scientific™ K-Alpha™ X-ray photoelectron spectrometer. All spectra are collected using Al K α radiation (1486.6 eV), monochromatized by a twin crystal monochromator, yielding a focused X-ray spot (elliptical in shape with a major axis length of 400 μm) at 30 mA and 2 kV. For all the elements more than 50 spectra were recorded employing a step of 0.1 eV with a focused spot of 400 μm . Stoichiometry was calculated by peak

integration, using a theoretically estimated cross-section for each transition.⁴ Semiquantitative analysis has been estimated by areas of the deconvoluted peaks. Components were estimated using CasaXPS, a procedure involving Gaussian–Lorentzian line-shapes was fitted and the background in the spectra was subtracted by means of a linear or Shirley baseline

Variable temperature XPS: XPS measurements were carried out in a UHV apparatus with a base pressure in the 10^{-10} mbar range. Monochromatized Al K α radiation was used for XPS measurements (1486.6 eV, 100 W). The detector was an VSW hemispherical analyzer mounting a 16-channel detector, the angle between the analyzer axis and the X-ray source was 54.44° and the semicone angle of acceptance of the analyzer was 4°. The XPS spectra were measured with a fixed pass energy of 44 eV. The binding energy (BE) scale was calibrated setting the C1s signal of the sample at 285 eV. In order to minimize air exposure and atmospheric contamination, samples were mounted on a sample holder under dry nitrogen. Variable temperature experiments were performed using a liquid nitrogen-based cryostat connected to the XPS sample holder. Every spectrum represented herein results from averaging several spectra collected after 1 h of thermalization at a specific temperature. Stoichiometry was calculated by peak integration, using a theoretically estimated cross-section for each transition.⁴ Semiquantitative analysis has been estimated by areas of the deconvoluted peaks. Components were estimated using CasaXPS, a procedure involving Gaussian–Lorentzian line-shapes was fitted and the background in the spectra was subtracted by means of a linear or Shirley baseline.

X-Ray Absorption Spectroscopy (XAS). XAS experiments were performed at the BL29-BOREAS beamline of the Alba Synchrotron Light Facility (Barcelona, Spain). Fe and Co_{L_{2,3}}-edge spectra were recorded at different temperatures in HECTOR cryomagnet endstation in the 100 - 370 K range, the chamber pressure being lower than 1×10^{-10} mbar, and photon flux $\sim 5 \times 10^{11}$ s⁻¹ in total electron yield (TEY) method with an energy resolution of ~ 70 meV. XMCD spectra were recorded using alternatively left and right circularly polarized X-rays produced by an APPLE II undulator and a superconducting split coil setup generating a magnetic field up to 6 T in the direction of propagation of the incident photons.

Low temperature PXRD. PXRD diffraction data was collected at different temperatures using the PILATUS@SNBL diffractometer⁵ at the BM01A endstation of the Swiss–Norwegian Beamlines at the ESRF (Grenoble, France); the wavelength of the synchrotron radiation was set to $E = 19.92$ keV (0.62241 Å). For single crystal measurements, the detector was set to 100 mm horizontal and 80 mm vertical positions. The images were taken at a single ϕ , an exposure time of 0.1 sec/img with steps of 0.1° and 3600 number of images per period. PXRD

data was collected with the detector at 500 mm horizontal and 80 mm vertical positions, a single of rotation of 100° and an exposure time of 10s, both experiments in a shutter-free mode with the PILATUS2M detector. The raw data were processed with the SNBL Toolbox⁵; the integrated intensities were extracted from the frames, scaled, and corrected for absorption with the CrysAlisPro software⁶. The scans used to analyze the composition are an average of the last single scans once the positions of the peaks were not changing drastically.

7.2. Materials

All reagents were purchased and used without further purifications.

Silicon dioxide substrates. Silicon substrates were sonicated 3 × 15 min in freshly prepared H₂O₂/NH₄OH/H₂O (1:1:2) solutions, rinsed with milli-Q water, sonicated for 10 min in milli-Q water twice, and dried under a N₂ stream.

Silver substrates. They were prepared by thermal evaporation of silver on top of silicon dioxide or glass substrates previously covered with 2-3 nm of chromium as an adhesive layer. Mechanically roughened silver substrates were prepared by gently applying pressure with a sharp tip over the surface. They were cleaned under the flame and immersed for 6 h in a 1 mM anhydrous DMA solution of the complex. After that, they were washed and rinsed several times (6 times) with clean DMA to remove any physisorbed material and dried under N₂ stream.

7.3. References

- 1 G. M. Sheldrick, *Acta Crystallographica Section A: Foundations of Crystallography*, 2015, **71**, 3–8.
- 2 G. M. Sheldrick, *Acta Crystallographica Section C: Structural Chemistry*, 2015, **71**, 3–8.
- 3 O. v. Dolomanov, L. J. Bourhis, R. J. Gildea, J. A. K. Howard and H. Puschmann, *Journal of Applied Crystallography*, 2009, **42**, 339–341.
- 4 J. J. Yeh and I. Lindau, *Atomical Data and Nuclear Data Tables*, 1985, **32**, 1–155.
- 5 V. Dyadkin, P. Pattison, V. Dmitriev and D. Chernyshov, *Journal of Synchrotron Radiation*, 2016, **23**, 825–829.
- 6 Rigaku Oxford Diffraction, CrysAlisPro Software System. Version 1.171.38.41, <http://www.rigaku.com/en>.